IN VIVO TISSUE-LEVEL THRESHOLDS FOR SPINAL CORD INJURY

by

JASON MAIKOS

A Dissertation submitted to the

Graduate School-New Brunswick

Rutgers, The State University and

The Graduate School of Biomedical Sciences

University of Medicine and Dentistry of New Jersey

in partial fulfillment of the requirements

for the degree of

Doctor of Philosophy

Graduate Program in the Department of Biomedical Engineering

written under the direction of

David Shreiber

and approved by

_____

_____

_____

_____

New Brunswick, New Jersey

October 2007

ABSTRACT OF THE DISSERTATION

In Vivo Tissue Level Thresholds for Spinal Cord Injury

by JASON MAIKOS

Dissertation Director:
David Shreiber

Primary damage to the blood-spinal cord barrier (BSCB) is a nearly universal consequence of spinal cord injury that contributes significantly to the overall pathology. The in vivo tissue-level thresholds for mechanical disruption of the BSCB were identified by comparing the results of spinal cord contusions produced with weight drop injury to a finite element analysis (FEA) of the experimental model. The extent and severity of primary, physical disruption of the BSCB was quantified in adult rats five minutes after graded trauma induced with the Impactor weight drop model of spinal cord contusion. The volume of extravasation of three markers of distinct size – fluorescently labeled hydrazide (~730Da), fluorescently labeled bovine serum albumin (~70kDa), and immunohistochemically labeled red blood cells (~5μm) was evaluated in both the gray and white matter. Extravasation volumes increased with increasing drop height and decreasing species size, and were greater in gray matter than in white matter. A three-dimensional finite element analysis of the weight drop model was performed and validated with the in vivo experimental peak displacement of the spinal cord at two loading conditions. The peak compression of the model was within ten percent of the experimental results. A parametric analysis revealed that the model was most sensitive to changes in the viscoelastic properties of the spinal cord. The finite element

model provided temporal and spatial profiles of mechanical parameters that were used to identify tissue-level thresholds for BSCB injury using logistic regression analysis. Thirteen mechanical parameters, including measures of stress, strain, and strain rate were investigated as predictors of BSCB injury. Maximum principal strain (LEP) was considered the best predictor of injury in the gray matter, while von Mises strain (LEVM) was the best predictor of injury in the white matter, although the LEVM thresholds for white matter included relatively substantial error compared to the thresholds for gray matter. The results can be used to improve means and measures of preventing spinal cord injury in humans, define loading conditions for in vitro models of injury, and design new experimental models that produce specific patterns of injury.

TABLE OF CONTENTS

INDEX OF TABLES

INDEX OF FIGURES

CHAPTER 1: INTRODUCTION

In the United States, there are approximately 11,000 new spinal cord injuries each year, and about 300,000 individuals currently live with a spinal cord injury (SCI) (Berkowitz 1998), primarily affecting young adults. Motor vehicle crashes account for a majority of SCIs, followed by falls and acts of violence (Figure 1-1). Spinal cord injuries (SCIs) cost the nation an estimated $9.7 billion each year (Berkowitz 1998), yet, little is known about the mechanical mechanism of injury and tissue tolerance of SCI – that is, how the spinal cord is damaged.

The central hypothesis of this research is that the severity and extent of primary vascular damage during SCI can be predicted by the distributions of the mechanical states of stress and/or strain in the spinal cord during trauma. The goal of this thesis is to identify mechanical thresholds for spinal cord injury in the rat. SCI is caused by an initial, primary insult to spinal cord, which then generates secondary events that injure neighboring, intact tissue. The primary injury to the spinal cord vasculature, part of which is the disruption of the blood-spinal cord barrier (BSCB), plays a crucial role in the development of secondary events. A dual approach, comprising animal and finite element models, was used to determine the in vivo spinal cord damage required to cause BSCB injury.

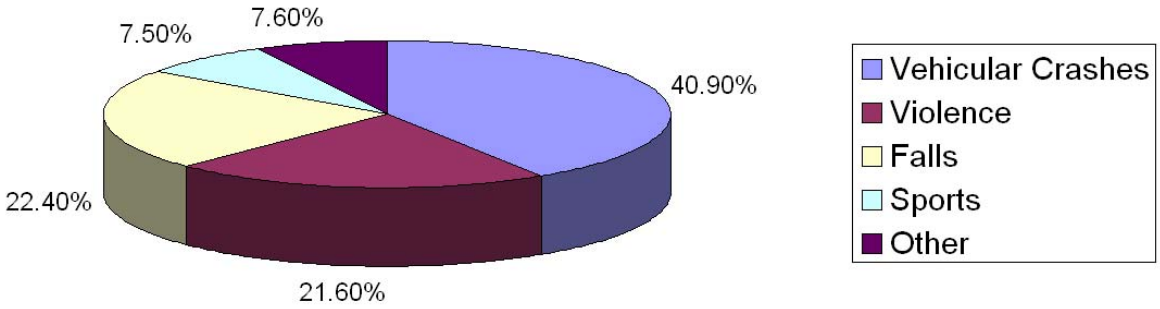

Figure 1-1: Etiology of SCI. Motor Vehicle Accidents account for 40.9% of SCIs, followed by falls at 22.4%

CLINICAL SIGNIFICANCE

In SCI, the initial mechanical insult causes the disruption of spinal cord structures known as primary injury. This is followed by secondary injury, which is an evolution of events including inflammation, ischemia, oxidative damage, and free radical development, as well as other factors that injure otherwise unaffected spinal cord tissue (Mautes, Weinzierl et al. 2000). The primary injury to the spinal cord vasculature, part of which is the disruption of the blood-spinal cord barrier (BSCB), plays a crucial role in the development of secondary events. However, the extent of secondary injury defines the overall degree of neuropathology. Contusions are the most common form of SCI and are defined as bruising of the spinal cord (Berkowitz 1998).

The severity of injury depends on the degree of mechanical insult as well as the location of injury within the spinal cord and which nerve fibers are damaged. An SCI at the thoracic vertebral level usually results in paraplegia, which is the loss of movement in legs and the trunk. An SCI to the cervical region usually results in quadriplegia, which is loss of function of all four limbs. In addition to paralysis, SCI patients also suffer from other symptoms, including loss of autonomic responses (breathing, bowel, and bladder control) (NSCIA 2006). SCI patients are also prone to infections and sores. To further classify SCIs, they are defined as either complete or incomplete. A complete injury is the total loss of function below the injury level, whereas an incomplete injury has some restored function (NSCIA 2006). Overall, currently 85% of SCI patients who survive the first 24 hours survive at least a decade later, which has been due to improvements in modern antibiotics and rehabilitation techniques (NSCIA 2006). The most common cause of death is respiratory ailment (NSCIA 2006).

The pathology following SCI has been extremely well studied and the functional time course of injury has been defined (Balentine 1978; Griffiths, Burns et al. 1978; Wagner and Stewart 1981; Noble and Wrathall 1989; Noble and Wrathall 1989; Popovich, Horner et al. 1996; Beattie, Bresnahan et al. 1997; Carlson, Parrish et al. 1998). Because secondary injury dictates the overall neuropathology of SCI, they are the principal targets of post-trauma therapy and have been researched extensively in laboratory and clinical settings (Blight 1985; Blight 1991; Blight 1992; Amar and Levy 1999). *However, the underlying tissue-level biomechanics of primary spinal cord injury - which by definition are what causes the injury - have received only superficial investigation even though primary injury significantly affects the development of secondary events.*

MECHANISMS OF SPINAL CORD CONTUSIONS

No one to date has confirmed a biomechanical mechanism of spinal cord contusion – that is, what mechanical parameter, and what value of that parameter, causes contusions of the spinal cord. A number of biomechanical and clinical factors can combine to cause SCI. However, most biomechanical studies for SCI have focused on closed spinal cord injuries or injury to the spinal column, such as fractures, extension-distraction, hyperextension, and buckling of the spine (Sances, Myklebust et al. 1984; Nightingale, McElhaney et al. 1996; Winkelstein and Myers 1997; Yoganandan, Kumaresan et al. 2001; Cusick and Yoganandan 2002). A natural outcome of a closed injury to the spine is injury to the spinal cord, resulting in the subsequent manifestations of SCI. However, after an injury to the spine that results in SCI, *it still remains unknown how the mechanical states of stress and strain are distributed in the spinal cord and how these distributions result in specific pathologies.*

Closed injuries often do not allow researchers to study spinal cord injury in a reproducible manner. Thus, researchers have developed many commonly used in vivo SCI models that emulate the clinical aspects of SCI to produce injuries, such as compression models (Beggs and Waggener 1976; Nacimiento, Bartels et al. 1986; Guth, Zhang et al. 1994; Jaeger and Blight 1997), ischemia models (Kanellopoulos, Kato et al. 1997), crush injuries (Zhang, Krebs et al. 1997), contusion models (Dohrmann, Panjabi et al. 1976; Noble and Wrathall 1989; Stokes 1992; Young 2002), and hemisections and transections (Goshgarian, Yu et al. 1989; Noble and Ellison 1989; Dusart and Schwab 1994). Hemisections and transections offer a more distinct reproducibility than other injury models, but have less relevance clinically. Many researchers have examined the primary and secondary effects of contusive SCI in animal models because of its more clinical significance (Stokes 1992; Young 2002). Reginald Allen first used the contusion model for studying SCI in dogs in 1911. It involved dropping a calibrated weight from a defined set of distances onto the exposed dura of the spinal cord (Allen, 1911). Since its inception, the weight drop model has been refined, modified, and standardized for other experimental animal models to generate reproducible injury (Campbell, DeCrescito et al. 1973; Yeo, Payne et al. 1975; Dohrmann, Panjabi et al. 1976; Koenig and Dohrmann 1977; Borovich, Peyser et al. 1978; Wrathall, Pettegrew et al. 1985; Stokes, Noyes et al. 1992; Young 2002). Another commonly used contusion model was developed by Stokes, et al., which uses an electromagnetic device to displace the spinal cord at a set rate and distance (Stokes 1992). Tarlov developed a technique to compress the spinal cord by balloons and cuffs, which produced reproducible central cord necrosis (Tarlov and Klinger 1954). Many previous studies have identified and emphasized various features of experimental spinal cord trauma.

This research thesis focused on the spinal cord contusion injury model; more specifically, we performed a complete biomechanical analysis of the Impactor weight drop model. Biomechanical analyses of the spinal cord have been mostly superficial, mainly focusing on correlating loading parameters to the extent of injury without understanding the intraparenchymal mechanics. Hung et. al. reported a preliminary biomechanical analysis of SCI, in which he investigated the mechanical forces of spinal cord injury in cats. They noted that dropping a 20 gram weight from 15 cm had a peak force of about 1.2 lb (0.544 kg), while the maximum impact stress was as high as 42 lb/in^2 (2200 mmHg) (Hung, Albin et al. 1975). In a later study, Koenig and Dorhmann studied the correlation of different mass and height combinations to the extent of SCI in cats. Even though each group received the same '400 g-cm' contusion, each height and weight combination showed different degrees of injury (Koenig and Dohrmann 1977). Similarly, Wagner et. al. researched how different spinal cord impact magnitudes affected the distribution of edema in the spinal cord in cats. They showed that higher magnitude impacts produced longitudinal increases in tissue water, as compared with lower magnitudes (Wagner and Stewart 1981). However, the mechanics of these models, especially at the tissue level, are poorly understood.

Our investigation focused on the severity and extent of in vivo blood-spinal cord barrier (BSCB) breakdown, a frequent occurrence in SCI experimental models, as well as clinical cases. We focused on BSCB breakdown immediately following injury to examine the effect of *primary* damage of the spinal cord – that is, the direct result of the mechanical insult. Clinically and in vivo, BSCB breakdown is exacerbated by secondary insults, but for a biomechanical analysis and ultimately injury prevention, a detailed understanding of the consequences of the primary mechanical insult is required.

The Impactor model and other devices have been used to thoroughly discern the neurohistological pathology of SCI as well as establish the functional time course following SCI. Vascular injury following SCI causes early hemorrhage in the highly vascularized gray matter, degradation of the BSCB, neuronal cell loss, and finally an inflammatory response (Amar and Levy 1999; Mautes, Weinzierl et al. 2000). These vascular events following SCI each lead to secondary injury. Secondary injury is not completely understood, but research has shown that ischemia, edema, and oxidative damage in the spinal cord lead to subsequent spinal cord injury, including affecting intact, uninjured tissue (Balentine 1978; Kwo, Young et al. 1989). This thesis focused on characterizing the tolerance of the microvasculature to trauma due to the large effect microvascular damage has on the resulting secondary pathogenesis. *We studied the intraparenchymal stresses and strains during trauma from the Impactor to discern the exact mechanisms of primary tissue injury and therefore were able to determine tissue tolerances.* These tissue-level tolerances can be used to computationally identify regions of the spinal cord that are susceptible to injury. Thus, we can understand how traumatic loading conditions experienced by a person, such as during car accidents or falls, lead to mechanical failure of the spinal cord tissue that are the proximal cause of the injury response. Through understanding the tolerance of the tissue responsible for microvascular hemorrhage and primary damage to the BSCB, we will provide a benchmark to prevent not only the initial injury, but also the chain of secondary pathologies that follow vascular disruption of SCI.

To our knowledge, this is the first characterization of the mechanical tolerance of the BSCB. Similar approaches have been used to study the biomechanics of brain injury. A study by Shreiber et al. examined the mechanical tolerance of the blood-brain barrier (BBB)

to cortical contusion. This study showed that while all potential mediators of mechanical injury were excellent predictors of BBB damage, only the maximum principal strain remained invariant across loading conditions and was identified as the best predictor of BBB damage (Shreiber 1998).

We implemented an integrative, multi-disciplinary approach to develop thresholds for predicting spinal cord vascular injury involving research from many facets of science and engineering, including in vivo experiments, material testing, and computational models. We narrowed the focus of our research onto two disciplines for understanding the tissue tolerance for spinal cord injury: an experimental model of spinal cord contusion (the Impactor Weight Drop Model), and a validated finite element analysis of that experimental model. We developed a computational simulation of the Impactor weight drop model that was used to understand the biomechanics of SCI, including injury to the blood-spinal cord barrier. These findings were used in conjunction with our experimental Impactor studies to investigate of the functional deficits that follow SCI and ultimately to determine mechanical thresholds for injury.

These areas represent the four main chapters of this thesis: Chapter 2, entitled *Immediate damage to the blood-spinal cord barrier due to mechanical trauma*, presents the results of our experimental study of spinal cord injury using the Impactor weight drop model. The experimental study provided spatial maps of injury, where the blood-spinal cord barrier breaks down as well as provided the data necessary to validate the finite element model. Chapter 3, *Mechanical properties of dura mater from the rat brain and spinal cord,* presents hyperelastic-viscoelastic constitutive laws for spinal cord dura mater that, when combined with published data on the rat spinal cord properties, provide a description of the structural

response of the spinal cord to mechanical loading. In chapter 4 entitled, *Finite element analysis of spinal cord injury in the rat*, we developed and validated a 3-dimensional finite element model that simulates the Impactor model employed in Chapter 2 using material properties derived in Chapter 3. We validated the model against the in vivo displacement from Chapter 2, while examining the mitigating factors in the development, and assessing the sensitivity of the analysis to various modeling assumptions. In Chapter 5, entitled *In Vivo Tissue-Level Thresholds for Mechanical Injury of the Blood-Spinal Cord Barrier*, we present our proposal for thresholds for mechanical injury to the BSCB. The thresholds are based on robust statistical comparisons of the experimental BSCB injury from Chapter 2 to the results of the finite element model from Chapter 4. Finally, a discussion of the overall results and future directions is presented in Chapter 6.

REFERENCES

AMAR, A. P. and LEVY, M. L. (1999). "Pathogenesis and pharmacological strategies for mitigating secondary damage in acute spinal cord injury." Neurosurgery **44**(5): 1027-39; discussion 1039-40.

BALENTINE, J. D. (1978). "Pathology of experimental spinal cord trauma. I. The necrotic lesion as a function of vascular injury." Lab Invest **39**(3): 236-53.

BEATTIE, M. S., BRESNAHAN, J. C., KOMON, J., et al. (1997). "Endogenous repair after spinal cord contusion injuries in the rat." Exp Neurol **148**(2): 453-63.

BEGGS, J. L. and WAGGENER, J. D. (1976). "Transendothelial vesicular transport of protein following compression injury to the spinal cord." Lab Invest **34**(4): 428-39.

BERKOWITZ, E. D. (1998). "Revealing America's welfare state. [Review of: Howard, C., The hidden welfare state: tax expenditures and social policy in the United States. Princeton University Press, 1997]." Rev Am Hist **26**(3): 620-4.

BLIGHT, A. R. (1985). "Delayed demyelination and macrophage invasion: a candidate for secondary cell damage in spinal cord injury." Cent Nerv Syst Trauma **2**(4): 299-315.

BLIGHT, A. R. (1991). "Morphometric analysis of a model of spinal cord injury in guinea pigs, with behavioral evidence of delayed secondary pathology." J Neurol Sci **103**(2): 156-71.

BLIGHT, A. R. (1992). "Macrophages and inflammatory damage in spinal cord injury." J Neurotrauma **9 Suppl 1**: S83-91.

BOROVICH, B., PEYSER, E. and GRUSKIEWICZ, J. (1978). "Acute central and intermediate cervical cord injury." Neurochirurgia (Stuttg) **21**(3): 77-84.

CAMPBELL, J. B., DECRESCITO, V., TOMASULA, J. J., DEMOPOULOS, H. B., FLAMM, E. S. and RANSOHOFF, J. (1973). "Experimental treatment of spinal cord contusion in the cat." Surg Neurol **1**(2): 102-6.

CARLSON, S. L., PARRISH, M. E., SPRINGER, J. E., DOTY, K. and DOSSETT, L. (1998). "Acute inflammatory response in spinal cord following impact injury." Exp Neurol **151**(1): 77-88.

CUSICK, J. F. and YOGANANDAN, N. (2002). "Biomechanics of the cervical spine 4: major injuries." Clin Biomech (Bristol, Avon) **17**(1): 1-20.

DOHRMANN, G. J., PANJABI, M. M. and WAGNER, F. C., JR. (1976). "An apparatus for quantitating experimental spinal cord trauma." Surg Neurol **5**(5): 315-8.

DUSART, I. and SCHWAB, M. E. (1994). "Secondary cell death and the inflammatory reaction after dorsal hemisection of the rat spinal cord." Eur J Neurosci **6**(5): 712-24.

GOSHGARIAN, H. G., YU, X. J. and RAFOLS, J. A. (1989). "Neuronal and glial changes in the rat phrenic nucleus occurring within hours after spinal cord injury." J Comp Neurol **284**(4): 519-33.

GRIFFITHS, I. R., BURNS, N. and CRAWFORD, A. R. (1978). "Early vascular changes in the spinal grey matter following impact injury." Acta Neuropathol (Berl) **41**(1): 33-9.

GUTH, L., ZHANG, Z., DIPROSPERO, N. A., JOUBIN, K. and FITCH, M. T. (1994). "Spinal cord injury in the rat: treatment with bacterial lipopolysaccharide and indomethacin enhances cellular repair and locomotor function." Exp Neurol **126**(1): 76-87.

HUNG, T. K., ALBIN, M. S., BROWN, T. D., BUNEGIN, L., ALBIN, R. and JANNETTA, P. J. (1975). "Biomechanical responses to open experimental spinal cord injury." Surg Neurol **4**(2): 271-6.

JAEGER, C. B. and BLIGHT, A. R. (1997). "Spinal cord compression injury in guinea pigs: structural changes of endothelium and its perivascular cell associations after blood-brain barrier breakdown and repair." Exp Neurol **144**(2): 381-99.

KANELLOPOULOS, G. K., KATO, H., HSU, C. Y. and KOUCHOUKOS, N. T. (1997). "Spinal cord ischemic injury. Development of a new model in the rat." Stroke **28**(12): 2532-8.

KOENIG, G. and DOHRMANN, G. J. (1977). "Histopathological variability in 'standardised' spinal cord trauma." J Neurol Neurosurg Psychiatry **40**(12): 1203-10.

KWO, S., YOUNG, W. and DECRESCITO, V. (1989). "Spinal cord sodium, potassium, calcium, and water concentration changes in rats after graded contusion injury." J Neurotrauma **6**(1): 13-24.

MAUTES, A. E., WEINZIERL, M. R., DONOVAN, F. and NOBLE, L. J. (2000). "Vascular events after spinal cord injury: contribution to secondary pathogenesis." Phys Ther **80**(7): 673-87.

NACIMIENTO, A. C., BARTELS, M. and LOEW, F. (1986). "Increased functional vulnerability to acute compression injury of a spinal cord segment under barbiturate anesthesia." Surg Neurol **26**(1): 9-12.

NIGHTINGALE, R. W., MCELHANEY, J. H., RICHARDSON, W. J. and MYERS, B. S. (1996). "Dynamic responses of the head and cervical spine to axial impact loading." J Biomech **29**(3): 307-18.

NOBLE, L. J. and ELLISON, J. A. (1989). "Effect of transection on the blood-spinal cord barrier of the rat after isolation from descending sources." Brain Res **487**(2): 299-310.

NOBLE, L. J. and WRATHALL, J. R. (1989). "Correlative analyses of lesion development and functional status after graded spinal cord contusive injuries in the rat." Exp Neurol **103**(1): 34-40.

NOBLE, L. J. and WRATHALL, J. R. (1989). "Distribution and time course of protein extravasation in the rat spinal cord after contusive injury." Brain Res **482**(1): 57-66.

POPOVICH, P. G., HORNER, P. J., MULLIN, B. B. and STOKES, B. T. (1996). "A quantitative spatial analysis of the blood-spinal cord barrier. I. Permeability changes after experimental spinal contusion injury." Exp Neurol **142**(2): 258-75.

SANCES, A., JR., MYKLEBUST, J. B., MAIMAN, D. J., LARSON, S. J., CUSICK, J. F. and JODAT, R. W. (1984). "The biomechanics of spinal injuries." Crit Rev Biomed Eng **11**(1): 1-76.

SHREIBER, D. I. (1998). In Vivo Failure Thresholds For Cortical Cerebrovascular Tissue. Bioengineering. Philadelphia, University of Philadelphia**:** 100.

STOKES, B. T. (1992). "Experimental spinal cord injury: a dynamic and verifiable injury device." J Neurotrauma **9**(2): 129-31; discussion 131-4.

STOKES, B. T., NOYES, D. H. and BEHRMANN, D. L. (1992). "An electromechanical spinal injury technique with dynamic sensitivity." J Neurotrauma **9**(3): 187-95.

TARLOV, I. M. and KLINGER, H. (1954). "Spinal cord compression studies. II. Time limits for recovery after acute compression in dogs." AMA Arch Neurol Psychiatry **71**(3): 271-90.

WAGNER, F. C., JR. and STEWART, W. B. (1981). "Effect of trauma dose on spinal cord edema." J Neurosurg **54**(6): 802-6.

WINKELSTEIN, B. A. and MYERS, B. S. (1997). "The biomechanics of cervical spine injury and implications for injury prevention." Med Sci Sports Exerc **29**(7 Suppl): S246-55.

WRATHALL, J. R., PETTEGREW, R. K. and HARVEY, F. (1985). "Spinal cord contusion in the rat: production of graded, reproducible, injury groups." Exp Neurol **88**(1): 108-22.

YEO, J. D., PAYNE, W., HINWOOD, B. and KIDMAN, A. D. (1975). "The experimental contusion injury of the spinal cord in sheep." Paraplegia **12**(4): 279-98.

YOGANANDAN, N., KUMARESAN, S. and PINTAR, F. A. (2001). "Biomechanics of the cervical spine Part 2. Cervical spine soft tissue responses and biomechanical modeling." Clin Biomech (Bristol, Avon) **16**(1): 1-27.

YOUNG, W. (2002). "Spinal cord contusion models." Prog Brain Res **137**: 231-55.

ZHANG, Z., KREBS, C. J. and GUTH, L. (1997). "Experimental analysis of progressive necrosis after spinal cord trauma in the rat: etiological role of the inflammatory response." Exp Neurol **143**(1): 141-52.

CHAPTER 2: IMMEDIATE DAMAGE TO THE BLOOD-SPINAL CORD BARRIER DUE TO MECHANICAL TRAUMA

ABSTRACT

Primary damage to the blood-spinal cord barrier (BSCB) is a nearly universal consequence of spinal cord injury that contributes significantly to the overall pathology. We have characterized quantitatively the extent and severity of primary, physical disruption of the BSCB in adult rats five minutes and fifteen minutes after graded trauma induced with the Impactor weight drop model of spinal cord contusion. Animals were injured by dropping a 10g mass 12.5, 25, or 50mm (n_{level}=8) on to the exposed mid-thoracic spinal cord. The volume of extravasation of three markers of distinct size – fluorescently labeled hydrazide (~730Da), fluorescently labeled bovine serum albumin (~70kDa), and immunohistochemically labeled red blood cells (~5μm dia) were quantified in both the gray and white matter. The results indicate that spinal cord trauma causes immediate, non-specific vascular changes that are well-predicted by mechanical parameters. Extravasation volume increased significantly with increasing drop height and decreasing marker size. Extravasation volumes for all three markers were greater in gray matter than in white matter, and were better correlated to the rate of spinal cord compression than to the depth of spinal cord compression, which suggests that tissue-level strain rate effects contribute to primary spinal cord microvasculature pathology. The relationship between the response of the spinal cord and the injury pattern points towards opportunities to control the distribution and extent of injury patterns in animal models of spinal cord injury through a precise understanding of model and tissue biomechanics, as well as potential improvements in means of preventing spinal cord injury.

INTRODUCTION

New spinal cord injuries (SCI) occur in approximately 11,000 people each year in the United States (Berkowitz 1998). Damage to the vasculature, notably the breakdown of the blood spinal-cord barrier (BSCB), is an almost universal consequence of SCI clinically as well as in animate models (Griffiths and Miller 1974; Balentine 1978; Faden, Gannon et al. 1988; Schlosshauer 1993; Noble, Mautes et al. 1996). During SCI, the initial mechanical insult can disrupt the BSCB (primary injury), causing the non-specific influx of normally impermeable molecules and agents into the contused spinal cord. The blood-borne species that cross the compromised vasculature can range from small molecules (due to minor BSCB permeability changes) to red blood cells from gross hemorrhage (Dohrmann and Wick 1971; Griffiths and Miller 1974; Beggs and Waggener 1976; Faden, Gannon et al. 1988; Noble and Wrathall 1989; Noble, Mautes et al. 1996; Popovich, Horner et al. 1996; Bilgen, Al-Hafez et al. 2005). It has been shown that small molecules can cross the BSCB as late as 28 days post injury (Popovich, Horner et al. 1996). The mechanical disruption of the vasculature and BSCB then contributes to the evolution of secondary events that injure neighboring tissue, including continued insults on uncompromised sections of the BSCB that affect its function and lead to increased permeability, dictating a significant portion of the overall pathology following SCI (Mautes, Weinzierl et al. 2000).

As such, the functional time course and neuropathology of vascular damage and BSCB breakdown has been studied extensively with several models of traumatic SCI, including weight drop (Albin, White et al. 1968; Dohrmann, Panjabi et al. 1976; Noble and Wrathall 1989; Gruner 1992; Basso, Beattie et al. 1996; Young 2002), pneumatic/electromagnetic impactor (Bresnahan, Beattie et al. 1987; Noyes 1987; Behrmann,

Bresnahan et al. 1992; Stokes, Noyes et al. 1992), and compression (Beggs and Waggener 1975; Rivlin and Tator 1978; Farooque, Zhang et al. 1992; Fehlings and Tator 1995; Jaeger and Blight 1997). A variety of techniques have been employed to evaluate BSCB injury, such as injection of probes (typically labeled albumin, labeled dextrans, or horseradish peroxidase) followed by qualitative or quantitative microscopy (Griffiths and Miller 1974; Beggs and Waggener 1975; Wagner and Stewart 1981; Noble and Wrathall 1987; Farooque, Zhang et al. 1992; Fehlings and Tator 1995; Jaeger and Blight 1997; Whetstone, Hsu et al. 2003), radiolabeled tracers followed by autoradiography (Popovich, Horner et al. 1996), and contrast-enhanced magnetic resonance imaging (MRI) (Terae, Takahashi et al. 1997; Bilgen and Narayana 2001). Most of these studies focused on BSCB permeability from hours-to-weeks post injury, but a few examined acute changes (< 5-minutes), where the bulk of injury can be assumed to be directly caused by overt vascular damage from primary mechanical perturbation of the tissue, rather than a combination of mechanics and secondary insults, which compromise BSCB function. Collectively, these studies indicate that initial permeability changes occur primarily in the gray matter and spread to the white matter during the first hours after injury, and can persist for as long as a month post injury (Popovich, Horner et al. 1996). While these studies demonstrate that the degree of permeability changes increases with the severity of injury parameters (e.g. drop height for weight drop injury), in no case has BSCB/microvascular integrity been correlated to the physical response of the tissue (for example, compression distance and compression rate during weight drop). Moreover, while microvascular injury/BSCB permeability changes following SCI have been documented for a wide range of molecules – including [^{14}C]-α-aminoisobutyric acid (molecular weight (MW) = 103Da), gadopentetate-dimeglumine (MW = 938Da), horseradish

peroxidase (MW = ~40KDa), albumin (MW~=70KDa), a wide range of dextrans (MW ~= 20,000 to 150,000), and red blood cells to indicate hemorrhage, it is difficult to draw quantitative conclusions regarding relative changes among these molecules because of the disparity of methods employed, and because, in most cases, changes were measured for only a single marker. A noted exception is Wagner and Stewart, where extravasation of fluorescein-labeled dextrans ranging from 20,000 to 150,000 molecular weight (MW) was examined, each in separate animals, 8 hours after injury, with no significant differences observed (Wagner and Stewart 1981).

In the present study, acute changes to the BSCB due to mechanical disruption were quantified following experimental SCI in the rat using the Impactor weight drop technique. The severity and extent of mechanically-mediated BSCB injury were evaluated by determining the volume of molecule-, protein-, and cell-sized species that extravasated across injured vasculature into spinal cord parenchyma 5-minutes and 15-minutes following trauma. Impact parameters (impact velocity, cord compression depth, and cord compression rate) measured during injury were correlated to the distribution of extravasation volume for a preliminary measure of BSCB sensitivity to specific mechanical variables, such as stress and strain.

MATERIALS AND METHODS

Surgical procedure

Standard procedures for the Impactor experiments were followed (Young 2002). Adult, female Long Evans Hooded rats, 77 +/- 5 days old (220-240 g; n=33) were obtained from Simonsen Labs (Gilroy, CA, USA) and housed for 1 week prior to experimentation to allow the rats to adapt to their environment. Following pentobarbital-induced anaesthesia (45mg/kg, i.p), a T9-T10 laminectomy was performed under sterile conditions.

Blood-borne species labeling scheme:

BSCB permeability was evaluated for three distinct species that spanned a wide range in size: Alexa Flour 568-labeled hydrazide (707Da, 576 nm excitation, 599 emission Molecular Probes, Eugene OR, USA); Alexa Flour 488-labeled bovine serum albumin (BSA) (~70kDa, 497 nm excitation, 520 nm emission, Molecular Probes, Eugene, OR, USA); and native red blood cells (~5μm diameter). Ten minutes prior to injury, animals were given an intravenous injection into the femoral vein of 1ml of tracer solution consisting of 1mg/kg of the labeled hydrazide and labeled BSA dissolved in 0.9% saline.

Injury and Post-Injury Procedures

All contusions were performed using the Impactor. The Impactor is a 10g rod, with a 2.5mm head. Rat spinal cords at age 77 days are approximately 3mm in width. Animals were suspended by clamping the T8 and T11 dorsal vertebral processes. The rod was centered over the laminectomy, raised to the appropriate height, and dropped onto the exposed dura. Impactor injury was performed at three drop heights (n_{height} = 8): 12.5mm, 25mm, and 50mm. Additional animals (n = 3) received only the surgery, and one (n = 1)

served as an unoperated control. Injury was produced 60 +/- 2 minutes after anesthesia induction.

The Impactor rod is mechanically linked to a digital optical potentiometer (S2 Series, US Digital, Vancouver, WA**),** which sends Transitor-Transitor Logic (TTL) pulses (±5V) for each small angular movement that allows the rod movements to be measured precisely at ±20 μm and ±20 μsec (Young 2002). A micromanipulator is used to lower the Impactor head precisely on the surface of the spinal cord to determine the zero point. The rod is then raised to appropriate drop height and released for impact. The software detects rod release from the change of rod position then collects a stream of TTL pulses from the digital potentiometers representing rod movements at a 20 KHz sampling rate (Young 2002). Contact with the spinal cord closes the circuit between the rod and the cord. The Impactor uses electrical contact to measure the time of contact, which allows the software to perform a linear regression of the rod movement 2msec before contact with the spinal cord to estimate impact velocity (Young 2002). A second probe is placed on the dorsal surface of the vertebral body immediately proximal to the laminectomy and is linked to a separate digital optical potentiometer to evaluate movement of the underlying spinal column. The depth of compression is then determined by subtracting the vertebral body motion from the motion of the impacting rod. Compression rate is determined from compression distance and compression time. Impact velocity, cord compression distance, and cord compression rate were recorded for each experiment (Figure 2-1).

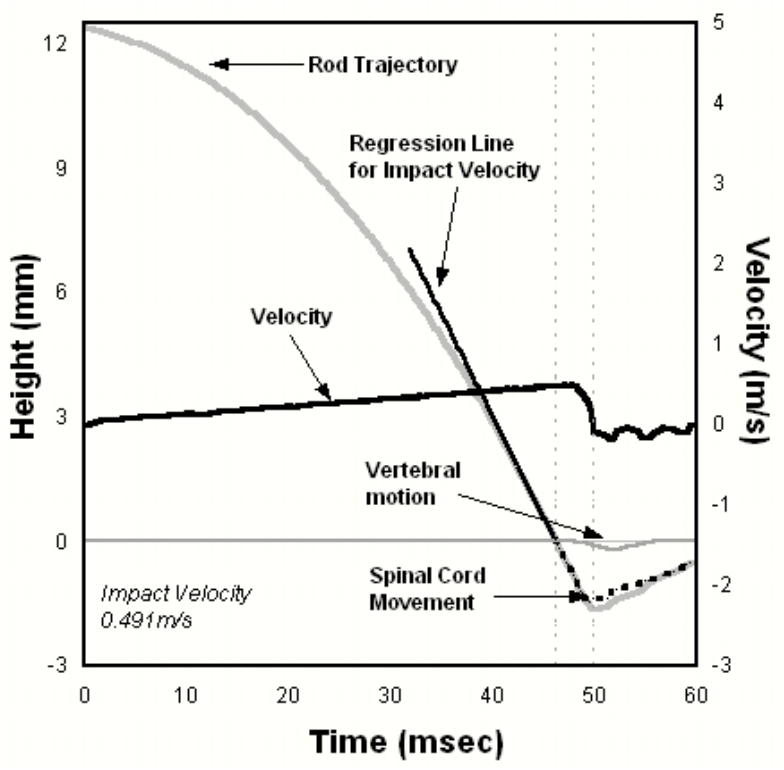

Figure 2-1: Example output following an Impactor weight drop injury (12.5mm drop height). Separate optical potentiometers record the motion of the impacting rod and the vertebral body adjacent to the impact site. Vertebral motion is subtracted from rod motion to arrive at the compression distance of the spinal cord. Vertebral motion contributed minimally to the total displacement of the spinal cord. The average motion was 0.059 +/ 0.051mm. The velocity is determined from the derivative of the rod trajectory position data, and velocity at impact is estimated by linearly regressing the position data 2ms prior to impact. Spinal cord compression rate is found by dividing the compression depth by the time interval between impact and reversal of the surface of the spinal cord.

At either five minutes or fifteen minutes following injury, animals were euthanized with a lethal dose of pentobarbital (60mg/kg), exsanguinated with 200ml heparinized saline, and perfused transcardially with 10% neutral buffered formalin. The spinal cords were removed and stored in 10% formalin until tissue processing. All procedures were approved by the Rutgers University Animal Care and Facilities Committee.

Tissue Preparation and Immunohistochemistry:

Fixed spinal cords were sectioned horizontally into 20μm sections with a cryostat (ThermoShandon, Pittsburgh, PA, USA). Sections were mounted on charged glass slides (Superfrost Plus, Fisher, Pittsburgh, PA, USA) in two serial sets. One set was immediately coverslipped (Prolong Antifade, Molecular Probes, Eugene OR, USA) and used for direct evaluation of extravasation of injected fluorophores. The other set was used to immunohistochemically label red blood cells using an immunostaining workstation (ThermoShandon, Pittsburgh, PA, USA). Slides were rinsed in wash buffer (phosphate buffered saline (PBS) +1% bovine serum albumin (BSA) + 0.5% triton) for 5 minutes at room temperature, and blocked for 1hr in 10% normal goat serum (NGS). Slides were incubated overnight at room temperature in a polyclonal rabbit anti-rat erythrocyte antibody (Research Diagnostics, Flanders, NJ, USA – optimal dilution 1:100). Specificity of binding was confirmed in preliminary experiments by comparing to parallel sets of slices incubated in rabbit IgG antibody (Jackson ImmunoResearch, West Grove, PA, USA), in which no immunoreactivity was observed. Slides were then washed for 5 minutes and incubated for 1 hour in goat anti-rabbit Alexa Flour 647 (650 nm excitation, 668 nm emission – Molecular

Probes, Eugene, OR, USA). Slides were rinsed for 5 minutes and coverslipped (Prolong Antifade, Molecular Probes, Eugene, OR, USA) in preparation for epifluorescence imaging.

Quantifying Microvascular Pathology – Extravasation Volume Calculation:

Horizontal sections were imaged with epifluorescent microscopy to detect fluorescently labeled hydrazide, albumin, and red blood cells. Approximately 40 sections were examined for each fluorophore for each spinal cord. In each section, separate mosaic images at each wavelength were generated using computer controlled microscopy (Olympus IX81, Olympus America, Center Valley, PA, USA). It was possible to identify general areas of uninjured gray and white matter in each section by visually comparing the section to parallel sections from unoperated controls (Figure 2-2A). These areas were generally at the proximal and/or distal extremes of the section, which were the farthest away from the impact site. In some sections, the gray/white matter border was masked by the extravasated fluorophore(s) or immunolabeled cells. In these cases, the borders were estimated by extending regions that were visible and again comparing to parallel sections from unoperated, unlabeled control tissue (Figure 2-2B). Representative areas of uninjured gray and white matter were then selected in each section, and the maximum pixel grayscale values in those areas were identified and used to threshold that section.

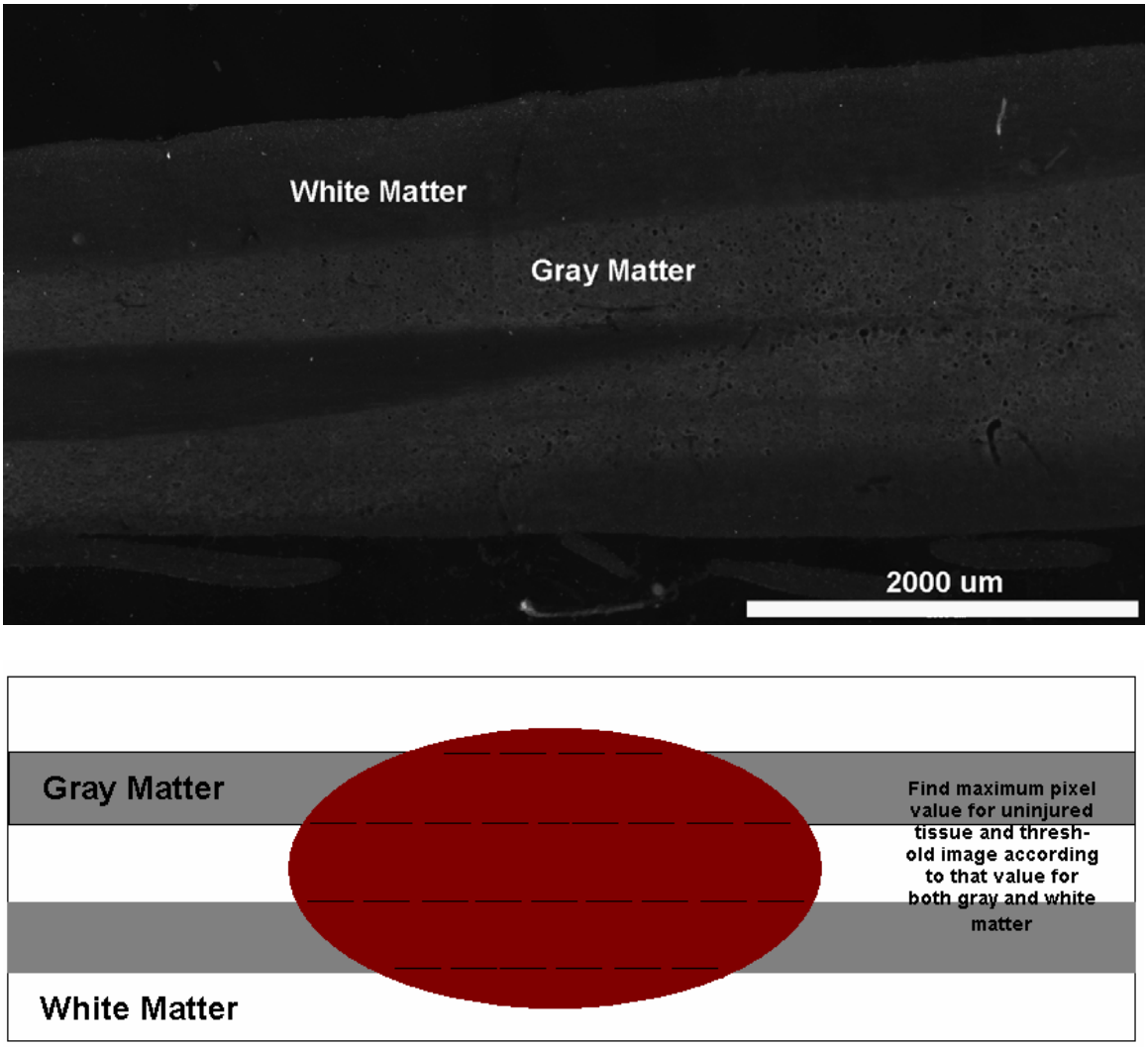

Figure 2-2: (A) Gray matter and white matter are easily distinguishable in spinal cord images. The lighter stripes correspond to gray matter, while the darker regions surrounding the strips correspond to white matter. (B) Often times, injury to the spinal cord caused the gray/white matter border to be masked by the extravasated fluorophore(s) or immunolabeled cells (shown as red in image B). In these cases, the borders were estimated by extending regions that were visible (as shown by the dotted lines) and again comparing to parallel sections from unoperated, unlabeled control tissue.

Any grayscale pixel value above the highest “uninjured” pixel value was considered injured (Figure 2-3). From the binary images, the areas of extravasation for both gray matter and white matter were calculated for each section, summed across sections, and multiplied by the linear distance between images to arrive at separate “extravasation volumes” for each fluorophore for gray and white matter. These gray and white matter volumes were then summed to arrive at a total extravasation volume for each fluorophore for each spinal cord.

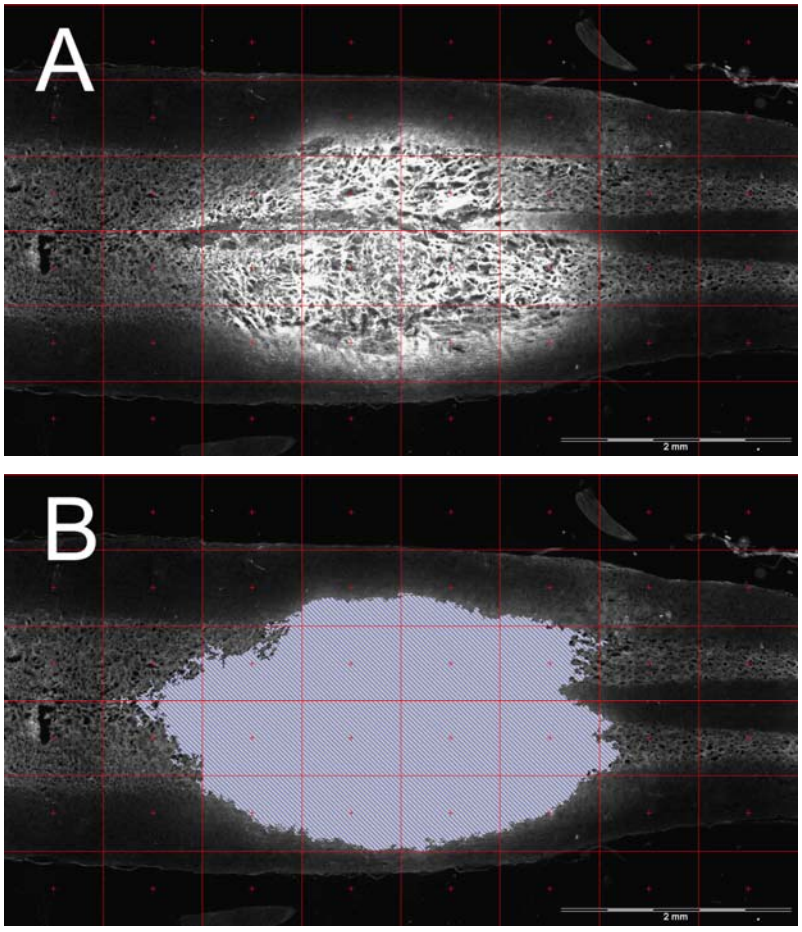

Figure 2-3*:* Lesion volume calculation. Bright areas in A) are injured tissue. A grayscale pixel value of injured tissue is determined from tissue far from the injury site. The image is then thresholded according to that value, and areas that lie above that value are shaded (B). These areas are summed across all sections and multiplied by the section thickness to arrive at an extravasation volume for that fluorophore.

Spinal Cord Dimension Analysis

To determine the maximum depth of compression for the spinal cords during an Impactor weight drop experiment, three separate measurement experiments were conducted.

First, a standard Impactor surgery was performed on two adult, female Long Evans Hooded rats, 77 +/- 5 days old, producing a T9/T10 laminectomy. Rats were suspended by clamping the T8 and T11 dorsal vertebral processes and a needle (gauge, length), attached to a micromanipulator, was centered over the laminectomy and slowly lowered to the dorsal surface of the spinal cord by microscopic inspection. The needle was then slowly lowered with a micromanipulator through the spinal cord until it reached the ventral side of the spinal cord and penetrated the spinal column. The distance to the spinal column was recorded. This measurement was repeated 6 times along the T9/T10 laminectomy.

Rat spinal cords were also measured in vitro. Rat spinal columns (n=10) were excised and the spinal cords removed. Prior to excising the cord, the positions of T9 and T10 vertebrae were marked on the spinal cord by counting the ribs. Using calipers, three measurements of the height and width of each freshly excised spinal cord were recorded.

Finally, freshly excised spinal columns (n=4) with a T9/T10 laminectomy were suspended by clamping the T8 and T11 dorsal vertebral processes. The spinal column was placed on a metal plate to prevent any column motion during impact. The Impactor rod was centered over the laminectomy, raised to the appropriate height, and dropped onto the exposed dura. Impactor injury was performed at two drop heights (n_{height} = 2): 25mm, and 50mm. Typical impact parameters were recorded, including vertebral motion and cord compression distance.

Data Analysis and Statistics:

The effects of drop height and fluorescent marker on extravasation volume were determined statistically with separate one-way ANOVAs ($P<0.05$). Additionally, injury volume measurements were linearly regressed against tissue compression rate, compression distance, and impact velocity measured experimentally to confirm any correlations.

RESULTS

Extravasation Morphology: The patterns of extravasation were similar for all three markers, and generally matched previously reported observations (Noble and Wrathall 1989) (Figure 2-4). In horizontal sections, areas demonstrating extravasation were roughly oblong in shape, with the major axis aligned axially with the spinal cord. Extravasation was more pronounced and extended further in the rostral and caudal directions in the highly vascular gray matter vs. white matter. Areas of extravasation in a given tissue slice were visibly larger as drop height increased and as the size of the labeled marker decreased.

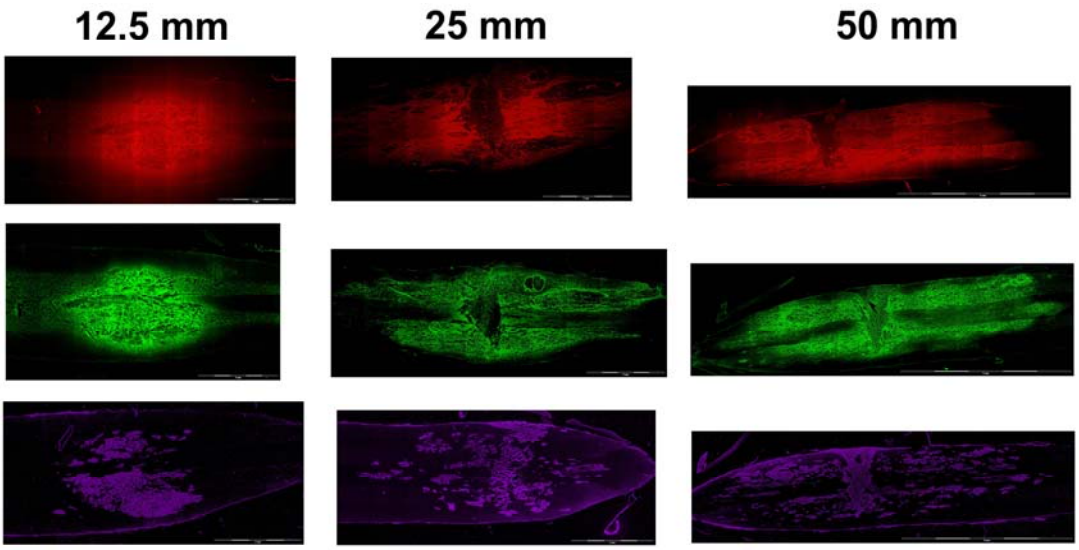

Figure 2-4*:* Representative spatial maps of injury from a 12.5, 25, and 50-mm drop height. The images have been pseudo-colored to distinguish the different fluorophores. Alexa 568-Labeled hydrazide (730 Da – red); Alexa 488-Labeled albumin (70 kDa – green); Alexa 647-Labeled red blood cells (5μm). (Note: Alexa 647 emits a red-orange color that we pseudo-color purple to better distinguish from the Alexa 568).Following an Impactor weight drop, the labeled hydrazide (red) and labeled BSA (green) are already in the tissue from an intravenous injection. Following sectioning the tissue, we immunohistochemically stained RBCs (purple) with an Alexa Fluor 647 secondary antibody. It takes a more severe injury to cause a larger hemorrhage, as seen in the 50 mm drop height. (Note: We pseudo-colored the RBCs purple to distinguish it from the labeled hydrazide).

Extravasation Volume: The volume of extravasation of each fluorescently labeled marker was quantified using image analysis by generating a binary image with the average grayscale pixel value of uninjured tissue in both gray and white matter as the thresholds. Extravasation volume increased significantly with increasing drop height (ANOVA, $P<0.001$) (Figure 2-5) and with decreasing marker size (ANOVA, $P<0.001$) (Figure 2-6). Post hoc, pairwise comparisons revealed significant differences between each pair of drop heights ($P<0.001$) and each pair of markers ($P<0.031$) (Scheffe's test). We also conducted a limited study at a longer survival duration (15min) to evaluate influence of diffusion on lesion volume calculations and determined that there were no significant differences between the 15-minute study and 5-minute study. Additionally, extravasation volumes were significantly greater in gray matter vs. white matter, and each significantly contributed to the total extravasation volume (ANOVA, followed by Scheffe's test, $P<0.001$). No extravasation of the labeled hydrazide, albumin, or erythrocytes was observed in either surgical shams or the unoperated control.

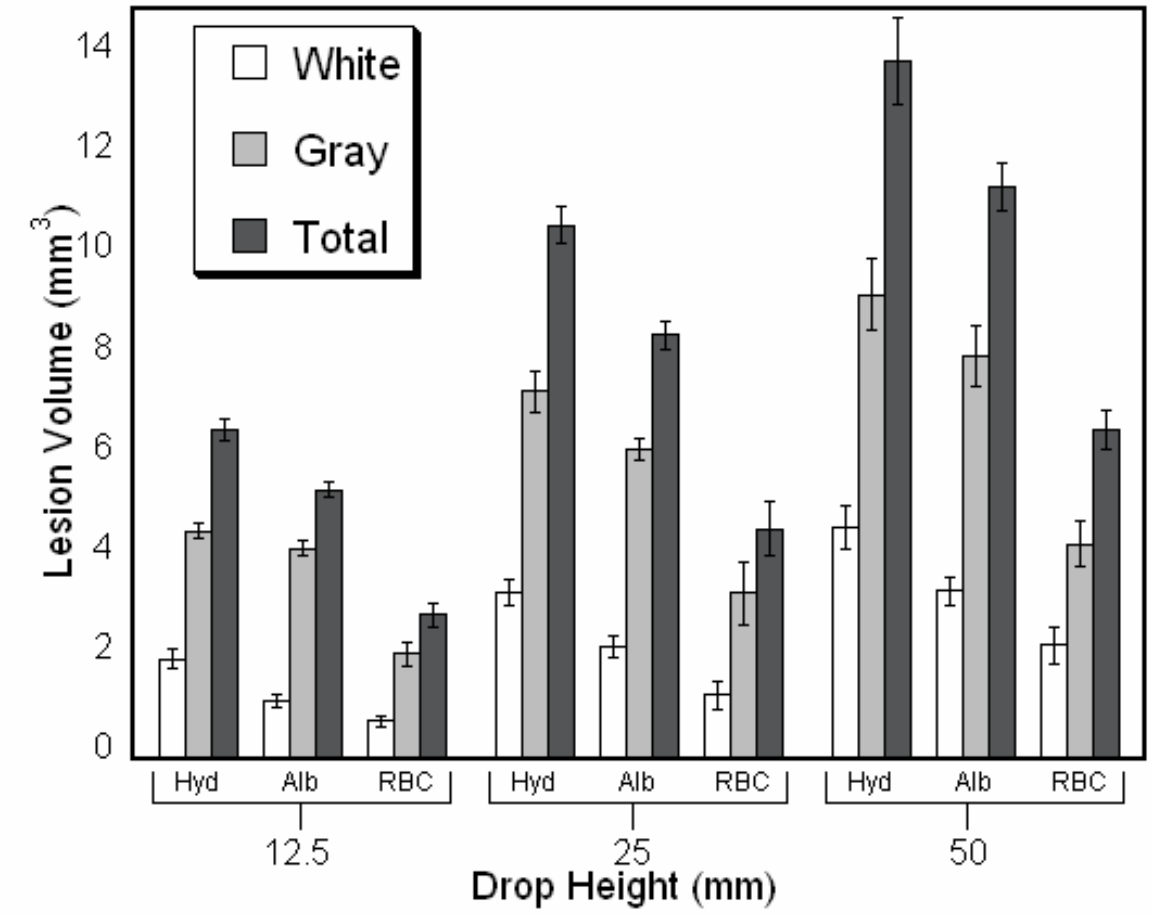

Figure 2-5: Extravasation volumes of the three species as functions of drop height. Extravasation volumes differed significantly with drop height and with injury marker (ANOVA, $P < 0.001$). Injury to the gray matter was significantly greater than injury to the white matter, and each contributed significantly to the overall, total extravasation volume (ANOVA, $P < 0.001$). Post-hoc pairwise comparisons revealed significant increases for each drop height combination for both gray and white matter (Scheffe's post hoc test, $P<0.01$).

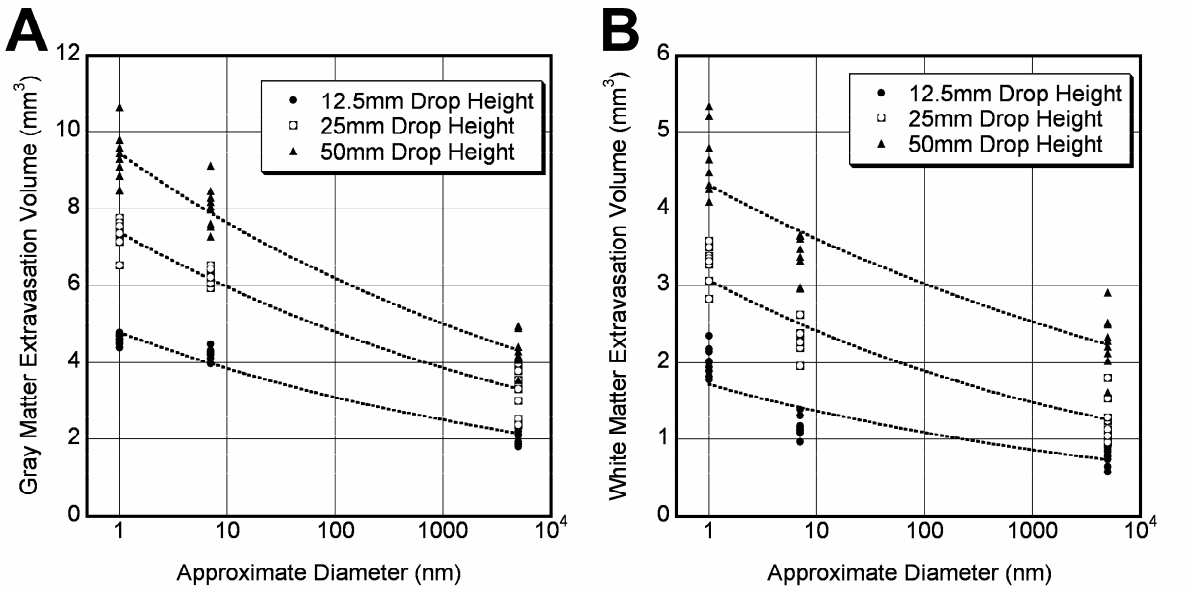

Figure 2-6: Consistent relationships were observed between extravasation volume and blood-borne marker diameter (Alexa 568 Hydrazide - ~1nm; Alexa 488 Albumin - ~7nm; Red blood cells - ~5μm) for both the gray matter (A) and the white matter (B) among the three drop heights. The extravasation volume in each tissue significantly depended on the marker size (ANOVA, $P<0.001$). Pairwise Post-hoc analysis (Scheffe's test) identified significant differences between each pair of markers ($P<0.05$).

Correlations to impact parameters: Average impact parameters (impact velocity, cord compression depth, and cord compression rate) for each loading condition are summarized in Table 2-1. Vertebral motion, which was subtracted from the displacement of the rod to arrive at the cord compression distance, contributed minimally to the overall displacement of the cord (average vertebral displacement = 0.059 +/- 0.051mm), and no consistent trends were observed relating the vertebral motion to drop height (ANOVA, P=0.078).

TABLE 2-1: Summary of impact parameters and lesion volumes. Results are average (std deviation).

Drop Height (mm)	N	Velocity $\left(\frac{mm}{ms}\right)$	Compression Depth (mm)	Compression Rate $\left(\frac{mm}{ms}\right)$	Extravasation Volume (mm^3)					
					Hydrazide		*Albumin*		*Red Blood Cells*	
					Gray	*White*	*Gray*	*White*	*Gray*	*White*
12.5	8	0.489 (0.011)	1.65 (0.194)	0.429 (0.145)	4.57 (0.150)	2.02 (0.195)	4.23 (0.146)	1.16 (0.132)	2.12 (0.238)	0.770 (0.110)
25	8	0.690 (0.007)	2.14 (0.168)	0.586 (0.023)	7.36 (0.411)	3.32 (0.260)	6.21 (0.212)	2.27 (0.224)	3.32 (0.620)	1.29 (0.273)
50	8	0.974 (0.012)	2.88 (0.157)	0.828 (0.032)	9.30 (0.727)	4.64 (0.447)	8.07 (0.589)	3.38 (0..285)	4.30 (0.458)	2.28 (0.383)

The results of linear correlations of gray and white matter extravasation volumes to the physical impact parameters measured during Impactor weight drop injury are summarized in 2-2. Impact velocity (Figure 2-7), cord compression distance (Figure 2-8), and cord compression rate (Figure 2-9) were highly correlated to extravasation volume for each marker (minimum $R^2 = 0.735$), although the coefficients were generally greater for impact velocity and compression rate than for compression distance.

TABLE 2-2: Summary of linear correlations between impact parameters and lesion volumes.

X	Y		Slope (+/- 95% Conf. Limits)	Intercept (+/- 95% Conf. Limits)	R^2	*Predicted Threshold*
Velocity (mm/ms)	Hydrazide (mm^3)	Gray	9.51 (8.13, 10.9)	0.259 (-0.766, 1.28)	0.899	-
		White	5.37 (4.71, 6.05)	-0.530 (-1.03, -0.03)	0.923	0.069
	Albumin (mm^3)	Gray	7.78 (6.86, 8.71)	0.584 (-0.105,1.27)	0.930	-
		White	4.54 (4.09, 5.00)	-0.992 (-1.33, -0.650)	0.948	0.191
	Red Blood Cell (mm^3)	Gray	4.42 (3.41, 5.43)	0.074 (-0.680, 0.829)	0.779	-
		White	3.11 (2.49, 3.73)	-0.787 (-1.25, -0.326)	0.824	0.246
Compress Depth (mm)	Hydrazide (mm^3)	Gray	3.28 (2.47, 4.10)	-0.232 (-2.09, 1.63)	0.750	-
		White	1.86 (1.42, 2.29)	-0.805 (-1.81, 0.195)	0.769	-
	Albumin (mm^3)	Gray	2.78 (2.24, 3.32)	-0.017 (-1.25, 1.21)	0.832	-
		White	1.61 (1.29, 1.92)	-1.31 (-2.02, -0.591)	0.830	0.794
	Red Blood Cell (mm^3)	Gray	1.62 (1.20, 2.04)	-0.359 (-1.31, 0.596)	0.735	-
		White	1.14 (0.878, 1.40)	-1.09 (-1.69, -0.492)	0.778	0.973
Compress Rate (mm/ms)	Hydrazide (mm^3)	Gray	11.1 (9.17, 13.1)	0.229 (-1.0, 1.49)	0.855	-
		White	6.51 (5.79, 7.23)	-0.673 (-1.13, -0.214)	0.938	0.134
	Albumin (mm^3)	Gray	9.17 (7.79,10.5)	0.535 (-0.339, 1.41)	0.892	-
		White	5.45 (4.88, 6.02)	-1.08 (-1.44, -0.716)	0.945	0.220
	Red Blood Cell (mm^3)	Gray	5.21 (3.91, 6.51)	0.046 (-0.782, 0.874)	0.747	-
		White	3.69 (2.89, 4.48)	-0.819 (-1.32, -0.315)	0.800	0.297
*Drop Height (mm)	Velocity^2 (mm^2/ms^2)		0.019 (0.0185, 0.0193)	0.002 (-0.011, 0.016)	0.997	N/A
**Velocity (mm/ms)	Compression Rate (mm/ms)		0.826 (0.778, 0.872)	0.022 (-0.016, 0.057)	0.983	N/A

*Assuming a gravitational acceleration constant of 9.8m/s^2, the theoretical slope of the (Velocity^2 vs. Drop Height) line should be 0.0196 mm/ms^2. The 3% error observed is due to frictional losses.

**The correlation coefficient (R^2) between Compression Rate and Velocity is used as a measure of the quality of Impactor experiments and experimenter proficiency. Values above 0.9 are generally considered acceptable.

In many cases, the y-intercept of the correlation was negative, which implies a positive x-intercept, because of the positive slope for all lines. A positive value of the x-intercept indicates the minimum magnitude of the particular impact parameter required to produce non-zero extravasation, and can be viewed as a threshold for injury. However, the 95% confidence intervals for the y-intercept for all of the correlations of extravasation volumes in gray matter to impact parameters encompass zero; the 'thresholds' cannot, therefore, be distinguished from zero, and any compression will be predicted to produce injury to gray matter. For the white matter, only one correlation (hydrazide vs. compression depth) yielded confidence intervals on the y-intercept that encompassed zero. Inverse correlations of the remaining white matter extravasation volumes to impact parameters (injury volumes as the independent variables, impact parameters as the dependent variables) showed increasing thresholds for larger species than smaller ones. Collectively, the results indicate that microvasculature in the gray matter is more sensitive to compressive loads than that in the white matter, and that above certain thresholds for tissue compression and rate of tissue compression, the microvasculature of the white matter can be injured. Table 2-2 also includes correlation coefficients relating drop height to velocity^2 (which should be related by 2x the gravitational constant) and velocity to cord compression rate, both of which are often used to evaluate the quality and reproducibility of Impactor experiments.

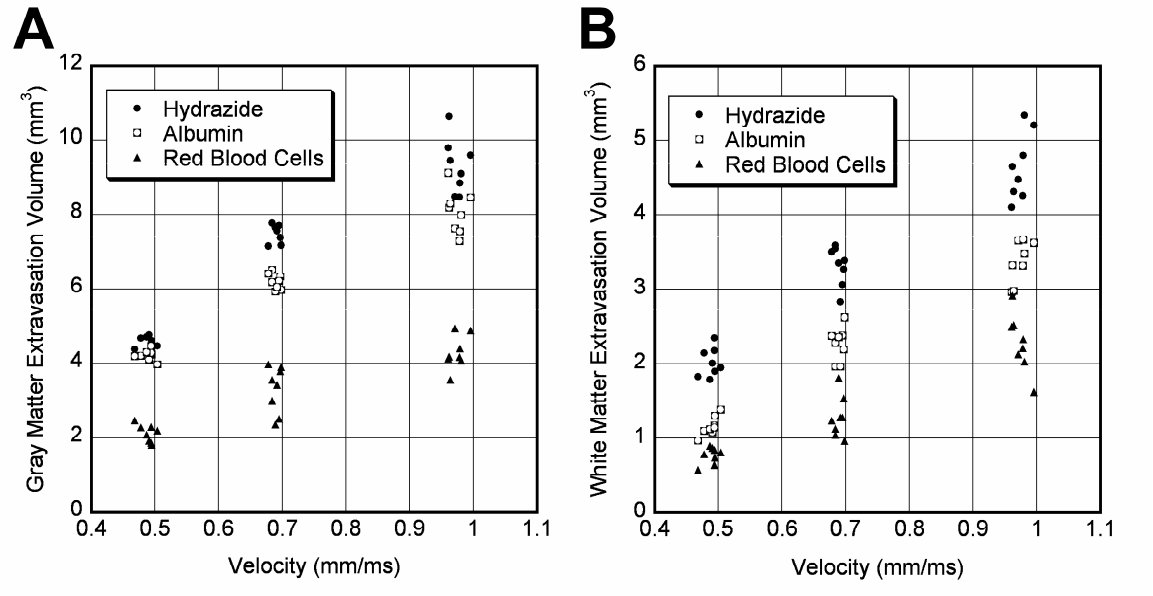

Figure 2-7: Gray matter and white matter extravasation volumes of the three species as a function of impact velocity. Linear correlations of injury volumes to velocity indicated that gray matter was more sensitive to changes in impact velocity than white matter. (minimum $R^2 = 0.779$ – summarized in Table 2-2).

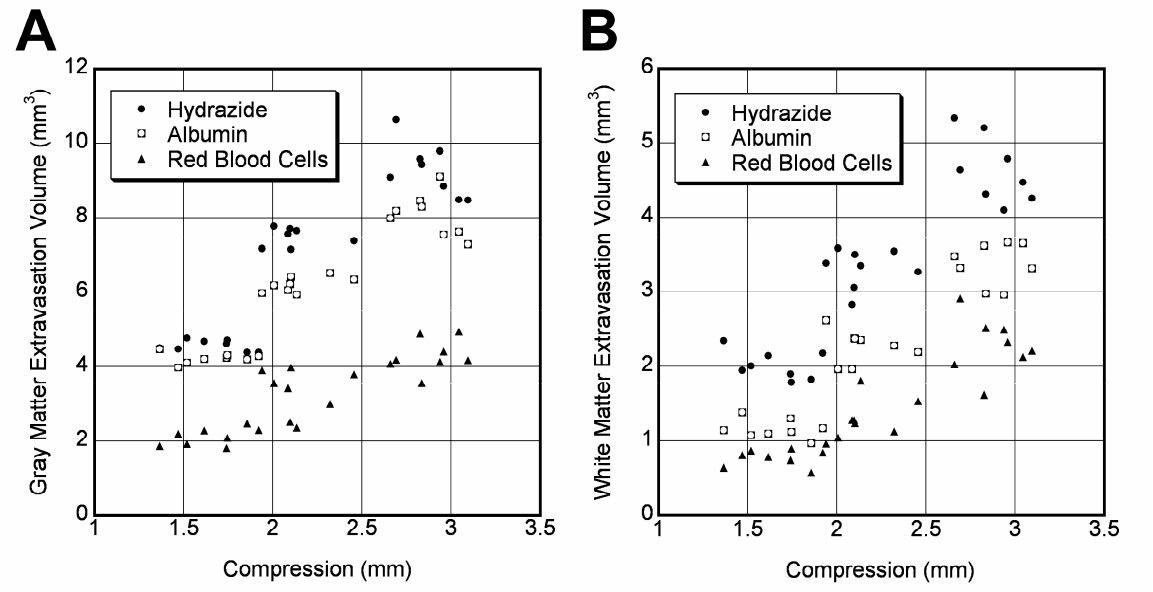

Figure 2-8*:* Gray matter and white matter extravasation volumes of the three species as a function of cord compression distance. Compression distance is related to the magnitude of mechanical strain experienced by the tissue. Extravasation volumes were linearly correlated to compression (minimum $R^2 = 0.735$ – summarized in Table 2-2). Gray matter was more sensitive than white matter to changes in compression depth.

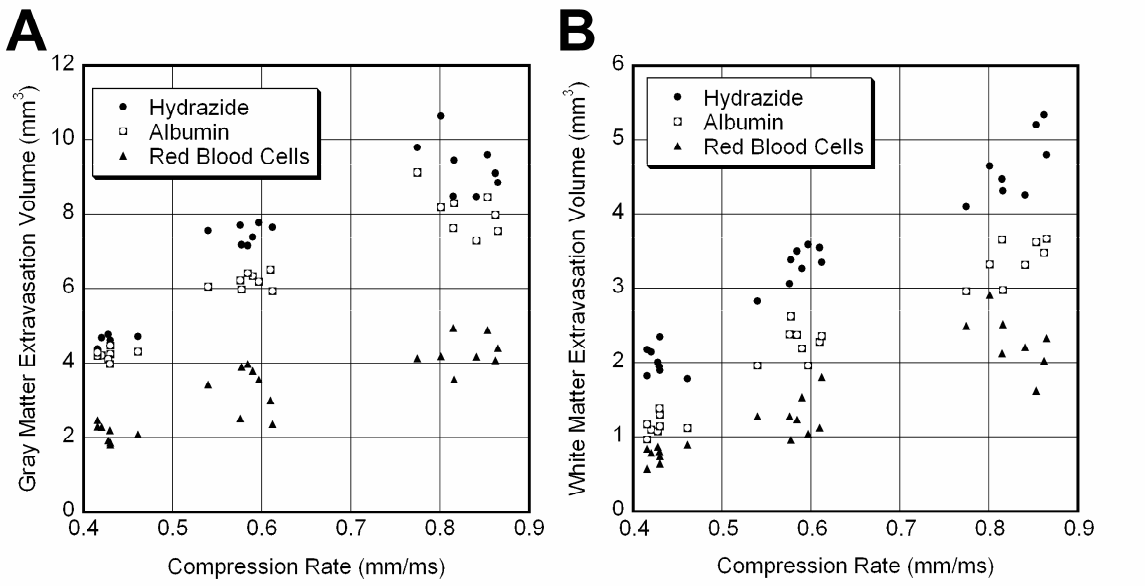

Figure 2-9*:* Gray matter and white matter extravasation volumes of the three species as a function of cord compression rate. Compression rate is related to the magnitude of strain rate experienced by the tissue during trauma. Extravasation volumes were linearly correlated to compression rate (minimum R^2 = 0.747 – summarized in 2-2). As with the other measures, gray matter was more sensitive than white matter to changes in compression rate.

Analysis of the maximum spinal cord depth

The results of the spinal cord measurements are summarized in Table 2-3. Briefly, the in vivo needle puncture experiments were used to find the maximum compression the spinal cord could displace during an Impactor weight drop experiment. The value represents the distance from the dorsal surface of the dura to the bottom of the spinal column or the maximum displacement the spinal cord could compress, which was approximately 2.68mm.

The in vitro spinal cord height measurements, obtained from 15 excised spinal cords, showed an average of 2.56mm. This value represents an estimate of the spinal cord height since an excised spinal cord loses some of it structure and has neither cerebrospinal fluid nor perfusive pressure.

Performing an Impactor weight drop experiment on excised spinal columns allowed us to determine the role and extent of column displacement during the weight drop as well as determine a maximum average of cord compression. All drops heights showed averages above the in vivo experiments. Since there an absence of CSF pressure and the tissue most likely settled to the bottom of the column, we would expect the compression distances increase compared to our in vivo averages. From the output of the Impactor software, the vertebral motion in all experiments was zero. Furthermore, it should be noted that the compression depth values for the 50mm drops were impossibly large when compared to the dimensions of the rat spinal cord. The 50mm drop resulted in cord compression values that were over 100% of the cord height or greater. This suggests that a severe injury causes complete transection of the cord and may slightly compress and remodel the bone of the spinal column, which was not detected by the vertebral motion detector.

TABLE 2-3: Summary of Spinal Cord Height dimensions

Experiment	Number of animals		Maximum Height/Max Compression Depth Average (Std. Dev)
In vivo needle puncture	2		2.68mm (0.083)
In vitro measurement of an excised spinal cord	15		2.56mm (0.149)
Impactor experiment on excised spinal column	25mm	2	2.22mm
	50mm	2	3.2mm

DISCUSSION

We have chosen to focus on characterizing the immediate breakdown of the microvasculature due to trauma because of the dramatic effects microvascular damage has on the secondary events and neuropathology following SCI. Secondary injury is an evolution of events including inflammation, ischemia, oxidative damage, as well as other factors, such as toxic amounts of nitric oxide (NO) production, that injure otherwise unaffected spinal cord tissue (Mautes, Weinzierl et al. 2000). These secondary effects are the principal targets of post-trauma therapy, and as such, have been researched extensively in laboratory and clinical settings (Ducker and Assenmacher 1969; Senter and Venes 1978; Blight 1992; Travlos, Anton et al. 1994; Popovich, Wei et al. 1997; Carlson, Parrish et al. 1998; Amar and Levy 1999). By identifying the early breakdown of the spinal cord microvasculature via primary, mechanical damage to the BSCB, we can provide strategies for SCI therapies or prevention to limit the effect of the secondary sequelae.

Herein, we have presented a simple means of characterizing the severity and extent of primary damage to the BSCB in the spinal cord gray and white matter following SCI. Severity and extent are often difficult to distinguish in any model of CNS trauma. Also, there is no strict time point along the functional time course of injury of when secondary injury adds to the spinal cord damage. In many cases, a binary measure of injury is used that indicates the presence or absence of damage (for instance, cell death), from which an appraisal of the severity is inferred. Charting the causal factors that dictate the severity and extent of injury becomes increasingly difficult with time, as secondary insults add to the picture. We focused on BSCB breakdown immediately following injury to examine the effect of *primary* damage of the spinal cord – that is, the direct result of the mechanical

insult. Clinically and in vivo, BSCB breakdown is exacerbated by secondary insults, but for a biomechanical analysis and ultimately injury prevention, a detailed understanding of the consequences of the primary mechanical insult is required. In order to study the effects of the primary mechanical insult to the BSCB, we needed to evaluate the severity and extent of BSCB damage before any secondary insults exacerbated the primary injury. Thus, in addition to our 5-minute study, we conducted a limited 15-minute study (n=9) to determine the effects of diffusion of our fluorescent markers and to ensure we were isolating primary injury within the 5-minute survival time. Our results indicated that there were no significant differences between our 5-minute lesion volumes and our 15-minute lesion volume thus confirming that we effectively isolated primary injury. The BSCB offers a convenient structure to examine both the severity and extent of tissue damage, in that the spatial permeability to different sized species can be easily examined in the same animal following spinal cord trauma. Thus, the extent of injury can be assessed by examining the extravasation volume of a particular marker, and the severity can be assessed by comparing extravasation volumes among marker sizes.

To our knowledge, this represents the first attempt to discriminate size-dependent microvascular changes quantitatively in the same animal in a clinically relevant trauma model. Wagner and Stewart qualitatively examined the extravasation of a series of fluorescently-labeled dextrans and albumin eight hours following weight drop injury in the cat (Wagner and Stewart 1981), and the markers were studied in separate animals. Though the distance of migration from the injury epicenter was reported to be similar, it is difficult to compare to the results of this study because of the lack of quantitation, and because the extended survival time permits extravasation from secondary insults on the BSCB, as well as

significant diffusion of the markers during the 8 hours of circulation. Pan et al. have characterized temporal changes in the extent of BSCB permeability to sucrose, albumin, and tumor necrosis factor-α (TNF-α) following transection (Pan, Banks et al. 1997) or hemisection (Pan, Zhang et al. 2003) in the mouse, and found non-specific immediate permeability changes at the injury site consistent with mechanical injury, but subsequent species-specific variations that potentially depended on the specific cellular mechanisms that govern crossing of that molecule as well as the secondary insults. Thus, evaluating these changes for different degrees of mechanical insults acutely after injury, before significant secondary insults can manifest, allows improved correlation of extent and severity to the primary, mechanical parameters.

The trends relating BSCB damage to the physical parameters of Impactor weight drop spinal cord injury are consistent with previous measures of the volume of cell death, open field locomotor test scores (e.g. Basso, Beattie, Bresnahan Score – BBB), and white matter sparing (Young 2002). Not surprisingly, for all measures, the degree of injury significantly increases as the drop height is increased. In this study, both the severity and extent of injury increased with drop height and was greater in the gray matter than the white matter, though immediate, mechanically-mediated damage to the microvasculature of the white matter was observed. Correlation of the physical parameters measured during injury to the extravasation volumes allows a preliminary assessment of the sensitivity of the BSCB to specific mechanical variables. As with previous studies of lesion volume, BBB score, and white matter sparing, the extravasation volumes of each of the three species were better correlated (linearly) to impact velocity and compression rate than compression depth, though regression coefficients for all were statistically significant ($P<0.001$) (Noble and Wrathall 1987; Noble

and Wrathall 1989; Fehlings and Tator 1995; Basso, Beattie et al. 1996; Young 2002). For all measures, the slopes of the linear correlations indicated that the gray matter was more sensitive to the impact parameters than the white matter. It is known that the mechanical properties of gray and white matter are different (Bilston, Liu et al. 1997; Arbogast and Margulies 1998; Bilston, Liu et al. 2001; Bilston 2002; Miller and Chinzei 2002; Prange and Margulies 2002), which will alter tissue movement and deformation spatially and temporally following impact. Additionally, the gray matter is more vascularized with a denser and more isotropically oriented microvascular network than the white matter. Thus, the sensitivity of the microvasculature to injury may be affected by inherent physical differences in the microvessels, such as vessel caliber or constituent cells comprising the BSCB, and the distribution of stress and strain through the tissue, which is influenced at the microscopic and mesoscopic scales by the vascular network and other structural components of the spinal cord, such as axons and other glia.

Mechanical thresholds for injury, predicted from inverse correlations when the confidence intervals on the y-intercept did not span zero, indicated that the white matter could generally tolerate some compression before demonstrating a compromised BSCB. In no cases could the thresholds for gray matter injury be distinguished from zero. These thresholds are more specific to the weight drop injury technique and are difficult to generalize to other models or clinical situations because the geometry and boundary conditions of the Impactor are not considered. An improved prediction would be based on the tissue-level material response (eg tissue stress and/or strain) which could be predicted by a computational analysis and then generalized to other models and situations.

Interestingly, the slopes of the linear correlations between compression rate and lesion volume were greater than those between impact velocity and lesion volume for each of the three species, indicating the sensitivity of lesion volume to the rate of tissue displacement. Together, these suggest that the BSCB is sensitive to both mechanical strain and strain rate, indicating that the injury tolerance of the tissue depends on its viscoelastic properties. However, the only way to conclusively demonstrate the effect of strain rate on BSCB injury is to hold compression depth constant and vary compression rate or to vary compression depth and hold compression rate constant, which can be done with other pneumatic or electromagnetic impact devices (Stokes, Noyes et al. 1992) or by placing a mechanical stop that limits Impactor displacement and therefore the cord compression depth.

To evaluate the severity of BSCB damage, the size-dependent permeability of the BSCB following injury was examined. Three markers were chosen that spanned a wide range of sizes: Alexa 568 hydrazide, which is a 707Da non-toxic, fluorescently labeled ion most often used as a neuronal tracer; Alexa 488-labeled BSA, which has a molecular weight of approximately 70kDa; and red blood cells, which have a nominal diameter of ~5μm. The fluorescent hydrazide can be fixed in cells and tissues with common aldehyde-based fixatives. BSA has been routinely used as a marker of blood-brain barrier and BSCB injury, typically by labeling with Evans Blue (Griffiths and Miller 1974; Wagner and Stewart 1981; Noble and Maxwell 1983; Farooque, Zhang et al. 1992; Whetstone, Hsu et al. 2003). The hydrazide and BSA extravasation were visualized directly in the same tissue section. The red blood cells, a marker of hemorrhage, were indirectly visualized with immunohistochemistry in alternate sections. The initial hope was to examine all three markers in the same section to streamline post-processing and imaging and provide an identical section for snapshots of

injury severity. However, the fluorescence from the hydrazide weakened significantly during the immunohistochemical procedure, which prompted evaluating the directly labeled and indirectly labeled markers in different sections. It would be possible to circulate a red blood cell-specific labeled antibody, or to remove red blood cells, label them, and return them to circulation, to examine all markers in one section. The area of extravasation for a given species only changed gradually from section-to-section (20μm apart), indicating that the different markers could be compared fairly in adjacent sections.

We selected the hydrazide and albumin based on their molecular weight, but a better measure would be the geometric size of the molecule or protein, since the species are generally excluded by size. Injury of greater severity will generate bigger holes in the vasculature to allow larger species area-wise to extravasate into the parenchyma. The subsequent diffusion of these species through the parenchyma will also be dictated by their size. Whereas an effective diameter for red blood cells can be directly measured, the size of proteins and smaller molecules is typically determined from x-ray crystallography studies and/or molecular dynamics simulations. An estimate of the diameter of albumin (~7nm) was taken from such studies by Sugio et al. (Sugio, Kashima et al. 1999). However, no studies on the size of the labeled hydrazide were found. The diameter of a fluorescently labeled hydrazide ion, based on its molecular weight and specific gravity (1.032), was approximated at ~1nm, which is on the same order as that experimentally measured for similarly-sized tracers, such as Lucifer yellow (Stewart 1981). Extravasation volume is plotted versus the approximate diameter of the three species in Figure2-6. The three sets of data, one for each drop height, depict similar, semi-logarithmic trends. For all three species, no extravasation was observed in control tissue, demonstrating that the selective transport across the BSCB by

specific mechanisms is negligible. For an improved prediction of size-dependent permeability, other markers could be included at different molecular weights/effective diameters, such as lysine-fixable fluorescent dextrans, or labeled immunoglobulins. Calibrated microspheres and nanoparticles could also be employed.

These sizes were generally selected to span blood-borne elements that may contribute to the secondary insults. Most obviously, increasing the protein content of the extracellular space induces vasogenic edema (Beggs and Waggener 1975). Certain blood-borne molecules may have more specific effects following spinal cord injury. For example, quinolinic acid, a small neurotoxic molecule (~ 170 Da), causes overstimulation of neuronal cells, and serum-derived quinolinic acid that crosses the BSCB following trauma has been suggested to contribute significantly to cytotoxicity and secondary insults (Popovich, Reinhard et al. 1994). Endothelin-1 (ET-1), a 21-amino acid peptide, has been shown to cause an increase in blood spinal cord barrier disruption (Mautes, Weinzierl et al. 2000). As a vasoconstrictor, ET-1 can cause ischemia in the spinal cord, resulting in increased cell death (McKenzie, Hall et al. 1995; Westmark, Noble et al. 1995). Serum contains high concentrations of complement, which ranges in size from ~80-200kD (Anderson, Robert et al. 2004). Activation of several complement pathways has been demonstrated following spinal cord injury in vivo, and contributes to the demyelination and neurodegeneration in numerous pathological CNS conditions, including traumatic brain injury (Anderson, Robert et al. 2004). Neutrophils (8-15 μm) have been shown to amplify vascular injury by amassing at sites of vascular injury and secreting supplementary free oxygen radicals, furthering the vascular damage (Hernandez, Grisham et al. 1987; Sussman and Bulkley 1990). Since secondary insults to the BSCB may not produce non-specific breakdown, but rather distinct

permeability changes to different molecules, identifying the scope of primary, mechanically-mediated BSCB injury takes on enhanced importance in potentially predicting the pattern of secondary insults based on the location of non-specifically extravasated, blood-borne species. It also provides a template for potential acute delivery of neuroprotective molecules.

One long-term aim for this research is to link the patterns of BSCB primary injury, and ultimately other primary pathologies, to the tissue-level states of mechanical stress and strain. Herein, we have correlated the distribution of BSCB injury of varying severity to the physical parameters associated with the Impactor (impact velocity, compression depth, and compression rate), as can be done with other impact trauma models of SCI. Each model has unique features, such that, for instance, BSCB injury following trauma induced to the same compression depth with direct weight drop models, weight drop models with 'impact buttons', and controlled pneumatic or electromagnetic impactors can result in significantly different results, because of differences in the external loading conditions. However, the relationship between primary injury patterns in these models (and, in fact, any traumatic SCI) and the 'internal', tissue-level stress and/or strain will be the same. We hope to determine this relationship by simulating the biomechanics of the weight drop model with finite element techniques, and quantitatively comparing the results of the finite element model to the spatial profiles of immediate BSCB permeability changes to predict threshold levels of stress and strain responsible for a given injury severity. These thresholds represent tissue-level targets for preventing SCI. Moreover, similarly modeling the mechanics of other models computationally will allow improved comparisons of results from laboratory-to-laboratory based on the internal, tissue-level criteria, and ultimately to improved standardization of injury patterns.

REFERENCES

ALBIN, M. S., WHITE, R. J., ACOSTA-RUA, G. and YASHON, D. (1968). "Study of functional recovery produced by delayed localized cooling after spinal cord injury in primates." J Neurosurg **29**(2): 113-20.

AMAR, A. P. and LEVY, M. L. (1999). "Pathogenesis and pharmacological strategies for mitigating secondary damage in acute spinal cord injury." Neurosurgery **44**(5): 1027-39; discussion 1039-40.

ANDERSON, A. J., ROBERT, S., HUANG, W., YOUNG, W. and COTMAN, C. W. (2004). "Activation of complement pathways after contusion-induced spinal cord injury." J Neurotrauma **21**(12): 1831-46.

ARBOGAST, K. B. and MARGULIES, S. S. (1998). "Material characterization of the brainstem from oscillatory shear tests." J Biomech **31**(9): 801-7.

BALENTINE, J. D. (1978). "Pathology of experimental spinal cord trauma. I. The necrotic lesion as a function of vascular injury." Lab Invest **39**(3): 236-53.

BASSO, D. M., BEATTIE, M. S. and BRESNAHAN, J. C. (1996). "Graded histological and locomotor outcomes after spinal cord contusion using the NYU weight-drop device versus transection." Exp Neurol **139**(2): 244-56.

BEGGS, J. L. and WAGGENER, J. D. (1975). "Vasogenic edema in the injured spinal cord: a method of evaluating the extent of blood-brain barrier alteration to horseradish peroxidase." Exp Neurol **49**(1 Pt 1): 86-96.

BEGGS, J. L. and WAGGENER, J. D. (1976). "Transendothelial vesicular transport of protein following compression injury to the spinal cord." Lab Invest **34**(4): 428-39.

BEHRMANN, D. L., BRESNAHAN, J. C., BEATTIE, M. S. and SHAH, B. R. (1992). "Spinal cord injury produced by consistent mechanical displacement of the cord in rats: behavioral and histologic analysis." J Neurotrauma **9**(3): 197-217.

BERKOWITZ, E. D. (1998). "Revealing America's welfare state. [Review of: Howard, C., The hidden welfare state: tax expenditures and social policy in the United States. Princeton University Press, 1997]." Rev Am Hist **26**(3): 620-4.

BILGEN, M., AL-HAFEZ, B., T, M. M. and I, V. S. (2005). "Ex vivo magnetic resonance imaging of rat spinal cord at 9.4 T." Magn Reson Imaging **23**(4): 601-5.

BILGEN, M. and NARAYANA, P. A. (2001). "A pharmacokinetic model for quantitative evaluation of spinal cord injury with dynamic contrast-enhanced magnetic resonance imaging." Magn Reson Med **46**(6): 1099-106.

BILSTON, L. E. (2002). "The effect of perfusion on soft tissue mechanical properties: a computational model." Comput Methods Biomech Biomed Engin **5**(4): 283-90.

BILSTON, L. E., LIU, Z. and PHAN-THIEN, N. (1997). "Linear viscoelastic properties of bovine brain tissue in shear." Biorheology **34**(6): 377-85.

BILSTON, L. E., LIU, Z. and PHAN-THIEN, N. (2001). "Large strain behaviour of brain tissue in shear: some experimental data and differential constitutive model." Biorheology **38**(4): 335-45.

BLIGHT, A. R. (1992). "Macrophages and inflammatory damage in spinal cord injury." J Neurotrauma **9 Suppl 1**: S83-91.

BRESNAHAN, J. C., BEATTIE, M. S., TODD, F. D., 3RD and NOYES, D. H. (1987). "A behavioral and anatomical analysis of spinal cord injury produced by a feedback-controlled impaction device." Exp Neurol **95**(3): 548-70.

CARLSON, S. L., PARRISH, M. E., SPRINGER, J. E., DOTY, K. and DOSSETT, L. (1998). "Acute inflammatory response in spinal cord following impact injury." Exp Neurol **151**(1): 77-88.

DOHRMANN, G. J., PANJABI, M. M. and WAGNER, F. C., JR. (1976). "An apparatus for quantitating experimental spinal cord trauma." Surg Neurol **5**(5): 315-8.

DOHRMANN, G. J. and WICK, K. M. (1971). "Demonstration of the microvasculature of the spinal cord by intravenous injection of the fluorescent dye, thioflavine S." Stain Technol **46**(6): 321-2.

DUCKER, T. B. and ASSENMACHER, D. R. (1969). "Microvascular response to experimental spinal cord trauma." Surg Forum **20**: 428-30.

FADEN, A. I., GANNON, A. and BASBAUM, A. I. (1988). "Use of serotonin immunocytochemistry as a marker of injury severity after experimental spinal trauma in rats." Brain Res **450**(1-2): 94-100.

FAROOQUE, M., ZHANG, Y., HOLTZ, A. and OLSSON, Y. (1992). "Exudation of fibronectin and albumin after spinal cord injury in rats." Acta Neuropathol (Berl) **84**(6): 613-20.

FEHLINGS, M. G. and TATOR, C. H. (1995). "The relationships among the severity of spinal cord injury, residual neurological function, axon counts, and counts of retrogradely labeled neurons after experimental spinal cord injury." Exp Neurol **132**(2): 220-8.

GRIFFITHS, I. R. and MILLER, R. (1974). "Vascular permeability to protein and vasogenic oedema in experimental concussive injuries to the canine spinal cord." J Neurol Sci **22**(3): 291-304.

GRUNER, J. A. (1992). "A monitored contusion model of spinal cord injury in the rat." J Neurotrauma **9**(2): 123-6; discussion 126-8.

HERNANDEZ, L. A., GRISHAM, M. B., TWOHIG, B., ARFORS, K. E., HARLAN, J. M. and GRANGER, D. N. (1987). "Role of neutrophils in ischemia-reperfusion-induced microvascular injury." Am J Physiol **253**(3 Pt 2): H699-703.

JAEGER, C. B. and BLIGHT, A. R. (1997). "Spinal cord compression injury in guinea pigs: structural changes of endothelium and its perivascular cell associations after blood-brain barrier breakdown and repair." Exp Neurol **144**(2): 381-99.

MAUTES, A. E., WEINZIERL, M. R., DONOVAN, F. and NOBLE, L. J. (2000). "Vascular events after spinal cord injury: contribution to secondary pathogenesis." Phys Ther **80**(7): 673-87.

MCKENZIE, A. L., HALL, J. J., AIHARA, N., FUKUDA, K. and NOBLE, L. J. (1995). "Immunolocalization of endothelin in the traumatized spinal cord: relationship to blood-spinal cord barrier breakdown." J Neurotrauma **12**(3): 257-68.

MILLER, K. and CHINZEI, K. (2002). "Mechanical properties of brain tissue in tension." J Biomech **35**(4): 483-90.

NOBLE, L. J., MAUTES, A. E. and HALL, J. J. (1996). "Characterization of the microvascular glycocalyx in normal and injured spinal cord in the rat." J Comp Neurol **376**(4): 542-56.

NOBLE, L. J. and MAXWELL, D. S. (1983). "Blood-spinal cord barrier response to transection." Exp Neurol **79**(1): 188-99.

NOBLE, L. J. and WRATHALL, J. R. (1987). "The blood-spinal cord barrier after injury: pattern of vascular events proximal and distal to a transection in the rat." Brain Res **424**(1): 177-88.

NOBLE, L. J. and WRATHALL, J. R. (1989). "Correlative analyses of lesion development and functional status after graded spinal cord contusive injuries in the rat." Exp Neurol **103**(1): 34-40.

NOBLE, L. J. and WRATHALL, J. R. (1989). "Distribution and time course of protein extravasation in the rat spinal cord after contusive injury." Brain Res **482**(1): 57-66.

NOYES, D. H. (1987). "Electromechanical impactor for producing experimental spinal cord injury in animals." Med Biol Eng Comput **25**(3): 335-40.

PAN, W., BANKS, W. A. and KASTIN, A. J. (1997). "Blood-brain barrier permeability to ebiratide and TNF in acute spinal cord injury." Exp Neurol **146**(2): 367-73.

PAN, W., ZHANG, L., LIAO, J., CSERNUS, B. and KASTIN, A. J. (2003). "Selective increase in TNF alpha permeation across the blood-spinal cord barrier after SCI." J Neuroimmunol **134**(1-2): 111-7.

POPOVICH, P. G., HORNER, P. J., MULLIN, B. B. and STOKES, B. T. (1996). "A quantitative spatial analysis of the blood-spinal cord barrier. I. Permeability changes after experimental spinal contusion injury." Exp Neurol **142**(2): 258-75.

POPOVICH, P. G., REINHARD, J. F., JR., FLANAGAN, E. M. and STOKES, B. T. (1994). "Elevation of the neurotoxin quinolinic acid occurs following spinal cord trauma." Brain Res **633**(1-2): 348-52.

POPOVICH, P. G., WEI, P. and STOKES, B. T. (1997). "Cellular inflammatory response after spinal cord injury in Sprague-Dawley and Lewis rats." J Comp Neurol **377**(3): 443-64.

PRANGE, M. T. and MARGULIES, S. S. (2002). "Regional, directional, and age-dependent properties of the brain undergoing large deformation." J Biomech Eng **124**(2): 244-52.

RIVLIN, A. S. and TATOR, C. H. (1978). "Effect of duration of acute spinal cord compression in a new acute cord injury model in the rat." Surg Neurol **10**(1): 38-43.

SCHLOSSHAUER, B. (1993). "The blood-brain barrier: morphology, molecules, and neurothelin." Bioessays **15**(5): 341-6.

SENTER, H. J. and VENES, J. L. (1978). "Altered blood flow and secondary injury in experimental spinal cord trauma." J Neurosurg **49**(4): 569-78.

STEWART, W. W. (1981). "Lucifer dyes--highly fluorescent dyes for biological tracing." Nature **292**(5818): 17-21.

STOKES, B. T., NOYES, D. H. and BEHRMANN, D. L. (1992). "An electromechanical spinal injury technique with dynamic sensitivity." J Neurotrauma **9**(3): 187-95.

SUGIO, S., KASHIMA, A., MOCHIZUKI, S., NODA, M. and KOBAYASHI, K. (1999). "Crystal structure of human serum albumin at 2.5 A resolution." Protein Eng **12**(6): 439-46.

SUSSMAN, M. S. and BULKLEY, G. B. (1990). "Oxygen-derived free radicals in reperfusion injury." Methods Enzymol **186**: 711-23.

TERAE, S., TAKAHASHI, C., ABE, S., KIKUCHI, Y. and MIYASAKA, K. (1997). "Gd-DTPA-enhanced MR imaging of injured spinal cord." Clin Imaging **21**(2): 82-9.

TRAVLOS, A., ANTON, H. A. and WING, P. C. (1994). "Cerebrospinal fluid cell count following spinal cord injury." Arch Phys Med Rehabil **75**(3): 293-6.

WAGNER, F. C., JR. and STEWART, W. B. (1981). "Effect of trauma dose on spinal cord edema." J Neurosurg **54**(6): 802-6.

WESTMARK, R., NOBLE, L. J., FUKUDA, K., AIHARA, N. and MCKENZIE, A. L. (1995). "Intrathecal administration of endothelin-1 in the rat: impact on spinal cord blood flow and the blood-spinal cord barrier." Neurosci Lett **192**(3): 173-6.

WHETSTONE, W. D., HSU, J. Y., EISENBERG, M., WERB, Z. and NOBLE-HAEUSSLEIN, L. J. (2003). "Blood-spinal cord barrier after spinal cord injury: relation to revascularization and wound healing." J Neurosci Res **74**(2): 227-39.

YOUNG, W. (2002). "Spinal cord contusion models." Prog Brain Res **137**: 231-55.

CHAPTER 3: MECHANICAL PROPERTIES OF DURA MATER FROM THE RAT BRAIN AND SPINAL CORD

ABSTRACT

The dura mater is the outermost and most substantial meningial layer of central nervous system (CNS) tissue that acts as a protective membrane for the brain and spinal cord. In animal models of traumatic brain injury and spinal cord injury, mechanical insults are often delivered directly to the dura to injure the underlying tissue. As such, including a description of the mechanical properties of dura mater is critical for biomechanical analyses of these models. We have characterized the mechanical response of dura mater from the rat brain and spinal cord in uniaxial tension. Testing was performed at low ($0.0014 sec^{-1}$) and high ($19.42\ sec^{-1}$) strain rates. Both rat cranial dura and spinal dura demonstrated non-linear stress-strain responses characteristic of collagenous soft tissues. The non-linear increase in stress lagged in the spinal dura compared to the cranial dura. The slow rate data was fit to a 1-term Ogden hyperelastic constitutive law, and significant differences were observed for the stiffness, G, and the parameter, α, which nominally introduces non-linearity. High strain rate stress-relaxation tests were performed to 10% strain, which was held for 10 seconds. The relaxation was fit to a 4-term Prony series exponential decay. Cranial dura and spinal dura demonstrated similar overall relaxation, but significant differences were identified in the distribution of the relaxation over the Prony series parameters, which demonstrated that cranial dura tended to relax faster. Polarized light microscopy revealed that the structural entities of spinal dura were aligned in the axial direction, whereas cranial dura did not demonstrate a preferential alignment. This was confirmed qualitatively with Masson's Trichrome and Verhoeff's Van Gieson

staining for collagen and elastin, which also indicated greater elastin content for the spinal dura than for the cranial dura.

INTRODUCTION

The dura mater is the outermost and most substantial meningial layer of central nervous system (CNS) tissue that acts as a protective membrane for the brain and spinal cord (Weed 1938). In vivo, dura mater is subjected to stresses from stretching during movement and from cerebrospinal fluid (CSF) pressure changes (Patin, Eckstein et al. 1993). The dura is composed primarily of collagen fibers interspersed with fibroblasts and elastin, and is generally flexible and elastic when stretched and deformed (Vandenabeele, Creemers et al. 1996). The microstructural characteristics of dura mater fibers can vary with anatomy. For instance, human lumbar dura fibers tend to be structurally aligned in the longitudinal direction, thereby providing mechanical anisotropic properties, whereas human cranial dura fibers tend to lack directional orientation and lead to isotropic mechanical properties (McGarvey, Lee et al. 1984; Patin, Eckstein et al. 1993; Runza, Pietrabissa et al. 1999). Human spinal dura mater (~100MPa) (Patin, Eckstein et al. 1993; Runza, Pietrabissa et al. 1999) and bovine spinal cord dura mater (~60MPa) (Runza, Pietrabissa et al. 1999) are considerably stiffer than the spinal cords they surround (~1MPa for human and bovine) (Bilston and Thibault 1996; Ichihara, Taguchi et al. 2001). Similarly, human cranial dura mater (~60MPa) (McGarvey, Lee et al. 1984) is much stiffer than human brain tissue (less than 1KPa) (Prange and Margulies 2002). These large differences underlay the functions of the dura, especially in protection of central nervous system tissue, as well as allowing for pressure variations and movement (van Noort, Black et al. 1981).

Both spinal cord injury (SCI) and traumatic brain injury (TBI) are prevalent and costly problems in the United States (Kraus and McArthur 1996; Berkowitz 1998), and understanding the physical and functional responses of the spinal cord and brain structures to

trauma is necessary to design rational means and methods of injury prevention, as well as develop effective treatments. Animal models continue to be the gold standard for identifying the physiological and functional consequences of TBI and SCI, and by far, rat and mouse models are most often employed (Stokes and Jakeman 2002; Young 2002; Guertin 2005). Many of these models, such as fluid percussion, weight drop, and electromagnetic or pneumatic impactors (Dixon, Lyeth et al. 1987; Stokes, Noyes et al. 1992; Meaney, Ross et al. 1994; Ueno, Melvin et al. 1995; Young 2002), deliver the mechanical insult across the intact dura mater. Thus, to evaluate the tissue biomechanics associated with these models, particularly with computational simulations, the contribution of the dura mater to the overall mechanical response must be included. Interestingly, although rats are by far the most commonly used experimental animal to study TBI and SCI, only a few investigations have been presented for the material properties of rat central nervous system tissue of any kind (Gefen, Gefen et al. 2003; Fiford and Bilston 2005). While there have been investigations into the human, bovine, and canine dura, to our knowledge, there are no published reports of rat dura properties, and identifying these properties is an important component in accurately modeling injury biomechanics in these and similar commonly employed models.

The present study was aimed primarily at identifying the mechanical properties of rat dura mater from the brain and spinal cord at low and high strain rates**.** Dura from both regions were found to follow hyperelastic and viscoelastic behavior. Cranial dura demonstrated more acute non-linear stiffening. Polarized light microscopy and histology suggest that the differences in constitutive behavior are linked to the structural organization and composition of the tissues.

MATERIALS AND METHODS

Sample Preparation

Adult Long Evans Hooded rats (77+/-5 days old) (Simonsen Labs, Gilroy, CA) were euthanized with a lethal dose of sodium pentobarbital (65 mg/kg), and the spinal columns were immediately removed. The laminae were removed from the first cervical vertebra (C1) to the first lumbar vertebrae (L1). The dura was then marked into three 30mm segments with a permanent marker to designate original in situ length. Within each 30mm section, the central 12mm was also marked (Figure 3-1). The dura was carefully removed from the dorsal surface of the spinal cord and placed in fresh phosphate buffered saline (PBS). Dura samples were cut in strips of 30mm based on the in situ markings and kept hydrated in fresh PBS. Typically, three samples were harvested per cord, unless damage was noted upon visual inspection. Length and width measurements were taken at the central 12mm with digital calipers. The dura samples were then transported to the mechanical testing device. The ends of each sample were removed, and thickness of these samples was measured optically with a calibrated, motorized microscope stage (Prior Scientific, Inc, Rockland, MD) by focusing on the bottom surface of the sample, recording the stage position in microns, and then focusing on the top surface of the sample and again recording stage position in microns.

Dura from the rat brain was harvested from Long Evans Hooded Rats (77 +/- 5 days). Animals were euthanized as described above and decapitated. The skull was removed to expose the dura. The dura mater covering the brain was demarcated in situ into 4mm segments with an indelible marker (Figure 3-1). The dura was then removed and placed in PBS prior to testing. Typically, four samples were harvested per animal. Length and width measurements were taken at the central 8mm with calipers. The dura samples were then

transported to the mechanical testing device. Parts of the dura not used for mechanical testing were removed for height measurements. All experimental procedures involving animals were approved by the Rutgers University Animal Care and Facilities Committee (IACUC#02-015).

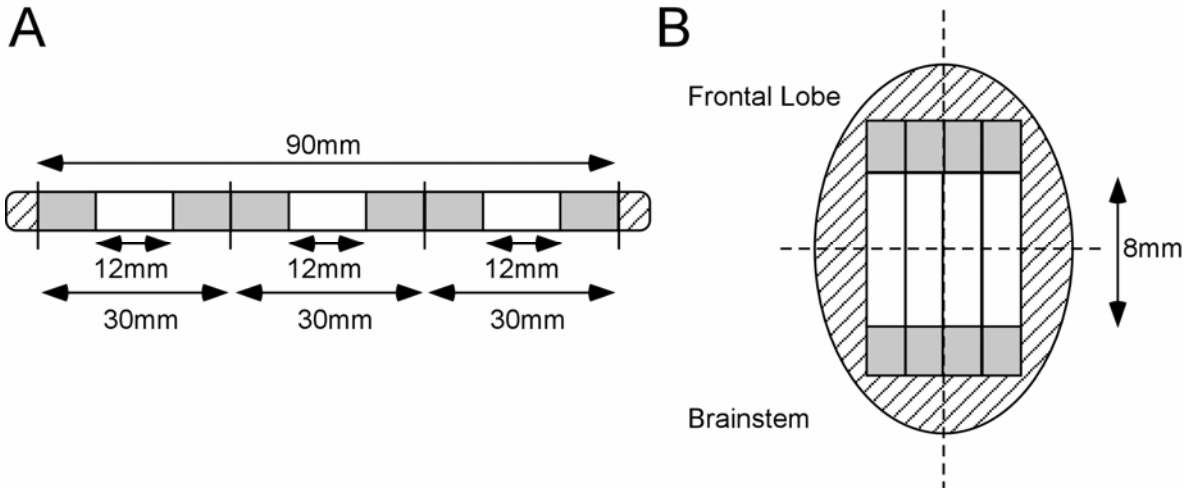

Figure 3-1: Schematic describing sample removal for (A) spinal dura and (B) cranial dura. For spinal samples, the dura was marked in vivo into 30mm segments, and the central 12mm of each 30mm segmented was also marked. The remaining areas (gray) were used for gripping, and the hashed areas were used for thickness measurements. For cranial dura, 8mm-long samples were similarly marked.

Mechanical Testing

Spinal and cranial dura samples were tested in uniaxial tension using a Bose/Enduratec ELF 3200 (Bose Corporation, Eden Prairie, MN) with a 1N cantilever load cell (Measurement Specialties, Hampton, VA). The dura sample was placed on a plastic plate, which was clamped to the actuator with compression grips. The other end of the sample was placed on a second thin plastic plate that was rigidly bolted to the load cell. The dura was then covered with a cyanoacrylate adhesive (Krazy Glue, Columbus, OH), and another plastic plate was placed on top of the dura on each grip, sandwiching the dura between the plastic plates and creating plastic-plastic as well as dura-plastic adhesion to prevent any slipping of the dura relative to the plastic plate. Small pieces of glitter were placed on each dura sample to measure strain uniformity. During the entire process, the dura samples were kept well hydrated by an ultrasonic humidifier (Wachsmuth & Krogmann, Elk Grove Village, IL) positioned under the sample**.** Once engaged in the grips, the samples were slowly stretched back to the original in vivo length of 12mm for the spinal dura or 8mm for the cranial dura and allowed to equilibrate for several minutes. All mechanical tests were done within 2 hours of sacrifice to reduce tissue breakdown, since it was previously reported that post-mortem time can significantly affect the mechanical properties of biological tissues (Galford and McElhaney 1970; Bilston and Thibault 1996).

Samples of cranial and spinal dura mater were tested in uniaxial tension at one of two rates. Some samples (n = 8 for spinal dura, n = 8 for cranial dura) were subjected to stress-relaxation to 10% extension at a strain rate of $19.4s^{-1}$ and held for 10 seconds. The remaining samples (n=15 for spinal dura, n=8 for cranial dura) were loaded at a strain rate of $0.0014s^{-1}$ until failure. For these tests, dura samples were preconditioned at a strain rate of $0.0014s^{-1}$ to

10% strain. It was determined that 4 preconditioning cycles were necessary before stress-strain equilibrium was reached for spinal and cranial dura samples, after which these samples were uniaxially loaded until failure. The high strain rates and relatively large extension precluded cyclic preconditioning of the samples for high strain rate tests. Load and displacement were recorded for the duration of the test. Images were documented every 2mm of displacement using a digital camera (Nikon Coolpix S500, Melville, NY) to assess the uniformity of strain from the glitter using image analysis (Microsuite analysis software Olympic Scientific, Mellville, NY). Specifically, the strain in the dura was compared among pairs of markers, using the ends of the grips as additional points, by determining stretch ratio in each section and normalizing by the overall stretch ratio.

Constitutive modeling of the rat dura

The dura mater was modeled as hyperelastic-linearly viscoelastic continuum solid. At very fast rates (i.e. instantaneous) and very slow rates (i.e. quasistatic), the model assumes hyper-elastic behavior. An Ogden form of the hyperelastic strain energy potential function, W, which has previously been used to model both spinal cord and brain tissue (Bilston and Thibault 1996; Miller and Chinzei 2002), was used to model the elastic behavior of the dura:

$$W = \sum_{i=1}^{N} \frac{2G_i}{\alpha_i^2}\left(\lambda_1^{\alpha_i} + \lambda_2^{\alpha_i} + \lambda_3^{\alpha_i} - 3\right) \qquad \text{Equation 3-1}$$

where λ_i are the principal stretches, N is the complexity of the law, which is material dependent, and G_i and α_i are material-dependent parameters. For simple, uniaxial tension, assuming incompressibility, the relationship between nominal stress and stretch ratio for an Ogden material is:

$$\sigma = \sum_{i=1}^{N} \frac{2G_i}{\alpha_i}\left(\lambda_1^{\alpha_i - 1} - \lambda_1^{-0.5\alpha_i - 1}\right) \qquad \text{Equation 3-2}$$

Volumetric changes due to thermal expansion are ignored. The instantaneous shear modulus is therefore given by:

$$G0 = \sum_{i=1}^{M} Gi \qquad \text{Equation 3-3}$$

The viscoelastic portion of the material laws was described with a Prony series exponential decay:

$$G_R(t) = G_0\left[1 - \sum_{k=1}^{N} \overline{g}_k^P\left(1 - e^{-t/\tau_k}\right)\right] \qquad \text{Equation 3-4}$$

where the instantaneous shear modulus is multiplied by a normalized function that includes relative relaxations, g_k, at characteristic time constants, τ_k. The quasi-static shear modulus can then be related to the instantaneous modulus by:

$$G_\infty = G_0\left(1 - \sum_{k=1}^{N} \overline{g}_k^p\right) \qquad \text{Equation 3-5}$$

The slow rate response of the dura was fit with the Ogden hyperelastic representation of the quasi-static shear moduli based on Eq. 3-2 (Kaleidagraph, Synergy Software, Reading, PA). Viscoelastic time constants were determined by normalizing the relaxation portion of the stress vs. time curves of the high rate tests and fitting the curves to the bracketed term of Eq. 3-4 (Bilston and Thibault 1996; Miller and Chinzei 2002; Prange and Margulies 2002) (SPSS 15.0, Chicago, IL), and the two are combined to identify the instantaneous shear moduli via Eq.3- 5.

Data Analysis and Statistics:

Descriptive statistics were taken for all experimental results of the stress relaxation data, as well as the stress-strain data. Ogden and Prony Series parameters, as well as failure properties, were compared statistically between the cranial and spinal dura mater with one-way ANOVA ($P<0.05$).

Polarized Light Microscopy

Alignment of fibers in the dura mater was initially assessed qualitatively with polarized light microscopy. Long Evans hooded rats (77 days old) were euthanized with a lethal dose of sodium pentobarbital (65 mg/kg), exsanguinated with 200ml of heparinized saline, and perfused transcardially with 10% formalin. The spinal and cranial dura were removed and stored in 10% formalin for 2 hours. Dura samples were then mounted on charged glass slides (Superfrost Plus, Fisher Scientific, Pittsburgh, PA) and placed on the microscope stage between a linear polarizer and a linear analyzer oriented as 'cross-polars' with axes of polarization 90° apart. The dura samples were rotated between 0° and 180°. Separate mosaic images for the cranial and spinal dura were generated via a Hamamatsu ORCA CCD camera (Bridgewater, NJ) using computer controlled microscopy (Olympus IX81, Olympus America, Center Valley, PA, USA) to assess anisotropy in the tissue fibers.

Histology

Dura structure and composition were visualized with Masson's Tri-chrome for collagen or Verhoeff's Van Gieson stain for collagen and elastic tissue. Dura samples were harvested from transcardially perfused animals as described above and stored in 10%

formalin for 2 hours. Samples were then placed in 20% sucrose solution overnight for cryoprotection. Dura samples were sectioned horizontally into 20μm sections with a cryostat (ThermoShandon, Pittsburgh, PA). Sections were mounted on charged glass slides (Superfrost Plus, Fisher, Pittsburgh, PA) and stained for elastin, collagen, and cell nuclei using Sigma Accustain Elastic Stain kit or Tri-Chrome kit (Sigma Aldrich, St. Louis, MO) in accordance with the manufacturer's specifications. Samples were coverslipped using DPX histology mounting medium (Sigma), and brightfield images were captured with an upright microscope (Carl Zeiss Microimaging, Inc.,Thornwood, NY).

RESULTS

Low strain rate stress-strain response

Both cranial and spinal dura mater demonstrated non-linear stress-strain behavior typical of collagenous soft tissues when tested to failure in uniaxial tension at slow rates ($0.0014s^{-1}$). In general, the response of spinal dura was more variable than cranial dura, especially during the elastic portion of the curve, where the onset of the non-linear portion shifted considerably. Consistent behavior was not observed past the perceived yield point for either cranial or spinal dura. Some samples failed completely soon after yielding, while others continued to carry increasing load, albeit at lower apparent stiffness than during the elastic portion. Digital image analysis (Microsuite Analysis software) was used to assess the uniformity of strain in the dura during uniaxial tensile testing. The stretch ratio in the dura was compared among 3 pairs of markers, using the grips as additional points. No significant differences were detected for the stretch from the left grip to the first marker, the first to the second marker, or the second marker to right grip within the elastic region. During this time, the normalized stretch (stretch in a section divided by overall stretch) showed no discernable pattern and ranged from 0.99 to 1.01.

For each curve, the elastic portion was identified by fitting the linear portion of the stress-stretch curve and offsetting that line 0.2%. The average yield stress and stretch at yield (+/- std. dev) was lower for cranial dura (1.27MPa +/- 0.66MPa at λ = 1.13 +/- 0.01) than spinal dura (2.14MPa +/- 1.56MPa at λ = 1.24 +/- 0.16), but neither difference was significant (P = 0.148 and P = 0.085, respectively). The average ultimate tensile stress for spinal dura mater was 2.91MPa +/- 1.30MPa at an average stretch ratio of 1.43 +/- 0.183, and average ultimate tensile stress for cranial dura mater 2.49MPa +/- 2.03MPa at an average

stretch ratio of 1.39 +/- 0.133, which were also not significantly different (P = 0.55 and P = 0.57, respectively). Representative stress-strain curves from spinal and cranial dura mater are shown in Figure 3-2.

The elastic portion of each stress-stretch ratio curve was fit to a 1-term Ogden hyperelastic constitutive model (Eq. 2 with N = 1), which sufficiently captured the stress-strain behavior, to identify the material parameters for the spinal and cranial dura (Table 1). The stiffness, G of spinal dura was significantly greater than cranial dura (P = 0.012), whereas α, which generally introduces the non-linearity into the constitutive law, was significantly greater for cranial dura (P = 0.0002). The average Ogden formulations for cranial and spinal dura are plotted Figure 3-3.

Table 3-1 –Mechanical Characteristics

Dura Ogden Hyperelastic Constants for Spinal and Cranial Dura $\sigma = \frac{2G}{\alpha}\left(\lambda_1^{\alpha-1} - \lambda_1^{-0.5\alpha-1}\right)$			
	Spinal Dura	Cranial Dura	
Parameter	Average Value +/- Std. Dev.	Average Value +/- Std. Dev.	*P*-value
G (MPa)	1.20 +/- 0.79	0.42 +/- 0.19	0.012*
α	16.2 +/- 9.74	32.9 +/- 6.65	0.002*
Yield Stress (MPa)	2.14 +/- 1.56	1.27 +/- 0.66	0.148
Stretch at Yield	1.24 +/- 0.16	1.13 +/- 0.01	0.085
Ultimate Tensile Strength (MPa)	2.91 +/- 1.30	2.49 +/- 2.03	0.55
Stretch at UTS	1.43 +/- 0.183	1.39 +/- 0.133	0.53

*Significant difference observed between cranial and spinal dura, ANOVA, $P < 0.05$

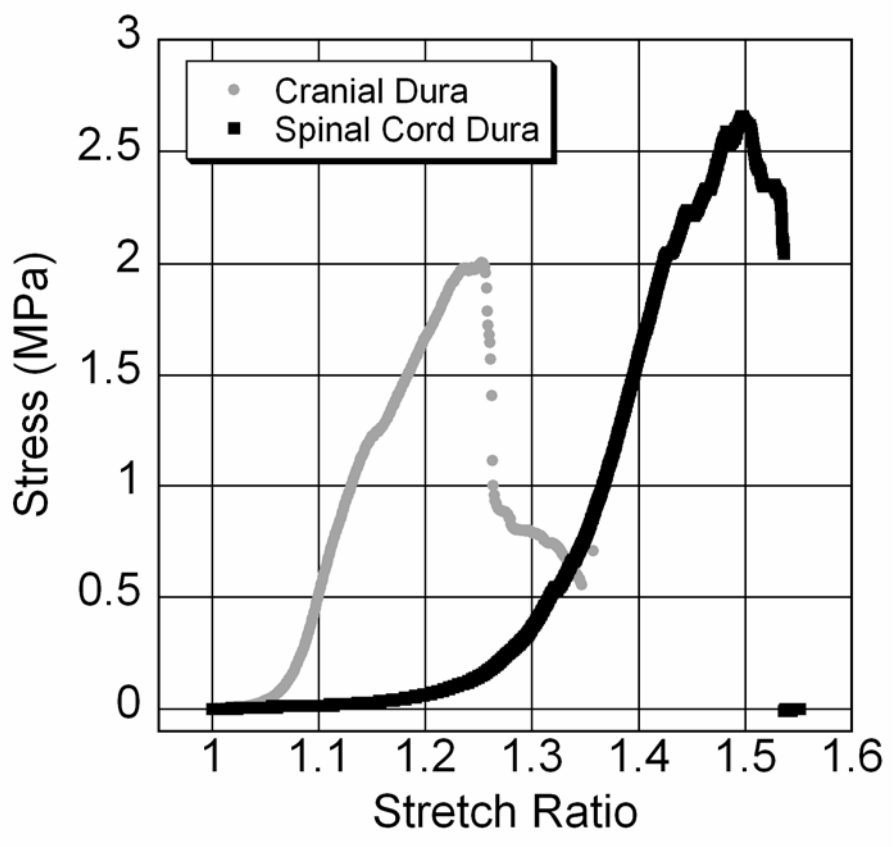

Figure 3-2: Representative stress-stretch curves for spinal and cranial dura. Dura samples were loaded in uniaxial tension at $0.014sec^{-1}$ until failure. Both spinal and cranial samples demonstrated non-linear stiffening consistent with load-bearing soft tissues. The behavior following yielding/microfracture was highly variable. In general, cranial samples demonstrated more acute non-linear stiffening at lower stretch ratios than spinal cord samples.

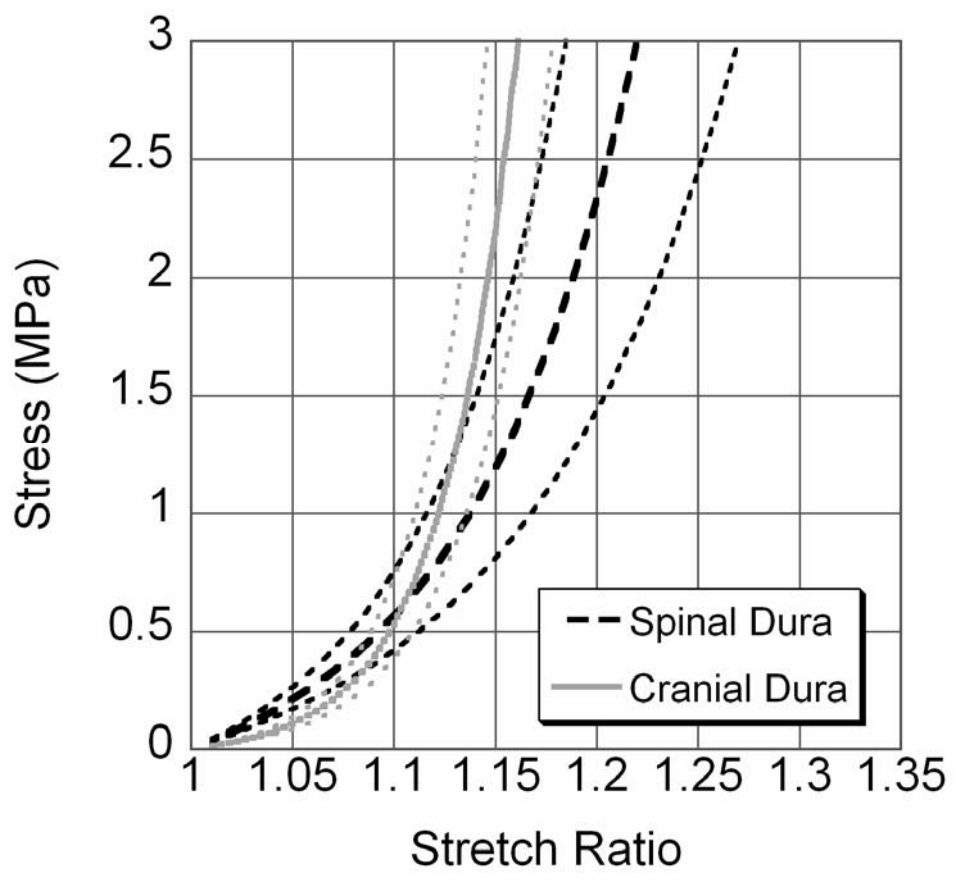

Figure 3-3: Ogden hyperelastic material laws derived from average properties (+/- standard error) for spinal and cranial dura. The yield point from each stress-stretch curve was identified by offsetting the linear portion of the curve by 0.2%. The 'elastic' portion of each curve was fit to a 1-term Ogden hyperelastic law to determine the stiffness parameter, G, and the exponent α, from Eq. 1, and the average of these parameters was used for the material law. Cranial dura demonstrates a lower stiffness at low stretch levels, but increases non-linearly at a greater rate than spinal dura.

Stress-relaxation response of the rat spinal dura

The viscoelastic response of the dura was assessed via stress relaxation by loading samples to 10% stretch at a strain rate of $19.4s^{-1}$ and holding at that stretch for 10sec, during which time both cranial and spinal dura mater exhibited significant relaxation (spinal dura ~ 64%; cranial dura ~ 69%). The mean stress relaxations for the rat spinal and cranial dura are shown in Figure 3-4. To identify time constants from the stress-relaxation data that are appropriate for biomechanics studies at different time scales, the decay function was fit with a 4-term Prony series decay function, which captured the early time constants necessary for modeling traumatic loading conditions, while still preserving the full decay time history without the cost of the accuracy of the shorter time constants. The individual constants from the Prony series from cranial and spinal dura mater were compared with one-way ANOVA, and the results indicated that the dura from the brain relaxes more quickly than that from the spinal cord. The first 2 time constants, τ_1, τ_2, were significantly different between the spinal and cranial dura ($P < 0.007$), while the last two time constants, τ_3, and τ_4, were not significantly different ($P > 0.1$). All four relative stress relaxation constants, $g_1, g_2, g_3,$ and g_4 were significantly different between the spinal and cranial dura ($P<0.002$). However, the net relaxation (sum g_1- g_4) was not significant ($P = 0.102$).

Table 3-2 – Relaxation Constants for the Dura

Summary of Relaxation Constants for Spinal and Cranial Dura

$$y = 1 - g_1\left(1 - \exp\left(\frac{-t}{\tau_1}\right)\right) - g_2\left(1 - \exp\left(\frac{-t}{\tau_2}\right)\right) - g_3\left(1 - \exp\left(\frac{-t}{\tau_3}\right)\right) - g_4\left(1 - \exp\left(\frac{-t}{\tau_4}\right)\right)$$

	Average Value (Std. Dev)		
Constant	**Spinal Dura**	**Cranial Dura**	**P-value**
g_1	0.329 (0.050)	0.240 (0.053)	0.004*
τ_1	0.009 (0.002)	0.005 (0.002)	0.007*
g_2	0.128 (0.030)	0.213 (0.027)	0.0001*
τ_2	0.081 (0.026)	0.044 (0.012)	0.003*
g_3	0.086 (0.021)	0.118 (0.011)	0.002*
τ_3	0.564 (0.190)	0.474 (0.071)	0.228
g_4	0.086 (0.013)	0.122 (0.019)	0.001*
τ_4	4.69 (1.202)	3.99 (0.490)	0.152
$g_1+g_2+g_3+g_4$	0.629 (0.089)	0.693 (0.054)	0.102
R^2	0.99	0.99	-

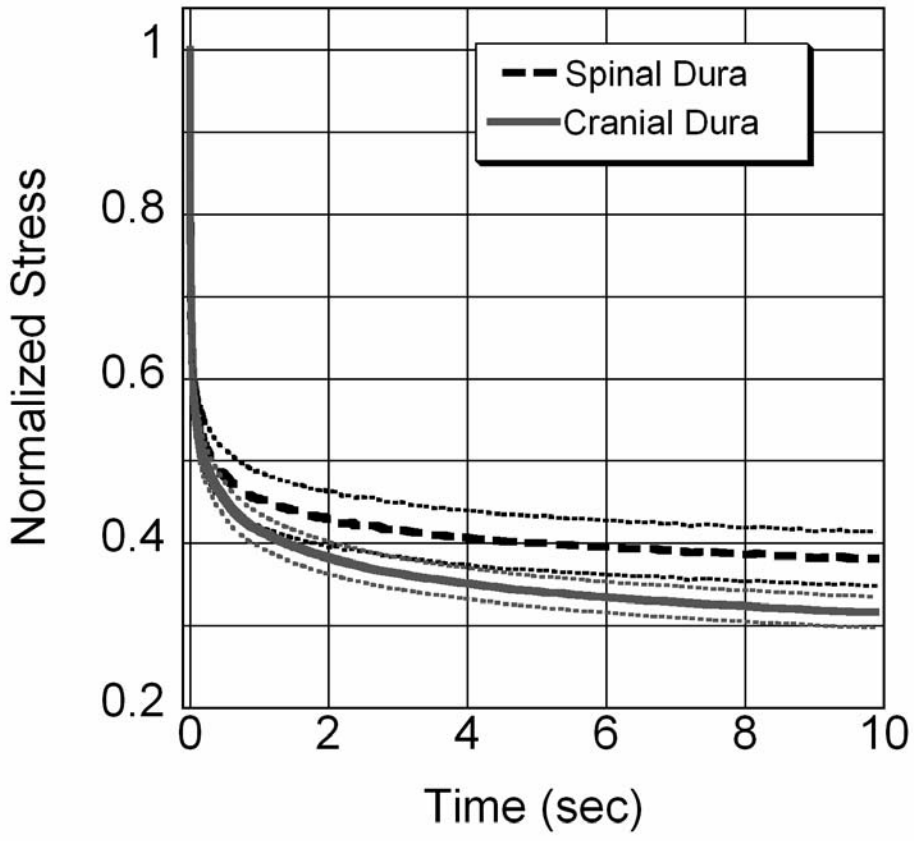

Figure 3-4: Mean relaxation response (+/- standard error) of spinal and cranial dura. Dura samples were loaded to 10% stretch at a rate of 19.4sec^{-1} and held at that stretch for 10sec. The resultant stress was normalized by peak stress and fit to a 4-term Prony series exponential decay, which is summarized in Table 3-2.

Polarized Light Microscopy and Elastic Stain Histology

Whole rat spinal and cranial dura samples were interrogated with polarized light to visualize anisotropy in the fibrillar matrix. Spinal dura samples demonstrated substantial alignment; when samples were placed coincident with the axis of polarization, nearly all light was extinguished (Figure 3-5A). However, when the sample was oriented at ~45° between polarizer and analyzer, the intensity increased significantly (Figure 3-5B), indicating alignment in the axial direction (though alignment in the transverse direction is also possible.) Unlike spinal dura samples, dura mater from the rat brain exhibited minimal alignment. Under cross-polars, intensity was moderate when samples were placed coincident with the axis of polarization (Figure 3-5C). The pattern of intensity when the sample was rotated to ~45° changed, but the overall intensity remained approximately the same. The average pixel intensity (on a scale of 0-255) of the images in Figure 3-5 was calculated with Olympus Microsuite Image Analysis Software. The average intensity rose from 24.6 to 84.8 when the spinal sample was rotated off-axis, whereas the average intensity of the cranial sample rose minimally from 44.3 to 50.4.

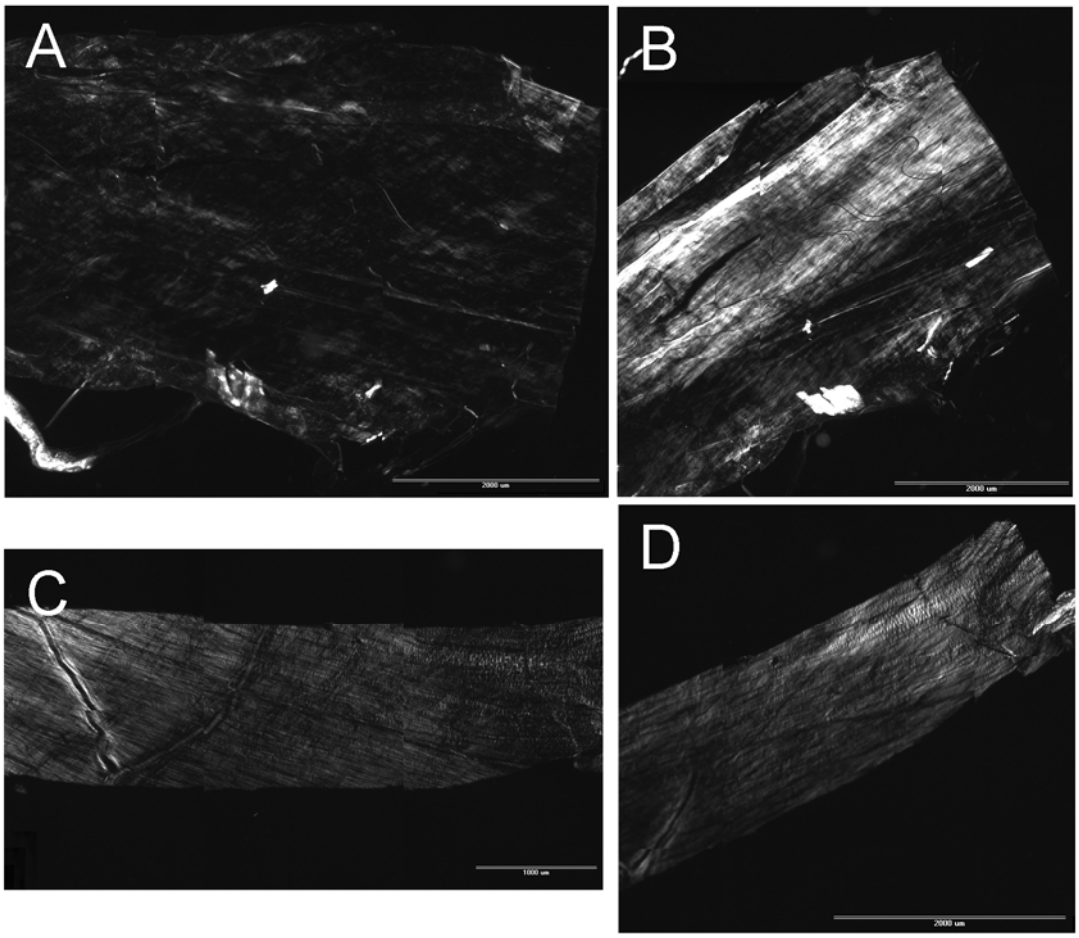

Figure 3-5: Assessment of alignment with polarized light microscopy. Whole-thickness dura samples were interrogated with linearly polarized light, which was subsequently passed through a second linear polarizer oriented 90° from the first polarizer to analyze the orientation. (A) Spinal dura samples oriented with the long axis of the sample coincident with the axis of polarization extinguished nearly all of the light (average intensity for this image = 24.6 on an 8-gray, 0-255). (B) A substantial increase in intensity was observed when the sample was rotated ~45°, indicating that the fibers comprising the spinal dura are oriented axially (average intensity = 84.8). (C) Cranial samples placed with the long axis of the sample coincident with the axis of polarization an inhomogeneous intensity field of moderate intensity (average intensity = 44.3). (D) Upon rotating the sample, a redistribution of intensity was observed, but the increase in overall intensity was small (average intensity = 50.4).

Histology

Verhoeff's Van Gieson Staining for collagen and elastin confirmed that the prevailing orientation of spinal dura was axial. The spinal dura in Figure 3-6A shows a prevalence of cell nuclei (blue-purple ovals) that are preferentially aligned along the collagen (pink) and elastin (blue-dark blue). Collagen in this section is organized in large bundles. Figure 3-6B reveals a considerable amount of elastin as well as collagen (pink) in the axially oriented matrix. Cranial dura samples stained with Verhoeff's Van Gieson stain showed random orientation of collagen fibers and fewer elastic fibers (Figure 3-6C). Tri-chrome staining of collagen revealed an interwoven meshwork of fibers in cranial dura (Figure 3-6D).

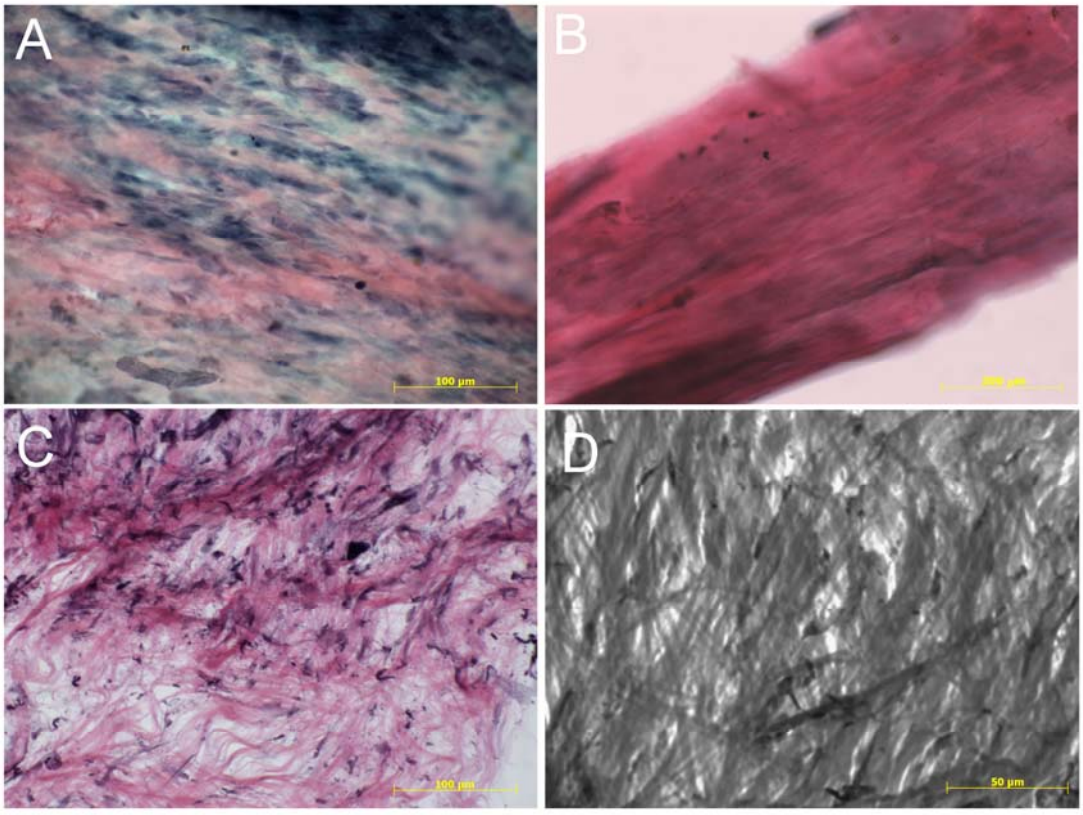

Figure 3-6: Histological staining of spinal (A, B) and cranial (C, D) dura. Verhoeff's Van Gieson staining (A, B, C) showed that spinal and cranial dura both include collagen (pink) and elastin (blue/dark blue), though the elastin content appeared to be greater in spinal samples. Spinal dura fibers appeared to be aligned axially (B), and induced orientation of cell nuclei in a cell-dense layer of the dura (A). In some areas, cranial dura fibers tended to appear randomly oriented and wavy (C), while in other areas, a cris-cross, hatched appearance was apparent (Tri-chrome staining) (D).

DISCUSSION

The primary purpose of this work was to describe the material properties of dura mater harvested from the rat brain and spinal cord. Rat models of TBI and SCI have been invaluable in identifying the pathological sequelae following trauma and in evaluating therapeutic means of intervention, and often deliver the mechanical insult across the intact dura mater. Thus, to evaluate the tissue biomechanics associated with these models, the contribution of the dura mater to the overall mechanical response must be included. The dura from both rat brain and rat spinal cord were modeled effectively with an Ogden hyperelastic-linear viscoelastic constitutive law. The stiffness parameter from the Ogden law for the cranial dura was lower than spinal dura, and the non-linear stiffening with increasing stretch was more pronounced for cranial dura than spinal dura. Analysis of relaxation data following high strain rate uniaxial loading indicated that, although the total relaxation of the samples was similar, the dura from the brain relaxed faster than that from the spinal cord.

As with the dura mater in other species, the rat dura mater is significantly stiffer than the CNS tissue it surrounds, which points to its protective role. For instance, Gefen et al. report that the in situ quasistatic shear modulus of rat brain is 0.1-1kPa, depending on the age of the tissue and whether it was preconditioned. By comparison, we found the rat cranial dura has a modulus on the order of 1MPa. Similarly, the rat spinal dura has a modulus in tension that is 2 orders of magnitude greater than the stiffness of rat spinal cord (Fiford and Bilston 2005). The dura, therefore, will contribute significantly to the overall mechanical response of the brain and/or spinal cord to traumatic loading and may absorb a large percentage of the kinetic energy, especially in models where the insult is delivered directly to the dura. As

such, the data described herein is valuable as input material parameters for simulations of rat models of TBI and SCI.

The differences in Ogden model properties of rat cranial and spinal dura mater may be linked to their mechanical functions. Whereas the brain is encased in a rigid skull, the enhanced mobility and flexibility of the spine requires the structures of the spinal cord to routinely experience mechanical loading during movement. For instance, MRI studies have shown that the human cervical spinal cord can experience 6-10% strain during flexion (Yuan, Dougherty et al. 1998). Thus, the extended lag phase in spinal dura can allow routine movement with less stress generation, which is not necessary in the cranial dura mater. The stress-strain behavior of cranial dura may therefore provide some compliance for smaller variations in CSF pressure while restricting expansion for larger increases.

Previous reports, collectively, have demonstrated that the properties of excised brain tissue are well correlated to those in vivo, provided that the tests on excised tissue are performed soon after sacrifice (Gefen, Gefen et al. 2003; Gefen and Margulies 2004). In this study, all samples were tested within 2hrs of euthanasia and harvest. In addition, both cranial and spinal dura were very thin (~80μm) and dehydrated quickly when exposed to air. To avoid the effects of dehydration, our samples were immersed in PBS during sample preparation, and a constant mist was provided during the actual mechanical testing. In preliminary experiments, we found that the stress-strain behavior and strain uniformity of the tissue was much more consistent when tissue was supplied with a constant, extremely fine mist via the ultrasonic humidifier vs. intermittent spray with saline (data not shown). Additionally, when not in solution, the dura tended to coil and fold onto itself. Special care was taken to avoid overlapping of the dura while placing the sample onto the grips, which

again resulted in improved consistency in the results. Recording the displacement along the length of the samples via fiduciary markers provided a means of evaluating strain uniformity and, additionally, a measure of the general quality of individual experiments. In general, the behavior in the elastic region was more consistent with cranial dura. Preliminary experiments demonstrated that the range and variability of spinal samples was the same in different regions (cervical, thoracic, lumbar – data not shown), and these samples were lumped together for the analysis.

The general, non-linear stress-strain response of rat dura mater is consistent with other collagenous, load bearing soft tissues, such as ligaments, tendons, and skin. In vivo, fibers from human dura tend to have an inherent undulated nature and are potentially aligned randomly (Frisen, Magi et al. 1969). During the initial stages of uniaxial tensile loading, those fibers begin to orient themselves in the direction of loading, straighten, and stretch, which leads to an initial compliance and lag in the stress (Viidik 1968; Frisen, Magi et al. 1969). As strain increases, the fibers further align and take on more load, which leads to a non-linear increase in stiffness (Viidik 1968; Frisen, Magi et al. 1969; Bilston and Thibault 1996; Fiford and Bilston 2005). Additionally, the dura has a significant number of elastin fibers, which are believed to contribute to the low-strain, toe-region of the stress-strain curve for soft tissues (Park 1984).

The differences in material behavior prompted us to preliminarily examine the structure and composition of the tissues. Polarized light microscopy indicated that the microstructure of spinal dura was significantly aligned, whereas cranial dura was more randomly oriented. Histological staining also indicated that the spinal dura was aligned along the axis of the spinal cord, but that orientation of the cranial dura was inhomogeneous and

often random. The histology also suggested that rat spinal dura maintains greater elastin content than cranial dura. The alignment of spinal dura was aligned in the direction of uniaxial testing, but also maintained greater elastin content. By comparison, the cranial dura showed a mesh-like structure and a lower elastin-content. The data suggests that transition from elastin to collagen loading is a strong factor in the non-linear stiffening of spinal dura, whereas rotation and alignment of collagen fibers in the direction of stretch is responsible for the non-linear stiffening in cranial dura. These results are qualitative, and a detailed, quantitative assessment of the structural organization via electron microscopy, small angle light scattering (SALS), or associated technique, as well as the composition via quantitative microscopy and digestive assays is necessary and warranted to develop a true structure-function relationship for these tissues.

The alignment we observed in the spinal and dura generally matches that found in human samples. Histology and scanning electron microscopy studies have shown that collagen fibers in the human lumbar dura mater demonstrated a preferential longitudinal orientation, which imparted transversely isotropic material properties. Stiffness in the direction of the fibers was ~5-10X the stiffness transverse to the fibers (Patin, Eckstein et al. 1993). In the present study, we only examined the mechanical properties of dura in the longitudinal/sagittal direction, primarily because the short width of the spinal samples precluded effective testing with our mechanical testing system in the transverse/coronal direction, and we are thus limited to an isotropic material law, when an anisotropic law is warranted, particularly for the spinal dura.

Unlike human lumbar dura, histological staining of canine lumbar dura mater showed no preferred longitudinal orientation, but instead an increased number of transverse fibers,

and an associated absence of directional properties (Patin, Eckstein et al. 1993). Additionally, bovine lumbar dura tested in uniaxial tension in the longitudinal direction demonstrated a much longer 'lag' portion compared to human lumbar dura tested parallel (Runza, Pietrabissa et al. 1999). Together, these data indicate there can be considerable species-to-species variation in the fundamental mechanical behavior of the dura mater, and it has been suggested that differences observed were partly due to the supine vs. upright nature of the species, as well as the associated lack of gravity-induced CSF pressure (Patin, Eckstein et al. 1993). The rat, of course, is a supine animal, yet rat spinal dura clearly demonstrated longitudinal alignment. Increased flexibility of the rat, coupled with a diminished hoop stress because of the smaller radius of the spinal cord, and, therefore, less need for circumferential reinforcement, may explain the preferred axial alignment in this species vs. other, larger supine animals.

The alignment we observed in the rat cranial dura generally matched that from human cranial dura. McGarvey et al. reported that the cranial dura fibers showed some local orientation, but often changed direction within a 5mm distance (McGarvey, Lee et al. 1984). They tested the cranial dura both longitudinally and transversely and determined that the cranial dura had an average stiffness of approximately 60MPa. Van Noort et al. performed tensile loading tests on human cranial dura and determined an average stiffness of 30MPa, but also noted that many of the samples were from cadavers older than 50 years, which could contribute to poor quality dura (van Noort, Black et al. 1981). They also determined through histology that at short distances, there are indications of preferred fiber orientation. Hamann et al. performed an in depth quantification of fibers orientation using SALS in the human cranial dura and determined that the fibers had multiple preferred orientations except in the

temporal region (Hamann, Sacks et al. 1998). Thus, it appears that dura mater from the brain may demonstrate anisotropic properties locally but tend towards isotropic properties in bulk measurements. The primary stresses experienced by the cranial dura are from CSF pressure, which would induce a roughly uniform membrane tension throughout the dura, with local variations due to anatomical/geometric factors that could lead to the local variations in alignment.

We performed stress relaxation tests at a significantly higher strain rate (~$20s^{-1}$) than those used in published studies of dura material properties of any species. High strain rate tests are necessary to capture the response of tissue in a regime that is relevant for neurotrauma clinically, as well as to emulate the strain rates applied in many in vivo SCI and TBI models (Dixon, Lyeth et al. 1987; Stokes, Noyes et al. 1992; Meaney, Ross et al. 1994; Young 2002). Previously, Patin et al. tested human lumbar dura in both longitudinal and transverse directions to a strain that corresponded to half failure at a rate of 10cm/min. They noted that 15-33% of the stress relaxed in 24 seconds, but unlike failure testing, stress relaxation testing showed no mechanical directionality (Patin, Eckstein et al. 1993). McGarvey et al, performed stress relaxation tests between $5\%min^{-1}$ and $500\%min^{-1}$ on human cranial dura and showed that on average approximately 20% of the stress relaxed in 1000 seconds. We found cranial and spinal dura mater demonstrated more than 60% relaxation when strained at the higher rates. This relaxation is substantially greater than previous reports, which undoubtedly is related to the generation of greater stresses at higher rates, essentially supplying more stress to relax than had been done in the previous studies.

We fit the relaxation data to a 4-term Prony series exponential decay. The four-term Prony series decay function allowed an accurate determination of short (<100msec),

intermediate (100msec – 1 sec), and long (>1sec) time constants, and provides a robust material determination for different biomechanical studies and simulations. Traumatic injury studies clearly call for accurate assessment of short time constants, and splitting the relaxation into 4 terms resulted in time constants on the same order as loading rates experienced in trauma and in models of TBI and SCI. However, there are other instances where loading of brain and spinal cord structures occurs over a longer time period and the mechanics may be more appropriately modeled with the intermediate and long time constants, and possibly constants determined from longer hold periods than the 10 seconds employed herein, although the majority of relaxation had already occurred. Robotic and virtual surgeries (Federspil, Geisthoff et al. 2003; Spicer, van Velsen et al. 2004), where the dynamic loads on the spinal and dura are within or just above physiological levels, chronic cord compression syndromes, such as syringomyelia (Loth, Yardimci et al. 2001; Carpenter, Berkouk et al. 2003) or hydrocephalus (Taylor and Miller 2004; Linninger, Xenos et al. 2007) that result in an increase in CSF pressure, or increased pressure from a myleoma, sarcoma, or other malignancies, are more appropriately modeled with longer hold times.

Whereas no significant differences were observed between the total relaxation of cranial and spinal dura, the distribution of relaxation among the 4-terms in the Prony series was different. Cranial dura had significantly shorter time constants for the first two terms than the spinal cord (5msec and 44msec vs. 9msec and 81msec). The first two terms contributed approximately equally to the total relaxation for cranial dura (~24% vs. 21%), whereas the spinal dura experienced greater relaxation over the first time constant than the second one (33% vs. 13%). Together, the two terms accounted for 45% and 46% of the total stress, but the brain relaxed nearly twice as fast. The cranial dura also demonstrated

significantly more relaxation at later time constants than the spinal dura (3rd and 4th term), though there were no significant differences in the time constants, themselves. A detailed analysis of composition and structure-function behavior is likely necessary to identify the source of the differences in relaxation behavior between spinal and cranial dura mater.

However, for both tissues, relaxing the dura stiffness may allow relief of the circumferential/hoop stress intracranial/intrathecal pressure by allowing some volume expansion, which may be especially significant for the cranial dura because of the larger radius. Additionally, relaxation in spinal dura is necessary to alleviate stresses during routine postural movements and extended times in flexion and extension. It is well known that fibroblasts, the chief cell type in dura mater, respond phenotypically to mechanical tension by altering their cytoskeleton and adhesion to the surrounding matrix and their synthesis of proteins and enzymes involved in matrix re-organization, including an increase in type I collagen synthesis, to appropriately adjust the tissue's properties. The large, cumulative relaxation in dura mater will also assist in shielding fibroblasts from these stresses to limit matrix remodeling of the tissue (Kessler, Dethlefsen et al. 2001; D'Addario, Arora et al. 2003; He, Macarak et al. 2004; Petroll, Vishwanath et al. 2004).

REFERENCES

BERKOWITZ, E. D. (1998). "Revealing America's welfare state. [Review of: Howard, C., The hidden welfare state: tax expenditures and social policy in the United States. Princeton University Press, 1997]." Rev Am Hist **26**(3): 620-4.

BILSTON, L. E. and THIBAULT, L. E. (1996). "The mechanical properties of the human cervical spinal cord in vitro." Ann Biomed Eng **24**(1): 67-74.

CARPENTER, P. W., BERKOUK, K. and LUCEY, A. D. (2003). "Pressure wave propagation in fluid-filled co-axial elastic tubes. Part 2: Mechanisms for the pathogenesis of syringomyelia." J Biomech Eng **125**(6): 857-63.

D'ADDARIO, M., ARORA, P. D., ELLEN, R. P. and MCCULLOCH, C. A. (2003). "Regulation of tension-induced mechanotranscriptional signals by the microtubule network in fibroblasts." J Biol Chem **278**(52): 53090-7.

DIXON, C. E., LYETH, B. G., POVLISHOCK, J. T., et al. (1987). "A fluid percussion model of experimental brain injury in the rat." J Neurosurg **67**(1): 110-9.

FEDERSPIL, P. A., GEISTHOFF, U. W., HENRICH, D. and PLINKERT, P. K. (2003). "Development of the first force-controlled robot for otoneurosurgery." Laryngoscope **113**(3): 465-71.

FIFORD, R. J. and BILSTON, L. E. (2005). "The mechanical properties of rat spinal cord in vitro." J Biomech **38**(7): 1509-15.

FRISEN, M., MAGI, M., SONNERUP, I. and VIIDIK, A. (1969). "Rheological analysis of soft collagenous tissue. Part I: theoretical considerations." J Biomech **2**(1): 13-20.

GALFORD, J. E. and MCELHANEY, J. H. (1970). "A viscoelastic study of scalp, brain, and dura." J Biomech **3**(2): 211-21.

GEFEN, A., GEFEN, N., ZHU, Q., RAGHUPATHI, R. and MARGULIES, S. S. (2003). "Age-dependent changes in material properties of the brain and braincase of the rat." J Neurotrauma **20**(11): 1163-77.

GEFEN, A. and MARGULIES, S. S. (2004). "Are in vivo and in situ brain tissues mechanically similar?" J Biomech **37**(9): 1339-52.

GUERTIN, P. A. (2005). "Paraplegic mice are leading to new advances in spinal cord injury research." Spinal Cord **43**(8): 459-61.

HAMANN, M. C., SACKS, M. S. and MALININ, T. I. (1998). "Quantification of the collagen fibre architecture of human cranial dura mater." J Anat **192 (Pt 1)**: 99-106.

HE, Y., MACARAK, E. J., KOROSTOFF, J. M. and HOWARD, P. S. (2004). "Compression and tension: differential effects on matrix accumulation by periodontal ligament fibroblasts in vitro." Connect Tissue Res **45**(1): 28-39.

ICHIHARA, K., TAGUCHI, T., SHIMADA, Y., SAKURAMOTO, I., KAWANO, S. and KAWAI, S. (2001). "Gray matter of the bovine cervical spinal cord is mechanically more rigid and fragile than the white matter." J Neurotrauma **18**(3): 361-7.

KESSLER, D., DETHLEFSEN, S., HAASE, I., et al. (2001). "Fibroblasts in mechanically stressed collagen lattices assume a "synthetic" phenotype." J Biol Chem **276**(39): 36575-85.

KRAUS, J. F. and MCARTHUR, D. L. (1996). "Epidemiologic aspects of brain injury." Neurol Clin **14**(2): 435-50.

LINNINGER, A. A., XENOS, M., ZHU, D. C., SOMAYAJI, M. R., KONDAPALLI, S. and PENN, R. D. (2007). "Cerebrospinal fluid flow in the normal and hydrocephalic human brain." IEEE Trans Biomed Eng **54**(2): 291-302.

LOTH, F., YARDIMCI, M. A. and ALPERIN, N. (2001). "Hydrodynamic modeling of cerebrospinal fluid motion within the spinal cavity." J Biomech Eng **123**(1): 71-9.

MCGARVEY, K. A., LEE, J. M. and BOUGHNER, D. R. (1984). "Mechanical suitability of glycerol-preserved human dura mater for construction of prosthetic cardiac valves." Biomaterials **5**(2): 109-17.

MEANEY, D. F., ROSS, D. T., WINKELSTEIN, B. A., et al. (1994). "Modification of the cortical impact model to produce axonal injury in the rat cerebral cortex." J Neurotrauma **11**(5): 599-612.

MILLER, K. and CHINZEI, K. (2002). "Mechanical properties of brain tissue in tension." J Biomech **35**(4): 483-90.

PARK, J. B. (1984). Biomaterials Science and Engineering. New York, Plenum Press.

PATIN, D. J., ECKSTEIN, E. C., HARUM, K. and PALLARES, V. S. (1993). "Anatomic and biomechanical properties of human lumbar dura mater." Anesth Analg **76**(3): 535-40.

PETROLL, W. M., VISHWANATH, M. and MA, L. (2004). "Corneal fibroblasts respond rapidly to changes in local mechanical stress." Invest Ophthalmol Vis Sci **45**(10): 3466-74.

PRANGE, M. T. and MARGULIES, S. S. (2002). "Regional, directional, and age-dependent properties of the brain undergoing large deformation." J Biomech Eng **124**(2): 244-52.

RUNZA, M., PIETRABISSA, R., MANTERO, S., ALBANI, A., QUAGLINI, V. and CONTRO, R. (1999). "Lumbar dura mater biomechanics: experimental characterization and scanning electron microscopy observations." Anesth Analg **88**(6): 1317-21.

SPICER, M. A., VAN VELSEN, M., CAFFREY, J. P. and APUZZO, M. L. (2004). "Virtual reality neurosurgery: a simulator blueprint." Neurosurgery **54**(4): 783-97; discussion 797-8.

STOKES, B. T. and JAKEMAN, L. B. (2002). "Experimental modelling of human spinal cord injury: a model that crosses the species barrier and mimics the spectrum of human cytopathology." Spinal Cord **40**(3): 101-9.

STOKES, B. T., NOYES, D. H. and BEHRMANN, D. L. (1992). "An electromechanical spinal injury technique with dynamic sensitivity." J Neurotrauma **9**(3): 187-95.

TAYLOR, Z. and MILLER, K. (2004). "Reassessment of brain elasticity for analysis of biomechanisms of hydrocephalus." J Biomech **37**(8): 1263-9.

UENO, K., MELVIN, J. W., LI, L. and LIGHTHALL, J. W. (1995). "Development of tissue level brain injury criteria by finite element analysis." J Neurotrauma **12**(4): 695-706.

VAN NOORT, R., BLACK, M. M., MARTIN, T. R. and MEANLEY, S. (1981). "A study of the uniaxial mechanical properties of human dura mater preserved in glycerol." Biomaterials **2**(1): 41-5.

VANDENABEELE, F., CREEMERS, J. and LAMBRICHTS, I. (1996). "Ultrastructure of the human spinal arachnoid mater and dura mater." J Anat **189 (Pt 2)**: 417-30.

VIIDIK, A. (1968). "A rheological model for uncalcified parallel-fibred collagenous tissue." J Biomech **1**(1): 3-11.

WEED, L. H. (1938). "Meninges and Cerebrospinal Fluid." J Anat **72**(Pt 2): 181-215.

YOUNG, W. (2002). "Spinal cord contusion models." Prog Brain Res **137**: 231-55.

YUAN, Q., DOUGHERTY, L. and MARGULIES, S. S. (1998). "In vivo human cervical spinal cord deformation and displacement in flexion." Spine **23**(15): 1677-83.

CHAPTER 4: FINITE ELEMENT ANALYSIS OF SPINAL CORD INJURY IN THE RAT.

ABSTRACT

A computational three-dimensional finite element model (FEM) of traumatic spinal cord injury (SCI) that simulates the Impactor weight drop experimental model was developed. The model consists of the rat spinal cord, with distinct element sets for the gray and white matter, the cerebrospinal fluid (CSF), the dura mater, as well as a rigid rat spinal column, and a rigid impactor. In total, there were 94,893 nodes and 55,196 elements in the deformable components of the model and 14,004 nodes and 27,929 elements in the rigid spinal column. Loading conditions were taken from the average impact velocities determined from our parallel Impactor experiments for two drop heights: 12.5mm and 25mm. The compression depth and rate for each drop height simulation fell within the range of experimental values and was within 10% of the mean experimental values. Parametric studies were carried out to determine the sensitivity of the model to the relevant material properties, loading conditions, as well as essential boundary conditions. Alterations in the material law used for gray and white matter most influenced the validation data, as well as the patterns of peak maximum principal stress and strain. A simulation was run to determine the changes in the intraparenchymal patterns of SP and LEP for an off-center contusion. Measures of peak displacement were not significantly different than the standard model, but the patterns of peak maximum principal stress and strain were shifted toward the off-centered impact site. Our FEM was also modified to simulate a displacement-controlled electropneumatic impactor device. Preliminary analysis of the displacement-controlled impactor showed that the patterns of stress and strain are the same as in the weight drop. A

parametric analysis of the boundary conditions demonstrated that the chosen length of the spinal cord did not influence the response of the model. Further analysis of the material constants of the spinal cord structures revealed that changes in the viscoelastic properties influenced peak displacement, as well as peak values of stress and strain. Overall, this validated finite element model will provide temporal and spatial profiles of mechanical parameters that will be used to identify tissue-level thresholds for spinal cord microvascular injury. Moreover, the results will be used to improve means and measures of preventing spinal cord injury in humans.

INTRODUCTION

Traumatic loading conditions, such as those experienced during car accidents or falls, can lead to spinal cord injury (SCI), resulting in permanent functional damage. Studies of the biomechanical causes of SCI have centered on failure mechanisms of the spine and have nearly exclusively utilized vertebral motion segments or whole cadavers for experimentation. Conversely, to understand the pathophysiological and functional consequences of SCI, and ultimately to develop treatments to overcome these deficits, the neuroscience community has relied heavily on small animal models (Ducker and Assenmacher 1969; Dohrmann, Panjabi et al. 1976; Rivlin and Tator 1978; Noble and Wrathall 1985; Gruner 1992; Beattie, Bresnahan et al. 1997; Jaeger and Blight 1997; Popovich, Wei et al. 1997; Young 2002). Knowledge of the tolerance of spinal cord tissue to mechanical loading is critical in understanding how mechanisms of injury lead to neurologic deficits, as well as designing methods to prevent SCI. Whereas biomechanical analyses of animate models of brain injury, which allow a direct comparison of the tissue level states of stress and strain to injury patterns and outcomes, are becoming more common (Ueno, Melvin et al. 1995; Shreiber 1997), to our knowledge, no characterizations of the tissue level mechanics of animate models of SCI exist.

The spinal cord is an inhomogeneous, composite material with complex boundaries. Therefore, it is clear that understanding the underlying biomechanics of spinal cord injury can prove to be difficult. However, finite element analysis (FEA) has become an important and effective tool to investigate the biomechanics of trauma, including brain and spine injury mechanics (Ruan, Khalil et al. 1991; Ruan, Khalil et al. 1994; Ueno, Melvin et al. 1995; Voo, Kumaresan et al. 1996; Shreiber 1997; Winkelstein and Myers 1997; Yoganandan,

Kumaresan et al. 1997; Willinger, Kang et al. 1999; Wheeldon, Khouphongsy et al. 2000), but there have been no published analyses of SCI mechanics.

Early FE models of the central nervous system (CNS) tissue focused on the human brain, simulating the effects of rotational loading of the head and brain (Ruan, Khalil et al. 1991; Ruan, Khalil et al. 1994; Bandak 1995; Ueno, Melvin et al. 1995), while more recently, studies have investigated real-world impacts (Willinger, Kang et al. 1999; Franklyn, Fildes et al. 2005; Viano, Casson et al. 2005). Even though neuroscientists have routinely used animate models, most notably the rat and mouse, in studying the neuropathophysiology and functional consequences of SCI and TBI, only recently have researchers used FEA as a viable tool to correlate injury mechanics in animal models to the information gathered from in vivo models (Shreiber 1997). Furthermore, despite the prevalence of rodent models in the neuroscience community used to study SCI, there have been no published FE simulations of in vivo models of SCI. A validated FEM can determine the internal stresses and strains that are generated during trauma and be used to develop injury prevention techniques.

In this investigation, we developed and validated a computational 3D FEM of SCI using ABAQUS (ABAQUS Inc., Pawtucket, RI.) that simulates the Impactor weight drop experimental model. The Impactor weight drop model, developed by Young, Gruner, and Mason, produces dynamic, graded injury to the rat spinal cord and is one of the most common and reproducible techniques for investigating SCI (See Chapter 2). The FEM was validated against compression rate and compression depth data from our parallel Impactor weight drop experiments. Parametric studies were carried out to determine the sensitivity of the model to the relevant material properties, loading conditions, as well as essential boundary conditions. Simulations were run at +/-20% for each of the parameters where

appropriate. The finite element analysis will provide temporal and spatial profiles of mechanical parameters that will be used to identify tissue-level thresholds for spinal cord microvascular injury. Moreover, the results will be used to improve means and measures of preventing spinal cord injury in humans.

METHODS

Impactor Model

The FEM was developed to simulate the Multicenter Animal Spinal Cord Injury Study (MASCIS) Impactor model of spinal cord contusion. The Impactor is a 10g rod, with a 2.5mm head. Animals are suspended by clamping the T8 and T11 dorsal vertebral processes. The rod is centered over a laminectomy performed at T9-T10, raised to a pre-defined height, and dropped onto the exposed dura. The rod is mechanically linked to a digital optical potentiometer that allows movement to be measured precisely at ±20μm and ±20μsec (Young 2002). A second probe is placed on the dorsal surface of the vertebral body immediately proximal to the laminectomy and is linked to a separate digital optical potentiometer to evaluate movement of the underlying spinal column. The depth of tissue compression is then determined by subtracting the vertebral body motion from the motion of the impacting rod. Compression rate is estimated by dividing the compression distance by the duration from impact to reversal of the surface of the spinal cord. Impact velocity, cord compression distance, and cord compression rate are recorded for each experiment (Figure 4-1). In all, 16 experiments were evenly divided between 12.5mm and 25mm drop heights (Maikos and Shreiber 2007).

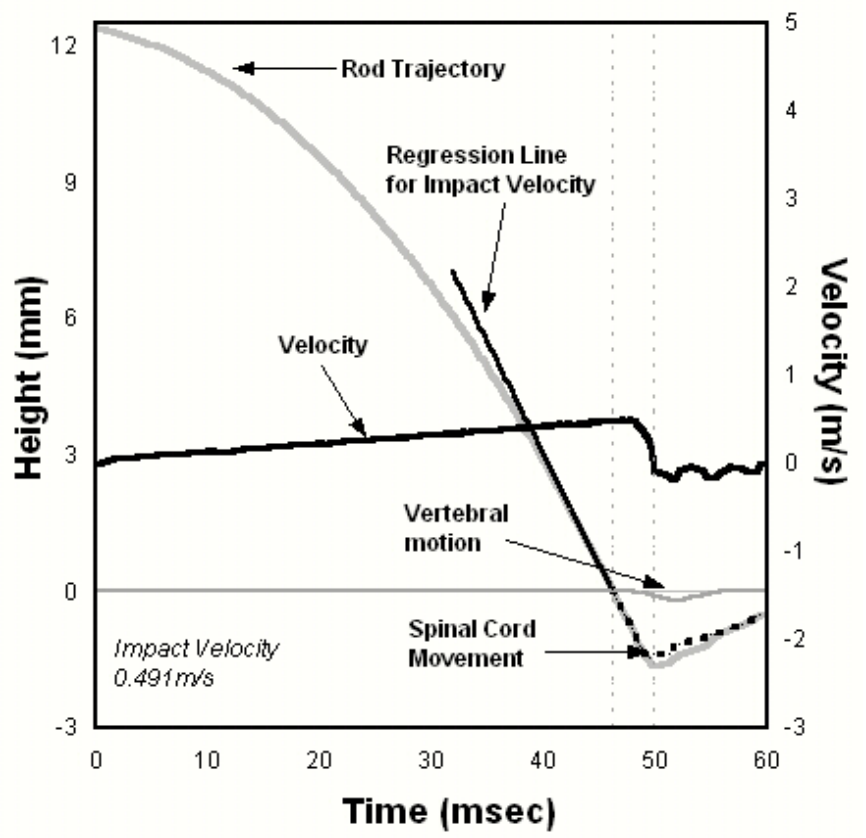

Figure 4-1: Example output following a 12.5mm Impactor weight drop injury. Separate optical potentiometers record the motion of the impacting rod and the vertebral body adjacent to the impact site. The velocity is measured by linearly regressing the rod position data 2msec prior to impact. Vertebral motion is subtracted from rod motion to arrive at the compression distance of the spinal cord. Vertebral motion contributed minimally to the total displacement of the spinal cord. Spinal cord compression rate is found by dividing the compression depth by the time between impact and reversal of the surface of the spinal cord.

Finite Element Model Generation

The model consists of the rat spinal cord, with distinct element sets for the gray and white matter, the cerebrospinal fluid (CSF), the dura mater, as well as a rigid rat spinal column, and a rigid impactor.

Spinal Cord

The geometry for the spinal cord was generated through magnetic resonance imaging (MRI) with a 4 Tesla horizontal bore magnet. A 77 day old female Long-Evans hooded rat (Simonsen Laboratories, Gilroy, CA) was euthanized with a lethal dose of sodium pentobarbital (65mg/kg) and the spinal column quickly excised. This age, gender, strain, and vendor match precisely those used in the parallel Impactor experiments, and in general match those specified by the MASCIS protocol (except for gender – either males or females can be used) (Young 2002). The excised column fit snugly in a standard 15mm conical tube and was imaged with a custom-built solenoid coil that wrapped around the tube. T2-weighted spin-echo MR images were taken every 0.5mm over ~3cm in length. The gray-white matter junction was clearly distinguished in the images (Figure 4-2), and the images were segmented manually into gray and white matter contours. These contours were smoothed with a snake algorithm and blended in the z-direction. The gray and white matter contours were then imported into ProEngineer (Parametric Technology Corporation, Needham, MA), which was used to generate surfaces over the central 1.4 cm portion of cord. The surfaces were imported into the preprocessor (Abaqus CAE), formed into solids, and partitioned into sub-units with more regular geometry to aid in mesh generation. The partitioned solids were meshed with 8-node, reduced integration, hexahedron, 'hourglass control' elements for use with Abaqus Explicit. The gray matter and white matter had independent element sets with

common nodes at the gray-white boundary to maintain overall continuity. The impact site of the spinal cord was meshed with a finer mesh seed. In total, the gray matter comprised 21,948 nodes and 11,250 elements, and the white matter comprised 54,225 nodes and 30,276 elements.

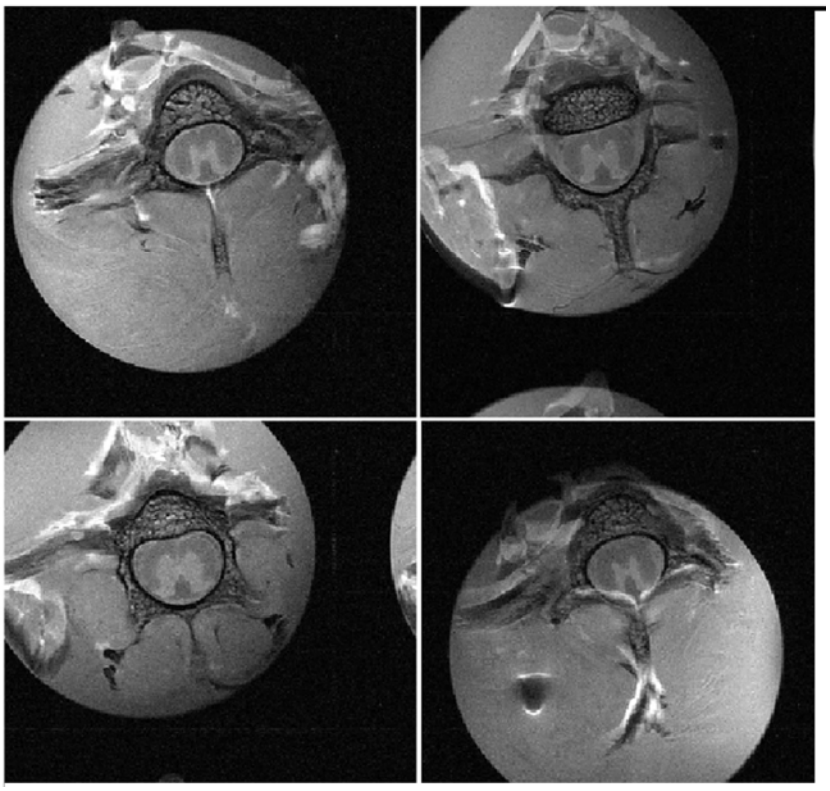

Figure 4-2: MR images of an excised spinal cord. A freshly excised spinal cord was inserted into a 15 ml conical tube and the remaining volume filled with saline. The tube was inserted into a custom-built solenoid MR coil and the contents imaged with spin-echo magnetization in a 4T magnet. The cord was imaged over 1.5cm in length; selected coronal sections are shown.

Cerebrospinal Fluid and Dura

The CSF and dura were generated in Abaqus by expanding the outer boundary of the white matter by 3% and 5%, respectively, based on average diameter values of the dura obtained from the MR images of the rat spinal cord (Figure 4-2). The dura, CSF, and spinal cord were then merged together, while maintaining distinct nodal boundaries. The dura was 50-80μm in thickness, while the CSF filled the space between the dura and spinal cord (also ~50-80μm). The dura and CSF were partitioned together along boundaries consistent with the spinal cord partitions and meshed with reduced integration hexagonal elements. The dura and CSF were each 1-element thick. The dura and CSF each comprised 9,360 nodes and 6,700 elements. The gray matter, white matter, CSF, and dura all had independent element sets with common nodes at the boundaries to maintain overall continuity (Figure 4-3). In total, there were 94,893 nodes and 55,196 elements in the deformable components of the model.

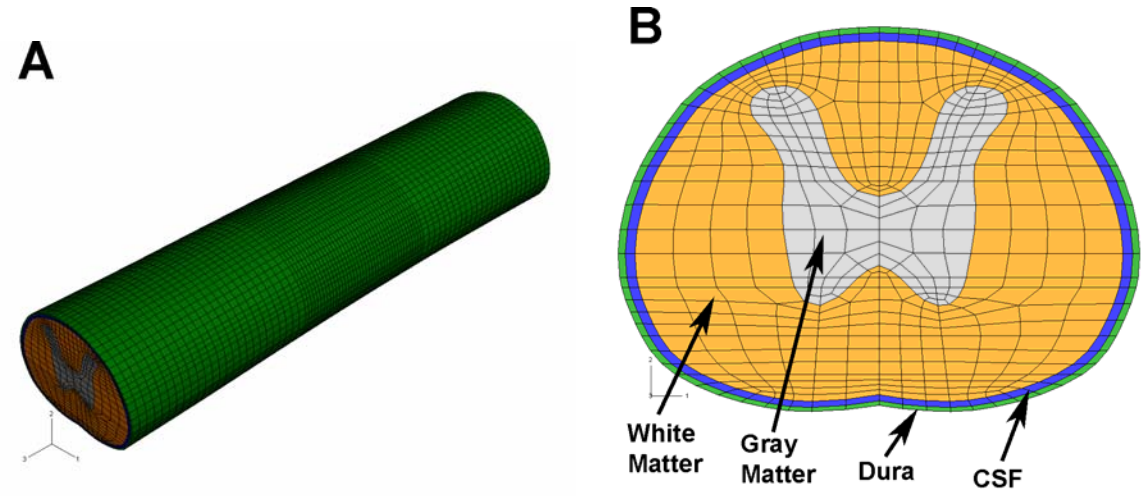

Figure 4-3: Mesh of the spinal cord with CSF and dura (A) and a cross-section of the spinal cord showing internal structures (B). The dura is the outer layer, shown in green. The CSF is between the dura and the white matter and displayed in blue. The white matter (shown as orange) and gray matter (shown as gray) make up the spinal cord. The CSF, dura, and spinal cord contain distinct element sets, but share common nodes at the each respective interface to maintain a continuous boundary.

Spinal Column

The geometry of the vertebral column was extracted from microCT imaging (Third-Generation microCT, Bio-Imaging Research, Lincolnshire, Illinois) of a similarly excised spinal column, to allow for better resolution of geometry changes in the axial direction. A T9/T10 laminectomy was performed identical to those performed in Impactor experiments, and the animal was then euthanized. The spinal column was removed and placed in a 15ml conical tube. The remaining volume was filled with saline. The column was imaged with microCT over 3cm in length at 80keV and 0.04mA. Image slices were acquired every 0.07mm (Figure 4-4). The images were segmented into contours, and a triangular surface mesh was generated with Autodesk Maya software (Autodesk, San Rafael, CA). This mesh, which comprised 14,004 nodes and 27,929 elements, was imported into Abaqus (Figure 4-4). The spinal cord mesh was positioned in the vertebral column such that the center of the laminectomy was superior to the appropriate position in the spinal cord, which was identified from the appearance of gray and white matter in cross-section.

Impactor

The impactor was modeled as a discrete rigid cylinder of mass (10 grams) and diameter (2.5mm), which match the dimensions used in Impactor experiments. The impactor was centered over the laminectomy and placed in direct contact with the dorsal surface of the dura (Figure 4-5).

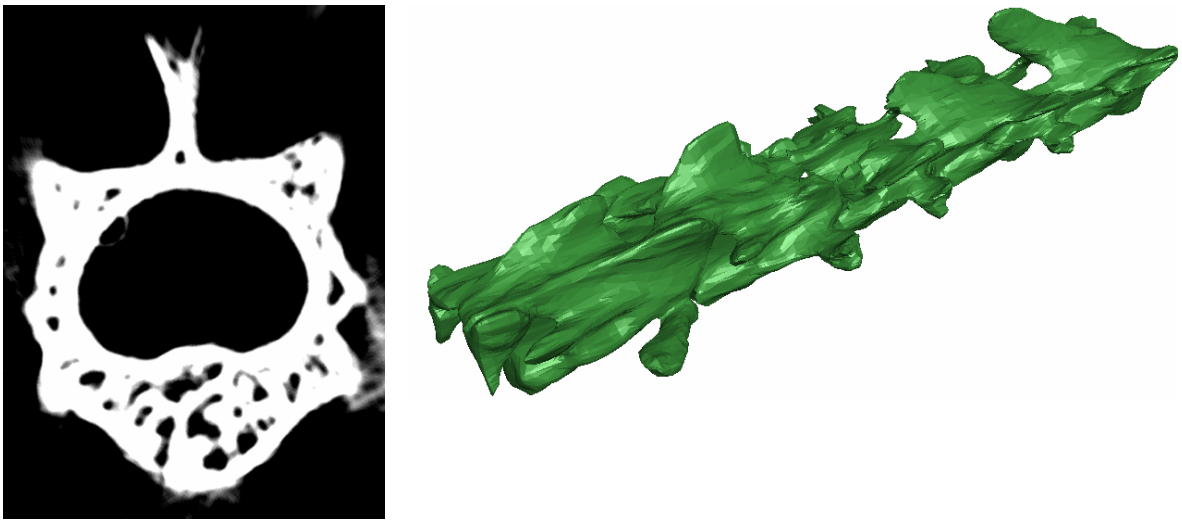

Figure 4-4: A representative image slice of a cross section of the rat spinal column showing the bone as well as the spinal cord canal. The column was imaged over ~3cm in length. Slices were acquired every 0.07mm. The column was imported into Abaqus and modeled as a rigid body.

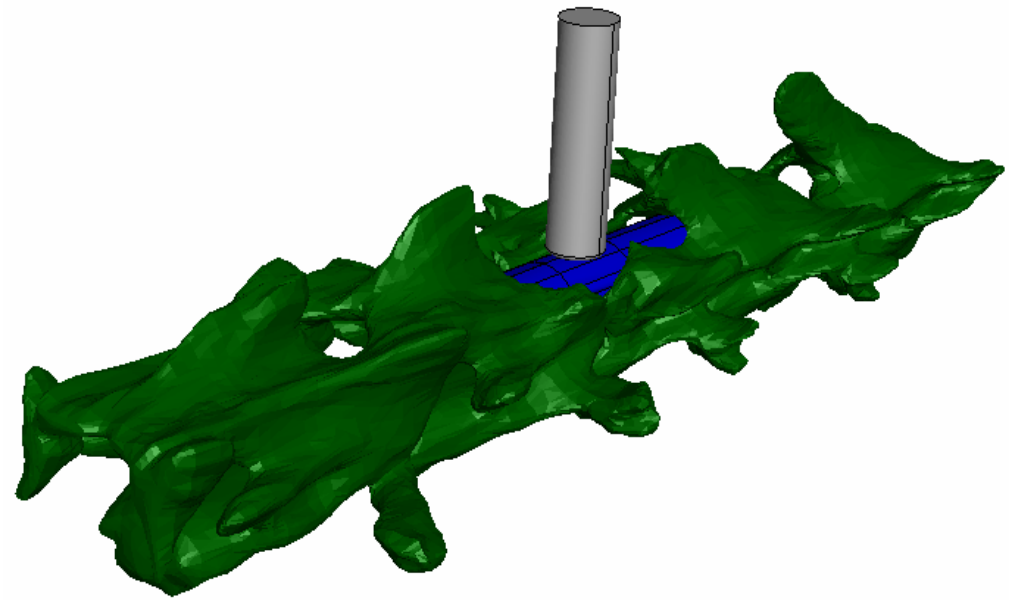

Figure 4-5: The spinal cord structures within the spinal column, with rigid impactor. The impactor (gray) is centered over theT9/T10 laminectomy and was modeled as a discrete rigid body permitted to only move in the vertical direction. A weight drop experiment was simulated by placing the impactor in direct contact with the dura and prescribing an initial velocity that matched the average value determined from our parallel weight drop experiments.

Material Properties

The spinal cord was assumed to be isotropic and homogenous, with identical properties assigned to gray and white matter. Experimental studies of the material properties of spinal cord and brain tissue from various species have demonstrated the non-linear and viscoelastic behavior of the tissue (Galford and McElhaney 1970; Metz, McElhaney et al. 1970; van Noort, Black et al. 1981; van Noort, Martin et al. 1981; Bilston and Thibault 1996; Arbogast and Margulies 1998; Bain and Meaney 2000; Miller, Chinzei et al. 2000; Miller and Chinzei 2002; Prange and Margulies 2002; Fiford and Bilston 2005). The spinal cord was modeled as an Ogden hyperelastic-linear viscoelastic material with a two term Prony series to describe the exponential decay of energy within the material. At very fast rates (i.e. instantaneous) and very slow rates (i.e. quasistatic), the model assumes hyper-elastic behavior. The Ogden form of the hyperelastic strain energy potential function, W, has previously been used to model both spinal cord and brain tissue (Bilston and Thibault 1996; Miller and Chinzei 2002; Prange and Margulies 2002):

$$W = \sum_{i=1}^{N} \frac{2G_i}{\alpha_i^2}\left(\lambda_1^{\alpha_i} + \lambda_2^{\alpha_i} + \lambda_3^{\alpha_i} - 3\right) \qquad \text{Equation 4-1}$$

where λi are the deviatoric principal stretches, N is the complexity of the law, which is material dependent, and Gi and αi are material-dependent parameters. Both brain and spinal cord have been adequately modeled with $N = 1$ (Bilston and Thibault 1996; Prange and Margulies 2002), which makes G equivalent to the shear modulus. Weight drop produces a complex strain field that may be best approximated as 'confined compression', and to our knowledge, no description of rat spinal cord gray and white matter has been published in this mode of testing. Fiford and Bilston have recently published the properties of rat spinal cord in uniaxial tension at very slow ($0.001s^{-1}$) to moderate ($\sim 0.1s^{-1}$) strain rates. To our

knowledge, these are the only published properties of rat spinal cord tissue, and this data was therefore used as the starting point for identifying model constants. Data from the Fiford and Bilston $0.001s^{-1}$ study was fit with the Ogden model, which produced an effective quasi-static shear modulus ~200kPa. However, though no properties for rat spinal cord in other modes of mechanical testing exist, rat brain tissue in compression and shear has been shown to be significantly more compliant, and the properties of the spinal cord were adjusted to achieve the temporal profile of Impactor displacement that best matched those from parallel weight drop experiments (Maikos and Shreiber 2007) (see *Validation & Sensitivity Analysis* below).

The viscoelastic portion of the material laws was described with a Prony series exponential decay:

$$G_R(t) = G_0\left[1 - \sum_{k=1}^{N} \bar{g}_k^P\left(1 - e^{-t/\tau}\right)\right] \qquad \text{Equation 4-2}$$

where the instantaneous shear modulus is multiplied by a normalized function that includes relative relaxations, g_k, at characteristic time constants, τ_k. The quasi-static shear modulus can then be related to the instantaneous modulus by:

$$G_\infty = G_0\left(1 - \sum_{k=1}^{N} \bar{g}_k^P\right) \qquad \text{Equation 4-3}$$

During a 25mm drop height Impactor experiment, the spinal cord experiences a peak compression of ~2.14mm in under 4msec, which translates to large deformation at an extremely fast strain rate. No data exists for rat CNS tissue at these rates. As such, the Prony series viscoelastic constants from a study of human brain tissue in compression at high strain and strain rate were employed (Mendis, Stalnaker et al. 1995). Both brain and spinal cord

tissue were prescribed a small measure of compressibility (Poisson's Ratio, ν = 0.45) to facilitate computational processing. Properties for the spinal cord are detailed in Tables 4-1 and 4-2. The influence of these assumptions, as well the rest of the material constants, were evaluated parametrically, as described in *Validation & Sensitivity Analysis*.

Dura Mater

Previous studies in our laboratory identified the mechanical properties of rat spinal cord dura mater in uniaxial tension. Both low strain rate (~0.001s^{-1}) and dynamic, stress-relaxation tests (strain rate ~20 sec^{-1}) were performed. The dura mater exhibited hyperelastic-viscoelastic behavior similar to other collagenous tissues, and was modeled as an Ogden hyperelastic (one term), linearly viscoelastic (4-term exponential decay) continuum solid. Poisson's ratio was set at 0.45. The dura was prescribed an instantaneous shear modulus previously found in our laboratory. Additionally, adaptive meshing (750 remeshing sweeps per increment) was performed on the surface of the dura that was directly exposed to impact to maintain a regular mesh.

Cerebrospinal Fluid

The CSF was modeled with solid elements with a low shear-to-bulk modulus to introduce fluid-like behavior (King, Ruan et al. 1995). The CSF was modeled as a Mooney-Rivlin hyperelastic material with an effective shear modulus ~240x less than the spinal cord:

$$W = C_{01}(I_1 - 3) + C_{10}(I_2 - 3) \qquad \text{Equation 4-4}$$

$$G = 2(C_{01} + C_{10}) \qquad \text{Equation 4-5}$$

where, for this model, $C_{01}=C_{10}$. Poisson's ratio was set at 0.49. Additionally, adaptive meshing (750 remeshing sweeps per increment) was performed for the CSF to maintain a regular mesh and permit 'flow' of CSF from one element to the next. The values for all material constants are delineated in Tables 4-1 to 4-3.

TABLE 4-1 - Material Properties used in the FEM

Material Characteristics					
Tissue	**Density (Kg/m^3)**	**Long Term Shear Modulus G_∞ (KPa)**	**Bulk Modulus K (KPa)**	**α**	**ν**
Spinal Cord	1000	32	309.33	4.7	0.45
Dura Mater	1000	1200	11600	16.2	0.45
CSF	1000	0.13	6.67	-	0.49

TABLE 4-2 – Spinal Cord Viscoelastic Constants

Summary of Spinal Cord Viscoelastic Constants Constants for Prony Series Exponential Decay:	
Constant	**Spinal Cord**
g_1	0.528
τ_1	0.009
g_2	0.302
τ_2	0.150

TABLE 4-3 – Dura Mater Viscoelastic Constants

Summary of Dura Viscoelastic Constants Constants for Prony Series Exponential Decay:	
Constant	**Dura**
g_1	0.329
τ_1	0.009
g_2	0.128
τ_2	0.081
g_3	0.086
τ_3	0.564
g_4	0.086
T_4	4.69

Boundary and Loading Conditions

Contact was permitted between the impactor and dura, as well as between the dura and the spinal column. The spinal column was fixed in space. The impactor was permitted to move only in the vertical direction and allowed to have direct contact with the dura. The coefficient of friction for interaction of the Impactor and the dura and interaction of the vertebrae and the dura was estimated at 0.15. Two experimental loading conditions were simulated: a 12.5mm weight drop and a 25mm weight drop. Simulations for the 12.5 and 25mm were run for 5.5 and 4.4msec, respectively. Peak nodal displacement occurred at approximately at 4.4msec for the 12.5mm drop, and 3.8msec for the 25mm drop. Preliminary analysis showed that peak values of maximum principal stress and strain occurred at peak nodal compression or less than 0.5msec following cord reversal. The impactor was placed in direct contact with the exposed dura and prescribed an initial velocity that matched the average value determined from the parallel weight drop experiments for that drop height.

Model Solution

The finite element simulation was performed using Abaqus/Explicit on 4 parallel processors (University of Minnesota Supercomputing Institute, IBM Power 4 System, AIX operating system, 1.7GHz Power4 Processors). The simulation was performed at the average velocity from parallel experiments at 12.5mm and 25mm drop heights. The results were compared to the spatial maps of injury for the 3 different sized markers used in the Impactor experiments (Hydrazide, Bovine Serum Albumin, Red Blood Cells).

Validation & Sensitivity Analysis

The analysis was validated by comparing the compression rate and the displacement of the mass post-"impact" to the actual parameters measured during an Impactor weight drop. The model was considered validated when the trajectory of the impactor at and immediately after peak compression fell within the range of actual trajectories for both 12.5mm and 25mm drop height experiments. Parametric studies were performed to examine the effect of different parameters, such as the coefficient of friction, velocity, boundary conditions, and the material constants, on the FEM results. Simulations were run at +/- 20% of the original value for each of the parameters.

RESULTS

Model Validation

The Impactor weight drop model offers the opportunity to validate the computational model with measurements of the in vivo spinal cord compression distance and compression rate. The finite element model of SCI was validated by matching the peak displacement of the spinal cord after contusion to the mean spinal cord compression depth and rate measured experimentally for each of the loading conditions from our parallel Impactor experiments.

Compression Depth and Rate Validation

The compression depth and rate for each drop height simulation fell within the range of experimental values and was within 10% of the mean experimental values, determined from our parallel Impactor experiments. The peak displacement and rate were determined by averaging the peak displacement for nodes within a 2.5mm diameter at the center of the contusion, to approximate the impactor diameter. Figure 4-6 displays the Impactor validation data, as well as the average nodal displacement and rate from the FEM. Convergence was addressed by simulating a 12.5mm weight drop with a 20% finer mesh. Peak nodal compression in the finer mesh resulted in less than a 1% change from the standard model.

Boundary and Loading Conditions

Separate parametric studies were performed to evaluate the sensitivity of the model to the boundary conditions and length of the spinal cord. The spinal cord was chosen to be 1.4cm in length. Reducing the length of the overall solid, which effectively decreased the total number of elements in the mesh, ultimately decreased the amount of computational time needed to run the simulation. However, a parametric analysis was performed to determine if

1.4cm was an adequate length that would not affect the stress and strain distributions in the simulation. Three separate boundary conditions were simulated, including a 20% shorter spinal cord, a 50% longer spinal cord, and a spinal cord that was constrained on the proximal and distal ends. Peak nodal displacement, peak maximum principal stress (SP) and maximum principal strain (LEP), and the distribution patterns of stress and strain in the spinal cord were compared between the altered models and the standard model to evaluate the sensitivity of the model to the boundary conditions. Results showed that peak nodal displacement for all 3 boundary conditions changed less than 1% for each boundary condition (Figure 4-7). Thus, compression depth and rate were not affected by the change in all 3 boundary conditions.

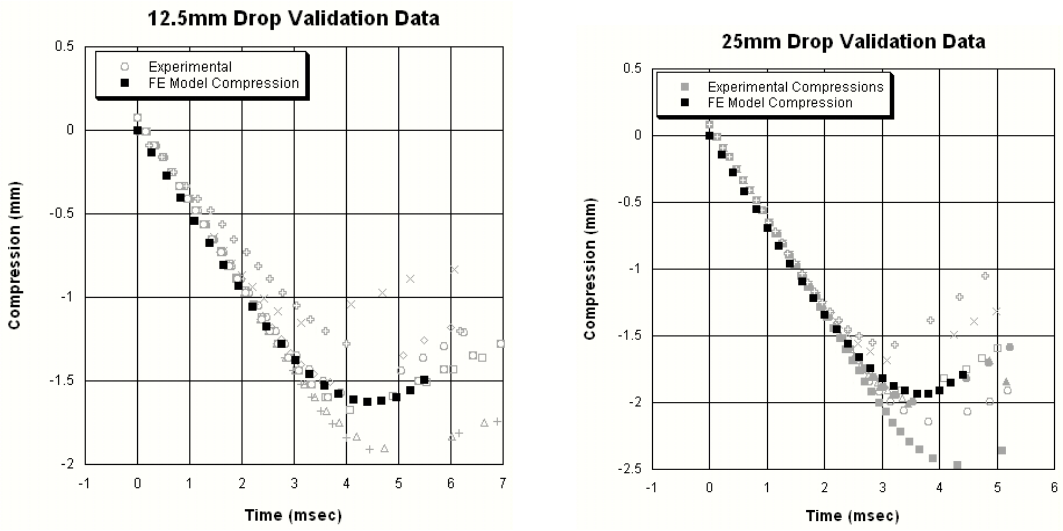

Figure 4-6: Experimental Impactor compression and compression rate for each weight drop experiment are shown in gray and the FEM simulation compression results are shown in black. Both the 12.5mm and 25mm compression and compression rate results from the FEM fall within the experimental results.

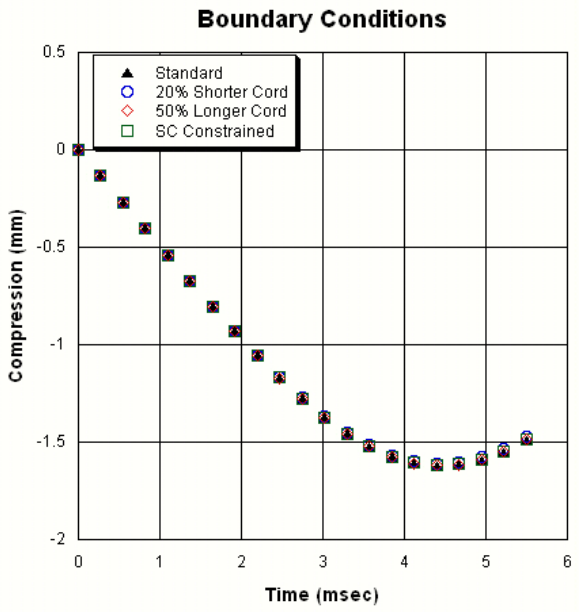

Figure 4-7: Peak nodal displacement for the boundary conditions of the spinal cord. Shortening, lengthening, and constraining the cord each resulted in less than a 1% change in the peak compression depth compared with the standard model.

A horizontal slice from the middle of the spinal cord model was chosen and the peak SP was analyzed for the 3 boundary conditions and compared to the standard model. The constrained and elongated spinal cord each showed a 1% increase in SP from the standard model, while the shortened spinal cord resulted in a 6% decrease in maximum principal stress. The intraparenchymal distribution of SP in the spinal cord slice showed that the constrained and 50% longer spinal cord closely matched the standard model, while the 20% shorter spinal cord resulted in a smaller central portion of the stress pattern (Figure 4-8).

Peak maximum principal strain (LEP) values for the same horizontal slice were analyzed for the 3 boundary conditions and compared with the standard model. The constrained and the 50% extended spinal cord showed a 2.7% and 1% decrease in the LEP, respectively, while the shorter cord resulted in a less than 1% increase in LEP. Analysis of the intraparenchymal distribution of LEP (Figure 4-9) showed that the shorter spinal cord closely matched the standard model. The constrained and longer spinal cord showed similar distributions of LEP in the central portion horizontal slice (where the LEP values are the largest) compared with the standard model, but a small portion of the lateral sections of the slice showed slightly different patterns for LEP. Overall, the LEP distributions for all 3 boundary conditions, closely matched the standard model.

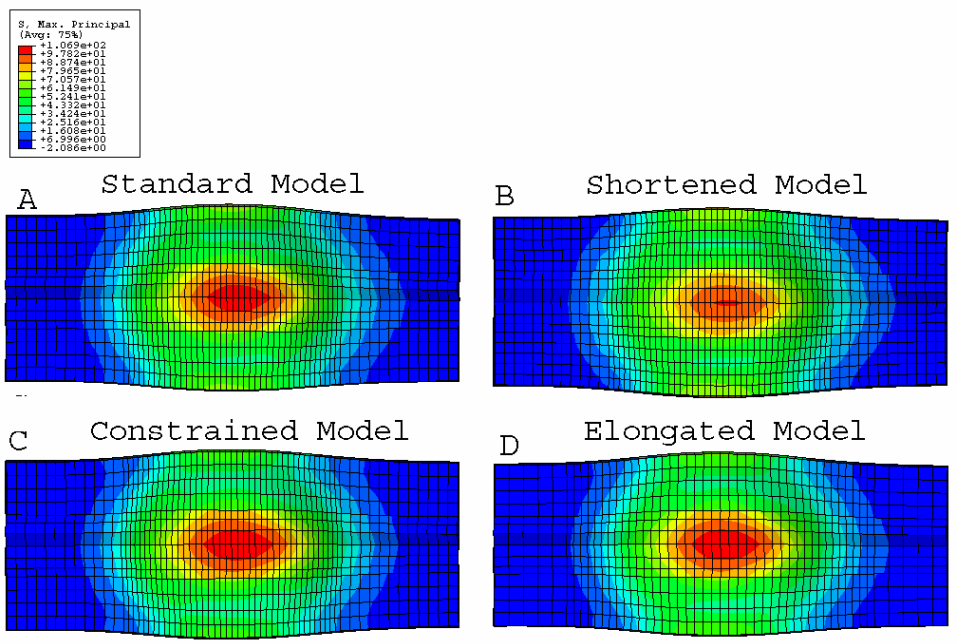

Figure 4-8: Peak maximum principal stress patterns for (A) the standard model, (B) the 20% shortened spinal cord, (C) the constrained spinal cord, and (D) the 50% longer spinal cord. Stress patterns for the constrained and longer spinal cord closely matched the pattern shown in the standard cord. The shorter cord resulted in a slightly different pattern, with a smaller central portion.

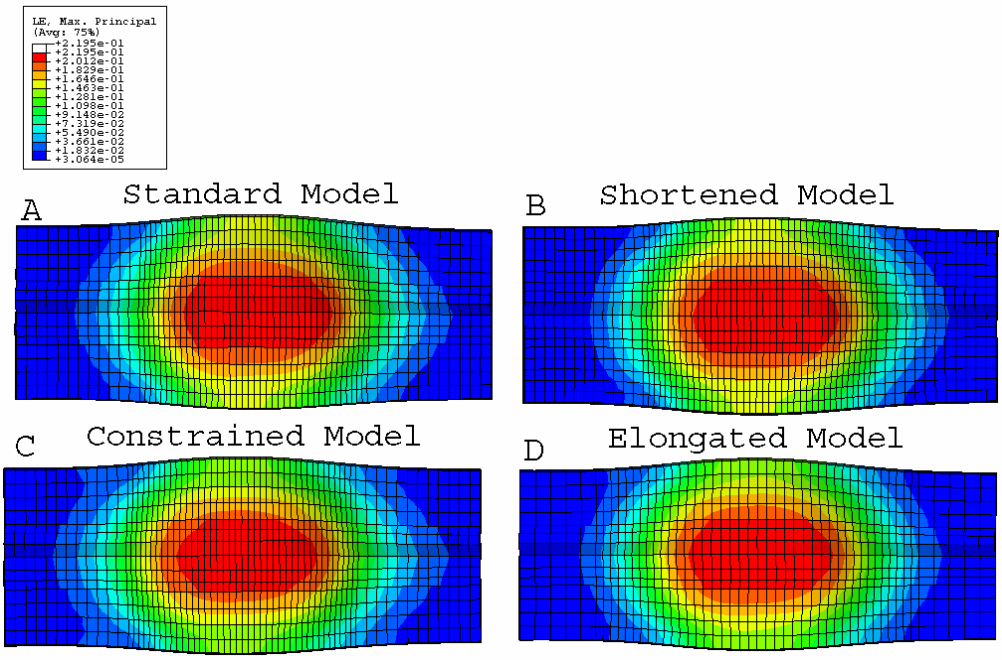

Figure 4-9: Maximum principal strain distributions for (A) the standard model, (B) the 20% shorter spinal cord, (C) the constrained spinal cord, and (D) the 50% longer spinal cord. Overall, the LEP patterns of the boundary conditions closely match the standard model. However, the constrained and 50% longer cord demonstrated slightly higher values of LEP in small portions of the lateral sections of the slice.

General Extravasation Morphology

Previously reported patterns of extravasation of hemorrhage or labeled markers in horizontal sections following SCI were described as roughly oblong in shape, with the major axis aligned axially with the spinal cord (Noble and Wrathall 1989). Often, extravasation was more pronounced and extended further in the rostral and caudal directions in the highly vascular gray matter vs. white matter and it was especially evident in higher drops. A previous study in our lab investigated the extravasation of 3 markers into the parenchyma of the spinal cord following a contusion: labeled hydrazide (~700Da), labeled bovine serum albumin (BSA) (~70kDa), and red blood cells (~5μm) (Maikos and Shreiber 2007). The extravasation of all 3 species was generally similar and matched previously reported observations of extravasation. Comparison of a horizontal section of the extravasation of the 3 markers demonstrated good correlation to the distribution of SP and LEP in the same anatomical section in the FEM (Figure 4-10). However, it was evident that in many slices, extravasation extended further in the rostral and caudal directions in the highly vascularized gray matter, which indicates that microvasculature in the gray matter is more sensitive to compressive loads than in the white matter (Figure 4-11). It is known that the mechanical properties of gray and white matter are different (Arbogast and Margulies 1998; Bilston, Liu et al. 2001; Miller and Chinzei 2002; Prange and Margulies 2002). The different properties for gray and white matter will affect tissue deformation spatially and temporally following impact as well as the distribution of stress and strain through the tissue. Simulations were also run in which the gray and white matter properties were varied individually. A comparison of a dorsal slice of extravasation and a slice from the same anatomic location from the FEM show regions of higher stress correlated well to the pronounced extravasation

in the gray matter. Therefore, determination of the individual properties for the gray and white matter of the rat spinal cord is a necessary and warranted study to aid in the modeling of SCI.

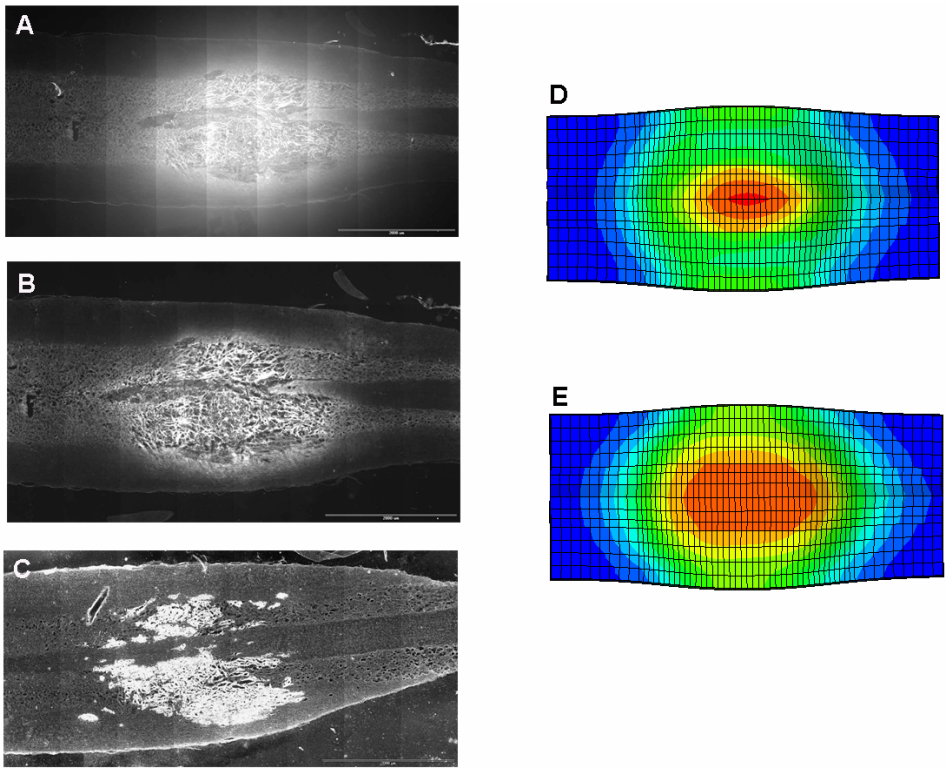

Figure 4-10: Extravasation of hydrazide (A), BSA (B), and RBC (C). Extravasation patterns (bright areas) were roughly oblong in shape extending in the rostral and caudal directions. Patterns of maximum principal stress (D) and maximum principal strain (E) closely resemble the extravasation patterns following SCI.

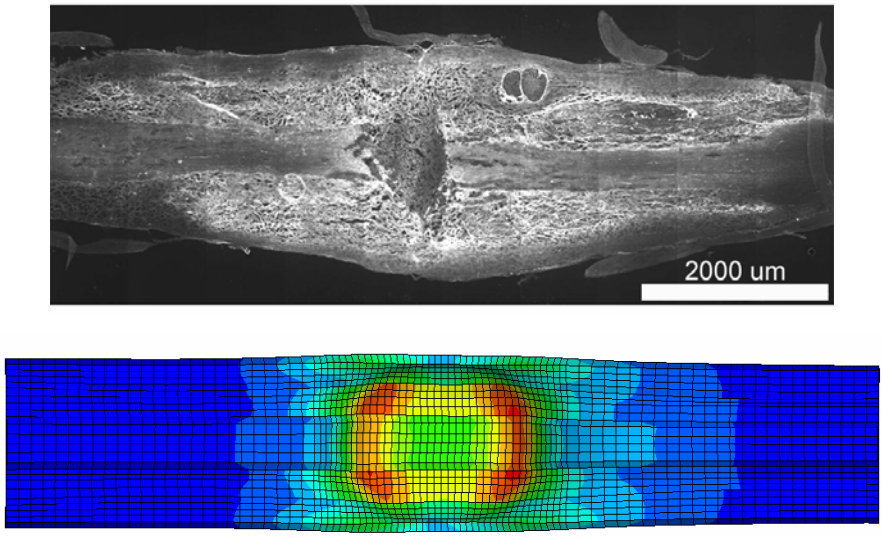

Figure 4-11: Extravasation of BSA in a dorsal horizontal slice following 25mm contusion in the rat spinal cord. Extravasation of the BSA extended further rostrally and caudally in the gray matter as compared with the white matter. Maximum principal stress patterns from a model with inhomogeneous properties for the gray and white matter from the same anatomical location show regions of higher stress that correlate to the extravasation of BSA in the gray matter.

Parametric Analysis

A parametric study was performed to evaluate the sensitivity of the model to the underlying material assumptions. Seven material variables, as well as the coefficient of friction were independently increased and decreased by 20% and simulated with a 12.5mm weight drop, as shown in Table 4-4. These variables include the Ogden hyperelastic constants, G and α, D, and the Prony series viscoelastic constants, g_1, g_2, tau_1, and tau_2. For the spinal cord, the changes were studied for both a homogeneous material and isotropic property model, in which the gray and white matter were changed simultaneously, as well as an inhomogeneous model where white and gray matter properties were changed independently. Peak nodal compression and compression rate, peak SP and LEP values, and the distributions of peak SP and LEP in a horizontal slice were evaluated to determine the sensitivity of the model to the material characteristics. Additionally, the maximum and minimum values of the experimental impact velocity for the 12.5mm weight drop injuries were simulated.

Table 4-4 – Parametric Analysis of the Material Assumptions

	Spinal Cord (Gray&White)			Dura		
Condition	**Standard**	**Increase**	**Decrease**	**Standard**	**Increase**	**Decrease**
Shear Modulus (KPa)	32	38.4	25.6	3250	3900	2600
α	4.7	5.64	3.76	16.2	19.4	12.96
D	6.46E-3	7.76E-3	5.17E-3	6.37E-05	7.63E-05	5.09E-05
G_1	0.528	0.6336	0.4224	0.329	0.395	0.2632
g_2	0.302	0.3624	0.2416	0.128	0.154	0.1024
τ_1	0.008	0.0096	0.0064	0.009	0.011	0.0072
τ_2	0.150	0.18	0.12	0.081	0.097	0.0648
Coeff Friction (μ)	0.150	0.18	0.12	0.150	0.18	0.12

Alterations in the material parameters were first carried out in the gray and white matter together. Changes in the quasi-static shear modulus, G_∞, for the gray and white matter, as well as the Prony series relaxation constants had the largest effect on the peak nodal compression depth and rate (Table 4-5). A 20% increase and decrease in G_∞ in both the gray and white matter showed a 5% decrease and increase in peak nodal displacement, respectively, from the standard model (Figure 4-12A). A horizontal slice of the FEM from the middle of the spinal cord was chosen and the peak SP and peak LEP values were analyzed. A 20% increase and decrease in G_∞ resulted in a 10% decrease and increase in peak SP, respectively. LEP had an 18% decrease when G_∞ was increased by 20%. Peak LEP increased by 16% when G_∞ was decreased by 20%. Inspection of the intraparenchymal distribution of SP and LEP in the spinal cord slice confirmed these findings (Figure 4-12B-

G). As G_∞ increased, the central portion of the horizontal slice, where SP is at a maximum, had a lager area of peak SP compared with the standard model. However, as G_∞ increase, the values in the central portion of the slice for LEP decreased compared with the standard model.

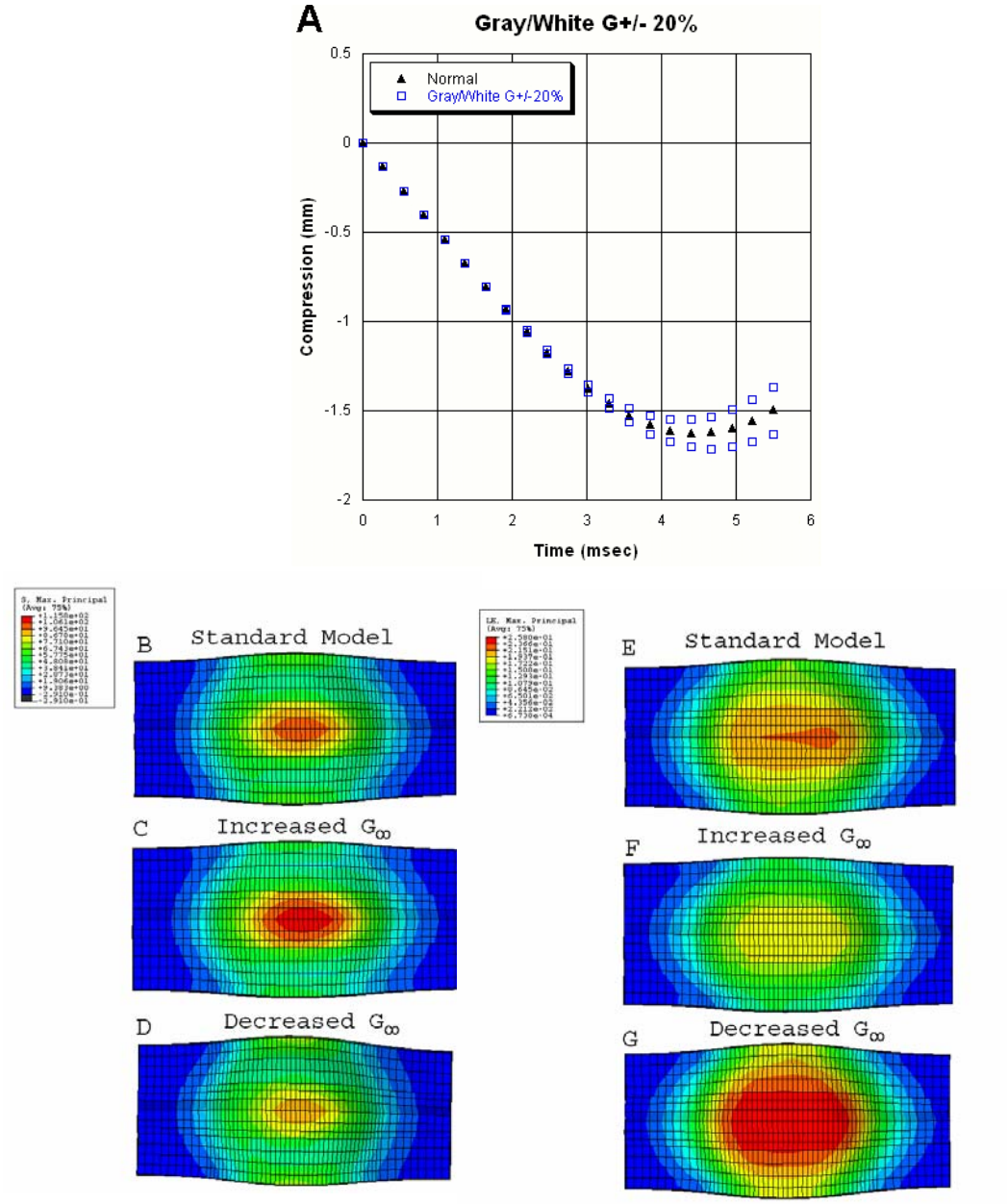

Figure 4-12: Parametric results from changing the shear modulus, G_∞, of the homogenous model +/- 20%. The peak nodal displacement (A) changed +/-5% from the standard model. The patterns of SP and LEP were consistent with findings of the peak values of SP and LEP. As G_∞ increased, the pattern of peak SP values enlarged, while the values of LEP decreased.

Changes in the Prony series relaxation constants showed the largest effect on the validation of the FEM. A 20% increase in the first Prony series relaxation constant, g_1, which effectively increased the instantaneous shear modulus (G_0), resulted in a 26% decrease in peak nodal displacement; a 20% decrease in g_1 showed a 12% increase in peak compression depth. There was a 53% increase in the peak value of SP and a 63% decrease in the peak value of LEP when g_1 was increased by 20%. Inspection of the distribution patterns of SP and LEP (Figure 4-13) confirms that an increase in g_1 results in an extended area of maximum SP, while causing a reduction in area of maximum LEP. Decreasing g_1 by 20% decreased peak SP by 13% and increased LEP by 38%, which is represented in the distribution patterns for SP and LEP. Increasing the second Prony series relaxation constant, g_2, by 20% resulted in a 12% decrease in peak nodal displacement, while a 20% decrease in g_2 resulted in a 7% increase in nodal displacement. Peak SP was increased by 23%, while peak LEP was decreased by 24% when g_2 was increased by 20%. A 20% reduction in g_2 resulted in a 13% decrease in peak SP and a 24% increase in peak LEP. Analysis of the SP and LEP patterns show that changes in the first relaxation constant had a greater effect on the distribution of SP and LEP than changes in the second relaxation constant. Parameterization of the Prony series time constants, τ_1 and τ_2, for the gray and white matter did not have a significant effect on the compression depth or the peak values of SP and LEP. All compression rates had less than a 5% change from the standard model.

Parametric analysis on the variables α, D, and the coefficient of friction resulted in less than 1% change in peak nodal displacement and peak values for SP and LEP.

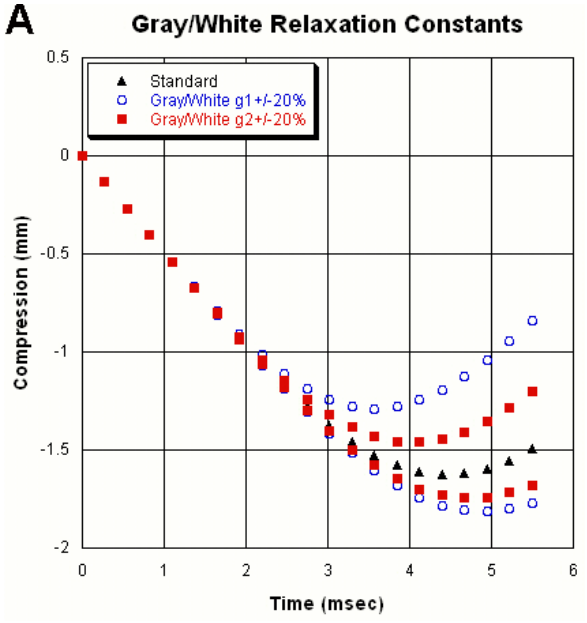

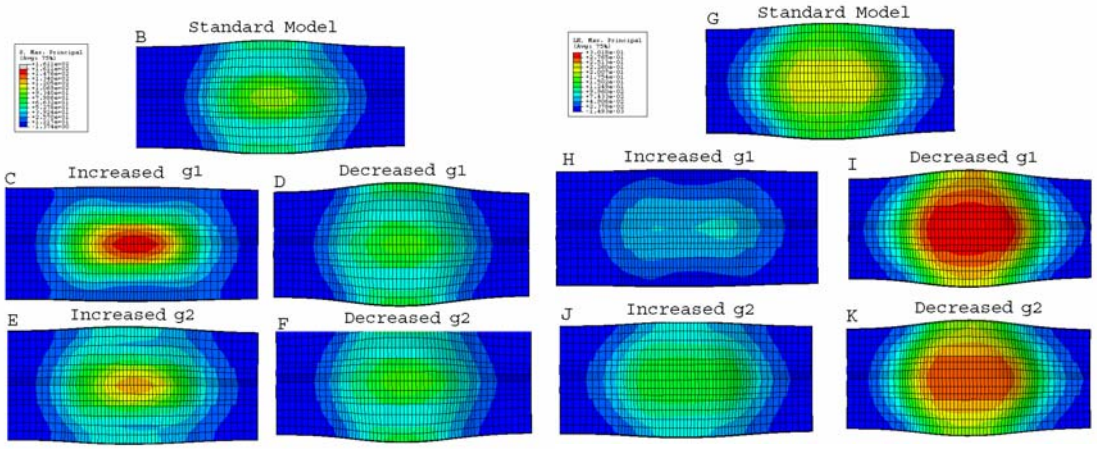

Figure 4-13: Parametric analysis of the Prony series relaxation constants, g_1 and g_2, during a 12.5mm weight drop. Changing the viscoelastic constants for the gray and white matter together had the greatest effect on the peak nodal displacement and rate (A). Peak maximum principal stress (SP) distribution for a middle slice for the standard model (B) g_1 +20% (C), g_1 -20% (D) and g_2 +20% (E), and g_2 -20% (F) showed that increasing g_1 resulted in the largest change in the distribution of SP. Peak maximum principal strain (LEP) distribution for a middle slice for the standard model (G) g_1 +20% (H), g_1 -20% (I), g_2 +20% (J), and g_2 -20% (K) showed that higher values of LEP were observed when G_∞ was decreased by 20% compared with the standard model.

Table 4-5: Outcomes measures of parametric analysis

Material	Condition	Peak Stress	Peak Strain	Peak Nodal Compression (mm)
Standard	-	105.6	0.2188	-1.624
Gray and White	$G\infty$ + 20%	115.8	0.1847	-1.549
Gray and White	$G\infty$ - 20%	95.3	0.2580	-1.713
Gray and White	G_1 + 20%	161.1	0.0807	-1.288
Gray and White	g_1 - 20%	88.5	0.3018	-1.814
Gray and White	G_2 + 20%	129.8	0.1501	-1.460
Gray and White	g_2 – 20%	91.4	0.2723	-1.746

A parametric analysis was also performed to study the gray and white matter separately. Adjustments to the quasistatic shear modulus, G_∞, and the 2 Prony series relaxation constants, g_1 and g_2, showed the greatest differences in peak nodal displacement, peak SP and LEP, and the intraparenchymal distributions of SP and LEP from the standard model (Table 4-6). A 20% increase and decrease in G_∞ for the gray matter resulted in a 1% decrease and increase in the peak nodal displacement, respectively (Figure 4-14A). The peak values of SP for a 20% increase and decrease in G_∞ for the gray matter were 4% higher and 5% lower than the standard model, respectively, while the peak LEP decreased by 7% and increased by 12% from the standard model.

In is not surprising that in an inhomogeneous model with different material properties for the gray and white matter, the patterns of peak SP and peak LEP preferentially affect the elements assigned to the gray and white matter. Visual inspection of the SP distribution patterns show that when G_∞ was increased for the gray matter, regions with the highest levels of stress (mainly in the gray matter) were approximately the same size regions as the standard model, but the magnitude was less (Figure 4-14C). When G_∞ was decreased, peak stress patterns enlarged compared to the standard model (Figure 4-14D). The LEP patterns show a preferential decrease and increase in the gray matter areas of peak LEP when G_∞ was increased and decreased, respectively (Figure 4-14E-F).

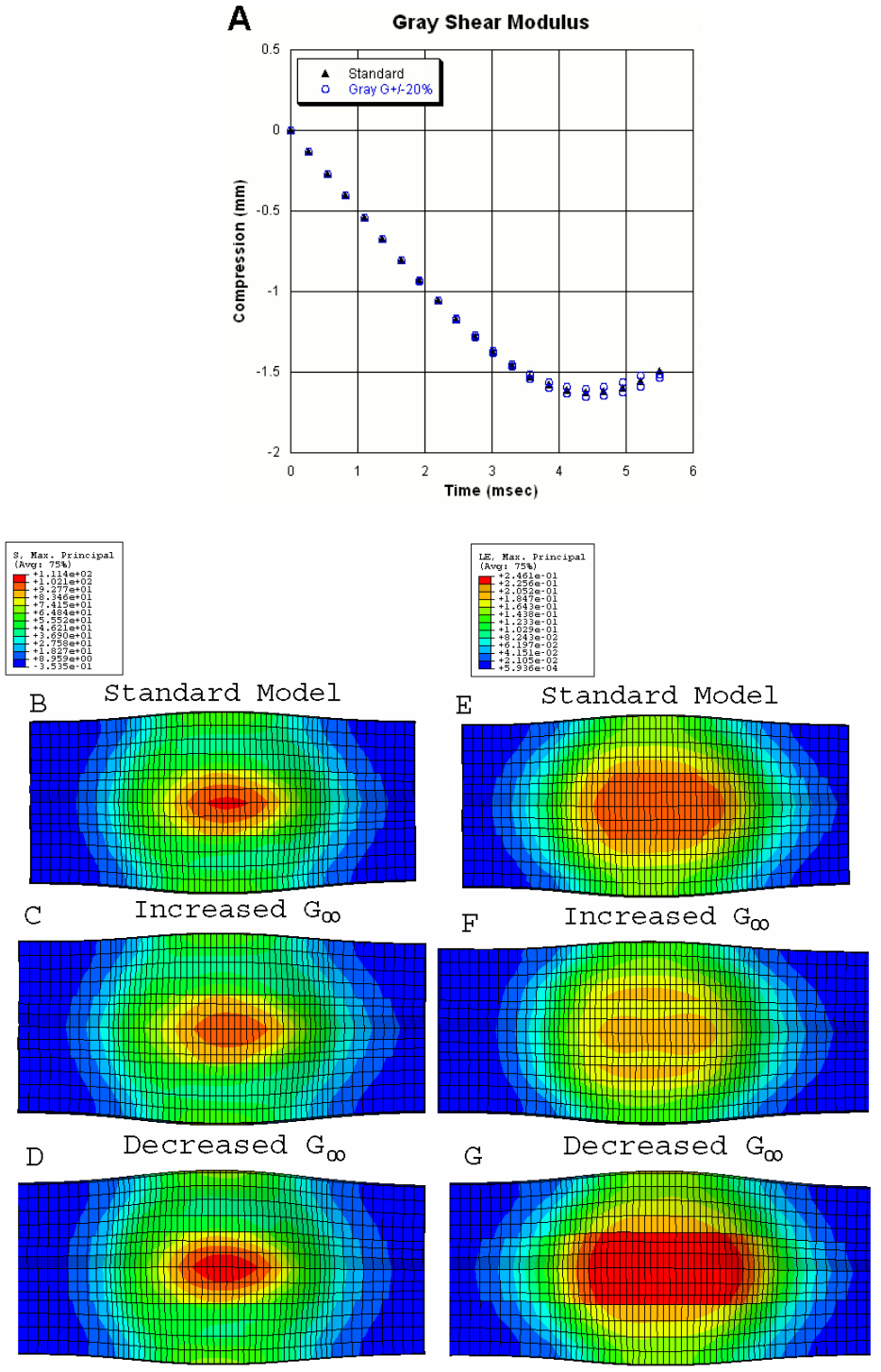

Figure 4-14: Parametric analysis results from independently changing the gray matter (A) shear modulus, G_{∞}, by 20% during a 12.5mm weight drop. Standard models patterns for SP and LEP are shown in at the top (B,E). Increasing G_{∞} by 20% resulted in smaller region of elevated stress (C), while decreasing gray G_{∞} resulted in a larger area of stress compared with the standard model (D). LEP in the gray matter decreased when G_{∞} was increased +20%, (F), while the gray matter elements had preferential increases in LEP when G_{∞} was decreased by 20% compared with the standard model.

A 20% increase and decrease in G_∞ for the white matter resulted in a 3% decrease and increase in the peak nodal displacement, respectively (Figure 4-15A). When G_∞ was raised by 20%, peak SP increased by 13%; when G_∞ was lowered by 20%, peak SP was decreased by 15%. Increasing and decreasing G_∞ by 20% resulted in a 4% decrease and 11% increase in peak LEP, respectively. The white matter elements showed decreases and increases in peak LEP areas when G_∞ was increased and decreased, respectively (Figure 4-15E-G). Regions of elevated SP were seen when G_∞ was increased, while SP decreased when G_∞ was decreased compared to the standard model (Figure 4-15B-D).

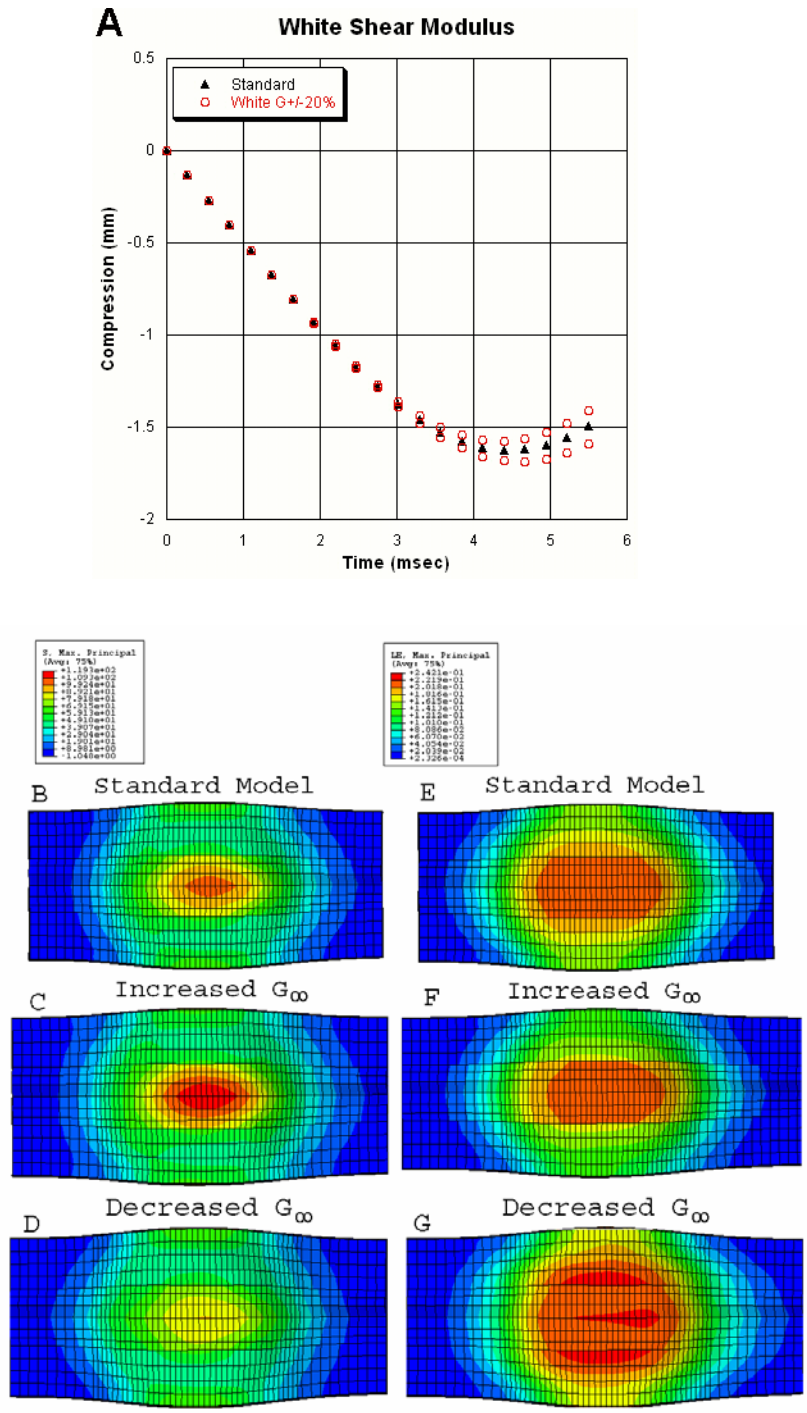

Figure 4-15: Increasing and decreasing the shear modulus of the white matter resulted in a 3% increase and decrease in the peak compression (A). Regions of elevated SP were seen when G_∞ was increased, while SP decreased when G_∞ was decreased compared to the standard model (B-D). The white matter elements showed decreases and increases in peak LEP areas when G_∞ was increased and decreased, respectively (B,C).

Altering the Prony series relaxation constants by 20% for the gray and white matter separately also had an effect on the peak nodal displacement, peak SP and LE, as well as the SP and LEP distribution patterns. Increasing g_1 for the gray matter resulted in an 8% decrease in peak nodal displacement, while a decrease in g_1 resulted in a 3% increase in peak nodal displacement (Figure 4-16). Peak SP increased by 90% and LEP decreased by 5% compared to the standard model when g_1 was increased by 20%. When g_1 was decreased, SP decreased by 12% while LEP increased by 27%. Analysis of the SP and LEP patterns show that the gray matter regions were most affected by the change in g_1. When g_1 was increased, the gray matter regions contained the highest values of SP. When g_1 was decreased, the region of SP was considerably smaller. As g_1 is increased in the gray matter, the white matter regions contained the elevated level of LEP. When g_1 decreased in the gray matter, there was an elevation in the peak regions of LEP in the gray matter areas. Altering the second relaxation constant, g_2, resulted in a less significant change in the compression depth; a 20% increase in g_2 showed a 3% decrease in compression depth, while a 20% decrease resulted in a 2% change. However, peak SP and LEP values decreased by 12% and 6%, respectively compared to the standard model when g_2 was increased by 20%. Peak SP values increased by 7% when g_2 was decreased; peak LEP values increased by 17%. Inspection of the patterns of stress and strain shows that g_2 did not have as much an effect on the FEM as g_1.

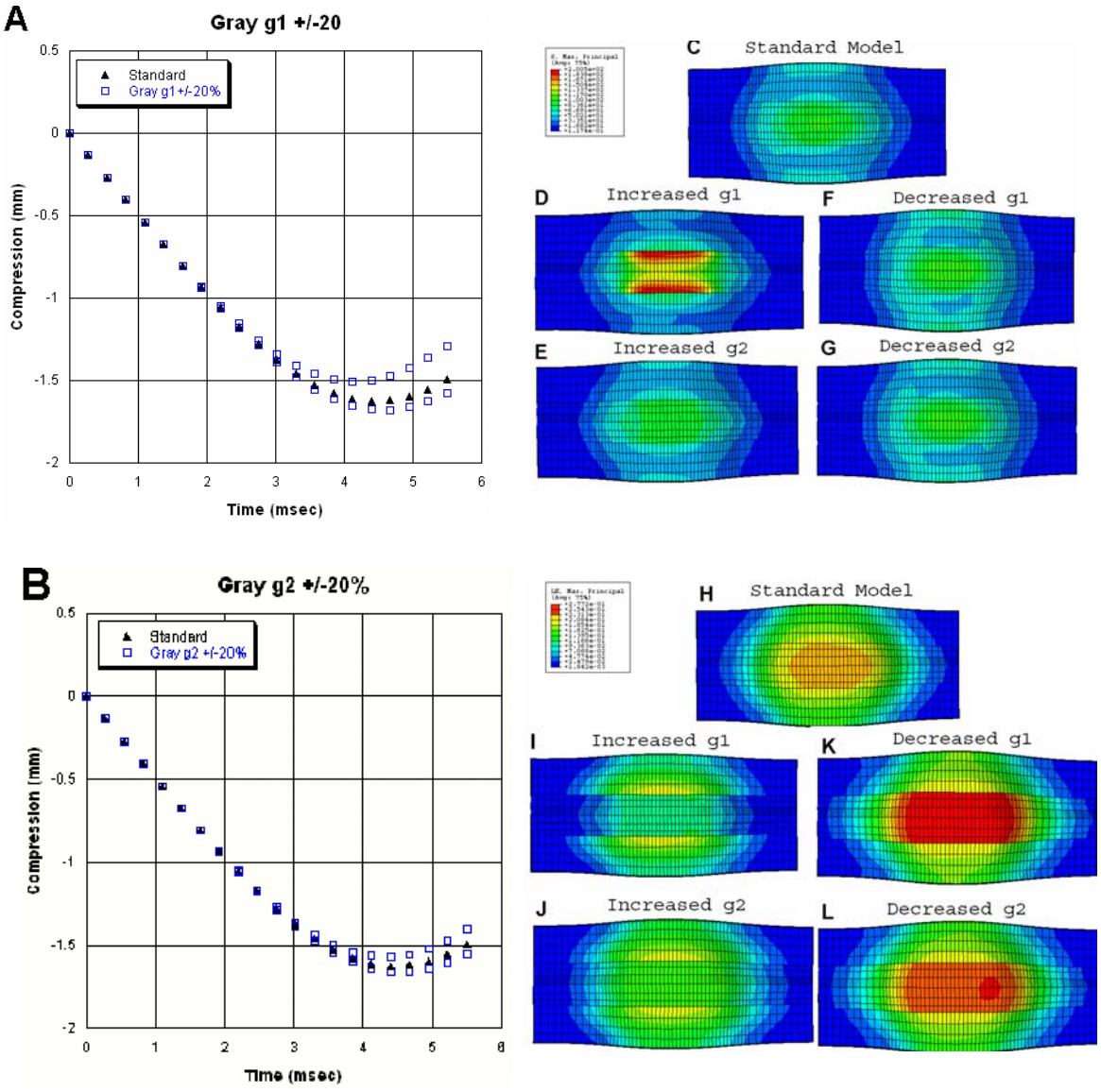

Figure 4-16: Increasing and decreasing g_1 had the greatest effect on peak displacement (A), while altering the second relaxation constant, g_2, resulted in a less significant change in the compression depth (B). When g_1 was increased, the gray matter regions contained the highest values of SP (D). When g_1 was decreased, the region of SP was considerably smaller (F). As g_1 is increased in the gray matter, the white matter regions contained the elevated level of LEP (H). When g_1 decreased in the gray matter, there was an elevation in the peak regions of LEP in the gray matter areas (K). The patterns of stress and strain showed that g_2 did not have as much an effect on the FEM output as g_1 (E,G,J,L).

A 20% increase in g_1 for the white matter resulted in a 22% decrease in peak nodal displacement (Figure 4-17A). A 20% decrease in g_1 resulted in an 8% increase in peak nodal displacement. Peak SP increased by 55% and peak LEP decreased by 10% when g_1 was increased by 20%. Peak SP decreased by 19% and LEP increased by 30% when g_1 was decreased by 20%. Inspection of the patterns of peak SP and LEP show that the areas that correspond to the white matter are preferentially altered. As g_1 decreases, the peak values of LEP increase more in the white matter than the gray (Figure 4-17J). As g_1 increases in the white matter, the gray matter contains the highest values of LEP (Figure 4-17I).

The white matter had an 8% decrease in peak nodal displacement and a 5% increase in peak nodal displacement when g_2 was raised and lowered by 20%, respectively (Figure 4-17B). Alteration in g_2 for the white matter did not influence the stress and strain patterns as much as changes to g_1. Overall, the white matter exhibited larger changes in peak nodal displacement, as well as peak SP and LEP. These differences can be attributed to the larger volume of the white matter compared with the gray matter.

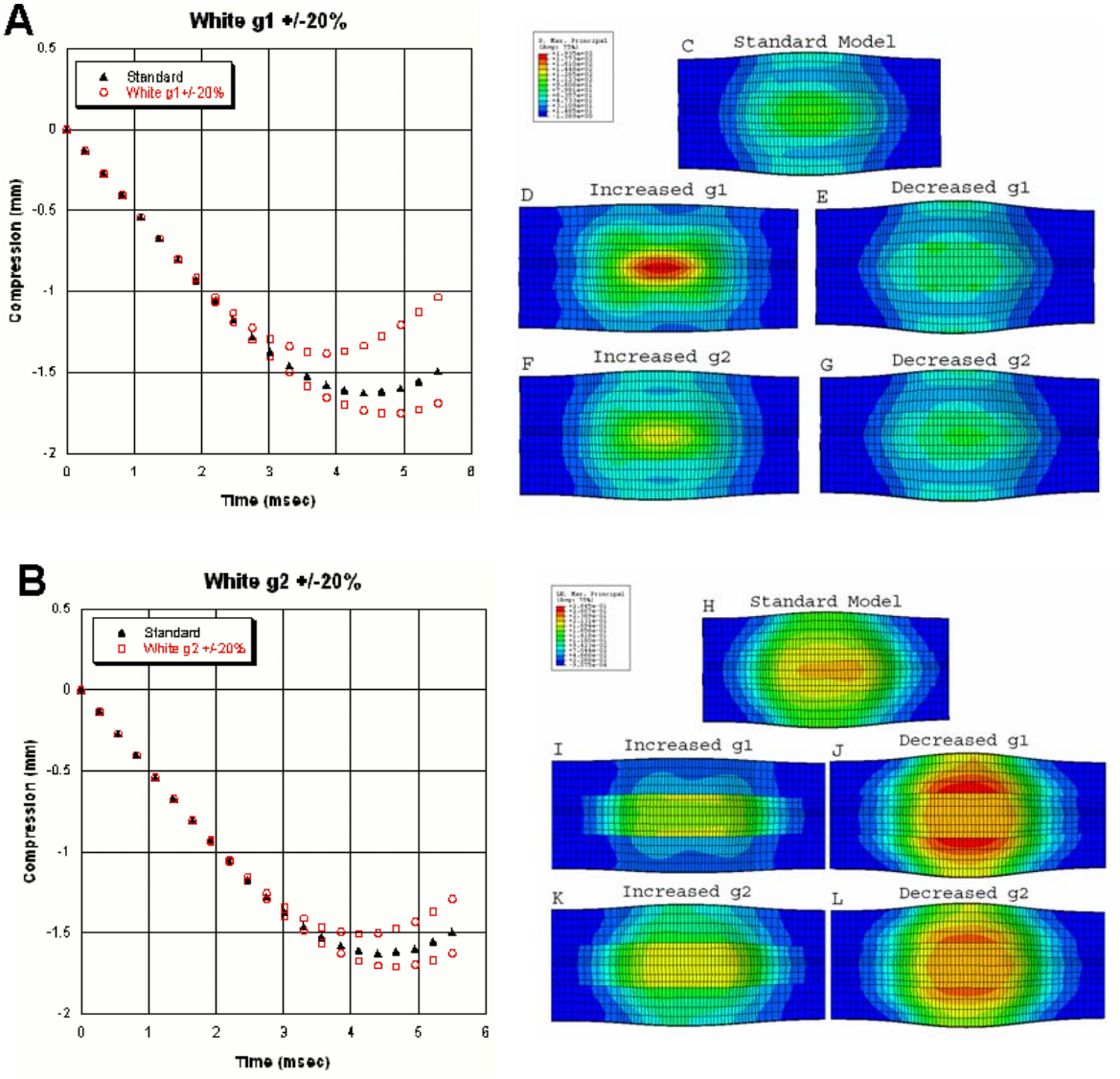

Figure 4-17: An increase in g_1 for the white matter resulted in a large decrease in peak nodal displacement (A). A decrease in g_1 resulted in an increase in peak nodal displacement. Patterns of peak SP and LEP show that the areas that correspond to the white matter are preferentially altered when g_1 was altered in the white matter. SP was mainly affected when g_1 was increased (D). As g_1 decreases, the peak values of LEP increase more in the white matter than the gray (J). As g_1 increases in the white matter, the gray matter contains the highest values of LEP (I). Alteration in g_2 for the white matter did not influence the stress and strain patterns as much as changes to g_1 (F,G,K,L).

Table 4-6 – Parametric Analysis Results for Peak Stress, Strain and Compression

Material	Condition	Peak Stress	Peak Strain	Peak Nodal Compression (mm)
Standard	-	105.6	0.2188	1.624
Gray	$G\infty$ + 20%	100.9	0.2043	1.549
Gray	$G\infty$ - 20%	111.4	0.2461	1.713
Gray	g_1 + 20%	200.5	0.2087	1.288
Gray	g_1 - 20%	118.2	0.2772	1.814
Gray	g_2 + 20%	92.54	0.2064	1.460
Gray	g_2 – 20%	113.6	0.2564	1.746
White	$G\infty$ + 20%	119.3	0.2106	1.575
White	$G\infty$ - 20%	89.95	0.2421	1.685
White	g_1 + 20%	193.5	0.1960	1.380
White	g_1 - 20%	85.68	0.2845	1.752
White	g_2 + 20%	140.4	0.2071	1.508
White	g_2 – 20%	85.08	0.2561	1.707

Adjustments in the values of α, D, and the coefficient of friction produced less than a 1% change in the peak nodal displacement. Furthermore, adjustments to all the variables investigated had less than a 5% change in the compression rate compared with the standard model.

To assess the sensitivity of the model to changes in the material properties for the dura mater, the Ogden hyperelastic parameters, the Prony series constants, and D were parameterized by 20%. Changes to all the variables resulted in less than a 1% increase or decrease in the nodal displacement and maximum values of SP and LEP from the standard model.

Additionally, the maximum and minimum values of the experimental impact velocity for the 12.5mm weight drop injuries were simulated. Peak nodal displacement increased and decreased 2% at the maximum and minimum experimental velocities, respectively. Peak values of SP were increased 7% and decreased 4% for the maximum and minimum

velocities, respectively. Peak values of LEP were increased and decreased less than 1% for the maximum and minimum velocities.

Off-Center Contusion and Electropneumatic Impact

A simulation was run to determine the changes in the intraparenchymal patterns of SP and LEP for a slightly off-center (0.35mm) contusion. While peak nodal displacement was less than 1% different than the standard model and peak values of SP and LEP were 3% and 1% higher respectively, the pattern of peak SP and LEP were shifted toward the off-centered impact site, as shown in Figure 4-18. A dorsal slice shows that the regions of elevated SP and LEP are shifted laterally compared with the standard model.

Displacement controlled devices have unique external loading features. The impactor is prescribed a specific displacement at a specific rate. The severity of the injury is determined by the magnitude of the displacement and the prescribed rate. The differences in loading conditions can cause significantly different injury outcome measures following trauma induced to the same compression depth compared with weight drop. However, as shown in Figure 4-19, the internal tissue-level strains generated are similar to the weight drop model. The peak values of strain were different for the models, but the difference can be attributed to the rate of compression. The standard model had a rate of 0.489m/sec, while the displacement controlled model had a rate of 0.225m/sec. Despite the differences in peak strain, the patterns of strain for each model are oblong in shape, radiating rostrally and caudally.

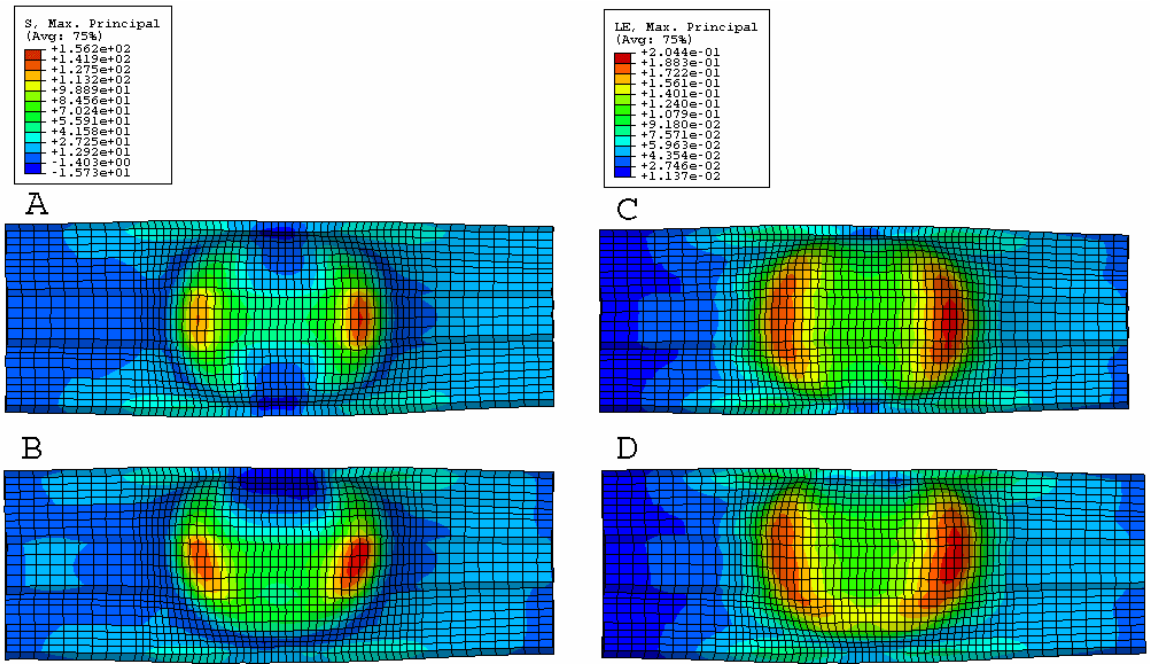

Figure 4-18: An off-center contusion produces injury patterns that shift towards the site of the impact. Regions of elevated SP and LEP are shifted up, compared with the standard model.

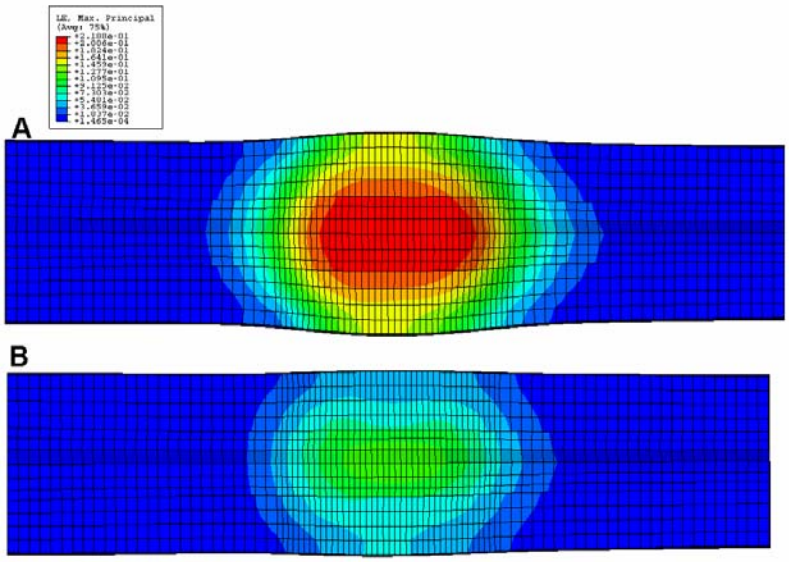

Figure 4-19: Comparison of the patterns of peak maximum principal strain for (A) the standard weight drop model and (B) the displacement controlled model. The peak values of strain were different for the models. The difference can be attributed to the rate of compression. The standard model had a rate of 0.489m/sec, while the displacement controlled model had a rate of 0.225m/sec. Despite the differences in peak strain, the patterns of strain are similar; roughly oblong in shape, radiating outward, similar to injury patterns seen during actual injury.

DISCUSSION

In this investigation, we developed and validated a computational 3D FEM of rat SCI using ABAQUS that simulates the Impactor weight drop model (See Chapter 2). The finite element model of rat SCI was developed to provide temporal and spatial profiles of mechanical parameters that will be used to identify tissue-level thresholds for spinal cord microvascular injury, which can be used to improve means and measures of preventing spinal cord injury in humans. Concerns regarding the length of the spinal cord were evaluated with separate models with altered boundary conditions. Mesh convergence was evaluated by simulating a 20% finer mesh. The FEM was validated against compression rate and compression depth data from our parallel Impactor weight drop experiments at 12.5mm and 25mm. Finally, a parametric analysis was performed to assess to sensitivity of the model to the underlying assumptions of the material properties.

This model is the first reported FEM of rodent SCI. The neuroscience community has extensively used small animal models, most notably the rat and the mouse, to study the pathophysiology and functional time course of SCI (Young 2002), but there have been no attempts to develop and validate a FEM of small animal SCI**.** Ueno et al. developed a brain injury model that simulated cortical impact in the ferret and investigated previously reported results (Ueno, Melvin et al. 1995). Shreiber et al. published a validated FEM of rat TBI and computationally compared the results to an experimental model of cortical contusion. Since then, other studies have employed real world loading conditions to study brain trauma (Willinger, Kang et al. 1999; Franklyn, Fildes et al. 2005; Viano, Casson et al. 2005). In this study, we modeled SCI based on a well established injury model, the Impactor weight drop technique, and compared the output from our simulations to the experimental results of SCI

in an effort to identify tissue-level tolerances for SCI. A combined experimental-computational offers the opportunity to investigate measures of injury that can be compared to the results of our FEM.

Performance of the model depends on the underlying assumptions during the development of the model. Critical in these assumptions is an accurate representation of the geometry of the spinal cord. Preliminary analysis of a simplified model of SCI, in which we modeled the spinal cord as a homogeneous model of white matter, showed that 1.4cm was the smallest length allowable without affecting the intraparenchymal stress and strain distributions in the simulation. A reduction in the total length of the spinal cord, especially in the proximal and distal regions unaffected by the contusion, showed a significant decrease in the amount of computational time needed to run the simulation. Furthermore, in the parallel Impactor experiments, it was noted that the maximum linear amount of extravasation in a single horizontal section of the spinal cord following a contusion was approximately 0.5cm. However, a parametric analysis was necessary and warranted to determine if the chosen length of the spinal cord affected the stress and strain distributions in the simulation. Thus, 3 separate boundary conditions were simulated: a 20% shorter spinal cord, a 50% longer spinal cord, and a constrained model in which the spinal cord was fixed on the proximal and distal ends.

In all 3 models, the results indicated that the selected length of the spinal cord did not adversely affect the distribution of stress and strain during compression. Peak nodal displacement showed less than a 1% change from the standard model in all boundary conditions tested. Changes in peak SP were minimal for the constrained and elongated spinal cord compared to the standard model, while the shortened spinal cord resulted in a 6%

decrease in maximum SP, which was seen in the distribution patterns of SP. This suggests that shortening the spinal cord may have adverse effects on the patterns of stress and strain, but the size of spinal cord in the standard model did not affect the distribution of stress. Peak LEP for the elongated model and shortened models were unaffected, while the constrained model showed a modest 2.7% increase in maximum LEP. Analysis of the distribution of maximum LEP showed that the central portion of the slice, where LEP is at a maximum, was preserved in all boundary conditions tested. Areas in at the lateral borders of the constrained and elongated spinal cords showed slightly larger values of LEP. Overall, the results indicated that the chosen length of the spinal cord behaved similarly to the elongated and constrained cord and did not influence the intraparenchymal distributions of stress and strain.

In this investigation, we were able to model our experimental studies of SCI to provide the most useful comparison to the computational results. In a previous study in our lab, we examined the extravasation of 3 fluorescent markers (730Da hydrazide, 70KDa BSA, and ~5μm red blood cells) into the parenchyma of the rat spinal cord following a weight drop injury, which enabled us to view spatial maps of blood-spinal cord barrier injury (Maikos and Shreiber 2007). The observed patterns of injury were similar to those previously reported in the literature (Noble and Wrathall 1989) as well as to reported profiles of necrotic, cystic cavities, which form as a consequence of the initial mechanical insult and progressive secondary damage (Noble and Wrathall 1989; Noble and Wrathall 1989). Extravasation often extended rostrally and caudally in the gray matter, which was especially evident in larger drop heights. Comparison of a horizontal section of the extravasation of the 3 markers to the distribution of SP and LEP in the same anatomical section in the FEM show that the peak maximum principal stress and strain patterns correlate to the extravasation

patterns. However, simulations in which the gray and white matter properties were individually changed, more accurately display the pronounced intraparenchymal patterns of injury in the rostral and caudal directions of the gray matter. The results of the experimental and computational model support previous investigations that the gray and white matter are mechanically different (Arbogast and Margulies 1998; Bilston, Liu et al. 2001; Ichihara, Taguchi et al. 2001; Miller and Chinzei 2002; Prange and Margulies 2002). This interpretation is somewhat complicated by the differences in the distribution and density of vascular elements, which may generate different injury patterns because more vascular tissue is available for injury.

Differences in mechanical properties of the gray and white matter can be partially attributed to the denser, more vascularized network of the gray matter compared to the white matter**.** The sensitivity of the microvessels to trauma may be affected by the inherent differences in the vessels. However, there are conflicting reports on the differences between the gray matter and white matter in compression and tension. The conventional assumption was that the white matter was more rigid than the gray matter, but recent studies have suggested the opposite (Ichihara, Taguchi et al. 2001). Despite conflicting results, there have been no published reports on separate material descriptions of the rat gray and white matter. In fact, the only properties reported for the rat spinal cord were in uniaxial tension at very slow ($0.001s^{-1}$) to moderate ($\sim 0.1s^{-1}$) strain rates (Fiford and Bilston 2005). These properties are critical in order to understand the mechanical response of the spinal cord tissue to mechanical loads. Not only will this information help discern the in vivo tissue-level thresholds to SCI, but can aid in the prediction of injury patterns in accidents, such as motor vehicle accidents or falls. The success of the FEM hinges on the accurate determination of

the individual load-bearing entities, including the gray matter, white matter, and dura mater. It is clear that an in vivo mechanical description of the rat spinal cord structures would provide the most accurate properties for use in an FEM. However, it is difficult to acquire precise properties of the spinal cord tissue in vivo due to the difficulty with applying and measuring controlled mechanical loads in vivo.

An inverse engineering approach is a possible solution to elucidate the individual properties of the gray and white matter. Inverse engineering has been applied to characterize the mechanical properties of soft tissues, such as the heart and breast (Azar, Metaxas et al. 2001; Ichihara, Taguchi et al. 2001, Hu, 2003). In a study by Ichihara et al., the investigators developed an FEM of spinal cord compression in the bovine spinal cord. The gray and white matter were assigned different mechanical properties in the model and the results from the computational model were compared to magnetic resonance (MR) images of deformation in the gray-white matter junction. The gray and white matter junctions were easily distinguished in the MR images, and compression was measured separately for the gray and white matter from the MR images. It is possible to have a similar approach to determine the individual properties for the rat spinal cord gray and white matter. In order to accurately estimate the stress-strain relationship, a known compressive force can be applied to a rat spinal cord in vivo and the deformation of the gray and white matter can be measured with MR images, thus fine-tuning the stress-strain constitutive laws.

The predictive power of the FEM primarily depends on the assumptions of the geometry of the model, the mechanical properties of the load-bearing constituents, the applied boundary conditions, and the loading conditions. Parametric studies were designed and implemented to investigate these assumptions. The results from the parametric analysis

show that mechanical properties of the spinal cord, including the shear modulus and the Prony series relaxation constants, had the greatest effect on spinal cord compression, peak SP and LEP, as well as the distribution of SP and LEP. Alterations of α, D, the coefficient of friction, and the Prony series time constants did not effect the validation of the FEM.

The shear and viscoelastic properties of the model demonstrated the greatest deviations in nodal displacement, peak SP and LEP, as well as the patterns of stress and strain. The only published properties of rat spinal cord tissue were recently reported by Fiford and Bilston. For this computational model, results from the Fiford and Bilston quasi-static uniaxial tension study were fit with the Ogden model, which produced an effective quasi-static shear modulus of approximately 200kPa. It has been shown that rat brain tissue in compression and shear is significantly more compliant than in tension. Thus, the properties of the spinal cord were fine tuned to achieve the desired compression depth and rate that best matched those from parallel weight drop experiments. Similarly, the viscoelastic properties reported by Fiford and Bilston were not performed at traumatic loading rates. Thus, viscoelastic relaxation and time constants were chosen from the material law proposed by Mendis derived from compression tests of human brain tissue (Mendis, Stalnaker et al. 1995). In that study, compression tests were performed at traumatic loading conditions and a 2-term Prony series, with an early and long term decay constant, was used to model the experimental results. The values for the quasi-static shear modulus and viscoelastic relaxation and time constants used in this FEM resulted in a good correlation of the peak nodal compression to the average experimental compression for the parallel Impactor experiments. However, for a complete FEM, it is necessary to perform a complete study on the material properties of the rat spinal cord to improve the validity of the FEM.

Our lab identified the mechanical properties of rat spinal cord dura mater in uniaxial tension at both low (~0.001s^{-1}) and high strain rates (~20 sec^{-1}). The dura mater was modeled as a 1-term Ogden hyperelastic, linearly viscoelastic (4-term exponential decay) solid and prescribed with the instantaneous shear modulus previously found. To evaluate the tissue biomechanics associated with the weight drop model, or any model that delivers an insult across the dura mater, the contribution of the dura mater to the overall mechanical response must be included. The rat dura mater is significantly stiffer than the spinal cord tissue it surrounds, which points to its protective role. It is important to note that although the dura was modeled as a solid (1 element thick) with an approximate thickness of 50-80μm, using membrane elements would more accurately represent the true nature of the dura. Membrane elements have an intrinsic thinness that more accurately portrays thin outer membranes, such as the dura. However, we determined that our preliminary FEMs, which modeled the dura with membrane elements, resulted in complicated contact interactions between dura and the CSF, which introduced errors due to element overclosures.

The cerebrospinal fluid was also modeled as solid (1 element thick) with a shear modulus ~240x less than the spinal cord. In our current FEM, Abaqus did not have effective means of including the CSF as a reservoir of pressurized fluid. Thus, the most common approach to model the CSF was as a low shear, high bulk modulus solid to introduce fluid-like behavior. Modeling the CSF as a low shear solid introduced geometric complexities that adversely affected the simulation, most notably for the higher weight drops. Because the CSF was modeled as a solid, it was unable to properly flow during compression. While inclusion of the CSF added a degree of compressibility, modeling the CSF as a true fluid would greatly enhance the fidelity of the model.

In this investigation, we simulated an off-center impact to determine how a lateral contusion could affect the internal patterns of stress and strain. Off-center contusions can significantly change injury outcome measures, such as measures of the volume of cell death and open field locomotor test scores (e.g. Basso, Beattie, Bresnahan Score – BBB). Off-center spinal cord injuries are clinically relevant, as contusions of the spinal column and vertebrae that result in SCI can affect different regions of the spinal cord. We determined that the peak displacement of the cord and peak values of strain did not vary from the standard model, but as can be predicted, the patterns of strain shifted laterally toward the contusion. Established tissue-level thresholds can aid in the prediction of possible differences in outcome measures that result from off-center impacts. For example, a lateral impact could potentially affect different regions of the cord, (i.e. affecting more regions of white matter), which have a different tolerances for BSCB injury. This could potentially alter measures of BBB, as well as white matter sparing, and volume of cell death. However, accurate thresholds for injury to the gray and white matter could help predict regions of the spinal cord more susceptible to vascular injury.

The central hypothesis of this research is that the severity and extent of primary damage during SCI can be predicted by the distributions of the mechanical states of stress and strain in the spinal cord during trauma. Herein, we have reported the first validated model of rat SCI. We have validated our model with experimental output from our parallel Impactor experiments at 2 loading conditions. The underlying assumptions, including assumptions of boundary conditions and material properties, resulted in peak compression depths that fell within the range of experimental values at both 12.5mm and 25mm. Furthermore the model presented here can be simulated with other impact trauma models of

SCI, such as weight drops with impact “buttons”, or electropneumatic impactors. We have performed a preliminary investigation in which we modified our weight drop FEM to simulate an electropneumatic impactor, which is a displacement controlled device. Displacement controlled devices, as well as other spinal cord contusion devices, each have unique external loading features that can produce significantly different injury outcome measures following trauma induced to the same compression depth. These differences can be attributed to the subtle differences in loading conditions. However, the link between the internal tissue-level stress and strain generated with the different SCI models and the patterns of injury they produce will be the same. Our preliminary analysis of the displacement-controlled impactor, in which the severity of the injury is determined by the magnitude and rate of the displacement, showed that the patterns of stress and strain are the same as in the weight drop, even though the peak values may be different. The goal for this research is to link the these patterns, specifically for BSCB primary injury, to the states of mechanical stress and strain in the spinal cord by quantitatively comparing our experimental results of BSCB injury from our parallel Impactor experiments to the output of our FEM to predict threshold levels of stress and strain. The thresholds will provide a benchmark for improved means of preventing SCI, as well as developing therapeutic interventions. Moreover, the thresholds found in the rat spinal cord can be used to approximate the thresholds in humans. Therefore, we can provide a valuable link between the traumatic loading conditions during SCI and tissue failure in humans.

REFERENCES

ARBOGAST, K. B. and MARGULIES, S. S. (1998). "Material characterization of the brainstem from oscillatory shear tests." J Biomech **31**(9): 801-7.

AZAR, F. S., METAXAS, D. N. and SCHNALL, M. D. (2001). "A deformable finite element model of the breast for predicting mechanical deformations under external perturbations." Acad Radiol **8**(10): 965-75.

BAIN, A. C. and MEANEY, D. F. (2000). "Tissue-level thresholds for axonal damage in an experimental model of central nervous system white matter injury." J Biomech Eng **122**(6): 615-22.

BANDAK, F. A. (1995). "On the mechanics of impact neurotrauma: a review and critical synthesis." J Neurotrauma **12**(4): 635-49.

BEATTIE, M. S., BRESNAHAN, J. C., KOMON, J., et al. (1997). "Endogenous repair after spinal cord contusion injuries in the rat." Exp Neurol **148**(2): 453-63.

BILSTON, L. E., LIU, Z. and PHAN-THIEN, N. (2001). "Large strain behaviour of brain tissue in shear: some experimental data and differential constitutive model." Biorheology **38**(4): 335-45.

BILSTON, L. E. and THIBAULT, L. E. (1996). "The mechanical properties of the human cervical spinal cord in vitro." Ann Biomed Eng **24**(1): 67-74.

DOHRMANN, G. J., PANJABI, M. M. and WAGNER, F. C., JR. (1976). "An apparatus for quantitating experimental spinal cord trauma." Surg Neurol **5**(5): 315-8.

DUCKER, T. B. and ASSENMACHER, D. R. (1969). "Microvascular response to experimental spinal cord trauma." Surg Forum **20**: 428-30.

FIFORD, R. J. and BILSTON, L. E. (2005). "The mechanical properties of rat spinal cord in vitro." J Biomech **38**(7): 1509-15.

FRANKLYN, M., FILDES, B., ZHANG, L., YANG, K. and SPARKE, L. (2005). "Analysis of finite element models for head injury investigation: reconstruction of four real-world impacts." Stapp Car Crash J **49**: 1-32.

GALFORD, J. E. and MCELHANEY, J. H. (1970). "A viscoelastic study of scalp, brain, and dura." J Biomech **3**(2): 211-21.

GRUNER, J. A. (1992). "A monitored contusion model of spinal cord injury in the rat." J Neurotrauma **9**(2): 123-6; discussion 126-8.

ICHIHARA, K., TAGUCHI, T., SHIMADA, Y., SAKURAMOTO, I., KAWANO, S. and KAWAI, S. (2001). "Gray matter of the bovine cervical spinal cord is mechanically more rigid and fragile than the white matter." J Neurotrauma **18**(3): 361-7.

JAEGER, C. B. and BLIGHT, A. R. (1997). "Spinal cord compression injury in guinea pigs: structural changes of endothelium and its perivascular cell associations after blood-brain barrier breakdown and repair." Exp Neurol **144**(2): 381-99.

KING, A. I., RUAN, J. S., ZHOU, C., HARDY, W. N. and KHALIL, T. B. (1995). "Recent advances in biomechanics of brain injury research: a review." J Neurotrauma **12**(4): 651-8.

MAIKOS, J. T. and SHREIBER, D. I. (2007). "Immediate damage to the blood-spinal cord barrier due to mechanical trauma." J Neurotrauma **24**(3): 492-507.

MENDIS, K. K., STALNAKER, R. L. and ADVANI, S. H. (1995). "A constitutive relationship for large deformation finite element modeling of brain tissue." J Biomech Eng **117**(3): 279-85.

METZ, H., MCELHANEY, J. and OMMAYA, A. K. (1970). "A comparison of the elasticity of live, dead, and fixed brain tissue." J Biomech **3**(4): 453-8.

MILLER, K. and CHINZEI, K. (2002). "Mechanical properties of brain tissue in tension." J Biomech **35**(4): 483-90.

MILLER, K., CHINZEI, K., ORSSENGO, G. and BEDNARZ, P. (2000). "Mechanical properties of brain tissue in-vivo: experiment and computer simulation." J Biomech **33**(11): 1369-76.

NOBLE, L. J. and WRATHALL, J. R. (1985). "Spinal cord contusion in the rat: morphometric analyses of alterations in the spinal cord." Exp Neurol **88**(1): 135-49.

NOBLE, L. J. and WRATHALL, J. R. (1989). "Correlative analyses of lesion development and functional status after graded spinal cord contusive injuries in the rat." Exp Neurol **103**(1): 34-40.

NOBLE, L. J. and WRATHALL, J. R. (1989). "Distribution and time course of protein extravasation in the rat spinal cord after contusive injury." Brain Res **482**(1): 57-66.

POPOVICH, P. G., WEI, P. and STOKES, B. T. (1997). "Cellular inflammatory response after spinal cord injury in Sprague-Dawley and Lewis rats." J Comp Neurol **377**(3): 443-64.

PRANGE, M. T. and MARGULIES, S. S. (2002). "Regional, directional, and age-dependent properties of the brain undergoing large deformation." J Biomech Eng **124**(2): 244-52.

RIVLIN, A. S. and TATOR, C. H. (1978). "Effect of duration of acute spinal cord compression in a new acute cord injury model in the rat." Surg Neurol **10**(1): 38-43.

RUAN, J. S., KHALIL, T. and KING, A. I. (1991). "Human head dynamic response to side impact by finite element modeling." J Biomech Eng **113**(3): 276-83.

RUAN, J. S., KHALIL, T. and KING, A. I. (1994). "Dynamic response of the human head to impact by three-dimensional finite element analysis." J Biomech Eng **116**(1): 44-50.

SHREIBER, D. I., A. C. BAIN, ET AL. (1997). "In vivo thresholds for mechanical injury to the blood-brain barrier." SAE 1997 Transactions: Journal of Passenger Cars **106(6-2):**: 3792-3806.

UENO, K., MELVIN, J. W., LI, L. and LIGHTHALL, J. W. (1995). "Development of tissue level brain injury criteria by finite element analysis." J Neurotrauma **12**(4): 695-706.

VAN NOORT, R., BLACK, M. M., MARTIN, T. R. and MEANLEY, S. (1981). "A study of the uniaxial mechanical properties of human dura mater preserved in glycerol." Biomaterials **2**(1): 41-5.

VAN NOORT, R., MARTIN, T. R., BLACK, M. M., BARKER, A. T. and MONTERO, C. G. (1981). "The mechanical properties of human dura mater and the effects of storage media." Clin Phys Physiol Meas **2**(3): 197-203.

VIANO, D. C., CASSON, I. R., PELLMAN, E. J., ZHANG, L., KING, A. I. and YANG, K. H. (2005). "Concussion in professional football: brain responses by finite element analysis: part 9." Neurosurgery **57**(5): 891-916; discussion 891-916.

VOO, K., KUMARESAN, S., PINTAR, F. A., YOGANANDAN, N. and SANCES, A., JR. (1996). "Finite-element models of the human head." Med Biol Eng Comput **34**(5): 375-81.

WHEELDON, J., KHOUPHONGSY, P., KUMARESAN, S., YOGANANDAN, N. and PINTAR, F. A. (2000). "Finite element model of human cervical spinal column." Biomed Sci Instrum **36**: 337-42.

WILLINGER, R., KANG, H. S. and DIAW, B. (1999). "Three-dimensional human head finite-element model validation against two experimental impacts." Ann Biomed Eng **27**(3): 403-10.

WINKELSTEIN, B. A. and MYERS, B. S. (1997). "The biomechanics of cervical spine injury and implications for injury prevention." Med Sci Sports Exerc **29**(7 Suppl): S246-55.

YOGANANDAN, N., KUMARESAN, S., VOO, L. and PINTAR, F. A. (1997). "Finite element model of the human lower cervical spine: parametric analysis of the C4-C6 unit." J Biomech Eng **119**(1): 87-92.

YOUNG, W. (2002). "Spinal cord contusion models." Prog Brain Res **137**: 231-55.

CHAPTER 5: IN VIVO TISSUE-LEVEL THRESHOLDS FOR MECHANICAL INJURY TO THE BLOOD-SPINAL CORD BARRIER

ABSTRACT

In vivo tissue-level thresholds for blood-spinal cord barrier (BSCB) injury were developed by statistically comparing an experimental model of rat spinal cord injury (SCI) to a finite element analysis (FEA) with logistic regression analysis. Adult female rats were injured by the Impactor weight drop model of spinal cord contusion at 2 drop heights (12.5 and 25mm) and the extent and severity of primary, physical disruption of the BSCB was quantified by measuring the extravasation of three markers of distinct size – fluorescently labeled hydrazide (~730Da), fluorescently labeled bovine serum albumin (~70kDa), and immunohistochemically labeled red blood cells (~5μm diameter) in both the gray and white matter. A three-dimensional FEA of the Impactor weight drop model in the rat was performed and validated with the in vivo experimental peak displacement of the spinal cord at two loading conditions. The peak compression of the model was within ten percent of the experimental results. Horizontal sections of the FE mesh were extracted and superposed on the composite images of BSCB injury for the same anatomical section for each severity marker (molecule, protein, and cell). Elements were graded as either injured or uninjured based on pixel values for injured tissue. Thirteen mechanical parameters, including measures of stress, strain, and strain rate, were investigated as predictors of BSCB injury. Maximum principal strain (LEP) was considered the best predictor of injury in the gray matter, while von Mises strain (LEVM) was the best predictor of injury in the white matter, although the LEVM thresholds for white matter included relatively large substantial error compared to the thresholds for gray matter. A better understanding of the biomechanical causes of SCI and

knowledge of the tolerance of the spinal cord tissue to mechanical loading is critical in understanding how mechanisms of injury lead to neurological deficits, as well as designing methods to prevent SCI.

INTRODUCTION

Traumatic loading conditions, such as those experienced during car accidents or falls, can lead to spinal cord injury (SCI), resulting in permanent functional damage (Mautes, Weinzierl et al. 2000). Spinal cord injuries (SCI) are a persistent problem in the United States, resulting in approximately 11,000 new injuries each year (Berkowitz 1998). While there are no fully restorative therapies for SCI, prevention remains the only viable option. A better understanding of the biomechanical causes of SCI and knowledge of the tolerance of spinal cord tissue to mechanical loading is critical in understanding how mechanisms of injury lead to neurologic deficits, as well as designing methods to prevent SCI.

Contusions account for the majority of SCIs (Mautes, Weinzierl et al. 2000). During contusive SCI, the initial mechanical insult (primary injury) can disrupt many structures of the spinal cord, including the blood-spinal cord barrier (BSCB), causing the non-specific influx of normally impermeable molecules and agents into the contused tissue. The blood-borne species that extravasate into the spinal cord parenchyma range from small molecules to gross hemorrhage (Dohrmann and Wick 1971; Griffiths and Miller 1974; Beggs and Waggener 1976; Faden, Gannon et al. 1988; Noble and Wrathall 1989; Noble, Mautes et al. 1996; Popovich, Horner et al. 1996; Bilgen, Al-Hafez et al. 2005). Primary injury of the vasculature and BSCB then contributes to secondary injury, which is an evolution of events, such as inflammation, edema, and ischemia that injure neighboring tissue (Mautes, Weinzierl et al. 2000). Secondary injuries have been the principal targets of post-trauma therapy and have been researched extensively (Blight 1985; Blight 1991; Blight 1992; Amar and Levy 1999). However, the underlying tissue-level biomechanics of primary SCI, which cause the injury, have received only superficial investigation. For a biomechanical analysis and

ultimately injury prevention, a detailed understanding of the consequences of the primary mechanical insult is required. Despite the high incidence of spinal cord contusions, no one to date has confirmed a biomechanical mechanism of spinal cord contusion – that is, what mechanical parameter, and what value of that parameter, cause contusions of the spinal cord.

SCI, specifically BSCB breakdown, has been studied extensively with several animate models of traumatic SCI (Albin, White et al. 1968; Dohrmann, Panjabi et al. 1976; Noble and Wrathall 1989; Gruner 1992; Basso, Beattie et al. 1996; Young 2002). These injury models, which include pneumatic or electromagnetic impactors and weight drops models, have been used to thoroughly characterize the neurohistological pathology and functional consequences of SCI, but biomechanical analyses of the spinal cord have been mostly superficial, mainly focusing on correlating loading parameters to the extent of injury without understanding the intraparenchymal mechanics (Hung, Albin et al. 1975; Koenig and Dohrmann 1977; Wagner and Stewart 1981). The mechanics of these in vivo models, especially at the tissue-level, are poorly understood. It remains unknown how the mechanical states of stress and strain are distributed in the spinal cord and how these distributions result in specific pathologies.

Finite element analysis (FEA) has become an effective tool to investigate the biomechanics of trauma. FEA has been used to conduct a variety of biomechanical analyses of trauma, including brain injury and spine injury biomechanics (Shreiber 1997; Yoganandan, Kumaresan et al. 1997; Willinger, Kang et al. 1999). However, neuroscientists have heavily relied on small animate models, most notably the rat and mouse, in studying the neuropathophysiology and functional consequences of SCI, and only recently have researchers used FEA as a viable tool to correlate injury mechanics in animal models to the

information gathered from in vivo models (Shreiber 1997). Despite the reliance of rodent models in the neuroscience community used to study SCI, there have been no published FE simulations of in vivo models of SCI. Threshold criteria have been established for different types of brain injury (King, Ruan et al. 1995; Ueno, Melvin et al. 1995; Shreiber 1997), but there have been no published analyses of SCI mechanics or threshold criteria established for the spinal cord tissue.

In this investigation, we used a validated computational 3D FE model of SCI to provide temporal and spatial profiles of mechanical parameters during injury. The parameters were quantitatively compared to experimental results of BSCB injury, which were then used to identify tissue-level thresholds for spinal cord microvascular injury. We have chosen to focus on characterizing the immediate breakdown of the microvasculature due to trauma because of the dramatic effects microvascular damage has on the secondary events and neuropathology following SCI. Therefore, the tolerances to SCI represent tissue-level targets for preventing SCI. Through understanding the tolerance of the tissue responsible for microvascular hemorrhage and primary damage to the BSCB, we will provide a benchmark to prevent not only the initial injury, but also the chain of secondary pathologies that follow vascular disruption of SCI.

METHODS

Experimental Model

SCI was induced using the Multicenter Animal Spinal Cord Injury Study (MASCIS) Impactor Weight Drop Model, which produces dynamic increases of stress and strain that are clinically relevant. The Impactor is one of the most well characterized and widely used SCI models. It precisely drops a calibrated weight (10g, 2.5mm diameter head) on the exposed spinal cord of rats that are 77 +/- 5 days old. BSCB injury, which is a common injury seen in vivo as well as clinically, was evaluated by microscopically viewing the intraparenchymal extravasation of three markers chosen to span a wide range of size.

Surgical procedure

A detailed description of the surgical methods has been previously described (Chapter 2) and will be briefly summarized here. Standard procedures for MASCIS Impactor experiments were followed (Young 2002). A T9-T10 laminectomy was performed under sterile conditions on adult, female Long Evans Hooded rats, 77 +/- 5 days old (220-240 g; n=33).

Blood-borne species labeling scheme:

BSCB permeability was evaluated for three distinct species that spanned a wide range in size: Alexa Flour 568-labeled hydrazide (707Da, 576 nm excitation, 599 emission Molecular Probes, Eugene OR, USA); Alexa Flour 488-labeled bovine serum albumin (BSA) (~70kDa, 497 nm excitation, 520 nm emission, Molecular Probes, Eugene, OR, USA); and native red blood cells (~5μm diameter). Ten minutes prior to injury, animals were given an

intravenous injection into the femoral vein of 1ml of tracer solution consisting of 1mg/kg of the labeled hydrazide and labeled BSA dissolved in 0.9% saline.

Injury and Post-Injury Procedures

All contusions were performed using the MASCIS Impactor. The rod was centered over the laminectomy, raised to the appropriate height, and dropped onto the exposed dura of the spinal cord. Impactor injury was performed at two drop heights (n_{height} = 8): 12.5mm and 25mm. Additional animals (n = 3) received only the surgery, and one (n = 1) served as an unoperated control. Injury was produced 60 +/- 2 minutes after anesthesia induction. Typical output of the Impactor after injury is shown in Figure 5-1. Impact velocity, cord compression distance, and cord compression rate were recorded for each experiment.

At five minutes following injury, animals were euthanized with a lethal dose of pentobarbital (60mg/kg), exsanguinated with 200ml heparinized saline, and perfused transcardially with 10% neutral buffered formalin. The spinal cords were removed and stored in 10% formalin until tissue processing. All procedures were approved by the Rutgers University Animal Care and Facilities Committee.

Tissue Preparation and Immunohistochemistry for BSCB Damage:

Fixed spinal cords were sectioned horizontally into 20μm sections with a cryostat (ThermoShandon, Pittsburgh, PA, USA). Sections were mounted on charged glass slides (Superfrost Plus, Fisher, Pittsburgh, PA, USA) in two serial sets. One set was immediately coverslipped (Prolong Antifade, Molecular Probes, Eugene OR, USA) and used for direct evaluation of extravasation of injected fluorophores. The other set was used to

immunohistochemically label red blood cells using an immunostaining workstation (ThermoShandon, Pittsburgh, PA, USA).

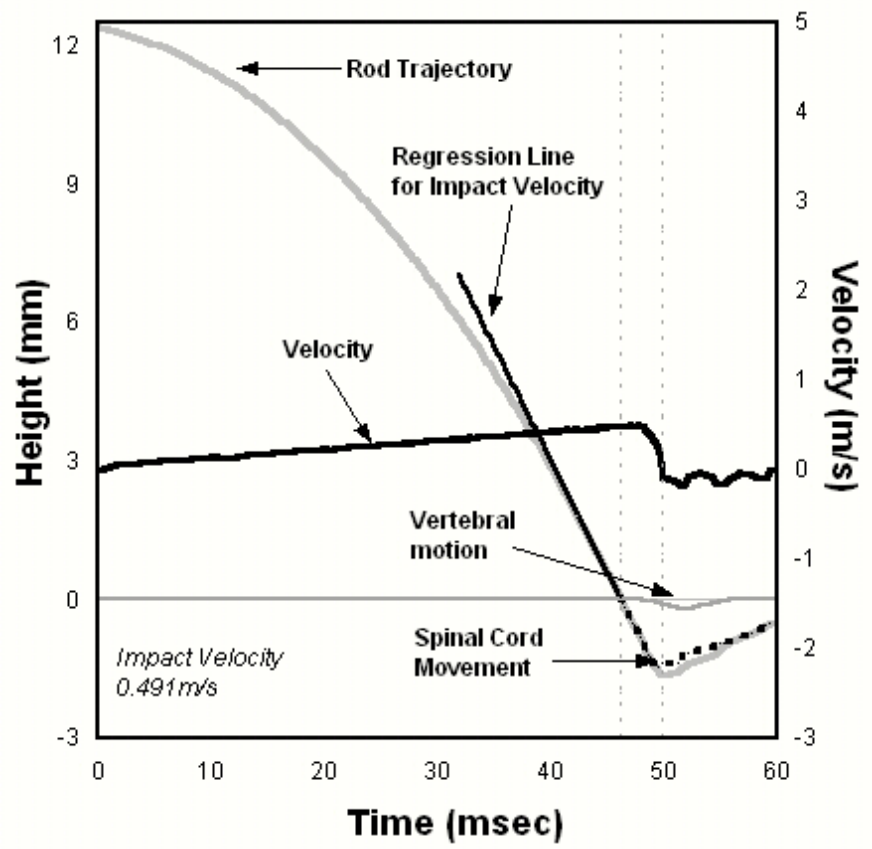

Figure 5-1: Example output following Impactor weight drop injury (12.5mm drop height). Separate optical potentiometers record the motion of the impacting rod and the vertebral body adjacent to the impact site. Vertebral motion is subtracted from rod motion to arrive at the compression distance of the spinal cord. Vertebral motion contributed minimally to the total displacement of the spinal cord. In this figure, the vertebral motion and resulting reduction in cord compression distance were scaled by a factor of 10 to make it easier to visualize the displacement of the spinal column. The actual average motion was 0.059 +/ 0.051mm. The velocity is determined from the derivative of the rod trajectory position data, and velocity at impact is estimated by linearly regressing the position data 2ms prior to impact. Spinal cord compression rate is found by dividing the compression depth by the time interval between impact and reversal of the surface of the spinal cord.

Quantifying Microvascular Pathology – Extravasation Volume Calculation:

Horizontal sections were imaged with epifluorescent microscopy to detect fluorescently labeled hydrazide, albumin, and red blood cells. Approximately 40 sections were examined for each fluorophore for each spinal cord. In each section, separate mosaic images at each wavelength were generated using computer controlled microscopy (Olympus IX81, Olympus America, Center Valley, PA, USA). It was possible to identify general areas of uninjured gray and white matter in each section by visually comparing the section to parallel sections from unoperated controls (Figure 2-2A). These areas were generally at the proximal and/or distal extremes of the section, which were the farthest away from the impact site. In some sections, the extravasated fluorophore(s) or immunolabeled cells masked the gray/white matter border. In these cases, the borders were estimated by extending regions that were visible and again comparing to parallel sections from unoperated, unlabeled control tissue (Figure 5-2B). Representative areas of uninjured gray and white matter were then selected in each section, and the maximum pixel grayscale values in those areas were identified and used to threshold that section. Any grayscale pixel value above the highest "uninjured" pixel value was considered injured (Figure 5-3). From the binary images, the areas of extravasation for both gray matter and white matter were calculated for each section, summed across sections, and multiplied by the linear distance between images to arrive at separate "extravasation volumes" for each fluorophore for gray and white matter. These gray and white matter volumes were then summed to arrive at a total extravasation volume for each fluorophore for each spinal cord.

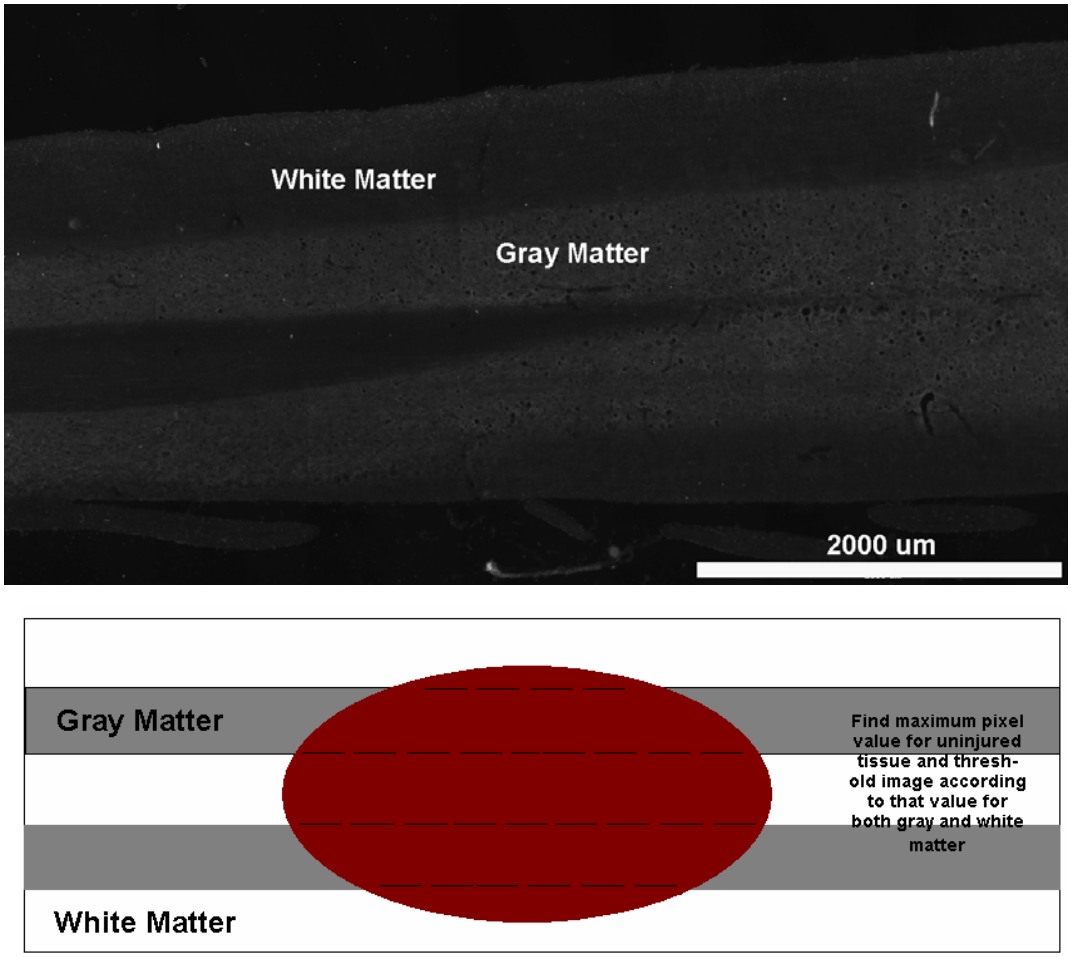

Figure 5-2: A fluorescent control image of a horizontal slice of spinal cord (A) and a schematic of injury masking the gray/white matter boundary (B). Gray matter and white matter are easily distinguishable in spinal cord images. The lighter stripes correspond to gray matter, while the darker regions surrounding the strips correspond to white matter. (B) Often times, injury to the spinal cord caused the gray/white matter border to be masked by the extravasated fluorophore(s) or immunolabeled cells. In these cases, the borders were estimated by extending regions that were visible (as shown by the dotted lines) and again comparing to parallel sections from unoperated, unlabeled control tissue.

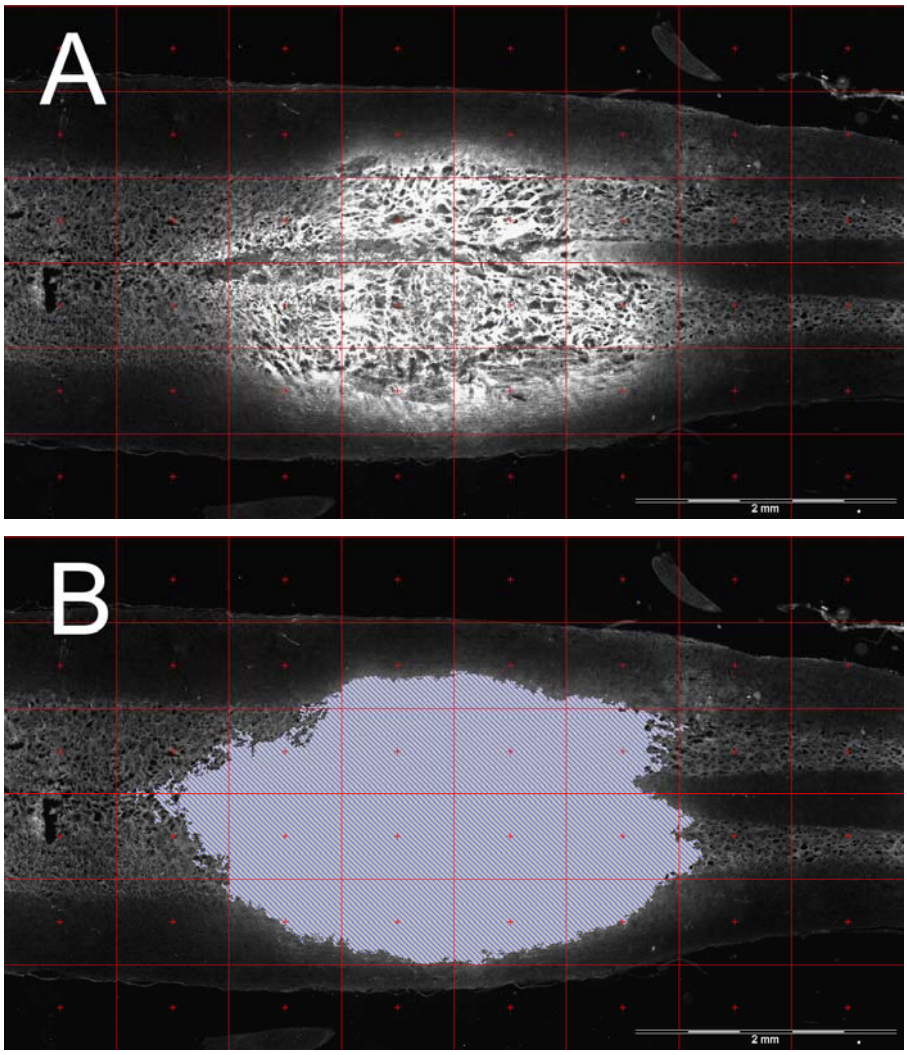

Figure 5-3: Lesion volume calculation. Bright areas in A) are injured tissue. A grayscale pixel value of injured tissue is determined from tissue far from the injury site. The image is then thresholded according to that value, and areas that lie above that value are shaded (B). These areas are summed across all sections and multiplied by the section thickness to arrive at an extravasation volume for that fluorophore.

Computational Model

A detailed description of the FEM of the spinal was previously presented (Chapter 4) and will be briefly reviewed here. We developed a 3D finite element model that simulated the Impactor Weight Drop Model using commercially available software (Abaqus/Explicit, HKS, Inc.). The model consists of the rat spinal cord, with distinct element sets for the gray and white matter, the cerebrospinal fluid (CSF), the dura mater, as well as a rigid rat spinal column, and a rigid impactor.

Spinal Cord

The geometry for the spinal cord was generated through magnetic resonance imaging (MRI) with a 4 Tesla horizontal bore magnet. The spinal cord was meshed with 8-node, reduced integration, hexahedron, 'hourglass control' elements for use with Abaqus Explicit (Figure 5-4). The gray matter and white matter had independent element sets with common nodes at the gray-white boundary to maintain overall continuity. In total, the gray matter comprised 21,948 nodes and 11,250 elements, and the white matter comprised 54,225 nodes and 30,276 elements.

Cerebrospinal Fluid and Dura

The CSF and dura were generated in Abaqus by expanding the outer boundary of the white matter by 3% and 5%, respectively, based on average diameter values of the dura obtained from the MR images of the rat spinal cord (Figure 5-5). The dura was 50-80μm in thickness, while the CSF filled the space between the dura and spinal cord (also ~50-80μm). The dura and CSF were each 1-element thick. Both the dura and CSF each comprised 9,360 nodes and 6,700 elements. The dura, CSF, and spinal cord were merged together as a single solid, while maintaining distinct nodal boundaries.

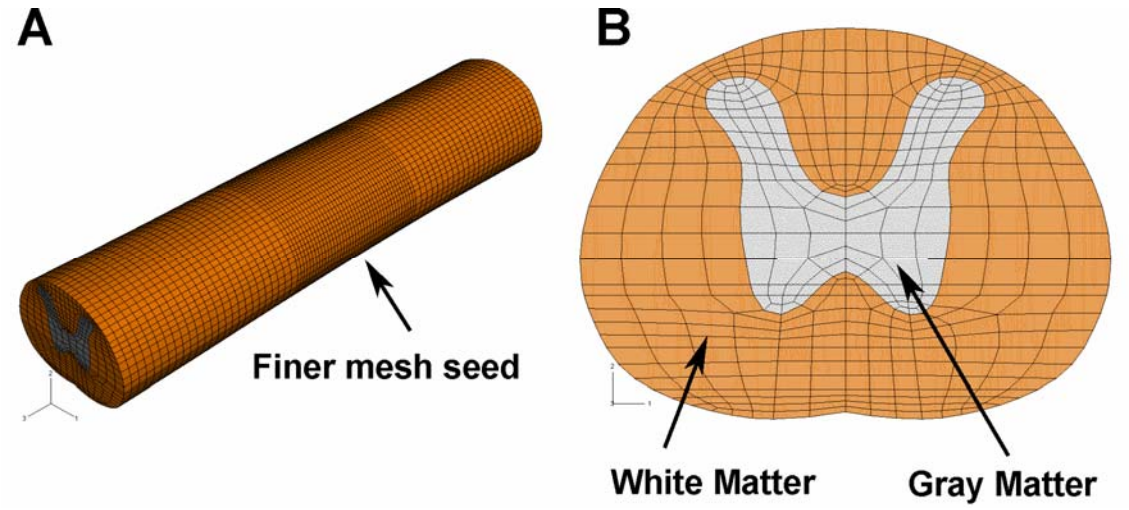

Figure 5-4: Mesh of the spinal cord (A), and a section of the spinal cord showing internal structures (B). We used a finer mesh seed in the central portion of the cord to enhance the resolution in the area of the most deformation. The gray and white matter contain distinct element sets, but share common nodes at the interface to maintain a continuous boundary.

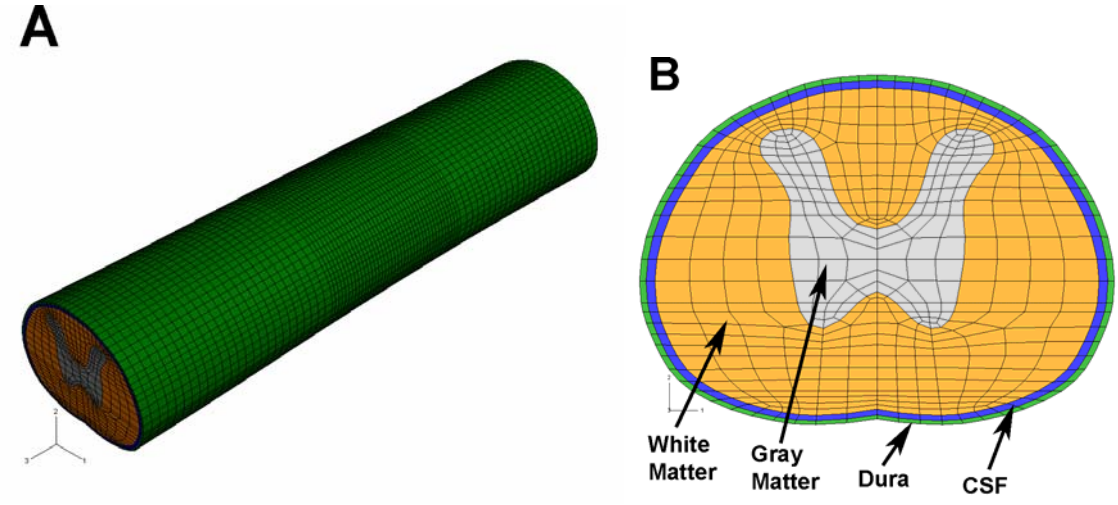

Figure 5-5: Mesh of the spinal cord with CSF and dura (A) and a cross-section of the spinal cord showing internal structures (B). The dura is the outer layer, shown in green. The CSF is between the dura and the white matter and displayed in blue. The white matter (shown as orange) and gray matter (shown as gray) make up the spinal cord. The CSF, dura, and spinal cord contain distinct element sets, but share common nodes at the each respective interface to maintain a continuous boundary.

Spinal Column

The geometry of the vertebral column was extracted from microCT imaging (Third-Generation microCT, Bio-Imaging Research, Lincolnshire, Illinois) of an excised spinal column with a T9/T10 laminectomy, to allow for better resolution of geometry changes in the axial direction. The mesh comprised 14,004 nodes and 27,929 elements (Figure 5-6). The spinal cord mesh was positioned in the vertebral column such that the center of the laminectomy was superior to the appropriate position in the spinal cord, which was identified from the appearance of gray and white matter in cross-section.

Impactor

The impactor was modeled as a discrete rigid cylinder of mass (10 grams) and diameter (2.5mm), which match the dimensions used in Impactor experiments. The impactor was centered over the laminectomy and placed in direct contact with the dorsal surface of the dura (Figure 5-7).

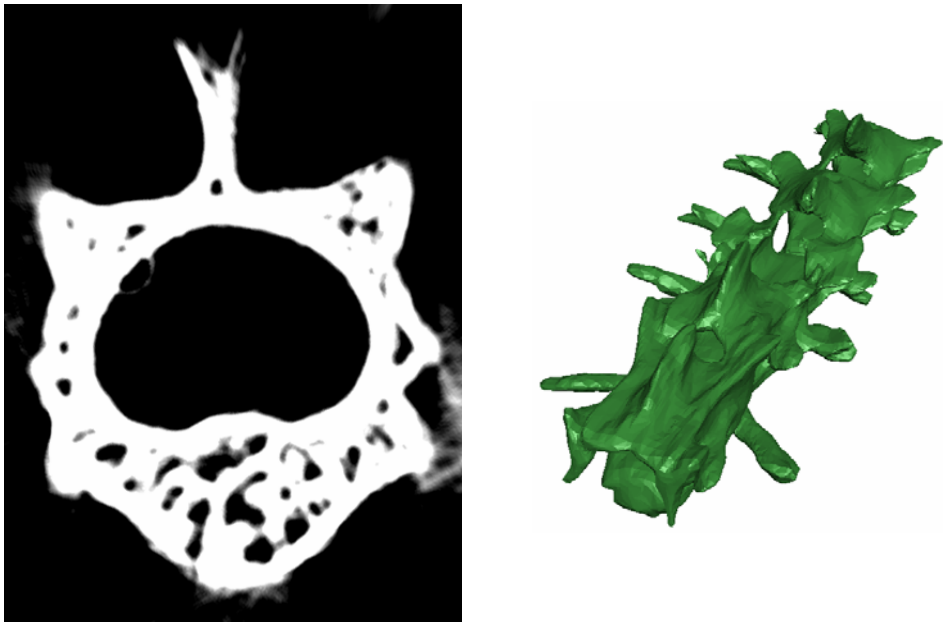

Figure 5-6: A representative image slice of a cross section of the rat spinal column showing the bone as well as the spinal cord canal. The column was imaged over ~3cm in length. Slices were acquired every 0.07mm. Image slices were formed into a 3D spinal column for use in the FEM.

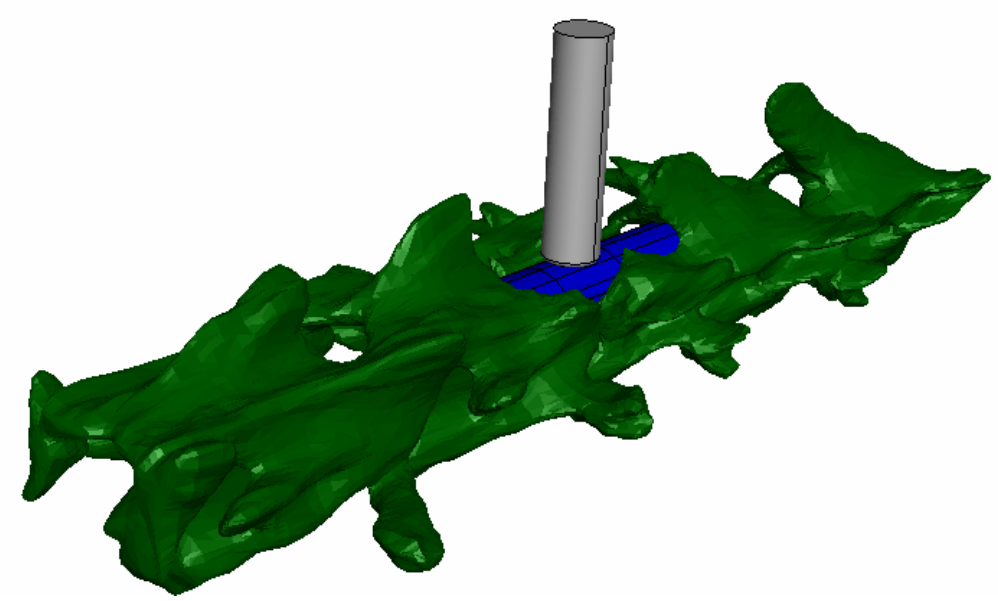

Figure 5-7: The spinal cord structures (blue) within the spinal column (green), with rigid impactor (gray). The impactor was centered over theT9/T10 laminectomy and was modeled as a discrete rigid body permitted to only move in the vertical direction. A weight drop experiment was simulated by placing the impactor in direct contact with the dura and prescribing an initial velocity that matched the average value determined from our parallel weight drop experiments.

Material Properties

Spinal Cord

The spinal cord was assumed to be isotropic and homogenous, with identical properties assigned to gray and white matter. The spinal cord was modeled as an Ogden hyperelastic-linear viscoelastic material with a two term Prony series to describe the exponential decay of energy within the material. The Ogden form of the hyperelastic strain energy potential function, *W*, has previously been used to model both spinal cord and brain tissue (Bilston and Thibault 1996; Miller and Chinzei 2002; Prange and Margulies 2002):

$$W = \sum_{i=1}^{N} \frac{2G_i}{\alpha_i^2}\left(\lambda_1^{\alpha_i} + \lambda_2^{\alpha_i} + \lambda_3^{\alpha_i} - 3\right) \qquad \text{Equation 5-1}$$

where λi are the deviatoric principal stretches, N is the complexity of the law, which is material dependent, and Gi and αi are material-dependent parameters.

The viscoelastic portion of the material laws was described with a Prony series exponential decay:

$$G_R(t) = G_0\left[1 - \sum_{k=1}^{N} \bar{g}_k^P\left(1 - e^{-t/\tau}\right)\right] \qquad \text{Equation 5-2}$$

where the instantaneous shear modulus is multiplied by a normalized function that includes relative relaxations, g_k, at characteristic time constants, τ_k. The quasi-static shear modulus can then be related to the instantaneous modulus by:

$$G_\infty = G_0\left(1 - \sum_{k=1}^{N} \bar{g}_k^P\right) \qquad \text{Equation 5-3}$$

Existing data from the literature for the properties of rat spinal cord in uniaxial tension at very slow ($0.001s^{-1}$) to moderate ($\sim 0.1s^{-1}$) strain rates was used as starting point for the

values for the material law (Fiford and Bilston 2005), and adjusted until the temporal profile of Impactor displacement that best matched those from parallel weight drop experiments (Table 5-1) (Maikos and Shreiber 2007) (see *Validation Analysis* below).

Dura Mater

Previous studies in our laboratory identified the mechanical properties of rat spinal cord dura mater in uniaxial tension. Both low strain rate (~0.001s^{-1}) and dynamic, stress-relaxation tests (strain rate ~20 sec^{-1}) were performed. The dura mater exhibited hyperelastic-viscoelastic behavior similar to other collagenous tissues, and was modeled as an Ogden hyperelastic (one term), linearly viscoelastic (4-term exponential decay) continuum solid. Poisson's ratio was set at 0.45. The dura was prescribed an instantaneous shear modulus previously found in our laboratory (Table 5-1).

Cerebrospinal Fluid

The CSF was modeled with solid elements with a low shear-to-bulk modulus to introduce fluid-like behavior (King, Ruan et al. 1995). The CSF was modeled as a Mooney-Rivlin hyperelastic material with an effective shear modulus ~240x less than the spinal cord:

$$W = C_{01}(I_1 - 3) + C_{10}(I_2 - 3) \qquad \text{Equation 5-4}$$

$$G = 2(C_{01} + C_{10}) \qquad \text{Equation 5-5}$$

where, for this model, C_{01}=C_{10}. Poisson's ratio was set at 0.49.

TABLE 5-1 – Material Characteristics used in the FEM

Material Characteristics					
Tissue	**Density (kg/m^3)**	**Long Term Shear Modulus G_∞ (kPa)**	**Bulk Modulus K (kPa)**	**α**	**ν**
Spinal Cord	1000	32	309.33	4.7	0.45
Dura Mater	1000	1200	11600	16.2	0.45
CSF	1000	0.13	6.67	-	0.49

Boundary and Loading Conditions

Contact was permitted between the impactor and dura, as well as between the dura and the spinal column. The spinal column was fixed in space. The impactor was permitted to move only in the vertical direction and allowed to have direct contact with the dura. The coefficient of friction for interaction of the Impactor and the dura and interaction of the vertebrae and the dura was estimated at 0.15. Two experimental loading conditions were simulated: a 12.5mm weight drop and a 25mm weight drop. Simulations for the 12.5 and 25mm were run for 5.5 and 4.4msec, respectively, which generally represents the duration required to achieve peak displacement and begin reversal. The impactor was placed in direct contact with the exposed dura and prescribed an initial velocity that matched the average value determined from the parallel weight drop experiments for that drop height. Our analysis was validated by comparing the compression rate and the displacement of the mass post-"impact" to the actual parameters measured during an Impactor weight drop.

Model Solution

The finite element simulation was performed using Abaqus/Explicit on 4 parallel processors (University of Minnesota Supercomputing Institute, IBM Power 4 System, AIX operating system, 1.7GHz Power4 Processors). The simulation was run for each average velocity of the complimentary Impactor experiments. The results were compared to the spatial maps of injury for the 3 different sized markers used in the Impactor experiments (Hydrazide, Bovine Serum Albumin, Red Blood Cells).

Data Analysis

We quantitatively compared the results from our experimental animal model for each injured spinal cord (n=16) to the output of the finite element analysis in with a statistical analysis to identify the in vivo tissue-level thresholds for the spinal cord. Our FE mesh was compared to our spatial maps of BSCB injury from the experimental study based on element-by-element comparisons. Specifically, 3 horizontal sections (dorsal, middle, and ventral) of the FE mesh were extracted and superposed on the composite images of BSCB injury for the same anatomical section for each severity marker (molecule, protein, cell) (Figure 5-8). Elements were graded as either injured (1) or uninjured (0) based on pixel values for injured tissue. We identified the brightest region (maximum pixel grayscale value) for uninjured tissue away from the injury site and thresholded each section according to that value. Any pixel value above the maximum uninjured value was considered injured. Tissue tears were also considered injured. For each experiment, the peak values of maximum principal stress (SP), maximum principal strain (LEP), von Mises stress (VM), von Mises strain (LEVM), compressive principal strain (LEC), compressive principal stress (SPC), pressure (P), and

strain energy (SEN) for each element were identified from the simulation with matching input loading conditions. Separate outputs were generated for elements corresponding to the gray and white matter of the spinal cord.

For each element, the injury status (1 or 0) was plotted against the peak values of the mechanical mediators of injury, and logistic regression analysis was performed to identify the dependence of injury on the parameter (Shreiber 1997).

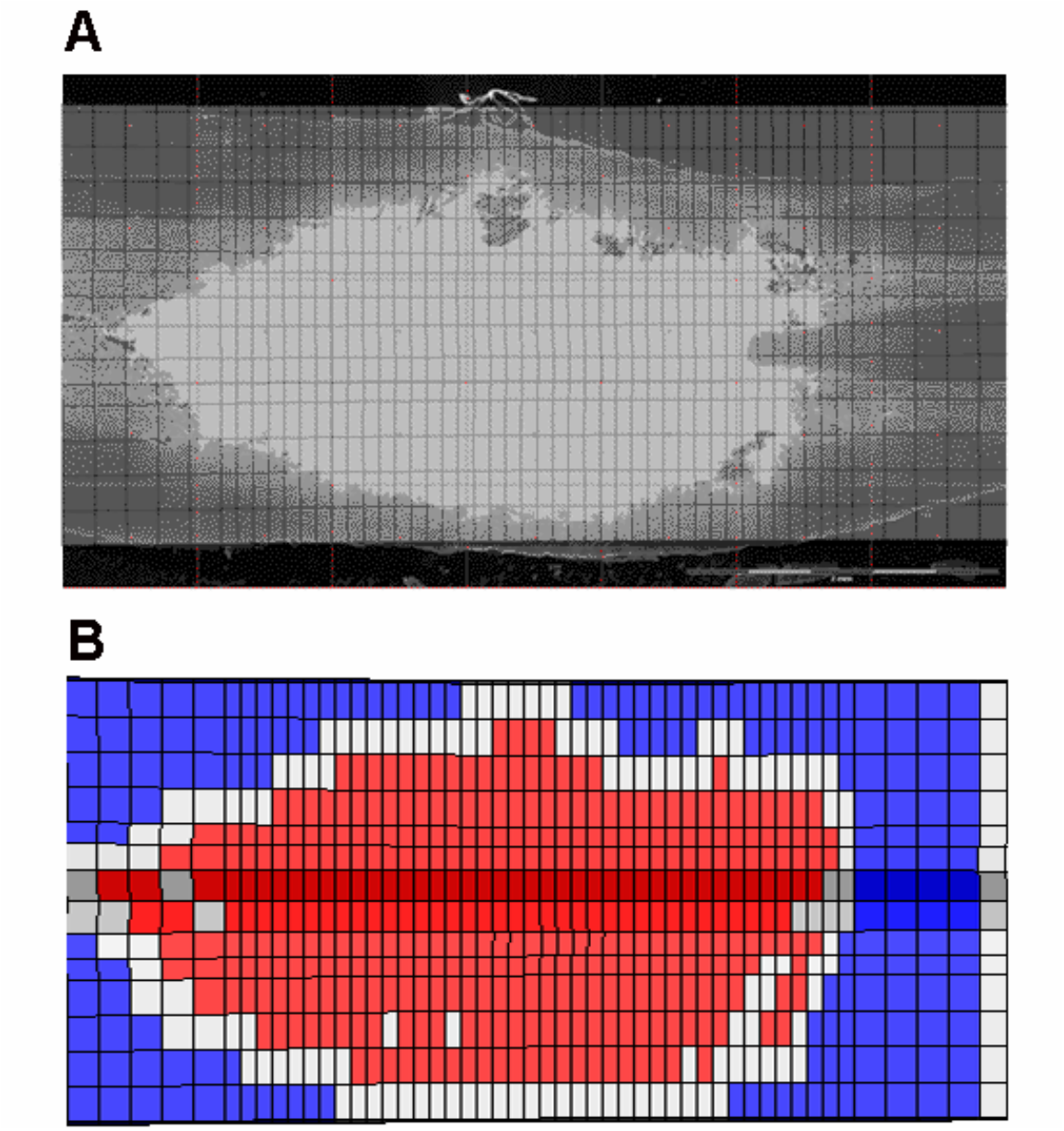

Figure 5-8: Element selection for logistic regression analysis. (A) A representative horizontal slice depicting albumin extravasation following a 12.5mm weight drop. The image is thresholded according to the peak grayscale value for uninjured tissue far from the injury site and areas that lie above that value are shaded. A slice of the FEM is superposed over the injury at the appropriate anatomical level. (B) Elements are graded as injured (red) or uninjured (blue). Gray elements were not picked for analysis.

Threshold Determination

From the logistic regression analysis, the number of true positives (TP), true negatives (TN), false positives (FP), and false negatives (FN) were determined by comparing actual injury status to predicted injury status based on the mechanical measure at each probability. Then, receiver operating characteristic (ROC) curves (Bain and Meaney 2000) were develop by identifying the sensitivity and specificity of the stress/strain value at 19 evenly distributed probability levels (5%-95% in 5% increments) and were calculated with SPSS according to the following equations:

$$sensitivity = \frac{TP}{TP + FN} \qquad \text{Equation 5-7}$$

$$specificity = \frac{TN}{TN + FP} \qquad \text{Equation 5-8}$$

The ROC curve is then generated as a plot of sensitivity vs. 1-specificity. The quality of the ROC depends on the area under the curve. The best predictors have an area of 1, while random guessing results in a diagonal line and an area of 0.5. Two threshold values for the best mechanical parameter were determined: a "conservative" threshold, for which sensitivity has no false negatives (all elements predicted to be injured are injured) and an "optimal" threshold, where the sum of sensitivity and specificity is maximized. A plot of (sensitivity + specificity) vs. probability revealed the probability value that results in the optimum threshold, where the (sensitivity + specificity) value is a maximum.

Parametric Analysis for Threshold Variables

For one of the loading conditions (12.5mm weight drop), a parametric analysis was performed to examine the various underlying assumptions, including modifying the shear modulus for the gray and white matter simultaneously, as well as independently, and how they affected the tissue-level thresholds. Simulations were run at +/- 20% of the original value for each of the parameters. Thresholds were calculated based on one of the experiments at that drop height.

Off-Centered Impact and Displacement-Controlled Simulation

A simulation was run in which the impactor was laterally displaced by 0.35mm to determine the changes in the intraparenchymal patterns of stress and strain. Furthermore, established tolerance criteria for the spinal cord tissue were used to determine which elements in the mesh exceeded the tissue threshold values. Elements were then compared to the standard model.

To ensure that the thresholds established in this investigation hold for other models of SCI, we performed a preliminary investigation in which we modified our weight drop FEM to simulate a displacement-controlled impactor device. The impactor was given a displacement of 0.9mm at a rate of 0.225m/sec.

RESULTS

Experimental Model

The patterns of extravasation were similar for all three markers, and generally matched previously reported observations (Noble and Wrathall 1989) (Figure 5-9). In horizontal sections, areas demonstrating extravasation were roughly oblong in shape, with the major axis aligned axially with the spinal cord. Extravasation was more pronounced and extended further in the rostral and caudal directions in the highly vascular gray matter vs. white matter. Areas of extravasation in a given tissue slice were visibly larger as drop height increased and as the size of the labeled marker decreased.

Extravasation Volume

The volume of extravasation of each fluorescently labeled marker was quantified using image analysis by generating a binary image with the average grayscale pixel value of uninjured tissue in both gray and white matter as the thresholds. Extravasation volume increased significantly with increasing drop height (ANOVA, $P<0.001$) (Figure 5-10). Additionally, extravasation volumes were significantly greater in gray matter vs. white matter, and each significantly contributed to the total extravasation volume (ANOVA, followed by Scheffe's test, $P<0.001$). No extravasation of the labeled hydrazide, albumin, or erythrocytes was observed in either surgical shams or the unoperated control.

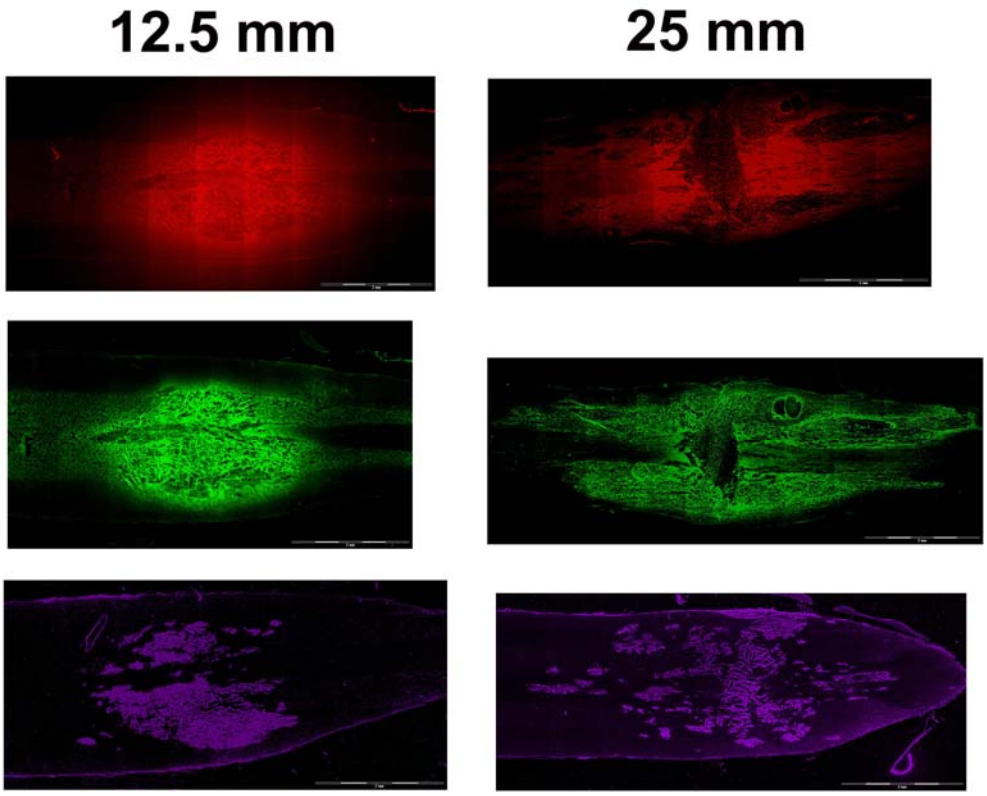

Figure 5-9: Representative spatial maps of injury from a 12.5 and 25-mm drop height. The images have been pseudo-colored to distinguish the different fluorophores. Alexa 568-Labeled hydrazide (730 Da – red); Alexa 488-Labeled albumin (70 kDa – green); Alexa 647-Labeled red blood cells (5μm – purple). (Note: Alexa 647 emits a red-orange color that we pseudo-color purple to better distinguish from the Alexa 568). Following an Impactor weight drop, the labeled hydrazide (red) and labeled BSA (green) are already in the tissue from an intravenous injection. Following sectioning the tissue, we immunohistochemically stained RBCs (purple) with an Alexa Fluor 647 secondary antibody. It takes a more severe injury to cause a larger hemorrhage, as seen in the 25 mm drop height.

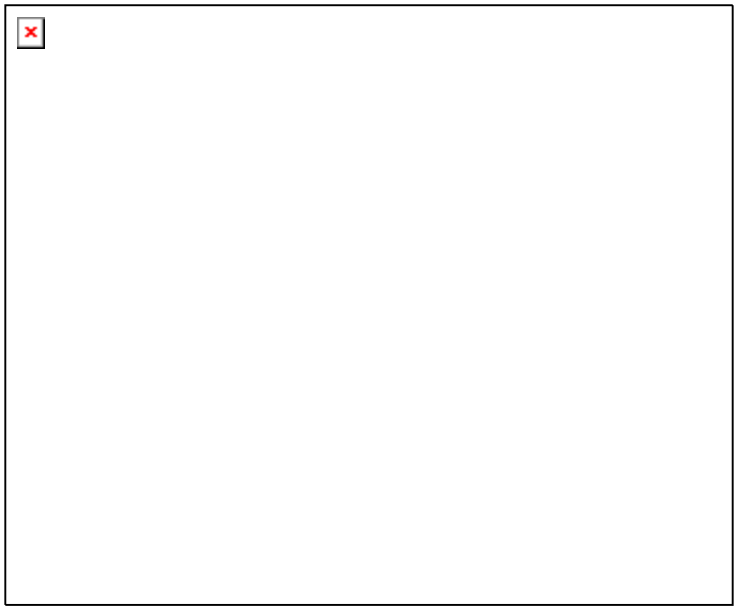

Fig 5-10: Extravasation volumes of the three species as functions of drop height. Extravasation volumes differed significantly with drop height and with injury marker (ANOVA, $P < 0.001$). Injury to the gray matter was significantly greater than injury to the white matter, and each contributed significantly to the overall, total extravasation volume (ANOVA, $P < 0.001$). Post-hoc pairwise comparisons revealed significant increases for each drop height combination for both gray and white matter (Scheffe's post hoc test, $P<0.01$).

Validation Parameters

Figure 5-1 shows a graph of the output of a typical Impactor experiment. Following a contusion of the spinal cord, the Impactor generates values of velocity, compression depth, and compression rate. Table 5-2 shows the average results of the Impactor experiments used for model validation. Peak values of displacement and compression rate of the spinal cords were consistent for each separate drop height.

TABLE 5-2 – Average Values of the Impactor Experiments

Drop Height (mm)	**n**	**Velocity (mm/msec)** Average (Std. Dev)	**Compression Depth (mm)** Average (Std. Dev)	**Compression Rate (mm/msec)** Average (Std. Dev)
12.5	8	0.489 (0.011)	1.65 (0.194)	0.429 (0.145)
25	8	0.690 (0.007)	2.14 (0.168)	0.586 (0.023)

Finite Element Analyses

Compression Depth and Rate Validation

The compression depth and rate for each drop height simulation fell within the range of experimental values and was within 10% of the mean experimental values, determined from our parallel Impactor experiments. The peak displacement and rate were determined by averaging the peak displacement for nodes within a 2.5mm diameter at the center of the contusion, to approximate the impactor diameter. Figure 5-11 displays the Impactor validation data, as well as the average nodal displacement and rate from the FEM.

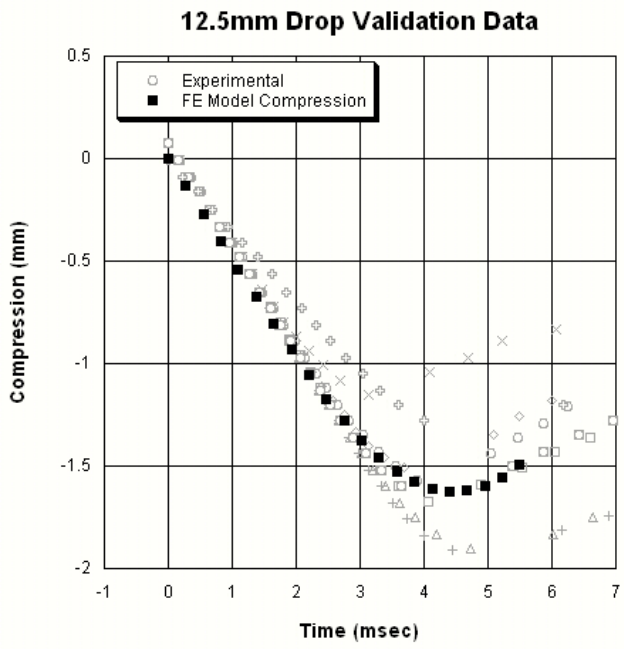

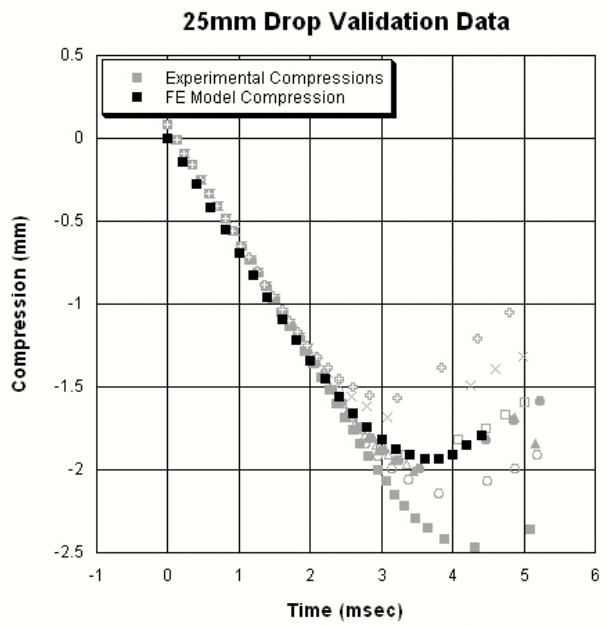

Figure 5-11: Experimental Impactor compression and compression rate for each weight drop experiment are shown in gray and the FEM simulation compression results are shown in black. Both the 12.5mm and 25mm compression and compression rate results from the FEM fall within the experimental results.

In Vivo Thresholds

The logistic regressions showed high significance in the estimation of the regression coefficient, β (Wald Test, $P<0.001$). However, the Hosmer-Lemeshow statistic, which is a measure of lack of fit between the observed results and the predicted results from the model (with the desired outcome non-significance), consistently showed no evidence of lack of fit for all mechanical parameters, except maximum principal stress ($P>0.05$).

The goal of the finite element analysis was to develop 2 threshold values: an optimal threshold, where the sum of sensitivity and specificity is maximized, and a conservative threshold, where all elements predicted to be injured are injured) for vascular injury of the rat spinal cord (gray and white matter were looked at together), as well as separate thresholds for the gray and white matter. To be considered useful as a predictor of injury, mechanical parameters should be invariant across loading conditions. This was not the case for the thresholds established for gray/white matter thresholds. ANOVA analysis of all the percentile values, as well as the optimal and conservative thresholds, grouped according to drop height, revealed that none of the mechanical parameters were statistically invariant across the two loading conditions ($P<0.02$). Optimal threshold values for maximum principal strain (LEP) were the least invariant (Figure 5-12), followed by compressive principal strain (LECompress) and von Mises strain (LEVM). Maximum principal stress (SP), compressive principal stress (SPCompress), von Mises stress (VM), pressure (P), and strain energy (SEnergy) were the most invariant across the loading conditions. Thresholds for gray and white matter separately revealed that LEP was statistically invariant across both loading conditions in the gray matter for all 3 species (hydrazide, albumin, and RBC) for the optimal threshold ($P>0.5$), while LEVM was statistically invariant across loading conditions in the

white matter for albumin and RBCs ($P>0.05$) (Figure 5-13). The LEVM threshold for hydrazide in the white matter statistically varied ($P<0.001$). All conservative thresholds for the spinal cord, the gray matter, and the white matter statistically varied across the 2 drop heights ($P<0.03$). A summary of the threshold analysis is presented in appendix 5-A.

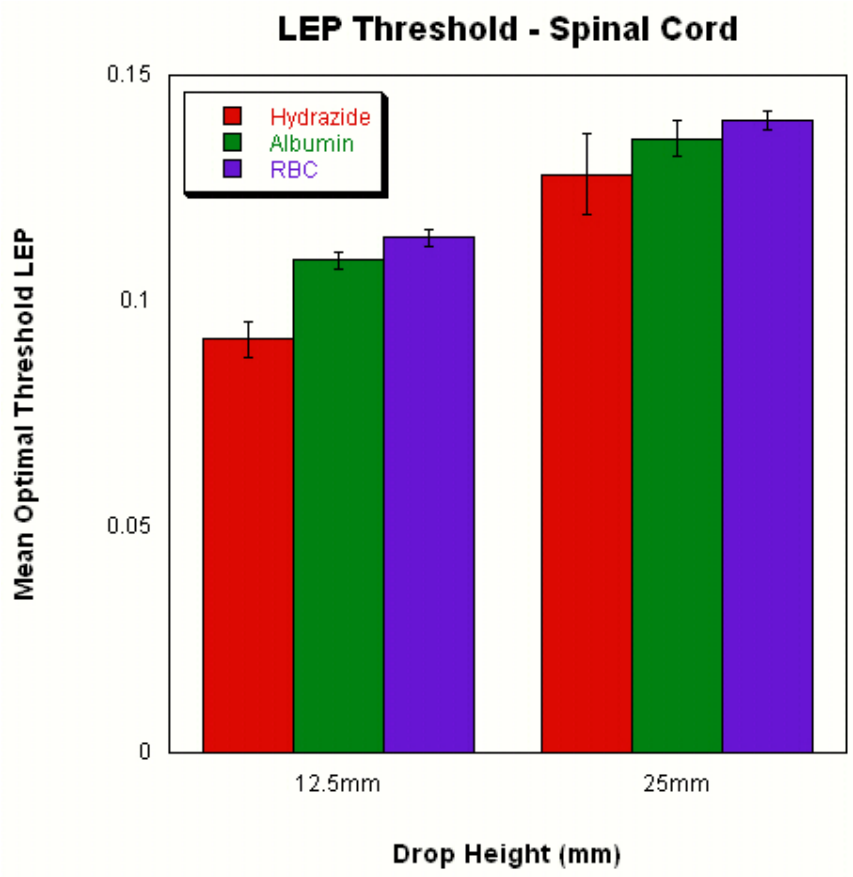

Figure 5-12: All mechanical parameters investigated for the thresholds in the spinal cord varied significantly across drop heights. Maximum principal strain was the least invariant threshold across the loading the conditions for the spinal cord. Error bars are std. error.

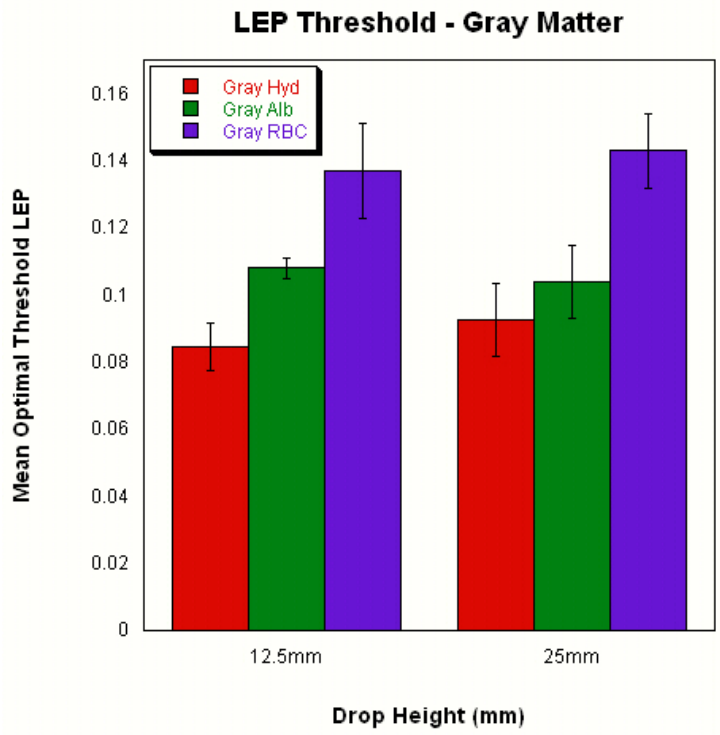

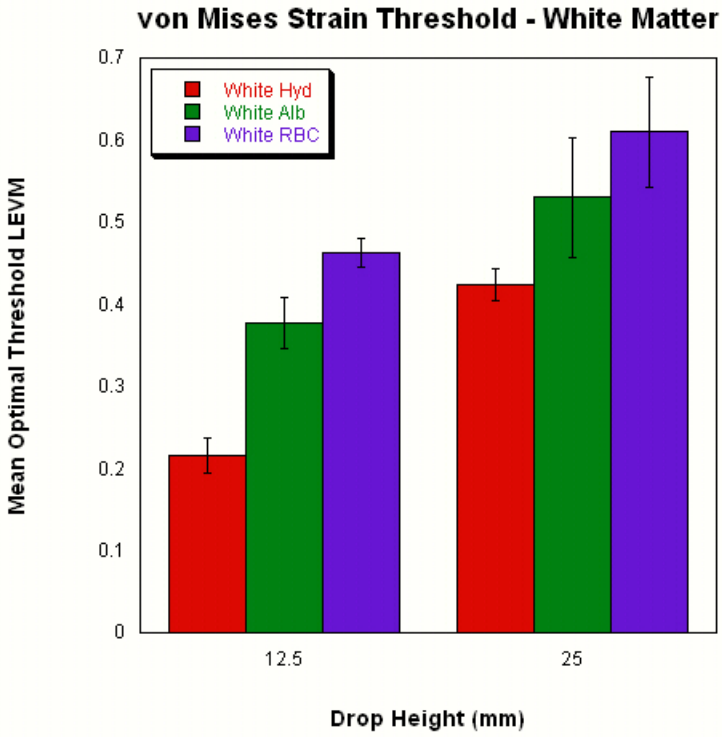

Figure 5-13: Results of the statistical analysis for the optimal thresholds according to drop height. Optimal threshold values for LEP were invariant across loading conditions for the gray matter, while threshold values for von Mises strain were invariant across loading conditions for the white matter. Error bars are std. error.

Representative plots of a logistic regression, ROC curve, and sensitivity+specificity vs. probability plots for the gray and white matter hydrazide, albumin, and RBC for a 12.5mm drop are shown in figure 5-14 and 5-15.

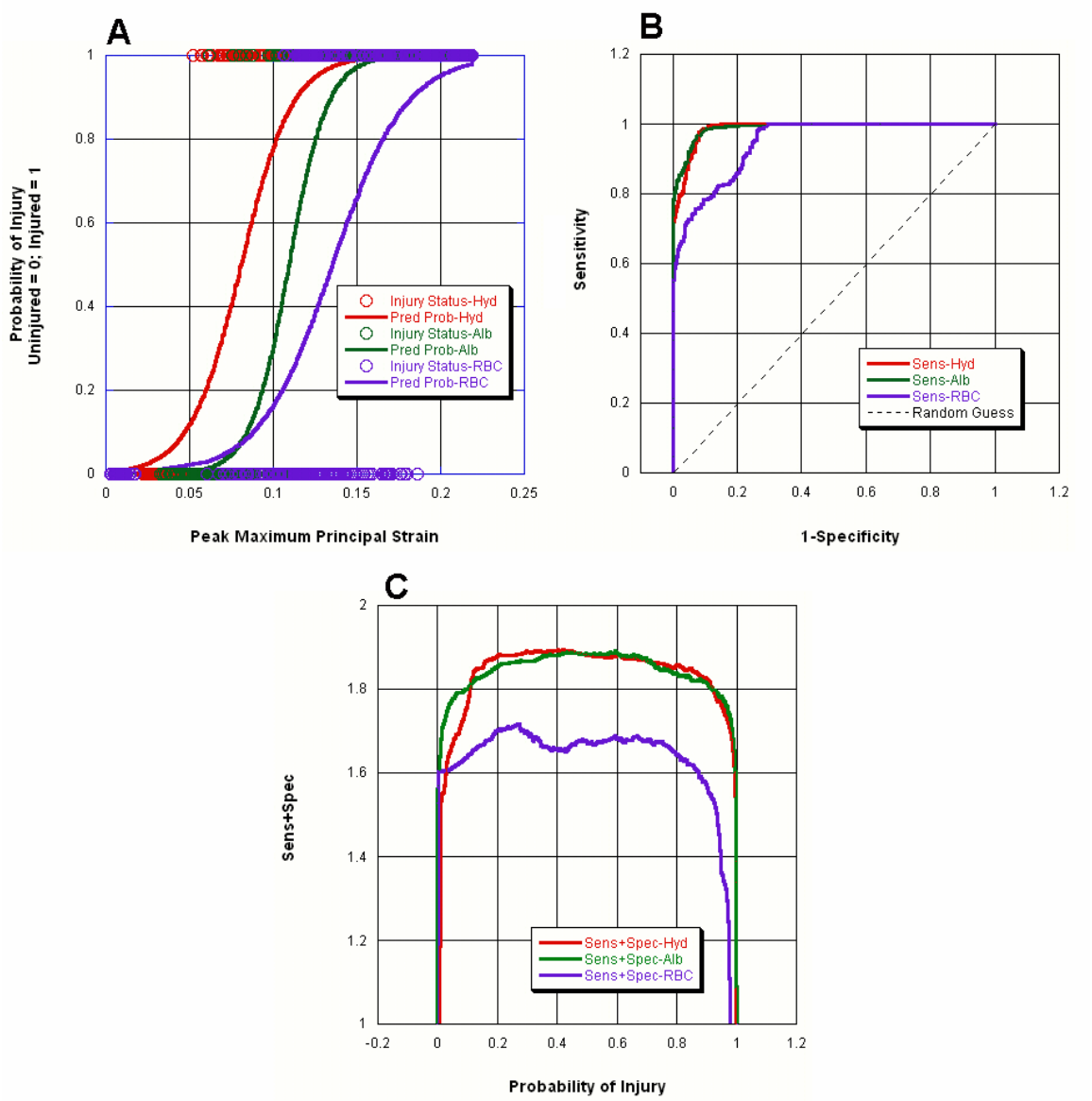

Figure 5-14: The LEP optimal threshold values (average +/- standard error) for the gray matter were 0.089 +/- 0.006 for hydrazide (red), 0.106 +/- 0.005 for albumin (green), and 0.140 +/- 0.008 for RBCs (purple). Post hoc testing (Scheffe's test) showed no significant differences between the thresholds for hydrazide and albumin ($P>0.5$), but the RBC threshold was significantly different than hydrazide and albumin threshold ($P<0.03$).

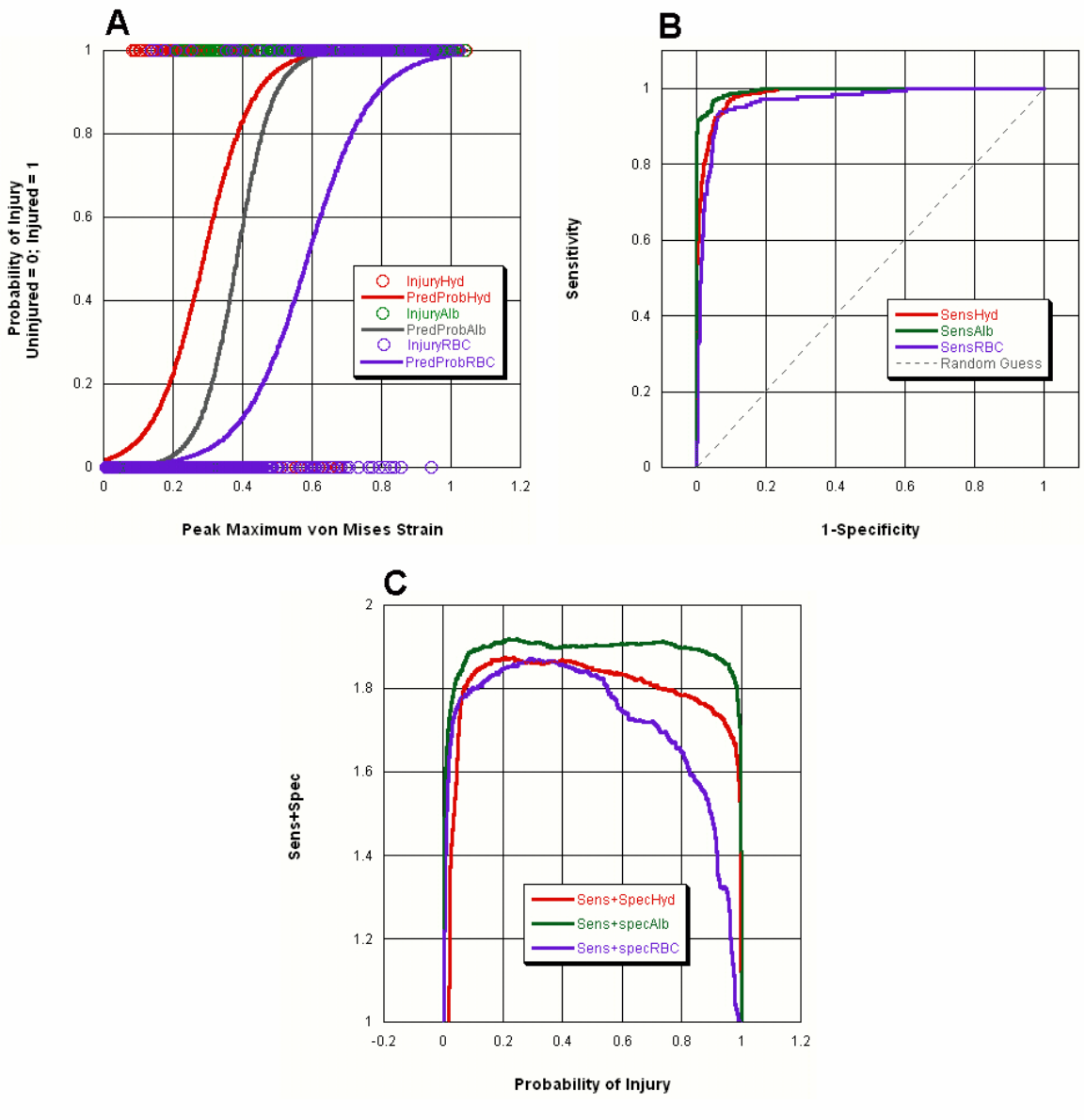

Figure 5-15: The LEVM optimal thresholds for the white matter (average +/- standard error) were 0.320 +/- 0.030 for hydrazide, 0.454 +/- 0.043 for albumin, and 0.536+/- 0.039 for RBC. Post hoc testing (Scheffe's test) showed significant differences between the threshold for hydrazide and the thresholds for albumin and RBC, but for there were no significant difference between the albumin threshold and the RBC threshold.

Parametric Analysis

A preliminary parametric analysis was performed on one 12.5mm weight drop experiment to determine the effect of changing the long-term shear modulus of the gray and white matter simultaneously, as well as independently. The gray matter LEP optimal thresholds for each species (hydrazide, albumin, and RBC) were most influenced by increasing the gray and white matter shear moduli together, while changing the white matter shear modulus had little effect on the thresholds (Figure 5-16). The white matter LEVM optimal threshold was most influenced by altering the gray and white matter shear modulus together, as well as modifying the white matter independently (Figure 5-17). Altering the gray matter shear modulus raised the threshold values, but had the least influence on the thresholds. A full parametric analysis on the gray and white matter thresholds is necessary for a full analysis of the model assumptions.

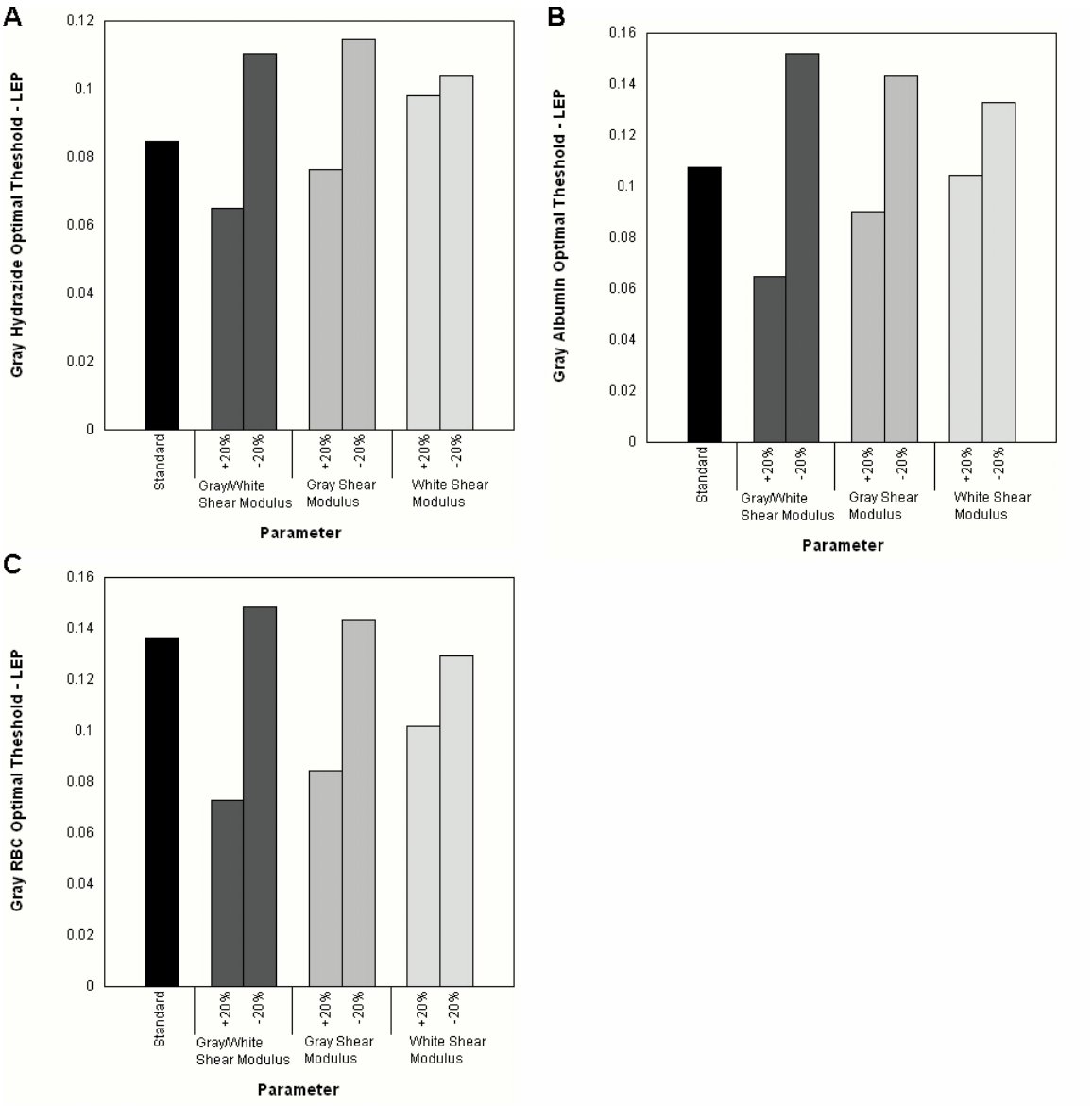

Figure 5-16: Preliminary parametric analysis of altering the long-term shear modulus of the gray and white matter revealed that the gray matter optimal LEP thresholds were most influenced by altering the gray and white matter shear modulus simultaneously. For all 3 species, changing the white matter shear modulus had the least effect on the thresholds, while alterations to the gray matter shear modulus resulted in a moderate change in the LEP threshold.

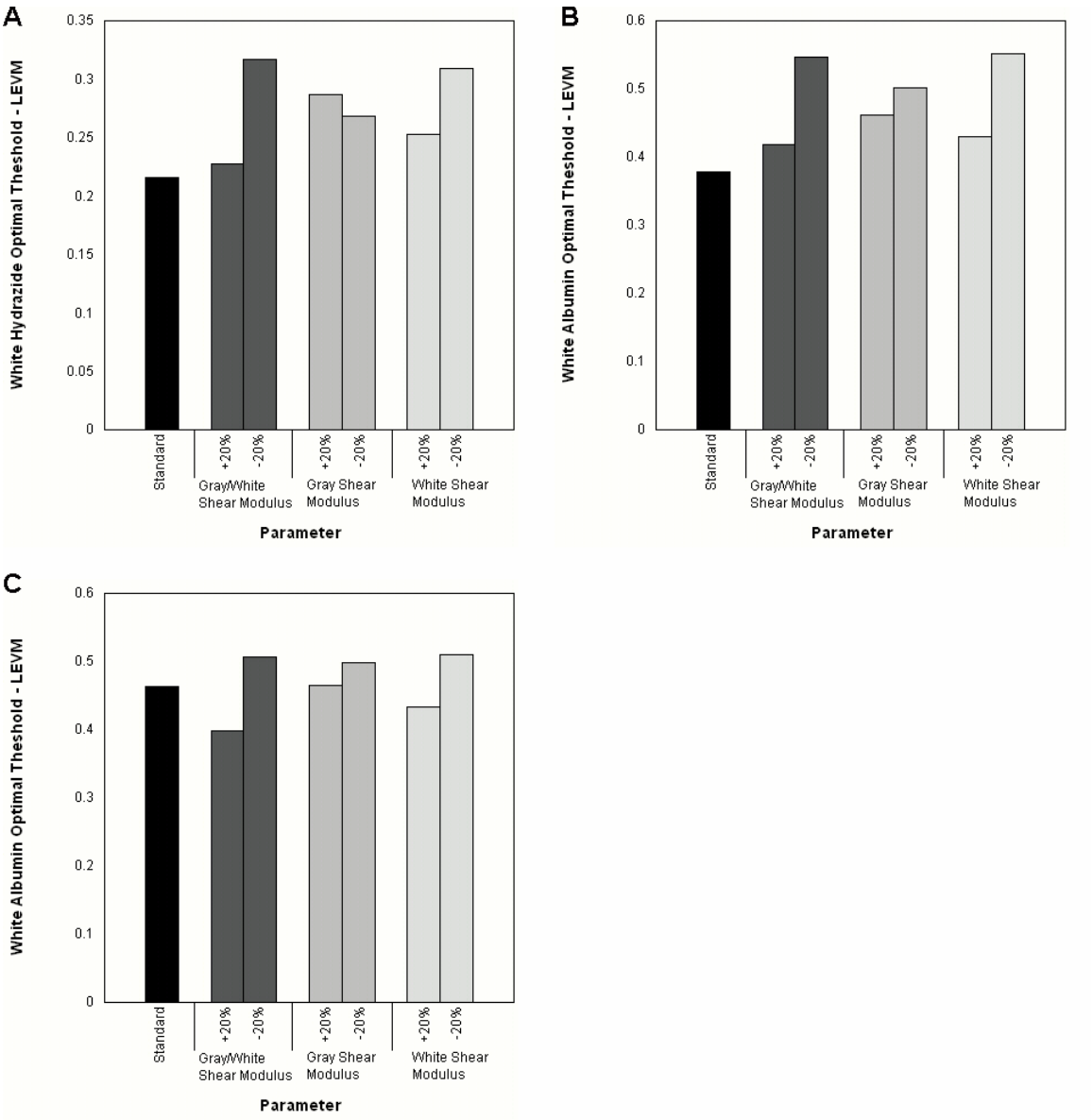

Figure 5-17: Parametric analysis of altering the long-term shear modulus of the gray and white matter revealed that the white matter LEVM optimal thresholds were most influenced by altering the gray and white matter shear modulus simultaneously. For all 3 species, changing the gray matter shear modulus had the least effect on the thresholds, while alterations to the gray matter shear modulus resulted in a moderate change in the LEP threshold.

Off-Center Impact:

A simulation was performed in which the impactor was moved 0.35mm off center. Based on the predicted thresholds of injury, we were able to determine where injury would occur in the gray and white matter. While peak nodal displacement was less than 1% different than the standard model and peak values of LEP and LEVM were 1% higher, the pattern of peak LEP and LEVM were shifted toward the off-centered impact site. A dorsal slice of LEP in the gray matter shows that the regions of elevated LEP are shifted laterally compared with the standard model. Also, the elements which exceed the predicted threshold values of LEP are shifted towards the contusion.

Displacement-Controlled Simulation:

Displacement controlled devices have unique external loading features. The impactor is prescribed a specific displacement at a specific rate. The differences in loading conditions can cause significantly different injury outcome measures following trauma induced to the same compression depth compared with weight drop. However, as shown in Figure 5-19, the internal tissue-level strain generated and the reported patterns of injury produced (Popovich, Horner et al. 1996) are similar to the weight drop model. Thus, the thresholds for injury developed in this investigation should be valid for other contusion mechanisms. To ensure the thresholds developed for weight drop are valid for other models of BSCB injury, the methods presented for weight drop should be repeated with a different model of injury, such as a displacement-controlled device.

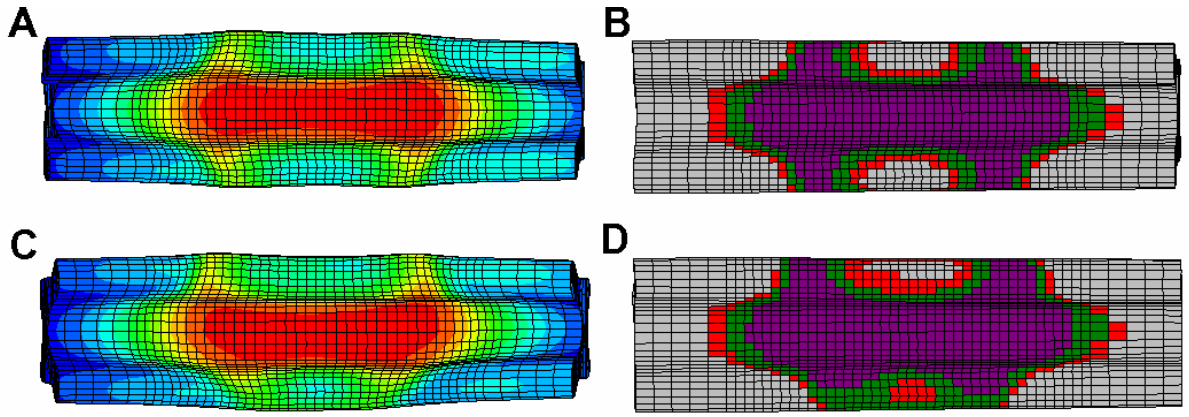

Figure 5-18: Patterns of maximum principal strain for a standard impact (A) and an off-center impact (C) with the predictions of injury for hydrazide (red), albumin (green) and hemorrhage (purple) (B,D) in a top down view of the gray matter. As can be seen from the predicted regions of injury, more injury occurs laterally in the off-centered impact, while more uniform injury occurs in the standard impact.

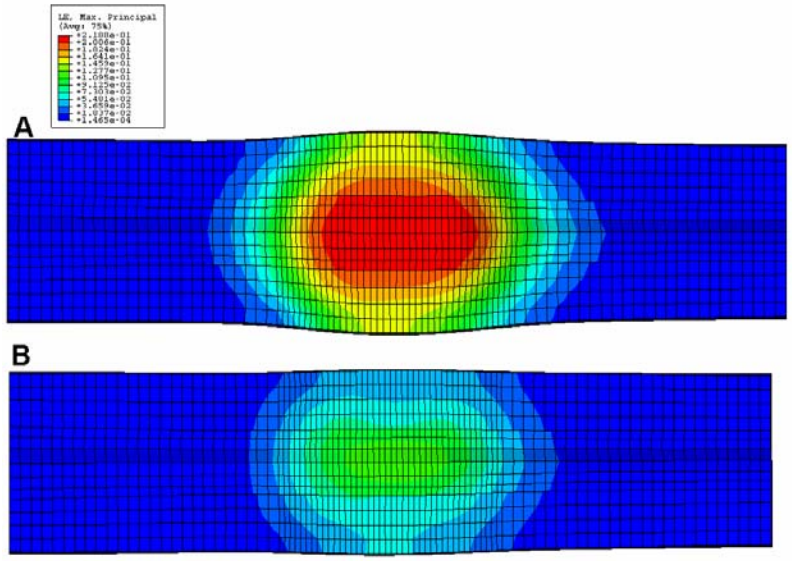

Figure 5-19: Comparison of the patterns of peak maximum principal strain for (A) the standard weight drop model and (B) the displacement controlled model. The peak values of strain were different for the models. The difference can be attributed to the rate of compression. The standard model had a rate of 0.489m/sec, while the displacement controlled model had a rate of 0.225m/sec. Despite the differences in peak strain, the patterns of strain are similar; roughly oblong in shape, radiating outward, similar to injury patterns seen during actual BSCB injury.

DISCUSSION

In the present study, we estimated tissue-level thresholds to injury of the rat blood-spinal cord barrier by simulating the Impactor weight drop model with finite element techniques. The FEM was validated by comparing the compression rate and the displacement of the mass post-"impact" to the actual parameters measured during an Impactor weight drop. Results from the experimental animal model were quantitatively compared to the output of the finite element analysis to predict thresholds to injury for different injury severities. Thirteen mechanical parameters were initially investigated, including measures of strain, strain rate, and stress and threshold values were established for these parameters at 19 evenly distributed probability levels (5%-95% in 5% increments). A conservative threshold, for which sensitivity has no false negatives, and an "optimal" threshold, where the sum of sensitivity and specificity is maximized, were also analyzed. ANOVA analysis revealed that for the optimal threshold, maximum principal strain (LEP) remained invariant across both loading conditions in the gray matter for all three species (hydrazide, albumin, and RBCs) investigated, while von Mises strain (LEVM) remained invariant across both loading conditions in the white matter for albumin and RBCs. The LEVM optimal threshold value for hydrazide in the white matter was statistically different for both loading conditions. Therefore, LEP was considered the best predictor of injury in the gray matter, while LEVM was a viable predictor of more severe injuries in the white matter, although the LEVM thresholds for white matter included relatively substantial error compared to the LEP thresholds for gray matter. Anisotropy in the white matter due to the large population of bundled axons may be a possible source of variation for the white matter thresholds. A preliminary parametric analysis was performed to assess the values of the thresholds for

changes in the shear modulus of the gray and white matter simultaneously, as well as independently. The parametric analysis revealed that changes in the gray/white shear moduli most influenced the optimal or the conservative thresholds, while changes in the both the gray and white matter together, as well as the gray matter independently resulted in small fluctuations in the thresholds.

To the best of our knowledge, this FEM represents the first computational model of SCI in the rat that has identified threshold values that predict microvascular injury following SCI. Previously, biomechanical studies of SCI have mostly focused on closed spinal cord injuries, such as fractures, extension-distractions, hyperextension, and buckling of the spine (Sances, Myklebust et al. 1984; Nightingale, McElhaney et al. 1996; Winkelstein and Myers 1997; Yoganandan, Kumaresan et al. 1997; Yoganandan, Kumaresan et al. 2001; Cusick and Yoganandan 2002). A natural outcome of injury to the spine is injury to the spinal cord, resulting in the subsequent manifestations of SCI. However, it remained unknown how the mechanical states of stress and strain were distributed in the spinal cord and which mechanical parameter best predicted spinal cord injury.

Early FE models of CNS tissue mainly focused on the brain tissue, simulating the effects of rotational loading of the head and brain (Ruan, Khalil et al. 1991; Ruan, Khalil et al. 1994; Bandak 1995; Ueno, Melvin et al. 1995), while more recently, studies have investigated real-world impacts (Willinger, Kang et al. 1999; Franklyn, Fildes et al. 2005; Viano, Casson et al. 2005). Biomechanical analyses of animate models of brain injury, which allow a direct comparison of the tissue level states of stress and strain to injury patterns and outcomes, are becoming more common (Ueno, Melvin et al. 1995; Shreiber 1997). Shreiber et. al published a validated FE model of cortical contusion of the rat brain, in which an FEM

simulated an experimental model of dynamic cortical deformation. In that model, maximum principal strain was shown to be the best predictor of BBB (Shreiber 1997). Ueno et al. developed a brain injury model that simulated cortical impact in the ferret and investigated previously reported results (Ueno, Melvin et al. 1995) and determined that shear stress and von Mises stress correlated well to cerebrovascular hemorrhage. Despite the prevalence of the rat and mouse model in studying the neuropathophysiology and functional consequences of SCI and TBI, only recently have researchers used FEA as a viable tool to correlate injury mechanics in animal models to the information gathered from in vivo models (Shreiber 1997), but there have been no previous published FE simulations of in vivo models of SCI.

In this investigation, logistic regression analysis was used to determine the number of true positives (TP), true negatives (TN), false positives (FP), and false negatives (FN) by comparing the actual injury status to the predicted status based on the mechanical measure at each probability (Bain and Meaney 2000). Receiver operating characteristic (ROC) curves and plots of sensitivity+specificity vs. probability were used to ideally establish two thresholds values (a conservative and optimal threshold) for each fluorescent marker used in the experimental study. Each separate threshold can be applied differently for the study of SCI. For example, the conservative threshold may be more appropriate in the development of prevention strategies for SCI, where the overestimation of injury may be necessary, even though the optimal threshold may be a more accurate estimation of injury in practice. However, statistical analysis revealed that conservative thresholds for each mechanical parameter significantly varied according to drop height. Therefore, conservative thresholds could not be established for vascular injury in the gray and white matter. Furthermore, while LEP was statistically invariant across both loading conditions in the gray matter for the

optimal threshold, no mechanical parameters were good predictors of for extravasation of hydrazide in the white matter. Only LEVM was invariant across both loading conditions for albumin and RBC. In theory, the optimum threshold reveals the probability value where the (sensitivity + specificity) value is a maximum. However, plots of sensitivity + specificity vs. probability for LEP and LEVM showed a large range of percentile values that closely approximated the maximum value, which, depending on the slope of the linear regression, could result in a large range of optimal threshold values.

The fidelity of the model and ultimately the predictive power of the analysis can be greatly improved with incremental improvements to the model, especially regarding the material definitions of the gray and white matter. Fiford and Bilston have recently published the properties of rat spinal cord in uniaxial tension at very slow ($0.001s^{-1}$) to moderate ($\sim 0.1s^{-1}$) strain rates. To our knowledge, these are the only published properties of rat spinal cord tissue, and this data was therefore used as the starting point for identifying model constants. However, it has been shown that rat brain tissue in compression and shear is significantly more compliant than from the reported values for the rat spinal cord. Thus, the properties of the spinal cord were adjusted to achieve the temporal profile of Impactor displacement that best matched those from parallel weight drop experiments (Maikos and Shreiber 2007). Furthermore, it is known that the properties of the gray matter and white matter are different, but those properties have not been elucidated for the rat spinal cord. In traumatic loading, such as those seen during Impactor experiments, large deformation occurs at an extremely fast strain rate. However, no data exists for rat CNS tissue at these rates, and as such, the Prony series viscoelastic constants from a study of human brain tissue in compression at high strain and strain rate were employed (Mendis, Stalnaker et al. 1995). As can be seen in our

spatial maps of BSCB injury, extravasation of our fluorescent probes extended further rostrally and caudally in the highly vascular gray matter, which indicates that microvasculature in the gray matter is more sensitive to compressive loads than in the white matter. However, due to the lack of material properties for the rat gray and white matter, our FEM of the rat spinal cord included homogeneous and isotropic properties for the gray and white matter, which may explain the lack of mechanical correlation for white matter vascular injury. Therefore, it is necessary to further investigate the mechanical properties of the rat spinal cord, especially at rates corresponding to traumatic loading conditions. These properties are critical in order to understand the mechanical response of the spinal cord tissue to mechanical loads, which will help improve the predictive power of the FEM. The success of the FEM hinges on the accurate determination of the individual load-bearing entities of the rat spinal cord, including the gray matter, white matter, and dura mater. It is clear that an in vivo mechanical description of the rat spinal cord structures would provide the most accurate properties for use in an FEM.

The performance of the FEM also depends upon the assumptions of the spinal cord geometry. While the cerebrospinal fluid was included in the model, it was modeled as a solid with a low shear and high bulk modulus to introduce fluid-like behavior, which has been done in other FEMs (King, Ruan et al. 1995). The CSF was assigned a shear modulus ~240x less than the spinal cord. A more accurate representation would include the CSF as a reservoir of pressurized fluid that can flow during compression. While inclusion of the CSF added a degree of compressibility, modeling the CSF as a fluid would greatly enhance the fidelity of the model. Furthermore, it is important to note that although the dura was modeled as a solid (1 element thick) with an approximate thickness of 50-80μm (similar to in vivo

measurements), using membrane elements would more accurately represent the true nature of the dura. Membrane elements have an intrinsic thinness that more accurately portrays thin outer membranes. However, it was determined from our preliminary FEMs that modeling the dura with membrane elements resulted in complicated contact interactions between dura and the CSF, which introduced errors due to overclosures.

Analysis of the optimal thresholds developed in this investigation indicated that there were no significant differences between the amount of strain necessary in the gray matter to cause an influx of species as small as the hydrazide (~730Da) (~8.9% strain) and as large as bovine serum albumin (~70KDa) (10.6%strain). The optimal LEP threshold in the gray matter for RBCs (~5μm) (~14% strain) was significantly larger for hemorrhage than both albumin and hydrazide, which confirms that it takes a more severe injury to cause extravasation of RBCs in the spinal cord. In the white matter, the mean von Mises strain necessary for hydrazide influx (32.00%) was significantly different than both the albumin (45.4%) and the RBC (53.6%) values. The albumin and RBC thresholds were not significantly different.

Strain has been shown to be the best predictor of BBB injury in the rat (Shreiber 1997) and axonal injury in the guinea pig (Bain and Meaney 2000). It was reported that the BBB can withstand strains up to 17% prior to injury sufficient enough to permit indiscriminate extravasation of species that are ~70kDa (the size of albumin) or smaller. In this investigation, we predicted that strains greater ~11% resulted in the same injury. However, differences can be attributed to the variation of material properties used for brain and spinal cord. Furthermore, the BBB study did not include some key geometrical features, such as the gray/white matter anatomy and junction, the dura mater, CSF, or ventricular

spaces, which would alter the deformation profile, as well as the values of strain in the brain tissue. Moreover, the dura, in many species including human, bovine, and canine, is significantly stiffer than the CNS tissue it surrounds, which points to its protective role (van Noort, Black et al. 1981; van Noort, Martin et al. 1981; Zarzur 1996; Runza, Pietrabissa et al. 1999). The dura, therefore, can contribute significantly to the overall mechanical response of the brain and/or spinal cord to traumatic loading and may absorb a large percentage of the kinetic energy.

A preliminary parametric study showed that the thresholds to BSCB injury were sensitive to changes in the gray and white matter shear moduli. In all cases, changing the shear moduli of the gray and white matter simultaneously had the largest effect on the thresholds. In the gray matter, the LEP threshold values ranged from 6.5% to 11.4% for the hydrazide, 6.5-15.2% for albumin, and 7.3-14.8% for RBC, which was still a relatively small range. The LEVM thresholds for white matter ranged from 22.8%-31.7% for the hydrazide, 41.9-55.1% for albumin, and 39.9-51.0% for RBC. However, a full parametric analysis is warranted to asses the variability of the threshold values on the model assumptions. Of particular importance would be to evaluate the influence of changing the material law separately for the gray and white and the effect on invariance of the thresholds across the loading conditions.

In addition to improvements to the geometry and material law used in the model, the methods presented in this study should be used in other models of SCI, including pneumatic impactors, compression models, and contusion models that use an “impact button” to show that the thresholds developed for weight drop are valid for other loading conditions. We have performed preliminary investigations in which we modified our weight drop FEM to simulate

an electropneumatic impactor, which is a displacement controlled device. Displacement controlled devices, as well as other spinal cord contusion devices, each have unique external loading features that can produce significantly different injury outcome measures following trauma induced to the same compression depth. These differences can be attributed to the subtle differences in loading conditions. However, the relationship between the internal tissue-level stress and strain generated with the different SCI models and the patterns of injury they produce will be the same. Previous reports of BSCB injury patterns produced with pneumatic impactors have similar morphology to patterns of BSCB injury induced by weight drop injuries (Popovich, Horner et al. 1996). Our preliminary analysis of a displacement-controlled impactor, in which the severity of the injury is determined by the magnitude and rate of the displacement, showed that the patterns of stress and strain are the same as in the weight drop. Thus, the thresholds for injury should be the same. Therefore, an analysis of other contusion models, or any model that produces damage to the vasculature of the spinal cord, would ensure the thresholds established with weight drop are valid for any model of BSCB injury.

Off-center contusions can significantly affect injury outcome measures, such as measures of the volume of cell death, open field locomotor test scores (e.g. Basso, Beattie, Bresnahan Score – BBB), and white matter sparing. Off-center spinal cord injuries are clinically relevant, as contusions of the spinal column and vertebrae that result in SCI can affect different regions of the spinal cord. The thresholds established in this investigation can help predict the changes in these outcome measures that result from off-center impacts. We simulated an off-center weight drop, in which the impactor was shifted laterally by 0.35mm. While the peak displacement of the cord and peak values of strain did not vary from

the standard model, the patterns of strain shifted laterally toward the contusion. Furthermore, the elements that experienced strain above the threshold followed the strain patterns. An off-center impact could potentially affect different regions of the cord, (i.e. affecting more regions of white matter), which have a different tolerances for injury. This could potentially alter measures of BBB, as well as white matter sparing, and volume of cell death. However, accurate thresholds established in this investigation for injury to the gray and white matter could help predict regions of the spinal cord more susceptible to vascular injury.

The thresholds found in this investigation are based on the rat spinal cord, but can be used to approximate the thresholds in humans. While the thresholds presented here can be more accurately predicted with improvements to the computational model, this model is an important first step in identifying the mechanical parameter (and a specific value of that mechanical parameter) that best predicts BSCB injury. While LEP was found to be the best predictor of injury in the gray matter and LEVM was a viable option as a predictor for more severe injuries in the white matter, other mechanical parameters that were not investigated may result in better predictions. For example, axial stress or strain may be appropriate parameters to investigate since the vasculature in the spinal cord is most likely aligned in the axial direction. Moreover, in studying neurophysiology, rats are commonly used as surrogates for humans. It is a fundamental assumption that for the spinal cord itself, the interspecies variability of the tissue is minimal (Metz, Curt et al. 2000). Unlike load bearing tissues, such as muscles or ligaments, the spinal cord does not bear significant dynamic loads. While there are subtle differences between human and rat spinal cords, such as the tissue volume, it can be assumed that there is a correlation between the rat and human spinal cord. The thresholds found for the rat spinal cord using the Impactor weight drop technique can

estimate the tolerance of human spinal cord tissue. Furthermore, our results can be combined with models of spine trauma to show how different types of injury mechanisms will result in specific kinds of spinal cord injury. Understanding tissue-level thresholds allows for prediction of injury patterns in other models, design new models to produce specific injury patterns, and define in vitro conditions appropriate for studying trauma. Ultimately, this can be an invaluable tool in preventing SCI in humans.

Understanding the sensitivity of the BSCB to mechanical damage can be aid in targeted drug to the spinal cord. Possible therapies include peptide growth factors, antibodies, and/or proteins which are generally larger than molecules that pass non-specifically through the barrier (<500Da). Following trauma, different regions of the BSCB will be comprised to different severities and extents. Thus, therapies delivered to the spinal cord via the bloodstream may be able to cross into the spinal cord parenchyma at regions with severe injury, but other areas, distal and proximal to the contusion, may not receive sufficient doses of the therapy (Sharma 2005). Furthermore, statins have been shown to reduce inflammation in the spinal cord following injury (Stanislaus, Singh et al. 2001; Pannu, Barbosa et al. 2005). It has also been reported that different statins maintain different abilities to cross the BSCB according to their lipophilicity. In some cases, indiscriminant crossing of statins into brain and spinal cord parenchyma causes significant CNS side effects (Guillot, Misslin et al. 1993; Sparks, Connor et al. 2002). Thus, understanding the size-specific severity of trauma to the BSCB can be critical in designing appropriate courses of therapies.

REFERENCES

ALBIN, M. S., WHITE, R. J., ACOSTA-RUA, G. and YASHON, D. (1968). "Study of functional recovery produced by delayed localized cooling after spinal cord injury in primates." J Neurosurg **29**(2): 113-20.

AMAR, A. P. and LEVY, M. L. (1999). "Pathogenesis and pharmacological strategies for mitigating secondary damage in acute spinal cord injury." Neurosurgery **44**(5): 1027-39; discussion 1039-40.

BAIN, A. C. and MEANEY, D. F. (2000). "Tissue-level thresholds for axonal damage in an experimental model of central nervous system white matter injury." J Biomech Eng **122**(6): 615-22.

BANDAK, F. A. (1995). "On the mechanics of impact neurotrauma: a review and critical synthesis." J Neurotrauma **12**(4): 635-49.

BASSO, D. M., BEATTIE, M. S. and BRESNAHAN, J. C. (1996). "Graded histological and locomotor outcomes after spinal cord contusion using the NYU weight-drop device versus transection." Exp Neurol **139**(2): 244-56.

BEGGS, J. L. and WAGGENER, J. D. (1976). "Transendothelial vesicular transport of protein following compression injury to the spinal cord." Lab Invest **34**(4): 428-39.

BERKOWITZ, E. D. (1998). "Revealing America's welfare state. [Review of: Howard, C., The hidden welfare state: tax expenditures and social policy in the United States. Princeton University Press, 1997]." Rev Am Hist **26**(3): 620-4.

BILGEN, M., AL-HAFEZ, B., T, M. M. and I, V. S. (2005). "Ex vivo magnetic resonance imaging of rat spinal cord at 9.4 T." Magn Reson Imaging **23**(4): 601-5.

BILSTON, L. E. and THIBAULT, L. E. (1996). "The mechanical properties of the human cervical spinal cord in vitro." Ann Biomed Eng **24**(1): 67-74.

BLIGHT, A. R. (1985). "Delayed demyelination and macrophage invasion: a candidate for secondary cell damage in spinal cord injury." Cent Nerv Syst Trauma **2**(4): 299-315.

BLIGHT, A. R. (1991). "Morphometric analysis of a model of spinal cord injury in guinea pigs, with behavioral evidence of delayed secondary pathology." J Neurol Sci **103**(2): 156-71.

BLIGHT, A. R. (1992). "Macrophages and inflammatory damage in spinal cord injury." J Neurotrauma **9 Suppl 1**: S83-91.

CUSICK, J. F. and YOGANANDAN, N. (2002). "Biomechanics of the cervical spine 4: major injuries." Clin Biomech (Bristol, Avon) **17**(1): 1-20.

DOHRMANN, G. J., PANJABI, M. M. and WAGNER, F. C., JR. (1976). "An apparatus for quantitating experimental spinal cord trauma." Surg Neurol **5**(5): 315-8.

DOHRMANN, G. J. and WICK, K. M. (1971). "Demonstration of the microvasculature of the spinal cord by intravenous injection of the fluorescent dye, thioflavine S." Stain Technol **46**(6): 321-2.

FADEN, A. I., GANNON, A. and BASBAUM, A. I. (1988). "Use of serotonin immunocytochemistry as a marker of injury severity after experimental spinal trauma in rats." Brain Res **450**(1-2): 94-100.

FIFORD, R. J. and BILSTON, L. E. (2005). "The mechanical properties of rat spinal cord in vitro." J Biomech **38**(7): 1509-15.

FRANKLYN, M., FILDES, B., ZHANG, L., YANG, K. and SPARKE, L. (2005). "Analysis of finite element models for head injury investigation: reconstruction of four real-world impacts." Stapp Car Crash J **49**: 1-32.

GRIFFITHS, I. R. and MILLER, R. (1974). "Vascular permeability to protein and vasogenic oedema in experimental concussive injuries to the canine spinal cord." J Neurol Sci **22**(3): 291-304.

GRUNER, J. A. (1992). "A monitored contusion model of spinal cord injury in the rat." J Neurotrauma **9**(2): 123-6; discussion 126-8.

GUILLOT, F., MISSLIN, P. and LEMAIRE, M. (1993). "Comparison of fluvastatin and lovastatin blood-brain barrier transfer using in vitro and in vivo methods." J Cardiovasc Pharmacol **21**(2): 339-46.

HUNG, T. K., ALBIN, M. S., BROWN, T. D., BUNEGIN, L., ALBIN, R. and JANNETTA, P. J. (1975). "Biomechanical responses to open experimental spinal cord injury." Surg Neurol **4**(2): 271-6.

KING, A. I., RUAN, J. S., ZHOU, C., HARDY, W. N. and KHALIL, T. B. (1995). "Recent advances in biomechanics of brain injury research: a review." J Neurotrauma **12**(4): 651-8.

KOENIG, G. and DOHRMANN, G. J. (1977). "Histopathological variability in 'standardised' spinal cord trauma." J Neurol Neurosurg Psychiatry **40**(12): 1203-10.

MAIKOS, J. T. and SHREIBER, D. I. (2007). "Immediate damage to the blood-spinal cord barrier due to mechanical trauma." J Neurotrauma **24**(3): 492-507.

MAUTES, A. E., WEINZIERL, M. R., DONOVAN, F. and NOBLE, L. J. (2000). "Vascular events after spinal cord injury: contribution to secondary pathogenesis." Phys Ther **80**(7): 673-87.

MENDIS, K. K., STALNAKER, R. L. and ADVANI, S. H. (1995). "A constitutive relationship for large deformation finite element modeling of brain tissue." J Biomech Eng **117**(3): 279-85.

METZ, G. A., CURT, A., VAN DE MEENT, H., KLUSMAN, I., SCHWAB, M. E. and DIETZ, V. (2000). "Validation of the weight-drop contusion model in rats: a comparative study of human spinal cord injury." J Neurotrauma **17**(1): 1-17.

MILLER, K. and CHINZEI, K. (2002). "Mechanical properties of brain tissue in tension." J Biomech **35**(4): 483-90.

NIGHTINGALE, R. W., MCELHANEY, J. H., RICHARDSON, W. J. and MYERS, B. S. (1996). "Dynamic responses of the head and cervical spine to axial impact loading." J Biomech **29**(3): 307-18.

NOBLE, L. J., MAUTES, A. E. and HALL, J. J. (1996). "Characterization of the microvascular glycocalyx in normal and injured spinal cord in the rat." J Comp Neurol **376**(4): 542-56.

NOBLE, L. J. and WRATHALL, J. R. (1989). "Correlative analyses of lesion development and functional status after graded spinal cord contusive injuries in the rat." Exp Neurol **103**(1): 34-40.

NOBLE, L. J. and WRATHALL, J. R. (1989). "Distribution and time course of protein extravasation in the rat spinal cord after contusive injury." Brain Res **482**(1): 57-66.

PANNU, R., BARBOSA, E., SINGH, A. K. and SINGH, I. (2005). "Attenuation of acute inflammatory response by atorvastatin after spinal cord injury in rats." J Neurosci Res **79**(3): 340-50.

POPOVICH, P. G., HORNER, P. J., MULLIN, B. B. and STOKES, B. T. (1996). "A quantitative spatial analysis of the blood-spinal cord barrier. I. Permeability changes after experimental spinal contusion injury." Exp Neurol **142**(2): 258-75.

PRANGE, M. T. and MARGULIES, S. S. (2002). "Regional, directional, and age-dependent properties of the brain undergoing large deformation." J Biomech Eng **124**(2): 244-52.

RUAN, J. S., KHALIL, T. and KING, A. I. (1991). "Human head dynamic response to side impact by finite element modeling." J Biomech Eng **113**(3): 276-83.

RUAN, J. S., KHALIL, T. and KING, A. I. (1994). "Dynamic response of the human head to impact by three-dimensional finite element analysis." J Biomech Eng **116**(1): 44-50.

RUNZA, M., PIETRABISSA, R., MANTERO, S., ALBANI, A., QUAGLINI, V. and CONTRO, R. (1999). "Lumbar dura mater biomechanics: experimental characterization and scanning electron microscopy observations." Anesth Analg **88**(6): 1317-21.

SANCES, A., JR., MYKLEBUST, J. B., MAIMAN, D. J., LARSON, S. J., CUSICK, J. F. and JODAT, R. W. (1984). "The biomechanics of spinal injuries." Crit Rev Biomed Eng **11**(1): 1-76.

SHARMA, H. S. (2005). "Pathophysiology of blood-spinal cord barrier in traumatic injury and repair." Curr Pharm Des **11**(11): 1353-89.

SHREIBER, D. I., A. C. BAIN, ET AL. (1997). "In vivo thresholds for mechanical injury to the blood-brain barrier." SAE 1997 Transactions: Journal of Passenger Cars **106(6-2):**: 3792-3806.

SPARKS, D. L., CONNOR, D. J., BROWNE, P. J., LOPEZ, J. E. and SABBAGH, M. N. (2002). "HMG-CoA reductase inhibitors (statins) in the treatment of Alzheimer's disease and why it would be ill-advise to use one that crosses the blood-brain barrier." J Nutr Health Aging **6**(5): 324-31.

STANISLAUS, R., SINGH, A. K. and SINGH, I. (2001). "Lovastatin treatment decreases mononuclear cell infiltration into the CNS of Lewis rats with experimental allergic encephalomyelitis." J Neurosci Res **66**(2): 155-62.

UENO, K., MELVIN, J. W., LI, L. and LIGHTHALL, J. W. (1995). "Development of tissue level brain injury criteria by finite element analysis." J Neurotrauma **12**(4): 695-706.

VAN NOORT, R., BLACK, M. M., MARTIN, T. R. and MEANLEY, S. (1981). "A study of the uniaxial mechanical properties of human dura mater preserved in glycerol." Biomaterials **2**(1): 41-5.

VAN NOORT, R., MARTIN, T. R., BLACK, M. M., BARKER, A. T. and MONTERO, C. G. (1981). "The mechanical properties of human dura mater and the effects of storage media." Clin Phys Physiol Meas **2**(3): 197-203.

VIANO, D. C., CASSON, I. R., PELLMAN, E. J., ZHANG, L., KING, A. I. and YANG, K. H. (2005). "Concussion in professional football: brain responses by finite element analysis: part 9." Neurosurgery **57**(5): 891-916; discussion 891-916.

WAGNER, F. C., JR. and STEWART, W. B. (1981). "Effect of trauma dose on spinal cord edema." J Neurosurg **54**(6): 802-6.

WILLINGER, R., KANG, H. S. and DIAW, B. (1999). "Three-dimensional human head finite-element model validation against two experimental impacts." Ann Biomed Eng **27**(3): 403-10.

WINKELSTEIN, B. A. and MYERS, B. S. (1997). "The biomechanics of cervical spine injury and implications for injury prevention." Med Sci Sports Exerc **29**(7 Suppl): S246-55.

YOGANANDAN, N., KUMARESAN, S. and PINTAR, F. A. (2001). "Biomechanics of the cervical spine Part 2. Cervical spine soft tissue responses and biomechanical modeling." Clin Biomech (Bristol, Avon) **16**(1): 1-27.

YOGANANDAN, N., KUMARESAN, S., VOO, L. and PINTAR, F. A. (1997). "Finite element model of the human lower cervical spine: parametric analysis of the C4-C6 unit." J Biomech Eng **119**(1): 87-92.

YOUNG, W. (2002). "Spinal cord contusion models." Prog Brain Res **137**: 231-55.

ZARZUR, E. (1996). "Mechanical properties of the human lumbar dura mater." Arq Neuropsiquiatr **54**(3): 455-60.

APPENDIX 5-A

Gray Matter LEP Threshold Analysis for 12.5mm Weight Drop						
	Hydrazide	**Std Dev**	**Albumin**	**Std Dev**	**RBC**	**Std Dev**
Optimal	0.085	0.020	0.108	0.008	0.137	0.040
Conserve	0.036	0.012	0.050	0.009	0.083	0.023
Spec=1	0.132	0.024	0.163	0.012	0.196	0.012
5%	0.029	0.012	0.049	0.019	0.059	0.023
10%	0.041	0.011	0.063	0.016	0.082	0.019
15%	0.048	0.010	0.072	0.015	0.096	0.018
20%	0.054	0.010	0.079	0.014	0.107	0.017
25%	0.059	0.010	0.085	0.013	0.116	0.016
30%	0.063	0.010	0.090	0.012	0.123	0.016
35%	0.067	0.010	0.094	0.012	0.130	0.017
40%	0.070	0.011	0.098	0.011	0.137	0.017
45%	0.073	0.011	0.102	0.011	0.143	0.018
50%	0.077	0.011	0.106	0.011	0.149	0.018
55%	0.080	0.012	0.110	0.011	0.155	0.019
60%	0.083	0.012	0.114	0.011	0.161	0.020
65%	0.087	0.013	0.118	0.011	0.168	0.021
70%	0.091	0.013	0.123	0.011	0.175	0.022
75%	0.095	0.014	0.128	0.011	0.183	0.024
80%	0.099	0.015	0.133	0.011	0.191	0.026
85%	0.105	0.016	0.140	0.012	0.186	0.023
90%	0.113	0.017	0.149	0.013	0.181	0.009
95%	0.125	0.020	0.163	0.015	0.198	0.009

Gray Matter LEP Threshold Analysis for 25mm Weight Drop						
	Hydrazide	**Std Dev**	**Albumin**	**Std Dev**	**RBC**	**Std Dev**
Optimal	0.092	0.032	0.104	0.031	0.143	0.031
Conserve	0.058	0.021	0.072	0.021	0.088	0.020
Spec=1	0.198	0.013	0.201	0.015	0.230	0.011
5%	0.039	0.027	0.055	0.023	0.065	0.022
10%	0.052	0.026	0.073	0.022	0.087	0.026
15%	0.064	0.023	0.084	0.021	0.105	0.023
20%	0.074	0.021	0.093	0.021	0.119	0.022
25%	0.081	0.020	0.100	0.021	0.130	0.021
30%	0.088	0.018	0.106	0.021	0.140	0.021
35%	0.094	0.017	0.111	0.021	0.149	0.020
40%	0.099	0.017	0.116	0.020	0.157	0.020
45%	0.105	0.016	0.121	0.020	0.165	0.020
50%	0.110	0.015	0.126	0.020	0.173	0.020
55%	0.115	0.015	0.131	0.021	0.181	0.021
60%	0.120	0.014	0.136	0.021	0.188	0.021
65%	0.126	0.014	0.141	0.021	0.197	0.022
70%	0.132	0.013	0.146	0.021	0.206	0.022
75%	0.138	0.014	0.152	0.021	0.211	0.020
80%	0.146	0.014	0.159	0.022	0.212	0.015
85%	0.155	0.015	0.168	0.022	0.224	0.015
90%	0.167	0.016	0.179	0.023	0.231	0.007
95%	0.187	0.019	0.197	0.024	0.143	0.031

White Matter LEVM Threshold Analysis for 25mm Weight Drop						
	Hydrazide	**Std Dev**	**Albumin**	**Std Dev**	**RBC**	**Std Dev**
Optimal	0.216	0.062	0.156	0.067	0.463	0.049
Conserve	0.070	0.015	0.226	0.063	0.109	0.064
Spec=1	0.493	0.096	0.270	0.062	2.149	1.687
5%	0.053	0.031	0.302	0.063	0.172	0.105
10%	0.101	0.027	0.329	0.064	0.278	0.084
15%	0.130	0.028	0.353	0.066	0.344	0.073
20%	0.153	0.030	0.374	0.067	0.393	0.067
25%	0.171	0.032	0.394	0.069	0.434	0.064
30%	0.187	0.035	0.413	0.071	0.470	0.062
35%	0.201	0.038	0.432	0.073	0.502	0.062
40%	0.215	0.041	0.451	0.075	0.533	0.063
45%	0.228	0.043	0.470	0.078	0.562	0.065
50%	0.241	0.046	0.490	0.081	0.590	0.067
55%	0.254	0.049	0.511	0.084	0.619	0.071
60%	0.267	0.053	0.535	0.087	0.648	0.075
65%	0.280	0.056	0.561	0.092	0.678	0.080
70%	0.295	0.060	0.594	0.097	0.711	0.086
75%	0.311	0.064	0.637	0.105	0.746	0.093
80%	0.329	0.068	0.707	0.118	0.787	0.101
85%	0.351	0.074	0.156	0.067	0.837	0.112
90%	0.381	0.082	0.226	0.063	0.871	0.096
95%	0.429	0.095	0.270	0.062	0.884	0.050

White Matter LEVM Threshold Analysis for 25mm Weight Drop						
	Hydrazide	**Std Dev**	**Albumin**	**Std Dev**	**RBC**	**Std Dev**
Optimal	0.424	0.053	0.530	0.203	2.909	2.599
Conserve	0.128	0.036	0.235	0.119	0.335	0.236
Spec=1	1.078	0.053	1.730	1.320	0.422	0.214
5%	0.123	0.109	0.265	0.232	0.503	0.192
10%	0.138	0.098	0.337	0.214	0.564	0.175
15%	0.190	0.096	0.401	0.202	0.615	0.162
20%	0.243	0.090	0.450	0.194	0.659	0.150
25%	0.286	0.085	0.490	0.188	0.698	0.140
30%	0.324	0.081	0.525	0.183	0.736	0.131
35%	0.359	0.078	0.557	0.179	0.772	0.122
40%	0.391	0.075	0.587	0.175	0.807	0.113
45%	0.422	0.072	0.615	0.172	0.842	0.105
50%	0.453	0.069	0.643	0.169	0.878	0.097
55%	0.483	0.067	0.671	0.167	0.915	0.089
60%	0.514	0.065	0.700	0.165	0.955	0.081
65%	0.547	0.063	0.730	0.163	0.999	0.074
70%	0.581	0.062	0.762	0.161	1.050	0.068
75%	0.619	0.061	0.797	0.160	1.111	0.063
80%	0.663	0.060	0.837	0.160	1.192	0.065
85%	0.716	0.060	0.886	0.161	1.274	0.051
90%	0.786	0.062	0.950	0.163	2.909	2.599
95%	0.900	0.068	1.013	0.134	0.335	0.236

CHAPTER 6: DISCUSSION AND FUTURE WORK

In this thesis, we have presented in vivo tissue-level thresholds for blood-spinal cord barrier (BSCB) injury in the rat following contusion. A parallel experimental and computational approach was utilized to compare primary spatial maps of BSCB injury to the results of our validated finite element model (FEM) to determine an optimal and conservative threshold value for gray and white matter at different severity levels. Analysis of the optimal thresholds developed in this investigation indicated that there were no significant differences between the amount of strain necessary in the gray matter to cause an influx of species as small as the hydrazide (~730Da) (~8.9% strain) and as large as bovine serum albumin (~70KDa) (10.6%strain). The optimal LEP threshold in the gray matter for RBCs (~5μm) (~14% strain) was significantly larger than both albumin and hydrazide, which confirms that it takes a more severe injury to cause extravasation of RBCs in the spinal cord. In the white matter, the mean von Mises strain necessary for hydrazide influx (32.00%) was significantly different than both the albumin (45.4%) and the RBC (53.6%) values. The albumin and RBC thresholds were not significantly different. However, LEVM was not an accurate predictor of hydrazide in the white matter since the thresholds statistically varied across loading conditions.

Neuroscientists have routinely used animate models, most notably the rat and mouse, in studying the neuropathophysiology and functional consequences of SCI and TBI (Young 2002). There has been a wealth of biological, physiological, and functional information gathered from in vivo experimental models of SCI. Despite the prevalence of information regarding injury, only recently have researchers used FEA as a viable tool to correlate injury mechanics in animal models to the information gathered from in vivo models (Shreiber

1997). Furthermore, even though rodent models are most widely used in the neuroscience community to study SCI, there have been no published FE simulations of in vivo models of SCI.

In this thesis, we were able to efficiently correlate the information generated from in vivo models of injury with a computational model to understand the mechanical response of the spinal cord tissue to loading. With the plethora of information generated from the in vivo models of SCI, we were able to specifically tailor our experiments to ultimately arrive at threshold predictions. Weight drop contusion models emulate the clinical aspects of spinal cord injury, but have the added advantage of a consistent, reproducible injury. Specifically, we used the Multicenter Animal Spinal Cord Injury Study (MASCIS) Impactor weight drop model to facilitate threshold prediction. The Impactor carefully drops a 10-gram rod precisely at select heights onto the T9-10 vertebral level exposed by laminectomy (Young 2002). Because of the direct transfer of force from the falling rod onto the dura, this not only aids in the reproducibility of the injury, but also simplifies the FEA, removing complicated contact interfaces that would be difficult to define. Second, the Impactor measures the movement of the 10-gram rod with a digital optical potentiometer, which allows the rod movements to be measured precisely at ±20μm and ±20μsec. The Impactor uses electrical contact to measure the exact time and point of contact for injury, while impact velocity is determined by sampling the rod trajectory during the 2msec before contact. It also records the movement of the spinal column underlying the impact site with a vertebral motion detector and subtracts out any bone movement from the overall displacement allowing a precise measurement of cord compression. Thus, for each in vivo weight drop, the Impactor

calculates impact velocity, cord compression distance, and cord compression time. This information allows for proper validation of the FEM.

The Impactor, and other SCI injury devices, commonly produce disruptions in the blood-spinal cord barrier (BSCB) (Mautes, Weinzierl et al. 2000). The BSCB offers a convenient structure to examine both the severity and extent of tissue damage, in that the spatial permeability to different sized species can be easily examined in the same animal following spinal cord trauma (Joo 1993; Schlosshauer 1993; Noble, Mautes et al. 1996). Thus, the extent of injury can be assessed by examining the extravasation volume of a particular marker, and the severity can be assessed by comparing extravasation volumes among marker sizes. Many researchers have evaluated BSCB injury by injection of probes (typically labeled albumin, labeled dextrans, or horseradish peroxidase) followed by qualitative or quantitative microscopy (Griffiths and Miller 1974; Beggs and Waggener 1975; Wagner and Stewart 1981; Noble and Wrathall 1987; Farooque, Zhang et al. 1992; Fehlings and Tator 1995; Jaeger and Blight 1997; Whetstone, Hsu et al. 2003). In this study, we used three fluorescent markers that spanned a wide range of sizes to evaluate BSCB injury: Alexa 568 hydrazide, which is a 707Da non-toxic, fluorescently labeled ion most often used as a neuronal tracer; Alexa 488-labeled BSA, which has a molecular weight of approximately 70kDa; and red blood cells, which have a nominal diameter of ~5μm. We selected the hydrazide and albumin based on their molecular weight, but a better measure would be the geometric size of a molecule or protein, since species are generally excluded by size. Injury of greater severity will generate bigger holes in the vasculature to allow larger species area-wise to extravasate into the parenchyma. The subsequent diffusion of these species through the parenchyma will also be dictated by their size. For an improved

prediction of size-dependent permeability, other markers could be included at different molecular weights/effective diameters, such as lysine-fixable fluorescent dextrans, or labeled immunoglobulins. Most importantly, since tissue sections were imaged with epifluorescent microscopy and mosaic tissue sections were created with computer-controlled microscopy for each fluorescent probe, these images served as spatial maps of injury that were compared to the results from our FEM mechanical output.

The FEM of SCI was developed concurrently with the parallel Impactor experiments to investigate the underlying biomechanics of injury. The simulation was performed at the average velocity from parallel experiments at 12.5mm and 25mm drop heights. The analysis was validated by comparing the compression rate and the displacement of the mass post-"impact" to the actual parameters measured during an Impactor weight drop. The compression depth and rate for each drop height simulation fell within the range of experimental values. Patterns of extravasation of for the 3 injury markers (hydrazide, albumin, and RBCs) in a horizontal slice were roughly oblong in shape, with the major axis aligned axially with the spinal cord (Noble and Wrathall 1989). Comparison of a horizontal section of the extravasation of the 3 markers demonstrated good correlation to the distribution of maximum principal stress and strain in the same anatomical section in the FEM. Parametric studies revealed that the validation of model was most sensitive to changes in the material properties of the gray and white matter, specifically the viscoelastic response, which suggests that BSCB injury is strain mediated.

Finally, we quantitatively compared the output from the simulation to the spatial maps of BSCB injury with a statistical analysis to identify the in vivo tissue-level thresholds for the spinal cord. Only recently have researchers used FEA as a viable tool to correlate

injury mechanics in animal models to the information gathered from in vivo models. Specifically, biomechanical analyses of animate models of brain injury, which allow a direct comparison of the tissue level states of stress and strain to injury patterns and outcomes, have become more common (Ueno, Melvin et al. 1995; Shreiber 1997). However, to our knowledge, no characterizations of the tissue level mechanics of animate models of SCI exist.

We quantitatively compared the results from our experimental animal model for each injured spinal cord (n=16) to peak measures of 13 mechanical parameters outputted by the finite element analysis. Our FE mesh was compared to our spatial maps of BSCB injury from the experimental study based on element-by-element comparisons. Specifically, 3 horizontal sections (dorsal, middle, and ventral) of the FE mesh were extracted and superposed on the composite images of BSCB injury for the same anatomical section for each severity marker (molecule, protein, cell). Elements were graded as either injured (1) or uninjured (0) based on pixel values for injured tissue. For each experiment, the peak values of maximum principal stress (SP), maximum principal compressive stress (SPCompress), maximum principal strain (LEP), von Mises stress (VM), von Mises strain (LEVM), compressive principal strain (LEC), pressure (P), and strain energy (SEN) for each element were identified from the simulation with matching input loading conditions. Separate outputs were generated for elements corresponding to the gray and white matter of the spinal cord.

For each element, the injury status (1 or 0) was plotted against the peak values of the mechanical mediators of injury, and logistic regression analysis was performed to identify the dependence of injury on the parameter. From the logistic regression analysis, receiver operating characteristic (ROC) curves (Shreiber 1997; Bain and Meaney 2000) were

developed by identifying the sensitivity and specificity of the stress/strain values. Ideally, we wanted to determine two threshold values for the best mechanical parameter for each measure of injury severity: a “conservative” threshold, for which sensitivity has no false negatives (all elements predicted to be injured are injured) and an “optimal” threshold, where the sum of sensitivity and specificity is maximized. A plot of (sensitivity + specificity) vs. probability revealed the probability value that results in the optimum threshold, where the (sensitivity + specificity) value is a maximum. It was shown that LEP was the best predictor of gray matter injury, while LEVM a viable predictor of more severe white matter injury.

A major conclusion of this research is the necessity of material properties for the rat spinal cord structures to aid in the prediction of BSCB injury. The success of the FEM hinges on the accurate determination of the individual load-bearing entities, including the gray matter, white matter, and dura mater. Specifically, separate material descriptions are warranted for the gray and the white matter. The lack of information concerning the material properties for the load-bearing spinal cord structures in the rat is a limiting factor in the fidelity of the model. Little research has focused on rat spinal cord mechanical properties. In fact, mechanical properties from injurious loading conditions have largely been ignored. It is expected that as more experimental data is developed regarding the rat spinal cord, more precise predictions can be made. Specifically, white matter injury can be more accurately predicted with a mechanical measure. Furthermore, incremental improvements in the computational model, such as the development of anisotropic material laws and modeling the CSF as a compressible fluid will greatly enhance the fidelity and predictive power of the model.

The goal for this research was to link the patterns of BSCB primary injury, and ultimately other primary pathologies, to the tissue-level states of mechanical stress and strain. We have shown that the methods presented in this study to develop thresholds to injury can be used in other impact trauma models of SCI, including newer contusion models, which are designed as displacement and/or force controlled. The different in vivo SCI impact models have unique external loading conditions. For example, pneumatic impactors, such as the Ohio State University Electromagnetic SCI device (Stokes, Noyes et al. 1992) is a displacement controlled model, while the Precision Systems and Instrumentation Infinite Horizons Impactor is force controlled. Contusions with the different models can result in significantly different injury outcome measures following trauma induced to the same compression depth. These differences can be attributed to the subtle differences in loading conditions. However, the relationship between the tissue-level stress and strain generated with each model and the patterns of injury they produce will be same. To simulate these models, the general geometry of the FEM would be preserved, but changes in impactor size and loading conditions would have to be taken into account. Simulating other contusion models would enhance the confidence of the threshold predictions presented in this thesis. Moreover, similarly modeling the mechanics of other models computationally will allow improved comparisons of results from laboratory-to-laboratory based on the internal, tissue-level criteria, and ultimately to improved standardization of injury patterns.

A benefit of the model developed in this investigation is the ability to examine injury to other entities of the spinal cord, such as axons or cell bodies, by generating appropriate spatial maps of primary injury. This shows the versatility of the model and methods used to determine in vivo thresholds for injury. The Impactor contusion model, or any mode of

injury, can be used to show that different entities of the spinal cord have different thresholds. The computational model can be compared to the spatial maps of injury for different entities and thresholds can be predicted for each entity. For example, immediate axonal permeability changes can be determined by injecting dye intrathecally. Damage to cell bodies can be determined by looking at green fluorescent (GFP) intensities in a "green rat". Alterations in gene transcription immediately after injury can be determined by examining in situ hybridization. Furthermore, we can use the techniques in this investigation to estimate in vivo thresholds for any injury to the spinal cord for which we can produce a spatial profile of mechanically-mediated injury. The model can be increased in complexity to study other factors, such as the orientation of blood vessels or complexities introduced by anisotropy of axons in the white matter. This is potentially invaluable information for the development of prevention techniques and restorative therapies for SCI.

This model is a first step in identifying the mechanical parameter that best predicts BSCB injury in humans. Rats are commonly used as surrogates for humans in studying neuropathology since it is a fundamental assumption that the interspecies variability in the spinal cord itself is minimal (Metz, Curt et al. 2000). While there are subtle differences between human and rat spinal cords, such as the amount of volume of tissue, it can be assumed that there is a correlation between the rat and human spinal cord. The thresholds found in this investigation are based on the rat spinal cord, but the methodology should be applied in other species, including the mouse, to assess interspecies variations. This would allow a better correlation of the thresholds found here in the rat to the human, which would provide a valuable link between the traumatic loading conditions during SCI and tissue

failure in humans. This can ultimately be effective in therapeutic interventions and preventative strategies to injury.

Understanding the size-specific severity of trauma to the BSCB can also be critical in determining a course of therapies to ameliorate the damage. For instance, statins have recently been shown to reduce CNS inflammation following SCI (Stanislaus, Singh et al. 2001; Pannu, Barbosa et al. 2005). Stanislaus et al. reported that after induction of experimental allergic encephalomyelitis (EAE) (the animal disease for multiple sclerosis) in rats, Lovastatin helped stabilize the BSCB by decreasing mononuclear cell penetration into the spinal cord, as well as obstructing the expression of inducible nitric oxide synthase (iNOS) and proinflammatory cytokines (Stanislaus, Pahan et al. 1999; Stanislaus, Singh et al. 2001). Mooradian et al. demonstrated that statins improved BBB function in a rat model of diabetes, limiting permeability of species as small as 40kD (the smallest tested) (Mooradian, Haas et al. 2005). Different statin formulations maintain different abilities to cross the blood-brain/blood-spinal cord barrier according to their lipophilicity, and there is evidence that, in some cases, indiscriminant crossing of statins into brain and spinal cord parenchyma causes significant CNS side effects and is deleterious to long-term viability (Botti, Triscari et al. 1991; Guillot, Misslin et al. 1993; Kostis, Rosen et al. 1994; Quion and Jones 1994; Sparks, Connor et al. 2002). As such, combination therapies could be designed that provide one measure for mildly injured areas (for instance, atorvastatins to begin to seal the BSCB), and another measure for severely injured ones (for instance, potent mediators of inflammatory cell adhesion). Poly(ethylene glycol) (PEG) has also been shown to assist in sealing damaged axonal membranes (Borgens and Shi 2000), and it has been used to administer plasmid DNA intrathecally to improve transgene expression over naked plasma (Shi, Tang et al. 2003).

Since the molecular weight of PEG is easily controlled, and it is easily grafted to other molecules, specifically-sized therapies could be designed to limit drug exposure or target transfection of populations of cells most affected by the trauma. By addressing BSCB damage as early as possible, these therapies could reduce the severity of secondary damage to the spinal cord, though the designed therapy could be modified to reflect delivery through the BSCB that has been additionally compromised by secondary insults.

Understanding the sensitivity of the BSCB to mechanical perturbations potentially has important implications in targeted drug and gene delivery to the spinal cord. While methylprednisolone – the most effective drug to date clinically (Baptiste and Fehlings 2006; Eck, Nachtigall et al. 2006)– is a steroid that will naturally cross the blood-spinal cord barrier – other promising therapies include peptide growth factors, antibodies, and/or proteins which are generally larger than molecules that pass non-specifically through the barrier (<500Da). In many cases, it is assumed that the compromised BSCB offers no resistance to therapies delivered via the circulatory system (Sharma 2005). Clearly, following clinically relevant trauma, the BSCB is almost universally compromised to a graded extent and severity, and different sized blood-borne species will differentially cross into the parenchyma. Thus, therapies delivered to the spinal cord via the bloodstream (either directly or absorbed) will be naturally delivered to specific regions according to the severity of BSCB injury at the particular locations, and certain areas may not receive sufficient doses of the therapy (Sharma 2005).

Understanding tissue-level thresholds allows for prediction of injury patterns in other models, designing new models to produce specific injury patterns, and defining in vitro

conditions appropriate for studying trauma. Ultimately, this can be an invaluable tool in preventing SCI in humans.

REFERENCES

BAIN, A. C. and MEANEY, D. F. (2000). "Tissue-level thresholds for axonal damage in an experimental model of central nervous system white matter injury." J Biomech Eng **122**(6): 615-22.

BAPTISTE, D. C. and FEHLINGS, M. G. (2006). "Pharmacological approaches to repair the injured spinal cord." J Neurotrauma **23**(3-4): 318-34.

BEGGS, J. L. and WAGGENER, J. D. (1975). "Vasogenic edema in the injured spinal cord: a method of evaluating the extent of blood-brain barrier alteration to horseradish peroxidase." Exp Neurol **49**(1 Pt 1): 86-96.

BORGENS, R. B. and SHI, R. (2000). "Immediate recovery from spinal cord injury through molecular repair of nerve membranes with polyethylene glycol." Faseb J **14**(1): 27-35.

BOTTI, R. E., TRISCARI, J., PAN, H. Y. and ZAYAT, J. (1991). "Concentrations of pravastatin and lovastatin in cerebrospinal fluid in healthy subjects." Clin Neuropharmacol **14**(3): 256-61.

ECK, J. C., NACHTIGALL, D., HUMPHREYS, S. C. and HODGES, S. D. (2006). "Questionnaire survey of spine surgeons on the use of methylprednisolone for acute spinal cord injury." Spine **31**(9): E250-3.

FAROOQUE, M., ZHANG, Y., HOLTZ, A. and OLSSON, Y. (1992). "Exudation of fibronectin and albumin after spinal cord injury in rats." Acta Neuropathol (Berl) **84**(6): 613-20.

FEHLINGS, M. G. and TATOR, C. H. (1995). "The relationships among the severity of spinal cord injury, residual neurological function, axon counts, and counts of retrogradely labeled neurons after experimental spinal cord injury." Exp Neurol **132**(2): 220-8.

GRIFFITHS, I. R. and MILLER, R. (1974). "Vascular permeability to protein and vasogenic oedema in experimental concussive injuries to the canine spinal cord." J Neurol Sci **22**(3): 291-304.

GUILLOT, F., MISSLIN, P. and LEMAIRE, M. (1993). "Comparison of fluvastatin and lovastatin blood-brain barrier transfer using in vitro and in vivo methods." J Cardiovasc Pharmacol **21**(2): 339-46.

JAEGER, C. B. and BLIGHT, A. R. (1997). "Spinal cord compression injury in guinea pigs: structural changes of endothelium and its perivascular cell associations after blood-brain barrier breakdown and repair." Exp Neurol **144**(2): 381-99.

JOO, F. (1993). "The blood-brain barrier in vitro: the second decade." Neurochem Int **23**(6): 499-521.

KOSTIS, J. B., ROSEN, R. C. and WILSON, A. C. (1994). "Central nervous system effects of HMG CoA reductase inhibitors: lovastatin and pravastatin on sleep and cognitive performance in patients with hypercholesterolemia." J Clin Pharmacol **34**(10): 989-96.

MAUTES, A. E., WEINZIERL, M. R., DONOVAN, F. and NOBLE, L. J. (2000). "Vascular events after spinal cord injury: contribution to secondary pathogenesis." Phys Ther **80**(7): 673-87.

METZ, G. A., CURT, A., VAN DE MEENT, H., KLUSMAN, I., SCHWAB, M. E. and DIETZ, V. (2000). "Validation of the weight-drop contusion model in rats: a comparative study of human spinal cord injury." J Neurotrauma **17**(1): 1-17.

MOORADIAN, A. D., HAAS, M. J., BATEJKO, O., HOVSEPYAN, M. and FEMAN, S. S. (2005). "Statins ameliorate endothelial barrier permeability changes in the cerebral tissue of streptozotocin-induced diabetic rats." Diabetes **54**(10): 2977-82.

NOBLE, L. J., MAUTES, A. E. and HALL, J. J. (1996). "Characterization of the microvascular glycocalyx in normal and injured spinal cord in the rat." J Comp Neurol **376**(4): 542-56.

NOBLE, L. J. and WRATHALL, J. R. (1987). "The blood-spinal cord barrier after injury: pattern of vascular events proximal and distal to a transection in the rat." Brain Res **424**(1): 177-88.

NOBLE, L. J. and WRATHALL, J. R. (1989). "Correlative analyses of lesion development and functional status after graded spinal cord contusive injuries in the rat." Exp Neurol **103**(1): 34-40.

PANNU, R., BARBOSA, E., SINGH, A. K. and SINGH, I. (2005). "Attenuation of acute inflammatory response by atorvastatin after spinal cord injury in rats." J Neurosci Res **79**(3): 340-50.

QUION, J. A. and JONES, P. H. (1994). "Clinical pharmacokinetics of pravastatin." Clin Pharmacokinet **27**(2): 94-103.

SCHLOSSHAUER, B. (1993). "The blood-brain barrier: morphology, molecules, and neurothelin." Bioessays **15**(5): 341-6.

SHARMA, H. S. (2005). "Pathophysiology of blood-spinal cord barrier in traumatic injury and repair." Curr Pharm Des **11**(11): 1353-89.

SHI, L., TANG, G. P., GAO, S. J., et al. (2003). "Repeated intrathecal administration of plasmid DNA complexed with polyethylene glycol-grafted polyethylenimine led to prolonged transgene expression in the spinal cord." Gene Ther **10**(14): 1179-88.

SHREIBER, D. I., A. C. BAIN, ET AL. (1997). "In vivo thresholds for mechanical injury to the blood-brain barrier." SAE 1997 Transactions: Journal of Passenger Cars **106(6-2):**: 3792-3806.

SPARKS, D. L., CONNOR, D. J., BROWNE, P. J., LOPEZ, J. E. and SABBAGH, M. N. (2002). "HMG-CoA reductase inhibitors (statins) in the treatment of Alzheimer's disease and why it would be ill-advise to use one that crosses the blood-brain barrier." J Nutr Health Aging **6**(5): 324-31.

STANISLAUS, R., PAHAN, K., SINGH, A. K. and SINGH, I. (1999). "Amelioration of experimental allergic encephalomyelitis in Lewis rats by lovastatin." Neurosci Lett **269**(2): 71-4.

STANISLAUS, R., SINGH, A. K. and SINGH, I. (2001). "Lovastatin treatment decreases mononuclear cell infiltration into the CNS of Lewis rats with experimental allergic encephalomyelitis." J Neurosci Res **66**(2): 155-62.

STOKES, B. T., NOYES, D. H. and BEHRMANN, D. L. (1992). "An electromechanical spinal injury technique with dynamic sensitivity." J Neurotrauma **9**(3): 187-95.

UENO, K., MELVIN, J. W., LI, L. and LIGHTHALL, J. W. (1995). "Development of tissue level brain injury criteria by finite element analysis." J Neurotrauma **12**(4): 695-706.

WAGNER, F. C., JR. and STEWART, W. B. (1981). "Effect of trauma dose on spinal cord edema." J Neurosurg **54**(6): 802-6.

WHETSTONE, W. D., HSU, J. Y., EISENBERG, M., WERB, Z. and NOBLE-HAEUSSLEIN, L. J. (2003). "Blood-spinal cord barrier after spinal cord injury: relation to revascularization and wound healing." J Neurosci Res **74**(2): 227-39.

YOUNG, W. (2002). "Spinal cord contusion models." Prog Brain Res **137**: 231-55.

BIBLIOGRAPHY

ALBIN, M. S., WHITE, R. J., ACOSTA-RUA, G. and YASHON, D. (1968). "Study of functional recovery produced by delayed localized cooling after spinal cord injury in primates." J Neurosurg 29(2): 113-20.

ALLEN, B. L., JR., FERGUSON, R. L., LEHMANN, T. R. and O'BRIEN, R. P. (1982). "A mechanistic classification of closed, indirect fractures and dislocations of the lower cervical spine." Spine 7(1): 1-27.

AMAR, A. P. and LEVY, M. L. (1999). "Pathogenesis and pharmacological strategies for mitigating secondary damage in acute spinal cord injury." Neurosurgery 44(5): 1027-39; discussion 1039-40.

ANKENY, D. P., MCTIGUE, D. M., GUAN, Z., et al. (2001). "Pegylated brain-derived neurotrophic factor shows improved distribution into the spinal cord and stimulates locomotor activity and morphological changes after injury." Exp Neurol 170(1): 85-100.

ARBOGAST, K. B. and MARGULIES, S. S. (1998). "Material characterization of the brainstem from oscillatory shear tests." J Biomech 31(9): 801-7.

BAIN, A. C. and MEANEY, D. F. (2000). "Tissue-level thresholds for axonal damage in an experimental model of central nervous system white matter injury." J Biomech Eng 122(6): 615-22.

BAIN, A. C., RAGHUPATHI, R. and MEANEY, D. F. (2001). "Dynamic stretch correlates to both morphological abnormalities and electrophysiological impairment in a model of traumatic axonal injury." J Neurotrauma 18(5): 499-511.

BALENTINE, J. D. (1978). "Pathology of experimental spinal cord trauma. I. The necrotic lesion as a function of vascular injury." Lab Invest 39(3): 236-53.

BANDAK, F. A. (1995). "On the mechanics of impact neurotrauma: a review and critical synthesis." J Neurotrauma 12(4): 635-49.

BANDAK, F. A., VANDER VORST, M. J., STUHMILLER, L. M., MLAKAR, P. F., CHILTON, W. E. and STUHMILLER, J. H. (1995). "An imaging-based computational and experimental study of skull fracture: finite element model development." J Neurotrauma 12(4): 679-88.

BAO, F., DEKABAN, G. A. and WEAVER, L. C. (2005). "Anti-CD11d antibody treatment reduces free radical formation and cell death in the injured spinal cord of rats." J Neurochem 94(5): 1361-73.

BAPTISTE, D. C. and FEHLINGS, M. G. (2006). "Pharmacological approaches to repair the injured spinal cord." J Neurotrauma 23(3-4): 318-34.

BASSO, D. M., BEATTIE, M. S. and BRESNAHAN, J. C. (1996). "Graded histological and locomotor outcomes after spinal cord contusion using the NYU weight-drop device versus transection." Exp Neurol 139(2): 244-56.

BEATTIE, M. S., BRESNAHAN, J. C., KOMON, J., et al. (1997). "Endogenous repair after spinal cord contusion injuries in the rat." Exp Neurol 148(2): 453-63.

BEGGS, J. L. and WAGGENER, J. D. (1975). "Vasogenic edema in the injured spinal cord: a method of evaluating the extent of blood-brain barrier alteration to horseradish peroxidase." Exp Neurol 49(1 Pt 1): 86-96.

BEGGS, J. L. and WAGGENER, J. D. (1976). "Transendothelial vesicular transport of protein following compression injury to the spinal cord." Lab Invest 34(4): 428-39.

BEHRMANN, D. L., BRESNAHAN, J. C., BEATTIE, M. S. and SHAH, B. R. (1992). "Spinal cord injury produced by consistent mechanical displacement of the cord in rats: behavioral and histologic analysis." J Neurotrauma 9(3): 197-217.

BERKOWITZ, E. D. (1998). "Revealing America's welfare state. [Review of: Howard, C., The hidden welfare state: tax expenditures and social policy in the United States. Princeton University Press, 1997]." Rev Am Hist 26(3): 620-4.

BILGEN, M., AL-HAFEZ, B., T, M. M. and I, V. S. (2005). "Ex vivo magnetic resonance imaging of rat spinal cord at 9.4 T." Magn Reson Imaging 23(4): 601-5.

BILGEN, M. and NARAYANA, P. A. (2001). "A pharmacokinetic model for quantitative evaluation of spinal cord injury with dynamic contrast-enhanced magnetic resonance imaging." Magn Reson Med 46(6): 1099-106.

BILSTON, L. E. (2002). "The effect of perfusion on soft tissue mechanical properties: a computational model." Comput Methods Biomech Biomed Engin 5(4): 283-90.

BILSTON, L. E., LIU, Z. and PHAN-THIEN, N. (1997). "Linear viscoelastic properties of bovine brain tissue in shear." Biorheology 34(6): 377-85.

BILSTON, L. E., LIU, Z. and PHAN-THIEN, N. (2001). "Large strain behaviour of brain tissue in shear: some experimental data and differential constitutive model." Biorheology 38(4): 335-45.

BILSTON, L. E. and THIBAULT, L. E. (1996). "The mechanical properties of the human cervical spinal cord in vitro." Ann Biomed Eng 24(1): 67-74.

BLIGHT, A. R. (1992). "Macrophages and inflammatory damage in spinal cord injury." J Neurotrauma 9 Suppl 1: S83-91.

BORGENS, R. B. and SHI, R. (2000). "Immediate recovery from spinal cord injury through molecular repair of nerve membranes with polyethylene glycol." Faseb J 14(1): 27-35.

BOTTI, R. E., TRISCARI, J., PAN, H. Y. and ZAYAT, J. (1991). "Concentrations of pravastatin and lovastatin in cerebrospinal fluid in healthy subjects." Clin Neuropharmacol 14(3): 256-61.

BRESNAHAN, J. C., BEATTIE, M. S., TODD, F. D., 3RD and NOYES, D. H. (1987). "A behavioral and anatomical analysis of spinal cord injury produced by a feedback-controlled impaction device." Exp Neurol 95(3): 548-70.

BULLOCK, R. and FUJISAWA, H. (1992). "The role of glutamate antagonists for the treatment of CNS injury." J Neurotrauma 9 Suppl 2: S443-62.

CARLSON, S. L., PARRISH, M. E., SPRINGER, J. E., DOTY, K. and DOSSETT, L. (1998). "Acute inflammatory response in spinal cord following impact injury." Exp Neurol 151(1): 77-88.

CHANG, G. L., HUNG, T. K., BLEYAERT, A. and JANNETTA, P. J. (1981). "Stress-strain measurement of the spinal cord of puppies and their neurological evaluation." J Trauma 21(9): 807-10.

CHANG, G. L., HUNG, T. K. and FENG, W. W. (1988). "An in-vivo measurement and analysis of viscoelastic properties of the spinal cord of cats." J Biomech Eng 110(2): 115-22.

CHENG, S. and BILSTON, L. E. (2005). "Unconfined compression of white matter." J Biomech.

CHU, C. S., LIN, M. S., HUANG, H. M. and LEE, M. C. (1994). "Finite element analysis of cerebral contusion." J Biomech 27(2): 187-94.

CUSICK, J. F. and YOGANANDAN, N. (2002). "Biomechanics of the cervical spine 4: major injuries." Clin Biomech (Bristol, Avon) 17(1): 1-20.

DEMJEN, D., KLUSSMANN, S., KLEBER, S., et al. (2004). "Neutralization of CD95 ligand promotes regeneration and functional recovery after spinal cord injury." Nat Med 10(4): 389-95.

DIMITROULAKOS, J., MARHIN, W. H., TOKUNAGA, J., et al. (2002). "Microarray and biochemical analysis of lovastatin-induced apoptosis of squamous cell carcinomas." Neoplasia 4(4): 337-46.

DOHRMANN, G. J., PANJABI, M. M. and WAGNER, F. C., JR. (1976). "An apparatus for quantitating experimental spinal cord trauma." Surg Neurol 5(5): 315-8.

DOHRMANN, G. J. and WICK, K. M. (1971). "Demonstration of the microvasculature of the spinal cord by intravenous injection of the fluorescent dye, thioflavine S." Stain Technol 46(6): 321-2.

DUCKER, T. B. and ASSENMACHER, D. R. (1969). "Microvascular response to experimental spinal cord trauma." Surg Forum 20: 428-30.
ECK, J. C., NACHTIGALL, D., HUMPHREYS, S. C. and HODGES, S. D. (2006). "Questionnaire survey of spine surgeons on the use of methylprednisolone for acute spinal cord injury." Spine 31(9): E250-3.

FADEN, A. I., GANNON, A. and BASBAUM, A. I. (1988). "Use of serotonin immunocytochemistry as a marker of injury severity after experimental spinal trauma in rats." Brain Res 450(1-2): 94-100.

FAROOQUE, M., ZHANG, Y., HOLTZ, A. and OLSSON, Y. (1992). "Exudation of fibronectin and albumin after spinal cord injury in rats." Acta Neuropathol (Berl) 84(6): 613-20.

FEHLINGS, M. G. and TATOR, C. H. (1995). "The relationships among the severity of spinal cord injury, residual neurological function, axon counts, and counts of retrogradely labeled neurons after experimental spinal cord injury." Exp Neurol 132(2): 220-8.

FIFORD, R. J. and BILSTON, L. E. (2005). "The mechanical properties of rat spinal cord in vitro." J Biomech 38(7): 1509-15.

FRANKLYN, M., FILDES, B., ZHANG, L., YANG, K. and SPARKE, L. (2005). "Analysis of finite element models for head injury investigation: reconstruction of four real-world impacts." Stapp Car Crash J 49: 1-32.

FRISEN, M., MAGI, M., SONNERUP, I. and VIIDIK, A. (1969). "Rheological analysis of soft collagenous tissue. Part I: theoretical considerations." J Biomech 2(1): 13-20.

FRISEN, M., MAGI, M., SONNERUP, L. and VIIDIK, A. (1969). "Rheological analysis of soft collagenous tissue. Part II: experimental evaluations and verifications." J Biomech 2(1): 21-8.

GALFORD, J. E. and MCELHANEY, J. H. (1970). "A viscoelastic study of scalp, brain, and dura." J Biomech 3(2): 211-21.
GEFEN, A. and MARGULIES, S. S. (2004). "Are in vivo and in situ brain tissues mechanically similar?" J Biomech 37(9): 1339-52.

GRIFFITHS, I. R. (1975). "Vasogenic edema following acute and chronic spinal cord compression in the dog." J Neurosurg 42(2): 155-65.
GRIFFITHS, I. R. and MILLER, R. (1974). "Vascular permeability to protein and vasogenic oedema in experimental concussive injuries to the canine spinal cord." J Neurol Sci 22(3): 291-304.

GRUNER, J. A. (1992). "A monitored contusion model of spinal cord injury in the rat." J Neurotrauma 9(2): 123-6; discussion 126-8.
GUILLOT, F., MISSLIN, P. and LEMAIRE, M. (1993). "Comparison of fluvastatin and lovastatin blood-brain barrier transfer using in vitro and in vivo methods." J Cardiovasc Pharmacol 21(2): 339-46.

HAMANN, M. C., SACKS, M. S. and MALININ, T. I. (1998). "Quantification of the collagen fibre architecture of human cranial dura mater." J Anat 192 (Pt 1): 99-106.

HAUPT, W. and STOFFT, E. (1978). "[Elasticity and tensile strength of human spinal dura mater]." Verh Anat Ges(72): 139-44.

HERNANDEZ, L. A., GRISHAM, M. B., TWOHIG, B., ARFORS, K. E., HARLAN, J. M. and GRANGER, D. N. (1987). "Role of neutrophils in ischemia-reperfusion-induced microvascular injury." Am J Physiol 253(3 Pt 2): H699-703.

HIBBITT, K., AND SORENSEN (2006). ABAQUS/Explicit User's Manual. Pawtucket, R.I., Hibbitt, Karlsson, & Sorensen, Inc.

HUNG, T. K. and CHANG, G. L. (1981). "Biomechanical and neurological response of the spinal cord of a puppy to uniaxial tension." J Biomech Eng 103(1): 43-7.

ICHIHARA, K., TAGUCHI, T., SHIMADA, Y., SAKURAMOTO, I., KAWANO, S. and KAWAI, S. (2001). "Gray matter of the bovine cervical spinal cord is mechanically more rigid and fragile than the white matter." J Neurotrauma 18(3): 361-7.

JAEGER, C. B. and BLIGHT, A. R. (1997). "Spinal cord compression injury in guinea pigs: structural changes of endothelium and its perivascular cell associations after blood-brain barrier breakdown and repair." Exp Neurol 144(2): 381-99.

JOO, F. (1993). "The blood-brain barrier in vitro: the second decade." Neurochem Int 23(6): 499-521.
KALDERON, N. (2005). "Cell elimination as a strategy for repair in acute spinal cord injury." Curr Pharm Des 11(10): 1237-45.

KING, A. I., RUAN, J. S., ZHOU, C., HARDY, W. N. and KHALIL, T. B. (1995). "Recent advances in biomechanics of brain injury research: a review." J Neurotrauma 12(4): 651-8.

KOENIG, G. and DOHRMANN, G. J. (1977). "Histopathological variability in 'standardised' spinal cord trauma." J Neurol Neurosurg Psychiatry 40(12): 1203-10.

KOSTIS, J. B., ROSEN, R. C. and WILSON, A. C. (1994). "Central nervous system effects of HMG CoA reductase inhibitors: lovastatin and pravastatin on sleep and cognitive performance in patients with hypercholesterolemia." J Clin Pharmacol 34(10): 989-96.

KUMARESAN, S., YOGANANDAN, N. and PINTAR, F. A. (1998). "Finite element modeling approaches of human cervical spine facet joint capsule." J Biomech 31(4): 371-6.

KUMARESAN, S., YOGANANDAN, N. and PINTAR, F. A. (1999). "Finite element analysis of the cervical spine: a material property sensitivity study." Clin Biomech (Bristol, Avon) 14(1): 41-53.

KUMARESAN, S., YOGANANDAN, N., PINTAR, F. A. and MAIMAN, D. J. (1999). "Finite element modeling of the cervical spine: role of intervertebral disc under axial and eccentric loads." Med Eng Phys 21(10): 689-700.

KUMARESAN, S., YOGANANDAN, N., PINTAR, F. A., MAIMAN, D. J. and KUPPA, S. (2000). "Biomechanical study of pediatric human cervical spine: a finite element approach." J Biomech Eng 122(1): 60-71.

KWO, S., YOUNG, W. and DECRESCITO, V. (1989). "Spinal cord sodium, potassium, calcium, and water concentration changes in rats after graded contusion injury." J Neurotrauma 6(1): 13-24.

LEBEL, C. P. and BONDY, S. C. (1991). "Oxygen radicals: common mediators of neurotoxicity." Neurotoxicol Teratol 13(3): 341-6.

LEVINE, D. N. (2004). "The pathogenesis of syringomyelia associated with lesions at the foramen magnum: a critical review of existing theories and proposal of a new hypothesis." J Neurol Sci 220(1-2): 3-21.

LIU, Z. and BILSTON, L. E. (2002). "Large deformation shear properties of liver tissue." Biorheology 39(6): 735-42.

MAIMAN, D. J., KUMARESAN, S., YOGANANDAN, N. and PINTAR, F. A. (1999). "Biomechanical effect of anterior cervical spine fusion on adjacent segments." Biomed Mater Eng 9(1): 27-38.

MAUTES, A. E., WEINZIERL, M. R., DONOVAN, F. and NOBLE, L. J. (2000). "Vascular events after spinal cord injury: contribution to secondary pathogenesis." Phys Ther 80(7): 673-87.

MCDONALD, J. W. (1999). "Repairing the damaged spinal cord." Sci Am 281(3): 64-73.

MCGARVEY, K. A., LEE, J. M. and BOUGHNER, D. R. (1984). "Mechanical suitability of glycerol-preserved human dura mater for construction of prosthetic cardiac valves." Biomaterials 5(2): 109-17.

MEANEY, D. F., ROSS, D. T., WINKELSTEIN, B. A., et al. (1994). "Modification of the cortical impact model to produce axonal injury in the rat cerebral cortex." J Neurotrauma 11(5): 599-612.

MEANEY, D. F., SMITH, D. H., SHREIBER, D. I., et al. (1995). "Biomechanical analysis of experimental diffuse axonal injury." J Neurotrauma 12(4): 689-94.

MENDELOW, A. D., BULLOCK, R., TEASDALE, G. M., GRAHAM, D. I. and MCCULLOCH, J. (1984). "Intracranial haemorrhage induced at arterial pressure in the rat. Part 2: Short term changes in local cerebral blood flow measured by autoradiography." Neurol Res 6(4): 189-93.

MENDIS, K. K., STALNAKER, R. L. and ADVANI, S. H. (1995). "A constitutive relationship for large deformation finite element modeling of brain tissue." J Biomech Eng 117(3): 279-85.

METZ, G. A., CURT, A., VAN DE MEENT, H., KLUSMAN, I., SCHWAB, M. E. and DIETZ, V. (2000). "Validation of the weight-drop contusion model in rats: a comparative study of human spinal cord injury." J Neurotrauma 17(1): 1-17.

METZ, H., MCELHANEY, J. and OMMAYA, A. K. (1970). "A comparison of the elasticity of live, dead, and fixed brain tissue." J Biomech 3(4): 453-8.

MILLER, K. and CHINZEI, K. (2002). "Mechanical properties of brain tissue in tension." J Biomech 35(4): 483-90.

MILLER, K., CHINZEI, K., ORSSENGO, G. and BEDNARZ, P. (2000). "Mechanical properties of brain tissue in-vivo: experiment and computer simulation." J Biomech 33(11): 1369-76.

MOORADIAN, A. D., HAAS, M. J., BATEJKO, O., HOVSEPYAN, M. and FEMAN, S. S. (2005). "Statins ameliorate endothelial barrier permeability changes in the cerebral tissue of streptozotocin-induced diabetic rats." Diabetes 54(10): 2977-82.

MORRISON, B., 3RD, CATER, H. L., BENHAM, C. D. and SUNDSTROM, L. E. (2006). "An in vitro model of traumatic brain injury utilising two-dimensional stretch of organotypic hippocampal slice cultures." J Neurosci Methods 150(2): 192-201.

NIGHTINGALE, R. W., CAMACHO, D. L., ARMSTRONG, A. J., ROBINETTE, J. J. and MYERS, B. S. (2000). "Inertial properties and loading rates affect buckling modes and injury mechanisms in the cervical spine." J Biomech 33(2): 191-7.

NIGHTINGALE, R. W., MCELHANEY, J. H., RICHARDSON, W. J. and MYERS, B. S. (1996). "Dynamic responses of the head and cervical spine to axial impact loading." J Biomech 29(3): 307-18.

NOBLE, L. J., MAUTES, A. E. and HALL, J. J. (1996). "Characterization of the microvascular glycocalyx in normal and injured spinal cord in the rat." J Comp Neurol 376(4): 542-56.

NOBLE, L. J. and MAXWELL, D. S. (1983). "Blood-spinal cord barrier response to transection." Exp Neurol 79(1): 188-99.

NOBLE, L. J. and WRATHALL, J. R. (1985). "Spinal cord contusion in the rat: morphometric analyses of alterations in the spinal cord." Exp Neurol 88(1): 135-49.

NOBLE, L. J. and WRATHALL, J. R. (1987). "The blood-spinal cord barrier after injury: pattern of vascular events proximal and distal to a transection in the rat." Brain Res 424(1): 177-88.

NOBLE, L. J. and WRATHALL, J. R. (1989). "Correlative analyses of lesion development and functional status after graded spinal cord contusive injuries in the rat." Exp Neurol 103(1): 34-40.

NOBLE, L. J. and WRATHALL, J. R. (1989). "Distribution and time course of protein extravasation in the rat spinal cord after contusive injury." Brain Res 482(1): 57-66.

NOYES, D. H. (1987). "Electromechanical impactor for producing experimental spinal cord injury in animals." Med Biol Eng Comput 25(3): 335-40.

PAHAN, K., SHEIKH, F. G., NAMBOODIRI, A. M. and SINGH, I. (1997). "Lovastatin and phenylacetate inhibit the induction of nitric oxide synthase and cytokines in rat primary astrocytes, microglia, and macrophages." J Clin Invest 100(11): 2671-9.

PAN, W., BANKS, W. A. and KASTIN, A. J. (1997). "Blood-brain barrier permeability to ebiratide and TNF in acute spinal cord injury." Exp Neurol 146(2): 367-73.

PAN, W., ZHANG, L., LIAO, J., CSERNUS, B. and KASTIN, A. J. (2003). "Selective increase in TNF alpha permeation across the blood-spinal cord barrier after SCI." J Neuroimmunol 134(1-2): 111-7.

PANNU, R., BARBOSA, E., SINGH, A. K. and SINGH, I. (2005). "Attenuation of acute inflammatory response by atorvastatin after spinal cord injury in rats." J Neurosci Res 79(3): 340-50.

PATIN, D. J., ECKSTEIN, E. C., HARUM, K. and PALLARES, V. S. (1993). "Anatomic and biomechanical properties of human lumbar dura mater." Anesth Analg 76(3): 535-40.

PINTAR, F. A., KUMARESAN, S., YOGANANDAN, N., YANG, A., STEMPER, B. and GENNARELLI, T. A. (2001). "Biomechanical modeling of penetrating traumatic head injuries: a finite element approach." Biomed Sci Instrum 37: 429-34.

POPOVICH, P. G., HORNER, P. J., MULLIN, B. B. and STOKES, B. T. (1996). "A quantitative spatial analysis of the blood-spinal cord barrier. I. Permeability changes after experimental spinal contusion injury." Exp Neurol 142(2): 258-75.

POPOVICH, P. G., REINHARD, J. F., JR., FLANAGAN, E. M. and STOKES, B. T. (1994). "Elevation of the neurotoxin quinolinic acid occurs following spinal cord trauma." Brain Res 633(1-2): 348-52.

POPOVICH, P. G., WEI, P. and STOKES, B. T. (1997). "Cellular inflammatory response after spinal cord injury in Sprague-Dawley and Lewis rats." J Comp Neurol 377(3): 443-64.

PRANGE, M. T. and MARGULIES, S. S. (2002). "Regional, directional, and age-dependent properties of the brain undergoing large deformation." J Biomech Eng 124(2): 244-52.

QUION, J. A. and JONES, P. H. (1994). "Clinical pharmacokinetics of pravastatin." Clin Pharmacokinet 27(2): 94-103.

RIVLIN, A. S. and TATOR, C. H. (1978). "Effect of duration of acute spinal cord compression in a new acute cord injury model in the rat." Surg Neurol 10(1): 38-43.

RUAN, J. S., KHALIL, T. and KING, A. I. (1991). "Human head dynamic response to side impact by finite element modeling." J Biomech Eng 113(3): 276-83.

RUAN, J. S., KHALIL, T. and KING, A. I. (1994). "Dynamic response of the human head to impact by three-dimensional finite element analysis." J Biomech Eng 116(1): 44-50.

RUNZA, M., PIETRABISSA, R., MANTERO, S., ALBANI, A., QUAGLINI, V. and CONTRO, R. (1999). "Lumbar dura mater biomechanics: experimental characterization and scanning electron microscopy observations." Anesth Analg 88(6): 1317-21.

SANCES, A., JR., MYKLEBUST, J. B., MAIMAN, D. J., LARSON, S. J., CUSICK, J. F. and JODAT, R. W. (1984). "The biomechanics of spinal injuries." Crit Rev Biomed Eng 11(1): 1-76.

SASAKI, S., SCHNEIDER, H. and RENZ, S. (1978). "Microcirculatory disturbances during the early phase following experimental spinal cord trauma in the rat." Adv Neurol 20: 423-31.

SAVILLE, L. R., POSPISIL, C. H., MAWHINNEY, L. A., et al. (2004). "A monoclonal antibody to CD11d reduces the inflammatory infiltrate into the injured spinal cord: a potential neuroprotective treatment." J Neuroimmunol 156(1-2): 42-57.

SCHEFF, S. W., RABCHEVSKY, A. G., FUGACCIA, I., MAIN, J. A. and LUMPP, J. E., JR. (2003). "Experimental modeling of spinal cord injury: characterization of a force-defined injury device." J Neurotrauma 20(2): 179-93.

SCHLOSSHAUER, B. (1993). "The blood-brain barrier: morphology, molecules, and neurothelin." Bioessays 15(5): 341-6.

SENTER, H. J. and VENES, J. L. (1978). "Altered blood flow and secondary injury in experimental spinal cord trauma." J Neurosurg 49(4): 569-78.

SHARMA, H. S. (2005). "Pathophysiology of blood-spinal cord barrier in traumatic injury and repair." Curr Pharm Des 11(11): 1353-89.

SHEN, F., TAY, T. E., LI, J. Z., NIGEN, S., LEE, P. V. and CHAN, H. K. (2006). "Modified Bilston nonlinear viscoelastic model for finite element head injury studies." J Biomech Eng 128(5): 797-801.

SHI, L., TANG, G. P., GAO, S. J., et al. (2003). "Repeated intrathecal administration of plasmid DNA complexed with polyethylene glycol-grafted polyethylenimine led to prolonged transgene expression in the spinal cord." Gene Ther 10(14): 1179-88.

SHREIBER, D. I., A. C. BAIN, ET AL. (1997). "In vivo thresholds for mechanical injury to the blood-brain barrier." SAE 1997 Transactions: Journal of Passenger Cars 106(6-2):: 3792-3806.

SHREIBER, D. I., SMITH, D. H. and MEANEY, D. F. (1999). "Immediate in vivo response of the cortex and the blood-brain barrier following dynamic cortical deformation in the rat." Neurosci Lett 259(1): 5-8.

SPARKS, D. L., CONNOR, D. J., BROWNE, P. J., LOPEZ, J. E. and SABBAGH, M. N. (2002). "HMG-CoA reductase inhibitors (statins) in the treatment of Alzheimer's disease and why it would be ill-advise to use one that crosses the blood-brain barrier." J Nutr Health Aging 6(5): 324-31.

STANISLAUS, R., PAHAN, K., SINGH, A. K. and SINGH, I. (1999). "Amelioration of experimental allergic encephalomyelitis in Lewis rats by lovastatin." Neurosci Lett 269(2): 71-4.

STANISLAUS, R., SINGH, A. K. and SINGH, I. (2001). "Lovastatin treatment decreases mononuclear cell infiltration into the CNS of Lewis rats with experimental allergic encephalomyelitis." J Neurosci Res 66(2): 155-62.

STEWART, W. W. (1981). "Lucifer dyes--highly fluorescent dyes for biological tracing." Nature 292(5818): 17-21.

STOKES, B. T., NOYES, D. H. and BEHRMANN, D. L. (1992). "An electromechanical spinal injury technique with dynamic sensitivity." J Neurotrauma 9(3): 187-95.

SUGIO, S., KASHIMA, A., MOCHIZUKI, S., NODA, M. and KOBAYASHI, K. (1999). "Crystal structure of human serum albumin at 2.5 A resolution." Protein Eng 12(6): 439-46.

SUSSMAN, M. S. and BULKLEY, G. B. (1990). "Oxygen-derived free radicals in reperfusion injury." Methods Enzymol 186: 711-23.

SVERDLIK, A. and LANIR, Y. (2002). "Time-dependent mechanical behavior of sheep digital tendons, including the effects of preconditioning." J Biomech Eng 124(1): 78-84.

TERAE, S., TAKAHASHI, C., ABE, S., KIKUCHI, Y. and MIYASAKA, K. (1997). "Gd-DTPA-enhanced MR imaging of injured spinal cord." Clin Imaging 21(2): 82-9.

TRAVLOS, A., ANTON, H. A. and WING, P. C. (1994). "Cerebrospinal fluid cell count following spinal cord injury." Arch Phys Med Rehabil 75(3): 293-6.

UENO, K., MELVIN, J. W., LI, L. and LIGHTHALL, J. W. (1995). "Development of tissue level brain injury criteria by finite element analysis." J Neurotrauma 12(4): 695-706.

UNGER, E. C., PORTER, T., CULP, W., LABELL, R., MATSUNAGA, T. and ZUTSHI, R. (2004). "Therapeutic applications of lipid-coated microbubbles." Adv Drug Deliv Rev 56(9): 1291-314.

VAN NOORT, R., BLACK, M. M., MARTIN, T. R. and MEANLEY, S. (1981). "A study of the uniaxial mechanical properties of human dura mater preserved in glycerol." Biomaterials 2(1): 41-5.

VAN NOORT, R., MARTIN, T. R., BLACK, M. M., BARKER, A. T. and MONTERO, C. G. (1981). "The mechanical properties of human dura mater and the effects of storage media." Clin Phys Physiol Meas 2(3): 197-203.
VANDENABEELE, F., CREEMERS, J. and LAMBRICHTS, I. (1996). "Ultrastructure of the human spinal arachnoid mater and dura mater." J Anat 189 (Pt 2): 417-30.

VIANO, D. C., CASSON, I. R., PELLMAN, E. J., ZHANG, L., KING, A. I. and YANG, K. H. (2005). "Concussion in professional football: brain responses by finite element analysis: part 9." Neurosurgery 57(5): 891-916; discussion 891-916.

VIIDIK, A. (1968). "A rheological model for uncalcified parallel-fibred collagenous tissue." J Biomech 1(1): 3-11.

VOO, K., KUMARESAN, S., PINTAR, F. A., YOGANANDAN, N. and SANCES, A., JR. (1996). "Finite-element models of the human head." Med Biol Eng Comput 34(5): 375-81.

WAGNER, F. C., JR. and STEWART, W. B. (1981). "Effect of trauma dose on spinal cord edema." J Neurosurg 54(6): 802-6.

WHEELDON, J., KHOUPHONGSY, P., KUMARESAN, S., YOGANANDAN, N. and PINTAR, F. A. (2000). "Finite element model of human cervical spinal column." Biomed Sci Instrum 36: 337-42.

WHETSTONE, W. D., HSU, J. Y., EISENBERG, M., WERB, Z. and NOBLE-HAEUSSLEIN, L. J. (2003). "Blood-spinal cord barrier after spinal cord injury: relation to revascularization and wound healing." J Neurosci Res 74(2): 227-39.

WILLINGER, R., KANG, H. S. and DIAW, B. (1999). "Three-dimensional human head finite-element model validation against two experimental impacts." Ann Biomed Eng 27(3): 403-10.

WINKELSTEIN, B. A. and MYERS, B. S. (1997). "The biomechanics of cervical spine injury and implications for injury prevention." Med Sci Sports Exerc 29(7 Suppl): S246-55.

WONG, W. W., TAN, M. M., XIA, Z., DIMITROULAKOS, J., MINDEN, M. D. and PENN, L. Z. (2001). "Cerivastatin triggers tumor-specific apoptosis with higher efficacy than lovastatin." Clin Cancer Res 7(7): 2067-75.

YOGANANDAN, N., KUMARESAN, S. and PINTAR, F. A. (2001). "Biomechanics of the cervical spine Part 2. Cervical spine soft tissue responses and biomechanical modeling." Clin Biomech (Bristol, Avon) 16(1): 1-27.

YOGANANDAN, N., KUMARESAN, S., VOO, L. and PINTAR, F. A. (1997). "Finite element model of the human lower cervical spine: parametric analysis of the C4-C6 unit." J Biomech Eng 119(1): 87-92.

YOUNG, W. (2002). "Spinal cord contusion models." Prog Brain Res 137: 231-55.

ZARZUR, E. (1996). "Mechanical properties of the human lumbar dura mater." Arq Neuropsiquiatr 54(3): 455-60.

ZONG, Z., LEE, H. P. and LU, C. (2006). "A three-dimensional human head finite element model and power flow in a human head subject to impact loading." J Biomech 39(2): 284-92.

Curriculum Vita

Jason Maikos

EDUCATION AND TRAINING

Doctor of Philosophy in Biomedical Engineering *September, 2001 – October, 2007*

Rutgers, The State University of New Jersey

Department of Biomedical Engineering
Piscataway, New Jersey

Bachelor of Science September, 1997 – May, 2001
Stevens Institute of Technology

Department of Chemical Biology
Hoboken, New Jersey

RESEARCH EXPERIENCE

Rutgers, The State University of New Jersey Piscataway, NJ
Graduate Fellow and Assistant September 2002 – June 2007

WORK EXPERIENCE

Stevens Institute of Technology Hoboken, NJ
Research Assistant August 1999 - August 2001

TEACHING EXPERIENCE

Rutgers, The State University of New Jersey Piscataway, NJ
Undergraduate Genetics Teaching Assistant September 2001 – December 2002

Rutgers, The State University of New Jersey Piscataway, NJ
Teaching Assistant Training Internship September 2003 – December 2003

PUBLICATIONS

J. Maikos, D.I. Shreiber, Characterization of Immediate Blood-Spinal Cord Barrier Damage due to Mechanical Trauma, NNS, San Diego, September 2004, p: 327

Maikos, J, Shreiber, D.I.. Characterization of Immediate Blood-Spinal Cord Barrier Damage due to Mechanical Tauma. Journal of Neurotrauma. 2007 Mar;24(3):492-507

Maikos, J, Elias, R, Shreiber, D.I.. Mechanical Properties of Rat Brain and Spinal Cord Dura. Journal of Neurotrauma. **Under Review**

Jason T. Maikos, Zhen Qian, Dimitris Metaxas, and David I. Shreiber, Finite element analysis of spinal cord injury in the rat, Journal of Neurotrauma. **Under Review**

PRESENTATIONS AND POSTERS

Presentations:

2004 NJCSCR Symposium, Princeton, NJ September, 2004
Title: In Vivo Tissue-Level Thresholds for Spinal Cord Injury

2004 BMES Annual Conference, Philadelphia, PA September, 2004
Title: Characterization of Immediate Blood-Spinal Cord Barrier Damage Due To Mechanical Trauma

2005 ASME Summer Bioengineering, Vail, CO June, 2005
Title: In Vivo Tissue-Level Thresholds for Spinal Cord Injury

2007 ASME Summer Bioengineering, Denver, CO June, 2007
Title: In Vivo Tissue-Level Thresholds for Spinal Cord Injury

Posters:

2004 National Neurotrauma Conference, San Diego, CA June, 2004
Title: Characterization of Immediate Blood-Spinal Cord Barrier Damage Due To Mechanical Trauma

2004 BMES Annual Conference, Philadelphia, PA September, 2004
Title: Generation of a 3D Finite Element Mesh of the Rat Spinal Cord from Magnetic Resonance Images

2005 New Jersey Biomedical Engineering Showcase, Newark, NJ March, 2005
Title: Characterization of Immediate Blood-Spinal Cord Barrier Damage Due To Mechanical Trauma

2005 NJCSCR Symposium, Newark, NJ May, 2005
Title: In Vivo Tissue-Level Thesholds for Spinal Cord Injury

2005 BMES Annual Conference, Baltimore, MD September, 2005
Title: Characterization of Immediate Blood-Spinal Cord Barrier Damage Due To Mechanical Trauma

2006 BMES, Chicago, IL October, 2006
Title: In Vivo Tissue-Level Thresholds for Spinal Cord Injury

HONORS AND SOCIETIES

- New Jersey Commission on Spinal Cord Research Fellow 2004 - 2006

- Student Member of the Biomedical Engineering Society 2003 - Current
- Laurence M. and Dorothy L. Leeds Endowed Scholarship Recipient 2003-2004
- Member of Alpha Epsilon Delta Premedical Honor Society 1999 – 2001
- 2005 BMES Conference "Outstanding Scientific and Engineering Innovation in a Poster Presentation" Award
- 2005 and 2007 ASME Summer Bioengineering Conference PhD Level Podium Competition Finalist
- 2007 New Jersey Commission on Science and Technology Post-Doctoral Fellow

US Citizen